UNIVERSITÉ DE MONTRÉAL

THERMODYNAMICS AND RHEOLOGY OF POLYMER/LAYERED SILICATE NANOCOMPOSITES: MODELING AND MEASUREMENT

HASSAN ESLAMI

DÉPARTEMENT DE GÉNIE CHIMIQUE

ÉCOLE POLYTECHNIQUE DE MONTRÉAL

THÈSE PRÉSENTÉE EN VUE DE L'OBTENTION

DU DIPLÔME DE PHILOSOPHIAE DOCTOR

(GÉNIE CHIMIQUE)

MAI 2009

©Hassan Eslami, 2009.

Library and Archives Canada

Published Heritage Branch

395 Wellington Street
Ottawa ON K1A 0N4
Canada

Bibliothèque et Archives Canada

Direction du Patrimoine de l'édition

395, rue Wellington
Ottawa ON K1A 0N4
Canada

Your file Votre référence
ISBN: 978-0-494-53795-4
Our file Notre référence
ISBN: 978-0-494-53795-4

NOTICE:

The author has granted a non-exclusive license allowing Library and Archives Canada to reproduce, publish, archive, preserve, conserve, communicate to the public by telecommunication or on the Internet, loan, distribute and sell theses worldwide, for commercial or non-commercial purposes, in microform, paper, electronic and/or any other formats.

The author retains copyright ownership and moral rights in this thesis. Neither the thesis nor substantial extracts from it may be printed or otherwise reproduced without the author's permission.

AVIS:

L'auteur a accordé une licence non exclusive permettant à la Bibliothèque et Archives Canada de reproduire, publier, archiver, sauvegarder, conserver, transmettre au public par télécommunication ou par l'Internet, prêter, distribuer et vendre des thèses partout dans le monde, à des fins commerciales ou autres, sur support microforme, papier, électronique et/ou autres formats.

L'auteur conserve la propriété du droit d'auteur et des droits moraux qui protège cette thèse. Ni la thèse ni des extraits substantiels de celle-ci ne doivent être imprimés ou autrement reproduits sans son autorisation.

In compliance with the Canadian Privacy Act some supporting forms may have been removed from this thesis.

While these forms may be included in the document page count, their removal does not represent any loss of content from the thesis.

Conformément à la loi canadienne sur la protection de la vie privée, quelques formulaires secondaires ont été enlevés de cette thèse.

Bien que ces formulaires aient inclus dans la pagination, il n'y aura aucun contenu manquant.

Canada

UNIVERSITÉ DE MONTRÉAL

ÉCOLE POLYTECHNIQUE DE MONTRÉAL

Cette thèse intitulée:

THERMODYNAMICS AND RHEOLOGY OF POLYMER/LAYERED SILICATE NANOCOMPOSITES: MODELING AND MEASUREMENT

présentée par: ESLAMI Hassan

en vue de l'obtention du diplôme de: Philosophiae Doctor

a été dûment acceptée par le jury d'examen constitué de:

M. LAFLEUR Pierre, Ph.D., président

M. GRMELA Miroslav, Ph.D., membre et directeur de recherche

M. BOUSMINA Mosto, Ph.D., membre et codirecteur de recherche

M. DUBOIS Charles, Ph.D., membre et codirecteur de recherche

M. AJJI Abdellah, Ph.D., membre

M. CHINESTA Francisco, Ph.D., membre

Dedicated to my parents and my wife

ACKNOWLEDGEMENTS

My heartfelt thanks to all my family and friends who have supported me throughout this work. This project would never have been completed without their help and encouragement.

My special thanks to my supervisor Professor Miroslav Grmela for the comments and insights he kindly offered to help shape the direction of this project.

I am also grateful to my co-supervisors Professor Mosto Bousmina and Professor Charles Dubois for their helpful guidance and suggestions.

Finally, I wish to express my gratitude to all secretaries and technical staff of the Chemical Engineering Department in Ecole Polytechnique de Montreal.

RÉSUMÉ

Dans la mise en œuvre des polymères, comme dans le cas de l'extrusion et du moulage par injection, les propriétés rhéologiques des matériaux, reliées à la microstructure macromoléculaire, jouent un rôle important. Dans les systèmes chargés, la concentration, la forme et l'orientation et/ou arrangement des particules dispersées ajoutent en complexité à la rhéologie. Dans le cas de nanocomposites polymère/couches de silicate (PLS), la taille nanométrique des particules dispersées amène une complexité additionnelle du fait de l'importance des intéractions entre le polymère et les particules et entre les particules elles mêmes.

Cette thèse se concentre particulièrement sur la rhéologie des nano suspensions des couches de silicate dans une matrice polymérique viscoélastique. La thermodynamique hors d'équilibre est employée de sorte à modéliser les comportements linéaires et non linéaires. Deux modèles rhéologiques sont développés au niveau mésoscopique dans le cas de suspensions isothermes pour des systèmes fondus partiellement et complètement exfoliés. Ces derniers tiennent compte des intéractions entre les chaînes polymériques, polymère/lamelle et lamelle/lamelle. En appliquant la base thermodynamique (GENERIC), ces aspects physiques sont incorporés dans les équations d'état qui sont le cœur des modèles rhéologiques. Les expressions des tenseurs extra-stress en découlent automatiquement. Le choix d'une description à l'échelle mésoscopique semble être un bon compromis entre le niveau de détail microscopique et la simplicité générale des équations d'état. Tout en étant apte à représenter les aspects physiques importants, le modèle permet d'obtenir aisément des solutions numériques aux équations d'état avec l'assistance du programme MATEMATICA. Des séries de résultats expérimentaux sont également présentés pour des nanocomposites PLS et contribuent à la littérature fortement présente dans le domaine de par le choix original d'une matrice biodégradable et d'une complétude nécessaire à des fins de comparaison entre le modèle et l'expérimental. Les prédictions obtenues par résolution numérique des équations d'état décrivent les réponses des suspensions à un écoulement en régime transitoire (démarrage et relaxation), permanent et

oscillatoire. Les données rhéologiques calculées par le modèle et mesurées expérimentalement et soutenues par la littérature sont par la suite comparées. Globalement, la capacité de prédiction des modèles établis semble être en accord avec les observations expérimentales.

ABSTRACT

In polymer processing, such as extrusion and injection molding, the rheological properties of polymeric materials, related to the microstructure of macromolecules, play a very important role. In filled polymer system, the extend of the dispersion, the shape and the orientation and/or arrangement of the dispersed particles add to the complexity of the rheology. In polymer/layered silicate (PLS) nanocomposites, the nanometric size of the dispersed particles brings still an additional complexity due to the importance of the polymer-particle and particle-particle interactions.

This thesis focuses on the rheology of the nano suspension of silicate layers in a viscoelastic polymer matrix. Non-equilibrium thermodynamics is employed to model its linear and nonlinear rheological behavior. Two rheological models on the mesoscopic level of description are developed for isothermal suspensions of completely and incompletely exfoliated silicate lamellae in polymer melts. The models take into account the polymer chain-polymer chain, polymer chain-lamella and lamella-lamella interactions. By following thermodynamic (GENERIC) framework, these physical features are then incorporated into governing equations of the rheological models. The expressions for the extra stress tensor arise automatically in the framework. The mesoscopic level of description chosen in this thesis appears to be a good compromise between microscopic details and overall simplicity of the governing equations. While still being able to express in the model important features of the physics involved, numerical solutions of the governing equations, needed to derive model predictions, are relatively easily (with the assistance of the software package MATEMATICA) obtained. A new set of experimental data for PLS nanocomposites is also reported. The experimental data contribute to the large pool of the data existing in literature for polymer nanocomposites by an original choice of the polymer (of particular interest due to its biodegradability) and by their completeness (that is needed for the comparison with model predictions). Predictions of the models, obtained by solving numerically their governing equations, are responses of the suspension to oscillatory, transient (start-up and relaxation) and steady shear flows. The calculated rheological data are compared with our measured experimental data and the

experimental data taken from the literature. Predictions of the models are found to be in a good agreement with results of experimental observations.

CONDENSÉ EN FRANÇAIS

Les nanocomposites dans lesquels des nanoparticules (nanotubes, nanofibres, couches de silicate) sont dispersées dans une matrice polymérique font l'objet de nombreuses études dans le domaine académique et industriel depuis les dernières années. Parmi cette technologie, une attention particulière a été prêtée aux nanocomposites polymères/silicate (PLS) de par leur disponibilité et le coût peu élevé des couches de silicate. Du fait de la taille nanométrique et du ratio de forme élevé des couches de silicate dispersées, leur incorporation même en petites quantités dans une matrice confère au nanocomposite résultant des propriétés améliorées en termes de stabilité thermique et dimensionnelles, de résistance UV et de barrière, de fini de surface et d'impression et bien entendu au niveau des propriétés mécaniques. Par rapport aux systèmes polymériques chargés conventionnels, des améliorations significatives sont obtenues à des niveaux de concentration de silicate faibles. Cela explique leur faible densité, ce qui les rend attrayant et compétitif par rapport aux autres matériaux dans le cas d'applications spécifiques. De ce fait, une quantité de travaux considérable a été réalisée d'un point de vue théorique et pratique de manière a améliorer constamment la préparation et leurs propriétés.

À des fins de caractérisation de l'état de dispersion des couches de silicate dans la matrice de polymère, la diffraction des rayons X (WAXD) et la microscopie électronique à transmission (TEM) sont couramment employés. Le TEM permet une compréhension qualitative de la structure interne du nanocomposite tandis que les pics de diffraction dans le cadre de la WAXD induisent le calcul de l'espace entre les couches de tactoides (i.e structure organisée de lamelles d'argile) de silicate dispersés dans la matrice. Néanmoins, un outil de caractérisation complémentaire semble indubitable afin de mieux cerner la structure de ces systèmes. En effet, les mesures rhéologiques sont sensibles à la microstructure et ont prouvé être une méthode effective dans le cadre des nanocomposites. De plus, la fabrication d'un produit final désirable à partir des nanocomposites PLS requière une connaissance affinée de la mise en œuvre de ces matériaux. Une telle connaissance peut être obtenue par le biais d'une compréhension poussée sur les phénomènes rhéologiques complexes aussi bien au

niveau expérimental que théorique.

Dans ce travail, un aperu de la littérature à propos de la structure des couches de silicate, les méthodes de préparation des nanocomposites et leurs caractérisations est exposé dans la section de revue de littérature avec une attention particulière sur les rôles essentiels des outils rhéologiques et de la mise en œuvre.

La thermodynamique hors d'équilibre est utilisée afin de modéliser le comportement rhéologique linéaire et non linéaire des nanocomposites PLS. Notons toutefois une complexité de l'étude rhéologique provenant de la nature et de l'orientation anisotropiques des lamelles de silicate, de leurs tailles nanométriques et bien entendu des interactions plaque-plaque et plaque-polymère. En intégrant ces paramètres physiques effectifs dans un modèle rhéologique par transformation mathématique et en étudiant leurs effets sur le comportement d'écoulement des nanocomposites, il est possible d'amener de nouvelles compréhensions au niveau de leur comportement rhéologique. Afin de pouvoir le réaliser, deux modèles rhéologiques sont développés à un niveau mésoscopique dans le cadre de suspensions isothermes de lamelles de silicate totalement exfoliées dans le mélange polymérique fondu. Ces modèles sont par la suite appliqués aux nanocomposites dans le cas de coexistence de structures intercalées/exfoliées.

Dans la première partie de cette étude, le niveau de description mésoscopique est choisi de sorte à développer un modèle rhéologique des suspensions de lamelles d'argile isothermes et incompressibles dans le mélange fondu (et de plus fournissant la transition entre la microstructure et le comportement non linéaire de l'écoulement). Lors de cette étape, l'hypothèse d'exfoliation complète et d'une dispersion homogène dans la matrice viscoélastique sont assumées pour les lamelles d'argile. Le modèle tient également compte des interactions polymère-lamelle et lamelle-lamelle. Dans ce premier modèle, deux variables d'état microstructurel sont fixés afin de caractériser la suspension. Les états des macromolécules composant le fondu sont caractérisés par le deuxième moment de distribution vectorielle bout à bout des macromolécules (i.e le tenseur de conformation $\boldsymbol{c}$) et les états des lamelles d'argile par le deuxième moment de distribution des vecteurs perpendiculaires aux lamelles

(i.e le tenseur de conformation $\boldsymbol{a}$). Après avoir choisi les variables d'état $\boldsymbol{a}$ et $\boldsymbol{c}$, le modèle est construit en débutant par le modèle FENE-P pour les polymères reformulé dans une forme générale GENERIC puis finalement appliquée aux suspensions de lamelles d'argiles dans le fondu polymérique. La base GENERIC garantit une compatibilité thermodynamique. L'expression du tenseur extra stress implique l'utilisation des énergies libres et du potentiel de dissipation et représente naturellement une partie des équations d'état.

Le niveau de description mésoscopique choisi semble être un bon compromis entre le degré de détail microscopique et la simplicité globale des équations d'état. Non seulement les aspects importants de la physique impliquée (par exemple les interactions polymère-lamelle) sont exprimés dans le modèle mais les équations d'état peuvent aussi être facilement résolues numériquement par des logiciels standards. Ces résultats numériques donnant lieu à une faculté de prédiction correspondent à des écoulements de cisaillement transitoires (start-up et relaxation) et de régime permanent des suspensions. Les données rhéologiques générées sont par la suite comparées avec les résultats expérimentaux énoncés dans la littérature. De manière générale, on note un accord dans le cas des écoulements start-up à hauts taux de cisaillements et une déviation à plus faible taux. Pour ce qui est des écoulements en régime permanent, la simulation et l'expérience sont en accord et plus particulièrement dans le cas de faibles concentrations de nanoparticules. Toutefois, des déviations sont observées à de faibles taux de cisaillement et à de hautes concentrations de silicates. Le challenge ici est donc d'identifier les processus physiques dominants dans ces situations et de les exprimer de manière efficace dans le modèle. La base du modèle demeure inchangé de part la nécessité de compatibilité thermodynamique.

La modélisation rhéologique signifie une relation entre le degré de détail microscopique et les propriétés et fonctions d'écoulements macroscopiques du fluide. La première étape vise donc à choisir un niveau de description microscopique comme point de départ. Dans le cas de fluides polymériques composés essentiellement de chaines macromoléculaires, le choix de niveau de théorie cinétique, réalisé par P.G de Gennes, donna naissance à un outil remarquable connu sous le nom de la théorie de la reptation.

Dans la deuxième étape de cette étude, la possibilité d'exprimer la physique de la reptation à un niveau d'avantage macroscopique est explorée. A ce niveau, le tenseur de conformation d'ordre deux remplace la fonction de distribution d'une chaîne en tant que variable d'état. Il y a trois raisons majeures de s'orienter vers le plan macroscopique : (i) le but ultime de cette thèse est d'étudier les suspensions de nanoparticules dans un fluide polymérique et nécessite ainsi une théorie relativement simple du fluide matriciel non chargée, (ii) les efforts requis d'interprétation et de corrélation entre les données micro et macroscopiques (rhéologie) sont minimisés, et (iii) la théorie de la reptation peut être améliorée en effectuant les descriptions à tous les niveaux.

Dans cette étape, les états des fluides polymériques sont caractérisés par les tenseurs définis symétriques et positifs de deuxième ordre. En suivant la base GENERIC, ce niveau est considéré comme un plan autonome et des éléments basiques de la physique de la reptation sont formulés dans le modèle rhéologique. Dans ce dernier, le fondu polymérique est assumé homogène, incompressible et isotherme. Les macromolécules sont représentées comme des vers assimilés à des sortes d'haltères localement (dumbbell). Deux types d'haltères sont systématiquement employés dans la modélisation : l'extensible FENE-P et l'inextensible/rigide. Rappelons que la variable caractérisant les états des chaines est l'ensemble des tenseurs de conformation $\boldsymbol{c}(s)$ où $-1 < s < 1$ est la coordonnée le long du squelette de la chaîne. Le passage d'un haltère a l'autre de manière locale permet d'introduite deux aspects : (i) un mécanisme de dissipation par reptation lors de la diffusion le long de la chaine et (ii) une énergie associée avec une interaction intra-chaîne non locales.

Afin de traduire le comportement physique de la reptation en langage mathématique, les modèles classiques d'haltères (dumbbell) sont appliquées aux fondus polymériques. L'idée principale est de passer d'une observation moléculaire des chaines sous forme de ces haltères a une description spécifique où les haltères sont présentes exclusivement de manière locale dans la chaîne. Les étapes concernant cette idée sont donc les suivantes : (i) Le tenseur de conformation local est considéré comme variable d'état, comme dans le cas de la théorie classique des haltères, (ii) les chaînes sont assumées continues (en forme de vers) afin de rem-

placer un bagage algébrique encombrant par un calcul différentiel et finalement (iii) en plus de l'extension élastique des haltères locales, de nouveaux types d'interactions intra-chaînes non local (pliage de la chaîne et autres actions) et inter-chaines exprimés sous forme de tube sous champs de force externe amenant à un dissipation par diffusion lors de la reptation. Alors que le processus énoncé précédemment n'est pas particulièrement nouveau, son implantation dans la base du formalisme GENERIC génère un nouveau modèle rhéologique et rallie les aspects attrayants de simplicité et de réalisme.

Les cinétiques respectives des haltères locales et isolées sont assumées égales dans les modèles classiques (i.e FENE-P dumbbell). Les nouveaux concepts émergeants de l'hypothèse de la reptation sont par la suite injectés dans la formule des énergies libres et des potentiels de dissipation. La motivation principale d'appliquer la reptation originale développée par de Gennes et Edwards a été justifiée de sorte à produire une meilleure cohésion avec les résultats expérimentaux rhéologiques et d'améliorer la perception physique en la rendant plus complète et intrinsèquement consistante. D'ailleurs, les prédictions à un niveau de description mésoscopique de la reptation s'accordent bien avec les observations expérimentales.

Le but ultime de cette thèse est donc de modéliser le comportement rhéologique des suspensions des couches de silicate dans les polymères fondus afin de prédire les fonctions rhéologiques linéaires et non linéaires avec un ensemble de paramètres réalistes. Ce faisant, une théorie relativement simple pour les matrices polymériques semble primordiale. Ainsi, dans la prochaine étape, les indices physiques récoltés par la théorie de la reptation sont utilisés pour refléter le comportement du fluide par le biais des tenseurs de conformation. De ce fait, des équations d'états au niveau des tenseurs de conformation sont établies en tant que base et sont directement supportées par la théorie cinétique de la reptation. Les interprétations physiques autant que la simplicité mathématique de ces dernières sont utiles dans l'atteinte du but ultime d'impliquer la théorie de la reptation dans les modèles rhéologiques dans le cas des nanocomposites développés lors de la première étape. Il est important de remarquer que la complexité apportée par la présence des nano particules rend impraticable la théorie cinétique basée sur des modèles rhéologiques.

C'est pourquoi, dans la troisième étape de ce projet, un modèle rhéologique est btit pour les suspensions isothermes des lamelles de silicate complètement exfoliées. De manière similaire aux étapes antérieures le niveau de description mésoscopique est employé. De plus, afin d'exprimer plus clairement et précisément la physique impliquée dans les faibles taux de cisaillement et faibles fréquences, les macromolécules composant le fondu sont modélisées comme des chaines confinées dans des tubes formés par les chaînes et lamelles environnantes. Dans le cas ou les chaînes sont analysés selon les haltères FENE-P, le modèle se réduit a celui développé lors de la première étape. En l'absence des lamelles, ce dernier se simplifie à un niveau mésoscopique de la reptation des chaînes énoncé lors de la deuxième étape. Du fait des interactions inter-polymériques et avec les lamelles, les macromolécules du fondu sont efficacement confinés a l'intérieur de tubes générés par l'environnement constitué d'autres macromolécules et des couches de silicate. Ce dernier aspect n'est malheureusement pas tenu compte dans la reptation d'un point de vue de détail microscopique en employant la formulation mésoscopique. Le modèle est btit en combinant le système rhéologique mésoscopique des nanocomposites PLS développé dans la première étape avec celui basé sur la reptation de l'état fondu discuté lors de la deuxième étape.

Une fois les variables d'état fixées, le modèle est formulé en construisant, en premier lieu, une base pour les équations d'état (garantissant les compatibilités thermodynamique et mécanique) puis en injectant les divers paramètres comme les données cinétiques, les variables d'état, l'énergie libre et le potentiel de dissipation. Finalement, les fonctions rhéologiques prédites pour un écoulement de cisaillement en régime permanent, transitoire et SAOS (cisaillement oscillatoire de faible amplitude) sont comparés avec des données expérimentales. Une attention particulière est prêtée dans la région de faibles fréquences et taux de cisaillement. Les prédictions basées sur le modèle établi montrent une bonne description générale du comportement rhéologique des nanocomposites PLS en les comparants aux données expérimentales.

Dans la dernière étape du projet, un nouvel ensemble de données expérimentales et leurs évaluations par les deux modèles mésoscopique sont développés pour les nanocom-

posites PLS. La création de ces données contribue directement à celles déjà présentes dans la littérature appropriée. Les propriétés viscoélastiques linéaire et non linéaire des nanocomposites PLS à l'état fondu sont évaluées en préparant des mélanges à l'état fondu de poly[butylene succinate-co-adipate] (PBSA) et des montmorillonite organiquement modifiées (Cloisite 30B). Les résultats des analyses WAXD combinés à ceux des images TEM révèlent la présence de certains tactoides. La région viscoélastique linéaire se trouve être sensible aux interactions provenant des couches de silicate et se réduit au fur et à mesure que la concentration d'argile est augmentée. Cette observation est attribuée à la taille nanométrique des lamelles d'argile et aux fortes interactions polymère/lamelle et lamelle/lamelle. Des mesures SAOS dans la région linéaire montrent une viscosité complexe croissante à de faibles fréquences et un plateau de module élastique (indication du comportement pseudo-solide) à une faible fréquence. Un comportement fortement rhéo-fluidifiant est observée pour les nanocomposites hautement chargés sur le spectre de taux de cisaillement. Un comportement inhabituel est observé dans le cas de la différence de contraintes normales dans un régime permanent. En effet, à de faibles taux de cisaillement, ces dernières sont supérieures à celles recensées pour le polymère pur. Une relation opposée est observée à des taux de cisaillement relativement élevés. Les comportements rhéologiques transitoires (démarrage et relaxation après arrêt de démarrage d'écoulement) sont aussi étudiés pour ce système de nanocomposites. Les deux modèles que nous avons développés dans la première et troisième étape nous permettent de corréler les comportements rhéologiques observés aux mécanismes physiques se produisant à une échelle mésoscopique dans le nanocomposite. Nous rappelons que les modèles établis tiennent compte des interactions entre les chaînes polymériques, entre ces dernières et les nano-lamelles d'argile et lamelles-lamelle. Avec ces considérations, il est également possible d'attribuer à chaque acteur, polymère ou nano charge, sa contribution. L'évolution de la microstructure des nanocomposites préparés est aussi abordée dans le cas d'écoulement de démarrage transitoire allez et retour. La structure des nanocomposites exposés à un écoulement est évaluée en réalisant des séries d'expériences rhéologiques de démarrage (croissance de contrainte) dans le cas de cisaillement en régime transitoire de type allez. La structure au repos est également

étudiée en effectuant des expériences d'inversion d'écoulement pour des niveaux de charge et taux de cisaillement différents. Une attention particulière est apportée à l'amplitude des dépassements sur la contrainte de cisaillement et la différence des contraintes normales pendant les tests de démarrage inversés. Par le biais des modèles, nous sommes capables d'interpréter et d'expliquer les phénomènes observés dans le cas d'expériences d'inversion d'écoulement.

TABLE OF CONTENTS

DEDICATION . . . . . **iv**

ACKNOWLEDGEMENTS . . . . . **v**

RÉSUMÉ . . . . . **vi**

ABSTRACT . . . . . **viii**

CONDENSÉ EN FRANÇAIS . . . . . **x**

TABLE OF CONTENTS . . . . . **xviii**

LIST OF FIGURES . . . . . **xxiv**

NOMENCLATURES . . . . . **xxx**

1 INTRODUCTION AND OBJECTIVE **1**

1.1 Introduction 1

1.2 Originality of the work 3

1.3 Objective 3

2 LITERATURE REVIEW **5**

2.1 Structure of layered silicates 5

2.2 Structure of nanocomposites 6

2.3 Preparative methods 8

2.3.1 In situ polymerization 8

2.3.2 Direct mixing 8
2.3.2.1 Solution mixing 9
2.3.2.2 Melt mixing 9
2.4 Characterization of nanocomposites 10
2.5 Rheological behavior of nanocomposites 11
2.5.1 Experimental rheology 12
2.5.1.1 Dynamic oscillatory shear measurements 13
2.5.1.2 Steady state shear measurements 17
2.5.1.3 Stress growth measurements 22
2.5.2 Theoretical modeling 24
2.5.2.1 Thermodynamic approach 27

3 ORGANIZATION OF THE ARTICLES 32

4 A MESOSCOPIC RHEOLOGICAL MODEL OF POLYMER/LAYERED SILICATE NANOCOMPOSITES 35

4.1 Introduction 36
4.2 Formulation of the model 37
4.2.1 FENE-P model 37
4.2.1.1 Standard formulation 38
4.2.1.2 Formulation with the free energy 40
4.2.1.3 Formulation with the free energy and the momentum equation 42
4.2.2 Lamellae 44
4.2.3 FENE-P dumbbells and lamellae 49
4.3 Results and discussion 54
4.3.1 Effects of the shear rate on transient material functions 59
4.3.2 Effects of the mobility coefficients on transient material functions . . 59
4.3.3 Effects of the nano-particle loading on material functions 62
4.3.4 Effects of the mobility tensors on material functions 65

4.3.5 Sensitivity of the model to other parameters 68
4.3.6 Comparison with experimental data 72
4.4 Concluding remarks 74
4.5 Appendix: GENERIC 76
4.5.1 Classical hydrodynamics: Standard formulation 76
4.5.2 GENERIC: Complex fluids 78
4.5.3 Examples of particular realizations of GENERIC 79
4.5.3.1 Classical hydrodynamics: GENERIC formulation 80
4.5.3.2 Kinetic theory (Boltzmann equation) 80
4.5.3.3 The rheological model developed in this paper 81
4.5.3.4 Fiber suspensions 81
Acknowledgements 83
References 83

5 MESOSCOPIC FORMULATION OF REPTATION 89
5.1 Introduction 90
5.2 Model formulation 93
5.2.1 Rigid or FENE-P dumbbell 94
5.2.2 Local rigid or FENE-P dumbbell 97
5.2.2.1 Free energy 100
5.2.2.2 Dissipation potential 101
5.2.2.3 Relation to the level $\mathcal{L}_{1kt}$ 102
5.3 Results and discussion 107
5.3.1 Model predictions and comparison with experimental data 110
5.3.1.1 Effects of the shear rate on transient material functions . . . 112
5.3.1.2 Effects of mobility coefficients on material functions 112
5.3.1.3 Sensitivity of the model to other parameters 116
5.3.1.4 Comparison with experimental data 118

5.4 Concluding remarks 122

Acknowledgements 125

References 125

6 A MESOSCOPIC TUBE MODEL OF POLYMER/LAYERED SILICATE NANOCOMPOSITES 129

6.1 Introduction 130

6.2 Model formulation 131

6.2.1 GENERIC constitutive relations 132

6.2.1.1 State variables 132

6.2.1.2 Kinematics 134

6.2.1.3 Dissipation 135

6.2.1.4 Free energy 138

6.2.2 Material parameters 140

6.3 Results and discussion 142

6.3.1 Model predictions 142

6.3.1.1 Effects of the shear rate on transient material functions . . . 143

6.3.1.2 Effects of the mobility coefficients on the material functions 145

6.3.1.3 Effects of the nano-particle loading on the material functions 148

6.3.2 Comparison with experimental data 153

6.4 Conclusion 160

6.5 Appendix: GENERIC framework 161

6.5.1 Free energy 161

6.5.2 Kinematics 161

6.5.3 Dissipation 162

6.5.4 Properties of solutions of GENERIC 162

Acknowledgements 163

References 163

7 LINEAR AND NONLINEAR RHEOLOGY OF POLYMER/LAYERED SILICATE NANOCOMPOSITES 166

7.1 Introduction 167

7.2 Experimental 169

7.2.1 Materials 169

7.2.2 Nanocomposite preparation 170

7.2.3 X-ray diffraction 171

7.2.4 Transmission electron microscopy 171

7.2.5 Rheological measurements 171

7.3 Modeling 172

7.3.1 Model I 173

7.3.2 Model II 176

7.3.3 Exfoliated and intercalated lamellae 179

7.4 Results and discussion 180

7.4.1 X-ray and microscopic analysis 180

7.4.2 Linear viscoelastic properties 184

7.4.3 Nonlinear viscoelastic properties 188

7.4.3.1 Effects of the shear rate on transient material functions . . . 189

7.4.3.2 Effects of the clay loading on the material functions 197

7.4.4 Model predictions and comparison with experimental data 206

7.5 Conclusions 210

Acknowledgements 211

References 212

8 STRUCTURE BUILD-UP AT REST IN POLYMER NANOCOMPOSITES: FLOW REVERSAL EXPERIMENTS 216

8.1 Introduction 217

8.2 Experimental 219

8.2.1 Materials 220
8.2.2 Preparation of nanocomposites 220
8.2.3 Characterization of nanocomposites 221
8.2.3.1 WAXD and TEM 221
8.2.3.2 Rheology 221
8.3 Modeling 222
8.4 Results and discussion 226
8.4.1 Morphology 226
8.4.2 Rheology 227
8.5 Conclusion 246
Acknowledgements 247
References 247

9 SUMMARY AND RECOMMENDATIONS 250
9.1 General discussion and conclusions 250
9.2 Recommendations 256

Bibliography 258

LIST OF FIGURES

2.1 Structure of 2:1 phyllosilicates. [Sinha Ray and Okamoto (2003b)]. 6

2.2 Schematic of different types of composites (a) phase separated microcomposite (b) intercalated nanocomposite (c) exfoliated nanocomposite [Alexandre and Dubois (2000)]. 7

4.1 Effect of the shear rate on the stress growth and relaxation of the material functions: (a) viscosity and (b) first normal stress coefficient. 60

4.2 Effect of the mobility coefficient of polymer Λ_0^{cc} on the stress growth and relaxation of the material functions: (a) viscosity and (b) first normal stress coefficient. 61

4.3 Effect of the mobility coefficient of plate Λ_0^{aa} on the stress growth and relaxation of the material functions: (a) viscosity and (b) first normal stress coefficient. 63

4.4 Effect of the interaction mobility coefficient Λ_0^{ca} on the stress growth and relaxation of the material functions: (a) viscosity and (b) first normal stress coefficient. 64

4.5 Effect of the nano-particle weight fraction on the stress growth and relaxation of the material functions: (a) viscosity and (b) first normal stress coefficient. 66

4.6 Effect of the nano-particle weight fraction on the steady shear flow material functions: (a) viscosity and (b) first normal stress coefficient. 67

4.7 Effect of the mobility tensor of plates, Λ^{aa} on the steady shear material functions: (a) viscosity and (b) first normal stress coefficient. 69

4.8 Effect of the parameter b on the stress growth and relaxation viscosity. . . . 70
4.9 Effect of the polymer-plate interaction κ' on the stress growth and relaxation viscosity. 71
4.10 Effect of the scaling parameter χ on the stress growth and relaxation viscosity. 71
4.11 Model predictions and comparison with experimental data in transient shear flow. Data are taken from Wu et al. (2005). 72
4.12 Model predictions and comparison with experimental data in transient shear flows. Data are taken from Ayyer and Leonov (2004). 73
4.13 Model predictions and comparison with experimental data in steady shear flow. Data are taken from Krishnamoorti et al. (2001). 73

5.1 Effect of the shear rate on the stress growth (a) viscosity and (b) first normal stress. 111
5.2 Effect of the local mobility coefficient Λ_0^{11} on the stress growth (a) viscosity and (b) first normal stress. 113
5.3 Effect of the reptation mobility coefficient Λ_0^{22} on the stress growth (a) viscosity and (b) first normal stress. 114
5.4 Effects of the local mobility coefficient Λ_0^{11} on the storage and loss modulus. 115
5.5 Effects of the reptation mobility coefficient Λ_0^{22} on the storage and loss modulus 116
5.6 Effects of the parameter K on the storage and loss modulus. 117
5.7 Effects of the parameter f on the storage and loss modulus 117
5.8 Model predictions and comparison with experimental data in small angle oscillatory shear flows: the storage and the loss modulus. 118
5.9 Model predictions and comparison with experimental data in steady shear flow. 119
5.10 Model predictions and comparison with experimental data in small angle oscillatory shear flows: the storage and the loss modulus. 120
5.11 Model predictions and comparison with experimental data in steady shear flow. 120

5.12 Model predictions and comparison with experimental data in transient shear flows. 121

5.13 Model predictions and comparison with experimental data in transient shear flow. 122

6.1 Effect of shear rate on stress growth material functions (a) shear viscosity (b)first normal stress differences 144

6.2 Effect of plate mobility coefficient Λ_0^{33} on stress growth material functions (a) shear viscosity (b)first normal stress differences 146

6.3 Effect of polymer plate interaction mobility coefficient on stress growth viscosity (a) effect of Λ_0^{13} (b) effect of Λ_0^{23} 147

6.4 Effect of the nano-particle weight fraction on stress growth material functions (a) shear stress (b) first normal stress differences 149

6.5 Effect of the nano-particle weight fraction on the (a) steady state viscosity (b) Cox-Merz relation 151

6.6 Effect of the nano-particle weight fraction on the (a) storage modulus G' (b) loss modulus G'' 152

6.7 Model predictions and comparison with experimental data in steady shear flow (a) steady viscosity (b) steady first normal stress versus shear stress (c) steady first normal stress versus shear rate 155

6.8 Model predictions and comparison with experimental data (a) Yield stress at different silicate loading, model predictions (b) Yield stress, comparison between model and experimental data. 157

6.9 Model predictions and comparison with experimental data in oscillatory shear flow (a) storage modulus G' (b) complex viscosity η^*. 159

7.1 X-ray patterns of pure PBSA, Cloisite 30B and PBSAC30BNs 181

7.2 TEM images of PBSAC30BN1 with two different magnifications 182

7.3 TEM images of PBSAC30BN4 with two different magnifications 183

7.4 Normalized storage modulus versus strain for pure PBSA and its nanocomposites 185
7.5 Linear viscoelastic data (a) storage modulus (b) complex viscosity 186
7.6 Storage modulus at low frequency ($\omega = 0.01 rad/s$) versus clay volume fraction. Lines are the linear regression through the corresponding data points. 188
7.7 Effect of shear rate on the start-up material functions of pure PBSA (a) shear stress (b) normal stress difference 190
7.8 Effect of shear rate on the relaxation material functions of pure PBSA (a) shear stress (b) normal stress difference 191
7.9 Effect of shear rate on the start-up material functions of PBSAC30BN2 (a) shear stress (b) normal stress difference 193
7.10 Effect of shear rate on the normalized start-up material functions of PBSAC30BN2 (a) shear stress (b) normal stress difference 194
7.11 Effect of shear rate on the relaxation material functions of PBSAC30BN2 (a) shear stress (b) normal stress difference 195
7.12 Effect of shear rate on the normalized relaxation material functions of PBSAC30BN2 (a) shear stress (b) normal stress difference 196
7.13 Effect of clay loading on the (a) steady state viscosity (b) yield stress 198
7.14 Effect of clay loading on the (a) start-up viscosity (b) stress relaxation . . . 200
7.15 Effect of clay loading on the steady state material functions (a) normal stress difference versus shear rate (b) normal stress difference versus shear stress . 203
7.16 Effect of clay loading on the normal stress difference (a) start-up (b) relaxation 205
7.17 Shear stress components arising from polymer contribution $\sigma_{12,c}$, particles contribution $\sigma_{12,a}$ and total shear stress σ_{12} (a) steady state shear stress (b) transient shear stress. 209

8.1 TEM micrograph of PN5.7S 226
8.2 WAXD patterns of pure PBSA, C30B and nanocomposites 227

8.3 Forward start-up experiments for samples used at different reverse start-up flow experiments (a) shear stress and (b) normalized shear stress 228

8.4 Forward start-up experiments for samples used at different reverse start-up flow experiments(a) normal stress difference and (b) normalized normal stress difference 229

8.5 Reverse start-up experiments after cessation of the forward start-up flow for various rest times (step 3) (a) shear stress and (b) normal stress difference . 231

8.6 Flow reversal experiment for PN3.4S at $\dot{\gamma}_0 = 0.2\ s^{-1}$ (a) normalized shear stress and (b) normalized normal stress difference 233

8.7 Flow reversal experiment for PN5.7S at $\dot{\gamma}_0 = 0.2\ s^{-1}$ (a) normalized shear stress and (b) normalized normal stress difference 234

8.8 Components of the lamellae conformation tensor a_{ij} as functions of time (a) in the forward start-up flow (b) in the relaxation following the forward start-up flow 236

8.9 Ellipsoidal representation of the conformation tensors during the forward start-up flow (a) polymer conformation tensor (b) lamellae conformation tensor . . 237

8.10 Ellipsoidal representation of the conformation tensors after the forward start-up flow at different rest times (a) polymer conformation tensor (b) lamellae conformation tensor 238

8.11 Amplitude of the overshoot for PN3.4S at $\dot{\gamma}_0 = 0.1\ s^{-1}$ at different rest times: model predictions and comparison with experimental data (a) shear stress (b) normal stress difference 240

8.12 Amplitude of the overshoot for PN5.7S at $\dot{\gamma}_0 = 0.1\ s^{-1}$ at different rest times: model predictions and comparison with experimental data (a) shear stress (b) normal stress difference 241

8.13 Components of the lamellae conformation tensor (a_{12} and a_{22}) as functions of time at different shear rates in the forward start-up flow. 242

8.14 Effect of clay loading on the amplitude of stress overshoots at $\dot{\gamma}_0 = 0.1\ s^{-1}$ at different rest times: model predictions and comparison with experimental data (a) normalized stress overshoot amplitude (b) master curve 243

8.15 Effect of the plate-plate interaction parameter on the structure build-up during the rest time (a) $\kappa = 1 \times 10^{-22}$ (b) $\kappa = 7 \times 10^{-23}$ (c) $\kappa = 3 \times 10^{-24}$. (—) and (...) indicate the ellipsoidal representation of lamellae conformation tensor at the end of the forward start-up flow and 30 min. after cessation of the forward start-up flow respectively. 244

8.16 Effect of the polymer-plate interaction parameter on the structure build-up during the rest time (a) $\kappa' = 1 \times 10^{-22}$ (b) $\kappa' = 6 \times 10^{-23}$ (c) $\kappa' = 5 \times 10^{-24}$. (—) and (...) depict the ellipsoidal representation of lamellae conformation tensor at the end of the forward start-up flow and 30 min. after cessation of the forward stat-up flow respectively. 245

Nomenclatures

Greek letters

α	clay volume fraction
α_{max}	maximum packing fraction
γ	strain
γ_0	strain amplitude
$\dot{\gamma}$	shear rate
$\boldsymbol{\delta}$	identity tensor
ζ	friction (bead-fluid) coefficient
η	shear viscosity
η_0	zero shear limit of the viscosity coefficient
η^*	complex viscosity
$[\eta]$	intrinsic viscosity
κ	topological plate-plate interaction
κ'	topological polymer-plate interaction
$\mathbf{\Lambda}^{cc}$	polymer mobility tensor
$\mathbf{\Lambda}^{aa}$	lamellae mobility tensor
$\mathbf{\Lambda}^{ca}$	polymer-lamellae interaction mobility tensor
ξ	Gordon-Schowalter phenomenological parameter
Ξ	dissipation potential
ρ	mass per unit volume

Greek letters continue...

ρ_c	mass density of the polymer
ρ_a	mass density of the lamellae
σ_{12}	shear stress
$\boldsymbol{\sigma}$	extra stress tensor
Φ	free energy
Φ^c	free energy of polymer macromolecules
Φ^a	free energy of lamellae
χ	rescaling parameter
$\psi(\boldsymbol{Q})$	distribution function of macromolecules
$\psi(\boldsymbol{n})$	distribution function of lamellae
Ψ_1	first normal stress differences coefficient
Ψ_2	second normal stress differences coefficient
Ψ_{10}	zero shear limit of the first normal stress differences coefficient
Ψ_{20}	zero shear limit of the second normal stress differences coefficient
ω	angular frequency
$\mathcal{L}_{ds}$	level of direct molecular simulations
$\mathcal{L}_{1kt}$	level of reptation theory
$\mathcal{L}_{ct}$	level of conformation tensor
$tan\ \delta$	loss factor

English letters

$\boldsymbol{a}$	plate conformation tensor
A_0	surface area of the lamella
b	extensibility parameter
$\boldsymbol{c}$	polymer conformation tensor
$E(x)$	energy
E^c	energy of polymer macromolecules
E^a	energy of lamellae
G'	storage modulus
G''	loss modulus
$G'_{HF,rel}$	relative high frequency storage modulus
G'_{HF}	high frequency storage modulus of nanocomposite
$G'_{HF,m}$	high frequency storage modulus of matrix
h	thickness of the lamella
H	elastic modulus of the dumbbell spring
k_B	Boltzmann constant
K_{flex}	parameter characterizing the flexibility of plates
L	Poisson bivector
$\boldsymbol{m}$	vector lying in the plane of the lamella
M_c	molecular weight of the polymer
$\boldsymbol{n}$	unit vector perpendicular to the lamella
n_c	number density of the polymer macromolecules
n_a	number density of the clay platelets
N_1	first normal stress difference
N_2	second normal stress difference
N_A	Avogadro number
p	scalar hydrostatic pressure

English letters continue...

$\boldsymbol{Q}$	end-to-end vector of macromolecules
Q_0	the largest extension of the dumbbell
$S(x)$	entropy
S^c	entropy of polymer macromolecules
S^a	entropy of lamellae
T	temperature
$\boldsymbol{u}$	overall momentum field
V	volume

Abbreviations

CEC	cation exchange capacity
C30B	Cloisite 30B
EVA	ethylene-vinyl acetate copolymer
GENERIC	General Equation of Non-Equilibrium Reversible-Irreversible Coupling
LVE	linear viscoelastic
PBSA	poly[(butylene succinate)-co-adipate]
PBT	poly(butylene terephthalate)
PEO	poly (ethylene oxide)
PLA	polylactide
PLS	polymer/layered silicate
PMMA	poly(methyl methacrylate)
PVA	poly (vinyl alcohol)
SAOS	small angle oscillatory shear
TEM	transmission electron microscopic
TGA	thermogravimetric analysis
WAXD	wide angle x-ray diffraction

CHAPTER 1

INTRODUCTION AND OBJECTIVE

1.1 Introduction

Polymer composites in which the size of dispersed particles is nanometric (at least in one dimension) are called nanocomposites. This type of suspensions has recently attracted a considerable interest in polymer science research and technology [Alexandre and Dubois (2000)]. Polymer/layered silicate (PLS) nanocomposites represent a well-know example of these materials. Due to the nanometric size and the high aspect ratio of dispersed silicate layers, their incorporation within polymer matrices results in an enhancement of the dimensional and thermal stability, UV resistance and barriers properties, surface finishing and surface printability, and to some extent also in mechanical properties [Alexandre and Dubois (2000); Sinha Ray and Okamoto (2003b); Sinha Ray and Bousmina (2005a)]. In contrast to conventional filled polymer system, dramatic improvements are seen already at low level of silicate loading. PLS nanocomposites are therefore lighter than conventional composites. This property by itself makes them superior to other materials in specific applications [Sinha Ray and Bousmina (2005a)]. Due to the importance of PLS nanocomposites for the scientific and technological advancement, a considerable amount of work, both experimental and theoret-

ical, has recently been devoted to them. One of the challenges in the preparation of PLS nanocomposites is the hydrophilic nature of clay lamellae which makes them incompatible with normally hydrophobic polymeric materials. An ion-exchange reaction is usually done to make the surface of silicate layers hydrophobic which then renders layered silicates compatible with polymer matrices. Different types of nanocomposite can be created by varying the strength of the interfacial interactions between the polymer matrix and clay lamellae and the methods used for their preparation. They are classified into three categories: intercalated, exfoliated and coexistence intercalated/exfoliated nanocomposites [Sinha Ray and Bousmina (2005a)]. Intercalated structure is achieved when a few extended polymeric chains are intercalated between clay galleries while exfoliated structure is obtained when the clay tactoids are completely delaminated and the individual clay lamellae are dispersed in the polymer matrix.

In order to characterize the state of dispersion of silicate layers in polymer matrix, wide angle x-ray diffraction (WAXD) and transmission electron microscopy (TEM) are commonly used. TEM gives qualitative understanding of the internal structure while diffraction peaks in WAXD allow calculation of the interlayer spacing of silicate tactoids dispersed in polymer matrix. Rheological measurements represent another, complementary to WAXD and TEM, way to obtain an information about the internal structure of the nanocomposites. Rheology has been found to be very sensitive to the microstructure and has already proved to be successful in the characterization of the nanocomposites [Solomon et al. (2001); Sinha Ray and Bousmina (2005b); Zhao et al. (2005); Krishnamoorti and Giannelis (1997); Wu et al. (2005); Krishnamoorti et al. (2001); Ayyer and Leonov (2004); Tung et al. (2005); Mobuchon et al. (2007)]. Moreover, producing a desirable end-use product fabricated by PLS nanocomposites requires a complete knowledge of the processability of these materials. Such a knowledge can be only obtained through a comprehensive understanding of the complex rheology of these systems from both experimental measurements and theoretical modeling points of view.

1.2 Originality of the work

A more complete understanding of the rheological behavior of complex fluids can be achieved by theoretical modeling of their flow behavior, by a systematic rheological measurements, and by the comparison of model predictions with results of the observations. The rheology of polymer nanocomposites is complex due to the anisotropic nature of the silicate platelets resulting in their flow induced orientation and/or organization, nanometric size of clay lamellae and complex plate-plate and polymer-plate interactions. An incorporation of these physical features into the rheological models and an investigation of their influence on the flow behavior bring a new understanding of the behavior of these systems. Even though rheological modeling of these system is believed to play an important role for understanding the processability and microstructure of these materials, comprehensive rheological models of these systems are still very rare. Moreover, so far no comprehensive rheological model based on thermodynamic approach has been developed for PLS nanocomposites.

1.3 Objective

The objective of this thesis is to develop rheological models of PLS nanocomposites, make systematic measurements of their flow behavior, and to compare results of measurements with model predictions. The models are original. They are based on non-equilibrium thermodynamics and predict both linear and nonlinear rheological material functions.

A complete set of rheological measurements is needed to evaluate the models. Although the rheological behavior of PLS nanocomposites have been extensively studied experimentally [Solomon et al. (2001); Sinha Ray and Bousmina (2005b); Zhao et al. (2005); Krishnamoorti and Giannelis (1997); Wu et al. (2005); Krishnamoorti et al. (2001); Ayyer and Leonov (2004); Tung et al. (2005); Mobuchon et al. (2007)], no complete set of rheological measurements that includes both linear and nonlinear material functions (especially the transient normal stress differences) for PLS nanocomposites has been, to the best of our knowledge, reported. The experimental part of the thesis includes therefore systematic rheological measurements that

are subsequently compared with the rheological models developed in the theoretical part.

CHAPTER 2

LITERATURE REVIEW

In this chapter we briefly review the literature dealing with the structure of layered silicates, preparation methods of the nanocomposites, and with their characterization. Special attention is paid to the role of rheology in the characterization and processing of these materials.

2.1 Structure of layered silicates

Mica, one of the most well known layered silicate, has relatively large sheets and strong bounds between the layers. On the other hand, phyllosilicates or smectic, the most commonly used layered silicate is composed of small sheets with relatively weak bonds between the adjacent layers [Ajayan et al. (2003)]. Montmorillonite, one of the wieldy used layered silicate in polymer nanocomposites, belongs to the family of 2:1 phyllosilicates. As shown in figure 2.1, the structure of 2:1 phyllosilicates consists of two sheets of silica tetrahedral with an edge-shared octahedral sheet of either aluminum or magnesium hydroxide [Ajayan et al. (2003); Sinha Ray and Okamoto (2003b); Sinha Ray and Bousmina (2005a)]. This family of layered silicates is usually characterized by a moderate negative surface charge (cation exchange capacity, CEC) which is usually expressed in meq/100 g. It should be noted that this charge differs from layer to layer, and the reported value is an average over the whole crystal.

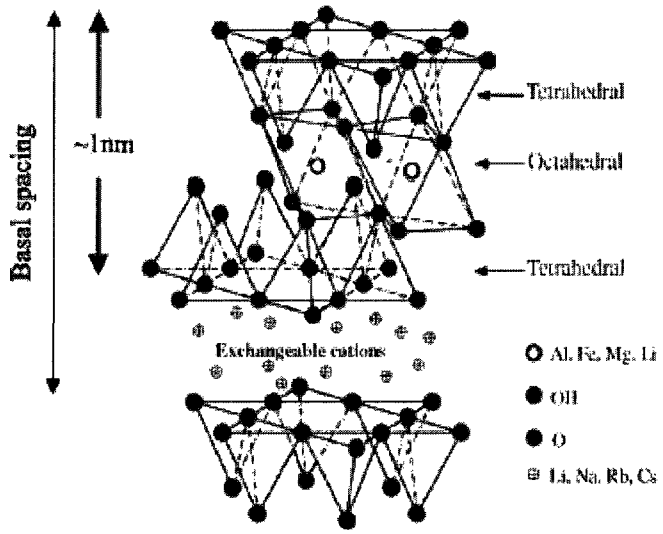

Figure 2.1: Structure of 2:1 phyllosilicates. [Sinha Ray and Okamoto (2003b)].

Silicate layers are intrinsically hydrophilic while the majority of polymeric materials are hydrophobic. Consequently, pristine clay is only compatible with the hydrophilic polymers, such as poly (ethylene oxide) (PEO) or poly (vinyl alcohol) (PVA) [Sinha Ray and Okamoto (2003b)]. To render layered silicates compatible with other polymer matrices, an exchange reaction can be performed to replace the inorganic exchange ions in the galleries between the layers with alkylammonium surfactants. This ion-exchange reaction does not make only the surface of silicate layers hydrophobic, it also increases the layer spacing of the pristine clay. A monomer or a polymeric chain can then readily enter into the space between the layers and consequently the PLS nanocomposite can be formed [Ajayan et al. (2003); Sinha Ray and Okamoto (2003b); Sinha Ray and Bousmina (2005a)].

2.2 Structure of nanocomposites

Depending on strength of the interfacial interactions between the polymer matrix and the layered silicate and also on the preparation method, three different types of the structure of

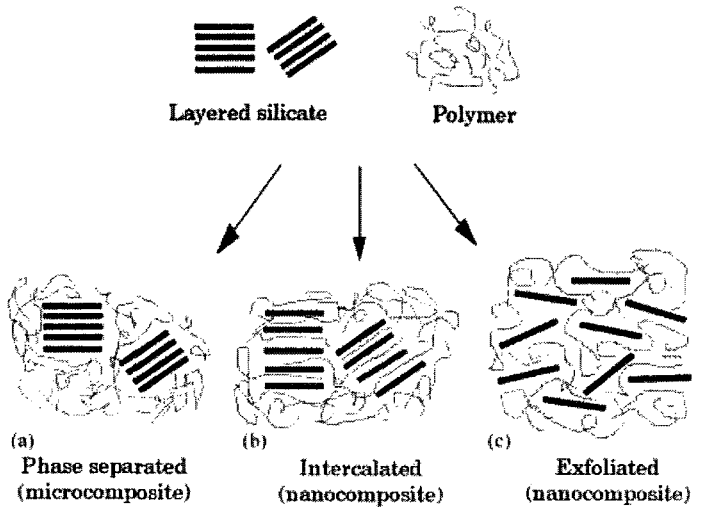

Figure 2.2: Schematic of different types of composites (a) phase separated microcomposite (b) intercalated nanocomposite (c) exfoliated nanocomposite [Alexandre and Dubois (2000)].

the PLS composites can be generated. Schematic representation of these three structures are shown in figure 2.2 [Alexandre and Dubois (2000)].

(i) Phase separated structure: this composite, also known as microcomposite, is obtained when polymeric chains are unable to intercalate between the silicate sheets.

(ii)- Intercalated structure: intercalated structure is achieved when a few extended polymeric chains are intercalated between clay galleries. This leads to a well ordered multilayer morphology in which the polymer is presented in the interlayer galleries but the layered structure of the silicate still remains unchanged. This kind of composites is called intercalated nanocomposites.

(iii)- Exfoliated structure: this structure is obtained when the clay tactoids are completely delaminated and the individual clay lamellae are dispersed in the polymer matrix. In this type of composites (also known as exfoliated nanocomposites) the clay content is much lower than that of the intercalated nanocomposites. The exfoliated nanocomposites themselves

may be divided in two categories: (i) ordered exfoliated nanocomposites where clay tactoids are broken into individual layers but still remained in an ordered array and (ii) disordered exfoliated nanocomposites where individual silicate layers are randomly dispersed in polymer matrix [Sinha Ray and Bousmina (2005a)].

2.3 Preparative methods

As already mentioned, in order to successfully prepare PLS nanocomposites, polymeric chains have to be intercalated into the silicate galleries. For this purpose, one can use either direct mixing method or in-situ polymerization method [Alexandre and Dubois (2000); Ajayan et al. (2003); Sinha Ray and Okamoto (2003b); Sinha Ray and Bousmina (2005a)]. Below, we briefly explain these methods.

2.3.1 In situ polymerization

In this method the clay layers are swollen within the liquid monomer or a monomer solution so that the polymerization can take place between the intercalated platelets. One of the advantages of this method is the ability to graft the polymer right on the surface of particles. So far, many different types of nanocomposites have been successfully prepared by the in-situ polymerization method. Some examples of nanocomposites prepared by this method are poly(methyl methacrylate) (PMMA) nanocomposites reported by Okamoto et al. (2000) and polystyrene (PS) nanocomposites reported by Okamoto et al. (2001).

2.3.2 Direct mixing

In this technique the polymeric chains are directly inserted between the silicate galleries either in the melt state or in solution.

2.3.2.1 Solution mixing

In solution mixing, also known as solvent-casting technique, silicate layers are first swollen in a solvent (e.g. water, chloroform, or toluene) and then the polymer is added to the resultant silicate layers. During the mixing process the polymeric chains displace the solvent present within the sheets of the clay. The solvent is then removed from the solution under vacuum [Sinha Ray and Okamoto (2003b); Sinha Ray and Bousmina (2005a)].

2.3.2.2 Melt mixing

Melt mixing is one of the most wieldy used techniques in polymer processing industry. This technique has been progressively used in the nanocomposites industry during recent past mainly because of its compatibility with the traditional melt mixing devices such as extrusion and injection molding. Another advantage of this method is its environmentally friendly nature because of the absence of the chemical solvent. In the melt mixing technique, clay platelets are mixed with the polymer matrix directly in the melt state. In this method, one can either first add silicate layers to polymer matrix in solid state and then mix them in the melt state or first melt the polymer and then add clay to the polymer in the melt state.

Different types of polymer nanocomposites (e.g. intercalate, exfoliate) have been successfully prepared by this technique. For example, polypropylene/clay nanocomposite was prepared by melt mixing of organophilic clay, polypropylene, and compatibilizer by Solomon et al. (2001) and the rheology of resultant nanocomposite was investigated. Melt intercalation method was also employed for the preparation of nanocomposite of polyamide 6 and organically modified montmorillonite using twin screw extruder. It was reported that the resultant nanocomposites for low clay contents was exfoliated [Liu et al. (1999)]. Nanocomposites of poly[(butylene succinate)-co-adipate] (PBSA) and different types of commercially available organically modified montmorillonite were also prepared by direct melt mixing [Sinha Ray and Bousmina (2005b); Sinha Ray et al. (2005)]. It was found that depending on the organically modified montmorillonite, different degrees of dispersion were achieved. Among

organically modified montmorillonite, Cloisite 30B was proven to be the most compatible with PBSA because of the strong interaction between the "CO" group on the PBSA and the diols on the Cloisite 30B [Sinha Ray and Bousmina (2005b); Sinha Ray et al. (2005)]. We also employ direct melt mixing method for preparation of the nanocomposites studied in this thesis.

2.4 Characterization of nanocomposites

In PLS nanocomposites, the state of dispersion of silicate layers in polymer matrix is usually monitored by using a wide angle x-ray diffraction (WAXD) analysis and transmission electron microscopic (TEM) observations.

WAXD offers a convenient method to identify the structure of intercalated nanocomposite by monitoring the position, shape, and intensity of the basal reflections of distributed silicate layers in the polymer matrix. The advantages of WAXD are its easiness and wieldy availability. It is the most commonly used tool in the investigation of the structure of PLS nanocomposites [Alexandre and Dubois (2000); Sinha Ray and Okamoto (2003b); Sinha Ray and Bousmina (2005a)]. As earlier mentioned, in the case of intercalated nanocomposites, a well ordered multilayer morphology can be obtained. In this kind of nanocomposites, the presence of multilayer ordered structure allows the interlayer spacing to be determined by WAXD. The diffraction peak of intercalated nanocomposites shifts to the lower angle relative to the pristine clay which means an increase in the interlayer spacing of clay layers. By using angular location of the peaks and by applying Bragg's law the interlayer spacing of clay lamellae can be determined (the equation $n\ \lambda = 2\ d\ sin\theta$ is called Bragg's law in which d is the distance between diffractional lattice planes, λ is the wave length of the incident X-ray beam used in the diffraction experiment, n is an integer and θ is the measured diffraction angle). However, In the case of large separated clay layers (i.e. $d > 8$ nm but still ordered silicate layers) or for exfoliated clay lamellae with disordered structure WAXD no longer displays diffraction peaks [Alexandre and Dubois (2000)]. Their disappearance in WAXD patterns

may be at least partially attributed to the delamination of the original silicate layers in the polymer matrix [Sinha Ray and Okamoto (2003b); Sinha Ray and Bousmina (2005a)].

Another useful tool for characterizing the structure of nanocomposites is the transmission electron microscopic. In contrast to WAXD, a qualitative understanding of the internal structure of polymer nanocomposites can be achieved by TEM.

Summing up, TEM gives only a qualitative information about the sample as a whole while diffraction peaks in WAXD allow to calculate also the interlayer spacing (quantitative information).

Even though both TEM and WAXD are useful tools for evaluating the structure of polymer nanocomposites, another complementary characterization method seems to be essential for better understanding the structure of these systems. Rheological measurements are very sensitive to microstructure and have been proven to be successful in the characterization of polymer nanocomposites. We shall discuss this issue in the next section.

2.5 Rheological behavior of nanocomposites

In polymer processing, such as extrusion and injection molding, the rheological properties of polymeric materials, related to the microstructure of macromolecules, are very important. In the case of filled polymer system, the state of the dispersion, the shape and the orientation and/or arrangement of the dispersed particles, and particle-particle interactions are adding to the complex rheology of polymer macromolecules. The rheology of PLS nanocomposites becomes even more complex due to the anisotropic nature of the silicate platelets, nanometric size of clay lamellae, and polymer-plate interactions. Therefore, an understanding of the rheology of PLS nanocomposites becomes very important.

In principle, the structure of dispersed silicate layers in polymeric matrix can be studied on three levels: (i) macroscopic level in which the rheological measurements are performed on the bulk of the system, (ii) microscopic level in which the dynamics of the individual silicate platelets and macromolecules are studied in detail, and (iii) mesoscopic level in which an

attempt is made to create a link between microstructure and bulk properties (macroscopic observations). This last technique (mesoscopic description) becomes even more important due to the critical dependence of the structure of PLS nanocomposites on the strength of the polymer/plate interaction and viscoelastic properties of the polymer matrix [Hyun et al. (2001)].

In general, an investigation of the linear and nonlinear melt-state viscoelastic properties of PLS nanocomposites are important for the following two reasons. First, a knowledge of nonlinear rheological properties is essential for understanding the processability of these materials. Second, the rheological measurements are very sensitive to the microstructure of the nanocomposites. Their importance for understanding the structure-property relationship in polymer nanocomposites has been well established. In this context, a lot of efforts have been devoted to the experimental rheological study of PLS nanocomposites [Solomon et al. (2001); Sinha Ray and Bousmina (2005b); Zhao et al. (2005); Krishnamoorti and Giannelis (1997); Wu et al. (2005); Krishnamoorti et al. (2001); Ayyer and Leonov (2004); Tung et al. (2005); Letwimolnun et al. (2007); Mobuchon et al. (2007); Naderi et al. (2008); Franchini et al. (2009); Laske et al. (2009)]. Majority of these works put into focus low amplitude dynamic measurements and their connections to the microstructure. There have also been a few studies regarding the rheological modeling of polymer nanocomposites [Song and Youn (2004); Sarvestani and Picu (2005); Kairn et al. (2005); Wang et al. (2006); Letwimolnun et al. (2007); Ma et al. (2008); Kagarise et al. (2008)]. In order to have a general picture regarding the rheology of PLS nanocomposites, some of these works from the literature are briefly reviewed in the next two sections from both experimental and modeling points of view.

2.5.1 Experimental rheology

As already mentioned, WAXD measurements and TEM images give a useful information about the structure of PLS nanocomposites. However, for exfoliated or delaminated structure, no diffraction peaks are observes in WAXD patterns. WAXD has also other drawbacks

such as the weak peak intensity and poor peak resolution especially for low clay loading. In these cases, slight changes in the mesoscopic structure of PLS nanocomposites can be detected by rheological measurements which may not be easily seen by WAXD. In the next three sections we review linear and nonlinear rheological properties of PLS nanocomposites and their relations with the microstructure.

2.5.1.1 Dynamic oscillatory shear measurements

In principle, dynamic oscillatory shear measurements can be performed in oscillatory mode with either small or large angle oscillations. Small angle oscillatory shear (SAOS) experiments are involved with unsteady response of materials (especially viscoelastic materials) in the linear viscoelastic zone. In SAOS the fluid under consideration is submitted to oscillatory imposed flows (i.e. the strain is given by $\gamma(t) = \gamma_0 \, sin \, \omega t$, where ω is the angular frequency and γ_0 is the strain amplitude). The resulting stress is given by $\sigma(t) = \gamma_0 \, (G' \, sin \, \omega t + G'' \, cos \, \omega t)$, where G' and G'' are the storage and loss moduli, respectively. The amplitude of the shear strain γ_0 is assumed to be sufficiently small so that the shear stress is linear in the strain γ or in the strain rate $\dot{\gamma}$. In SAOS flows, the ratio of viscous and elastic responses of viscoelastic materials, known as a loss factor, is defined by: $tan \, \delta = G''/G'$. This ratio becomes very large (i.e. $tan \, \delta >> 1$) for liquid-like materials and very small (i.e. $tan \, \delta << 1$) for solid-like materials [Bird et al. (1987a); Marrison (2001); Malkin (2009)].

The first step in the dynamic oscillatory shear measurements is an identification of the linear viscoelastic (LVE) range. As observed in traditional filled polymer system, this range is sensitive to the presence of the filler and becomes usually smaller when the filler content is increased. In polymer nanocomposites where the nanometric size of clay lamellae are dispersed in polymer melts this effect becomes even more important.

Solomon et al. (2001) performed strain sweep test for both the pure polymer matrix and the nanocomposites (polypropylene/clay hybrid materials). A deviation from linearity occurs at a strain which is approximately two orders of magnitude smaller than that observed in the polymer matrix. Similar results were also observed in [Li et al. (2003)] where the rheology

of polypropylene/montmorillonite was investigated. It was reported that the LVE range changes greatly in the presence of the intercalated clay. The deviation from linearity for their nanocomposites with 6 wt.% of organically modified montmorillonite occurs at the strain around 1%, which is much smaller than that observed in pure polypropylene. Similar results were reported in [Krishnamoorti et al. (2001); Wu et al. (2005); Jeon et al. (2004); Vermant et al. (2007)].

Ren and Krishnamoorti (2003) performed strain sweep test for a series of intercalated nanocomposites of an organically modified montmorillonite and a disordered styrene-isoprene diblock copolymer at two different frequencies ($\omega = 1\ rad/s$ and $\omega = 10\ rad/s$). Normalized complex viscosity as function of strain for polymer matrix and its nanocomposites is reported in Ren and Krishnamoorti (2003). Transition from linear to nonlinear behavior in complex viscosity is found to depend sensitively on the clay loading. This observation supports the previous observation regarding the LVE range. Moreover, results reported in Ren and Krishnamoorti (2003) revel a mild dependency of the onset of nonlinearity on the applied frequency. The LVE range becomes narrower when the frequency is increased.

Due to large variations in the LVE range in PLS nanocomposite (that can be partially attributed to the strong plate-polymer and plate-plate interactions), special care has to be paid when measuring it in polymer nanocomposites. More specifically, the linear viscoelastic region in such system has to be determined separately for each concentration of clay at least in two different frequencies.

One of the most often used experiment in SAOS measurements is the frequency sweep test. The behavior of the sample under investigation is examined at different time scales, usually starting from low frequency (long time scale) to high frequency (short time scale). Since the viscoelastic behavior of PLS nanocomposites varies significantly in different time scales, a valuable information is obtained.

Ren et al. (2000) studied the melt-state linear viscoelastic properties of intercalated nanocomposites composed of organically modified montmorillonite and disordered styrene-isoprene diblock copolymer. Results of their frequency sweep test reveal that the viscoelastic

response, especially the storage modulus G', becomes significantly less dependent on frequency at low frequency regime for nanocomposites than for the polymer matrix. In other words, at low frequencies, G' becomes almost independent of frequency (so-called pseudo-solid-like behavior) for high clay loading. Qualitatively the same results are also observed for the loss modulus G''. However, pseudo-solid-like behavior in G'' is less pronounced than G'. As also reported in Ren et al. (2000), no significant changes are observed for viscoelastic response at the high frequency regime with the exception of a monotonic increase with increasing the clay loading. In order to interpret the observed phenomena at low frequencies, the authors suggest that, above the percolation threshold volume fraction, the silicate tactoids form together with the individual clay lamellae that are presented in the suspension a network like structure which then causes the pseud-solid like behavior and hinders the relaxation to a completely isotropic dispersion.

In another study, the linear viscoelastic response of ethylene-vinyl acetate copolymer (EVA) nanocomposites prepared in a Brabender twin-screw extruder by melt mixing of different loadings of organically-modified clay with EVA was investigated by Gupta et al. (2005). They report a liquid-like behavior ($G' \propto \omega^2$ and $G'' \propto \omega$) for polymer matrix where G'' exceeds G' at low frequencies. However, a pseudo-solid-like behavior (similar to previous observations regarding intercalated nanocomposites) is observed for exfoliated nanocomposites. This is then attributed to a strong interaction between exfoliated clay layers and polymer chains. Moreover, they observe a large increase in G' at all ranges of frequencies for high clay loading. In other words, the authors observe in exfoliated nanocomposites with high clay loading a significant increase in moduli at both low and high frequencies. Similar results for exfoliated nanocomposites were also reported in [Krishnamoorti and Giannelis (1997); Lim and Park (2001)]. This observation was then compared with that of intercalated nanocomposites where no significant enhancement was reported for moduli at high frequencies [Lim and Park (2001)]. The conclusion is then that in an exfoliated nanocomposites interaction between clay layers and polymer chains is stronger than that of intercalated nanocomposites which leads to a slower relaxation in exfoliated system.

Linear viscoelastic data at high frequencies (data of storage and loss moduli) were further employed by Vermant et al. (2007) in order to assess the dispersion quality in PLS nanocomposites. They investigate the evolution of the relative high frequency moduli (the moduli of nanocomposites divided by the moduli of polymer matrix) as a function of clay volume fraction for nanocomposites with two different states of dispersion. The Krieger-Dougherty equation (Eq. 2.1) is then used to describe the observed behavior at high frequencies.

$$G'_{HF,rel} = \frac{G'_{HF}}{G'_{HF,m}} = \left[1 - \frac{\alpha}{\alpha_{max}}\right]^{[\eta]\alpha_{max}} \tag{2.1}$$

where $G'_{HF,rel}$ is relative high frequency storage modulus, G'_{HF} is high frequency storage modulus of nanocomposite, $G'_{HF,m}$ is high frequency storage modulus of matrix, α_{max} is the maximum packing fraction, α is clay volume fraction and $[\eta]$ is the intrinsic viscosity.

By using the approximate value of the intrinsic viscosity estimated from the Brenner equation [Brenner (1974)] (for more detail see Vermant et al. (2007)) and Krieger-Dougherty equation (Eq. 2.1), the maximum packing fraction is calculated. The authors then conclude that the lower value of α_{max} for better dispersed sample is in agreement with their other observations. Their results support the previous observations in [Krishnamoorti and Giannelis (1997); Lim and Park (2001); Gupta et al. (2005)] where the moduli of exfoliated nanocomposites are increased at high frequencies if compared with that of the polymer matrix.

Rheological measurements in the linear viscoelastic regime were also conducted by Sinha Ray and his co-workers [Sinha Ray and Okamoto (2003a); Sinha Ray and Bousmina (2005a)] for polylactide (PLA)/clay nanocomposites. They report the slope of G' and G'' in terminal zone for PLA and its intercalated nanocomposites. Their results show that the slope of G' and G'' are considerably lower for nanocomposites if compared with those of the polymer matrix. For nanocomposites with high clay loading, G' becomes almost independent of the frequency and its value becomes greater than that of G''. They also report that the viscoelastic responses of PLA nanocomposites gradually change from liquid-like to pseudo-solid-like with increasing silicate layers concentration. Dynamic complex viscosity of pure

PLA and its nanocomposites are also presented by Sinha Ray and his co-workers [Sinha Ray and Okamoto (2003a); Sinha Ray and Bousmina (2005a)]. Their results show that at low frequencies, pure PLA exhibits almost Newtonian behavior whereas all nanocomposites show a strong shear thinning behavior. This shear thinning tendency in nanocomposites becomes then stronger with increasing clay loading. Dramatic increase in dynamic complex viscosity at low frequencies is related to the flow restrictions of polymer chains in the molten state due to the presence of nanoparticles. Similar result is obtained for complex viscosity of intercalated nanocomposite reported in [Krishnamoorti et al. (2001)].

As already discussed, linear viscoelastic properties have been extensively studied for various PLS nanocomposites during recent years. The so-called pseudo-solid-like behavior, a characteristic of PLS nanocomposites, has been observed for both exfoliated and intercalated nanocomposites and is reported in [Krishnamoorti et al. (1996); Krishnamoorti and Giannelis (1997); Ren et al. (2000); Lim and Park (2001); Solomon et al. (2001); Galgali et al. (2001); Li et al. (2003); Jeon et al. (2004); Aubry et al. (2005); Gupta et al. (2005); Sinha Ray and Bousmina (2005b); Sinha Ray et al. (2005); Xu et al. (2005); Wu et al. (2005); Kim et al. (2007); Vermant et al. (2007)]. It should be noted that the term pseudo-solid like is used because G' does not exceed G'' by order of magnitude as it normally occurs in a true solid [Krishnamoorti and Giannelis (1997)]. This special characteristic of polymer nanocomposites manifests itself as low frequency plateau in moduli particulary in the storage modulus. It can be attributed to a network like structure of silicate tactoids and clay platelets above percolation threshold in intercalated nanocomposites or strong interaction between clay platelets and polymer chains in exfoliated nanocomposites.

2.5.1.2 Steady state shear measurements

Shear flows are found in many polymer processing operations, for example, in injection molding, extrusion, and in many rheometer flows. A simple shear flow is given by the momentum filed $u_1 = \dot{\gamma}_{(t)} x_2$, $u_2 = u_3 = 0$ in which the velocity gradient can be a function of time. The absolute value of $\dot{\gamma}_{(t)}$ is called a shear rate. For steady simple shear flows (called

also a viscometric flow), the shear rate is independent of time. The shear rate is assumed to be a constant for a sufficiently long time to make all stresses in the fluid independent of time [Bird et al. (1987a); Marrison (2001); Malkin (2009)].

Krishnamoorti et al. (2001) studied the steady state nonlinear viscoelastic properties, including viscosity η and first normal stress difference N_1, for a series of intercalated PLS nanocomposites. In their observations, the polymer matrix exhibits the Newtonian behavior at low shear rates and shear thinning at higher shear rates. However, no plateau in the curve of viscosity versus shear rate is observed in the nanocomposites, especially for high clay loading. This is an indication of non-Newtonian behavior for nanocomposites even at low shear rates. Moreover, above the percolation threshold and at low shear rate regime, the viscosity diverges. The authors then calculate the yield stress for these nanocomposites and conclude that above the percolation threshold a finite yield stress values exists. [Ren and Krishnamoorti (2003)]. The observed phenomena (non-Newtonian and shear thinning behavior even at low shear rates) are suggested to be attributed to the ability of the steady shear flow to orient anisotropic silicate layers and tactoids in the flow direction. At high shear rates, the steady state viscosity of nanocomposites is reported to be comparable to that of the polymer matrix. The authors then suggest that at high shear rates where clay platelets and tactoids are strongly oriented in the flow direction the rheological behavior is dominated by the polymer matrix.

Gupta et al. (2005) measured the steady state viscosity of exfoliated nanocomposites prepared by direct melt mixing method in a wide range of shear rates. The authors observe a higher zero-shear viscosity and an earlier onset of shear thinning behavior in nanocomposites with low clay loading if compared with that of the pure polymer matrix. The viscosity monotonically increases with increasing clay loading and the behavior becomes almost non-Newtonian for the whole ranges of shear rates. The higher zero-shear viscosity of polymer nanocomposites in comparison with that of the polymer matrix is attributed to the nanostructure of the nanocomposites at low shear rates. This nanostructure is suggested to be composed of strongly interacting dispersed clay platelets and polymer chains. In contrast to

the previous work [Ren and Krishnamoorti (2003)], the yield stress is not observed in these exfoliated nanocomposites even at high clay loading. The authors claim that the absence of the yield stress could not be an indication of weak interparticle interactions. They argue that clay-clay interactions become even stronger with increasing clay loading where the interparticle distance becomes small. The authors then conclude that the relaxation ability of polymer chains is limited because of the restriction created by the surrounding clay platelets. It should be noted that the yielding phenomenon observed in intercalated nanocomposite reported in [Ren and Krishnamoorti (2003)] is a result of their mesoscopic structure where the clay tactoids and occasional silicate layers are unable to relax independently. The observed phenomena for the steady state viscosity in exfoliated nanocomposites are further explained in terms of a network structure of clay lamellae which remained unchained at low shear rates. However, this network structure breaks down at relatively high shear rates and silicate layers become oriented in the flow direction. This then leads to the shear thinning behavior and to the approach of the viscosity to the one of the polymer matrix.

Lim et al. (2002) also reported the shear viscosity as a function of the shear rate for a biodegradable aliphatic polyester and its nanocomposites prepared by solvent-casting method. The viscosity is seen to increase with increasing clay loading over a broad range of shear rates. At relatively high shear rates, the shear thinning behavior is observed for all nanocomposites. It becomes stronger with increasing clay loading. However, at very low shear rates, a Newtonian plateau is observed even for high silicate loading. A similar trend was previously observed for a series of intercalated poly(dimethyldiphenylsiloxane)/ layered silicate nanocomposites [Krishnamoorti et al. (1996)] and for poly(ethylene oxide) PEO/organoclay nanocomposites prepared via solvent-casting technique [Hyun et al. (2001)]. This last observation (i.e. the Newtonian plateau at low shear rates even for high clay loading) was not reported in[Krishnamoorti et al. (2001)] and in [Gupta et al. (2005)] where nanocomposites displayed a shear thinning behavior in the entire range of shear rates.

Hyun et al. (2001) also investigated the effect of different organoclays on the steady state viscosity of nanocomposites. In other words, for a given clay loading, they study the effect of

different organoclays with a different initial interlayer spacing on the steady state viscosity. They observe larger values of the viscosity for nanocomposite composed of the organoclay which have larger initial interlayer spacing . The authors then relate the enhancement in the shear viscosity to the stronger interaction and better dispersion of clay in the polymer matrix. However, at higher shear rates the viscosity of all nanocomposites approaches the one of the polymer matrix. This is attributed to the preferential alignment and orientation of clay platelets in the polymer matrix.

Generally speaking, behavior of the steady state viscosity of PLS nanocomposites shows that the clay platelets manifest themselves mainly at low shear rate ranges and that the behavior of polymer nanocomposites at high shear rates is dominated by polymer matrix [Krishnamoorti et al. (2001); Gupta et al. (2005); Sinha Ray and Bousmina (2005b); Sinha Ray et al. (2005); Ren and Krishnamoorti (2003); Vermant et al. (2007); Letwimolnun et al. (2007)].

Although the exact mechanism of shear thinning behavior in PLS nanocomposites still needs to be clarified, there is a rather good agreement in the literature that the alignment and the orientation of silicate layers and clay tactoids are very likely responsible for it. From the practical point of view, the shear thinning represents a great advantage because it makes it possible to process the nanocomposites in the melt state using the conventional equipment available in the manufacturing line.

The empirical Cox-Merz relation which requires $\eta^*(\omega) = \eta(\dot{\gamma})$ where $\omega = \dot{\gamma}$ has been proven to be applicable for homopolymers. Validity of the Cox-Merz relation was also examined for PLS nanocomposites where a significant deviation has been noted [Krishnamoorti et al. (2001); Sinha Ray and Bousmina (2005b)]. Such a failure has been previously observed also for filled polymer systems. The reason for such failure is explained by Krishnamoorti et al. (2001). According to this explanation, in SAOS measurements (because of small deformations) no changes in the quiescent mesostructure are expected while in the steady shear measurements silicate layers and tactoids are oriented in the flow direction which dramatically modifies the mesostructure. An extension of the Cox-Merz rule for concentrated suspensions

and materials with a yield stress has been introduced by Doraiswamy et al. (1991). However, this extended Cox-Merz relation again fails in the case of nanocomposites.

Now, we turn our attention to the normal stress and to its role in the rheology of PLS nanocomposites. Although the emergence of normal stresses in viscoelastic materials and their role in the polymer processing has long been realized, less attention has been payed to clarifying their role in the rheology and subsequently in processing of PLS nanocomposites. So far, only a few works have been reported where the normal stress difference has been measured for PLS nanocomposites in shear flow [Krishnamoorti et al. (2001); Ren and Krishnamoorti (2003); Gupta et al. (2005)].

Krishnamoorti et al. (2001) and Ren and Krishnamoorti (2003) investigated the melt elasticity in intercalated nanocomposites by plotting N_1 versus σ_{12}. According to these authors, the recoverable strain (N_1/σ_{12}) is found to be independent of the silicate loading and close to that of the polymer matrix. The observed behavior is explained in terms of the orientation of two dimensional silicate layers in the flow field. It is also pointed out that σ_{12} and N_1 are both at steady states and that such universal relationship may not be observed for the transient $\sigma_{12}^{\pm}$ and $N_1^{\pm}$. The authors also mention that the reported data for σ_{12} and N_1 are dominated by the data at high shear rates where the steady state viscosity is found to be dominated by that of the polymer matrix. Moreover, it is argued that the orientation of silicate layers in the flow direction diminishes the effective clay-clay interactions which in turn reduces the contribution of silicate layers and tactoids to the elasticity and the viscosity of nanocomposites.

Gupta et al. (2005) also employed the same methodology to evaluate the elasticity of nanocomposites of exfoliated lamellae. They depict N_1 versus σ_{12} and conclude that the melt elasticity of their nanocomposites diminishes with increasing the clay loading. The authors then argue that this reduction of the elasticity may be related to the strong interaction between clay platelets and polymer chains which in turn reduces the mobility of the polymer chains in the presence of the silicate layers.

2.5.1.3 Stress growth measurements

As we have already discussed, measurements of the viscosity, one of the most common type of rheological measurements, are usually conducted for steady shear flows. When the fluid is subjected to a shear flow, before reaching its steady state value, the stress grows from zero at rest to its stationary value. This time-dependent experiments are well-known as stress growth or start-up experiments [Bird et al. (1987a); Marrison (2001)]. Generally speaking, stress growth experiments provide a valuable additional insight into the structure of complex fluids. In the case of the PLS nanocomposites, orientation and/or disorientation of silicate layers under flow and to some extend also creation and annihilation of the network structure can be evaluated by analyzing start-up experiments.

Wu et al. (2005) studied the stress growth of their nanocomposites which were prepared by direct melt mixing of poly(butylene terephthalate)(PBT) and organocally modified montmorillonite. Start-up experiment was then carried out at four different shear rates. Their results indicated that at low shear rate the stress grows monotonically and reaches its steady state value. With increasing shear rate a stress overshoot is observed. The time at which the overshoot begins is found to decrease with increasing shear rates. The amplitude of the stress overshoot is also found to depend strongly on the applied shear rate. The authors also report the transient stress versus strain and conclude that the stress overshoot scales with strain. In other words, stress overshoot in all shear rates appears at a certain strain.

The time evolution of shear stress at different shear rates was also investigated by Solomon et al. (2001). Similarly to previous observations [Wu et al. (2005)] they also report that at low shear rate shear stress increases monotonically whereas an overshoot is observed at higher shear rate. The magnitude of the stress overshoot increases and the time at which the overshoot appears decreases as the shear rate increases. Strain scaling of stress is also found to be valid. It is then concluded that the Brownian motion does not play any significant role in rheology. They also mention that the stress overshoot observed is attributed to the presence of silicate layers because the polymer matrix shows no significant stress overshoot

even at the highest shear rate considered in their experiments.

The effect of shear rate on the stress growth experiment was also investigated by Letwimolnun et al. (2007) for polypropylene/organoclay nanocomposites. They reported that the amplitude of the stress overshoot increases with increasing shear rate, but all overshoots appear at the same strain about 1.7. At a given clay loading, the amplitude of the stress overshoot is found to be related to the structure of the nanocomposites. More specifically, the magnitude of the stress overshoot increases as the degree of the clay exfoliation increases.

Lee and Han (2003) studied the melt-state linear and nonlinear rheology including transient rheological material functions (shear stress and first normal stress difference) of PLS nanocomposites with different degrees of dispersion. It is worth mentioning that they use different polymer matrix and two different organoclay (Cloisite 30B and Cloisite 15 A) in order to prepare nanocomposites with different states of dispersion. Results of their stress growth experiments show that in all nanocomposites the stress overshoot increases with increasing shear rate. However, the amplitude of the stress overshoots varies from one nanocomposite to another. The authors explain it in term of the existence of different interaction between polymeric chains and clay platelets. In other words, they find that the stronger the interaction between polymer and clay is, the larger magnitude for stress overshoot observes. Similar to previous observations [Solomon et al. (2001); Wu et al. (2005); Letwimolnun et al. (2007)] they also report that the strain scaling holds. The time evolution of the first normal stress difference N_1 is also investigated in Lee and Han (2003). A very irregular behavior for normalized N_1 over the entire range of applied strain is observed. The authors conclude that there is no strain scaling for N_1.

In filled polymer fluids, particularly in polymer nanocomposites, the stress overshoot is usually monitored as a measure of transition from one state of orientation and/or arrangement of particles to another state of orientation and/or arrangement. In order to investigate the structure build up at rest in PLS nanocomposites, flow reversal experiments are usually conducted at different rest times after cessation of the forward start-up flow. The structure recovery during rest time can then be measured by the reappearance of stress overshoot

during the reverse start-up flow. In the flow reversal experiments, the sample is subjected first to steady shear flows till a steady state is reached. The flow is then stopped and the sample is let to rest for a given time. Finally, the sample is sheared in the reverse direction till its steady state value.

Flow reversal experiments are employed by Solomon et al. (2001) to quantify the structural evolution in polypropylene/clay nanocomposites. During the reverse flow, the amplitude of the stress overshoot is found to be a strong function of the rest time. This means that the structure of nanocomposites evolves even during the rest time. The authors then conclude that the rupture and/or orientation of mesoscopic particulate domains of ordered platelets (particulate aggregate) is responsible for stress overshoots. The origin of the structure recovery at rest is then attributed to the attractive interaction among the multi-platelet domains. The Brownian motion is assumed to play no significant role in the structure build-up at rest. In other words, when the flow is stopped, attractive inter-particle interactions give rise to re-formation of the network structure which becomes more complete at longer rest times.

Letwimolnun et al. (2007) conducted flow reversal experiments for a series of nanocomposites with different degrees of dispersion. It is worth mentioning that the authors use different mixing device with different processing condition in order to obtain different microstructure in their nanocomposites. Their observation reveal that the structure build-up at rest is strongly dependent on the degree of exfoliation. The authors suggest that the stress overshoot is attributed to the breakdown and/or orientation of the structured clay network. During the rest time, the disorientation of clay platelets, which becomes nearly isotropic after a long rest time, is suggested to be responsible for the structure build-up at rest. The authors also investigate two possible mechanisms of structure recovery at rest (i.e. reappearance of stress overshoot during reverse flows) from the modeling point of view.

2.5.2 Theoretical modeling

As already discussed, the rheological behaviors of PLS nanocomposites have been extensively studied from the experimental point of view with special attention to the small amplitude

oscillatory shear measurements. However, it is still hard to find a comprehensive rheological model which could predict both linear and nonlinear rheological material functions for polymer nanocomposites. In this section some of the rheological models developed for polymeric materials charged with nanoparticles are reviewed. Some of these works may not be directly related to PLS systems, but their results can be helpful for understanding the complex rheology of PLS nanocomposites.

The rheology of polymer melts and concentrated solutions filled with nanoparticle is investigated by a frictional molecular model in [Sarvestani and Picu (2005)]. In their study the spherical rigid particles with strong interaction with polymer matrix are assumed to be homogeneously dispersed in polymer matrix. Particle-polymer and polymer-polymer interactions are included in the model. According to the author, the difference between the rheology of traditional filled polymer system with micron size particles and nanocomposites are attributed to the polymer-particle and particle-particle interactions which become important on the nanoscale. They focus on the system in which the inter-particle distance is assumed to be in the order of chain gyration radius where the interaction effects become very important. According to the author, the advantages of the the model are its simplicity and its easiness to fit with it the experimental data. However, the model is limited due to the assumption of homogenized representation of the polymer-filler attachments and the over-simplified representation for polymer matrix namely dumbbell representation.

Molecular dynamics simulations are employed by Kairn et al. (2005) to study the rheology of model polymer nanocomposites. In their study, different concentrations of spherical nanofiller particles are used and the simulated results are compared with experimental data of polypropylene filled with calcium carbonate. It is found that the simulated steady state shear viscosity is in a good agreement with the one observed in experimental measurements. In the simulated results the zero shear viscosity increases and the onset of shear thinning decreases with increasing filler loading. These findings are well supported by experimental observations.

Recently, in Ma et al. (2008) a new model for carbon nanotube aggregate suspensions

where untreated carbon nanotubes are assumed to be suspended within an epoxy resin, was proposed. The model formulation is based on the Fokker-Planck framework in which the concept of orientation and aggregation as well as the kinetics of aggregation-disaggregation of carbon nanotubes in the suspension are taken into account. The authors then suggest that the model based on the Fokker-Planck equation, where only orientation of carbon nanotubes is considered, is proven to be successful in the prediction of the rheological behavior of treated carbon nanotube suspensions where no significant amount of aggregated carbon nanotube is observed. The proposed model is able not only to capture the shear thinning behavior (experimentally observed for carbon nanotube suspensions) but also to provide some physical insight regarding to the aggregated carbon nanotube suspensions when they are subjected to shear flow. It is found that the model is able to predict a carbon nanotube network at low shear rate regime which becomes weaker (the network structure begins to breakdown) with increasing shear rate. These predictions are then supported by optical microscopic observations. The authors conclude that even though the steady shear response of carbon nanotube suspensions is successfully predicted by the proposed model, it cannot capture the experimentally observed viscoelastic behavior of these suspensions. To faithfully predict the viscoelasticity for carbon nanotube aggregated suspensions the concept of viscoelastic has to be included into the proposed model.

In order to model the phenomena observed in flow reversal experiment (i.e. the stress overshoot in start-up shear flow and its recovery during rest time) Letwimolnun et al. (2007) use two models originally formulated for concentrated colloidal suspensions and fiber suspensions. Moreover, they slightly modify the model developed for fiber suspension to take into account the structure build-up at rest. The authors introduce an additional molecular diffusion term in the Folgar-Tucker equation which, according to the authors, is interpreted as being related to the Brownian motion. The formulation of the first model (model originally developed for colloidal suspensions) is based on breakdown and build-up of suspension microstructure. It is found that the model is able to predict amplitudes of stress overshoots and their stationary values but it fails to predict the strain at which the stress overshoots ap-

pear. The second model (model originally developed for fiber suspensions) can qualitatively predict the stress overshoot in the forward start-up flow and an increase of its amplitude with increasing rest time in reverse start-up flow. However, stress overshoots appear at strains which decrease with increasing rest time whereas in experiments the strains are found to be independent of the rest time.

2.5.2.1 Thermodynamic approach

The goal of this section is to present and illustrate the use of thermodynamic methods, which we shall use in this thesis, in the rheological modeling of complex fluids. We want to summarize the framework of non-equilibrium thermodynamics. In general, the modeling based on thermodynamics follows the following four steps.

i) Choice of state variables:

The choice of suitable state variables is a key step. Depending on the type of experimental observations, our objectives, and molecular nature of the fluid under consideration, the variables used to describe states of the complex fluid under consideration are chosen.

ii) Kinematics of the state variables:

Having chosen the state variables, we need to know how they evolve in time in the absence of dissipation. In other words, the first step in the derivation of the time evolution equation is the derivation of the kinematics of the state variables. Following classical mechanics, the kinematics of the state variable can be expressed in a Poisson bracket.

iii) Specification of free energy:

In general, the free energy is composed of two parts: energy $E(x)$ and entropy $S(x)$. Energy includes all the interactions between the atoms or particles in the system, as well as the kinetic energies associated with their motions. The entropy is usually chosen to be the Boltzmann entropy.

iv) Specification of the dissipation potential:

Finally, we have to specify dissipation processes that take place in the dissipative part of the time evolution. The dissipation part of the time evolution equation is specified by

specifying the dissipation potential Ξ that is a function of thermodynamic forces Φ_x.

For isothermal and incompressible fluids, the equations governing the compatible with thermodynamics time evolution equation of state variables (hereafter we denote it by symbol x) is governed by [Grmela (1984, 1986, 1991); Beris and Edwards (1994); Grmela and Ottinger (1997); Ottinger and Grmela (1997); Grmela (2002); Ottinger (2005)]

$$\dot{x} = L\Phi_x - \frac{\partial \Xi}{\partial \Phi_x} \tag{2.2}$$

and in [Grmela and Ottinger (1997); Ottinger and Grmela (1997)] it called GENERIC (general equation of non-equilibrium reversible irreversible coupling). By $\dot{x}$ we denote the time derivative of x. The first term on the right hand side of (2.2) expresses the compatibility with mechanics, the second the compatibility with thermodynamics. The symbols appearing in (2.2) have the following meaning.

Free energy: $\Phi(x)$, a real valued function of x, has the physical meaning of the total free energy. By Φ_x we denote the derivative of Φ with respect to x.

Kinematics: The operator L, hereafter called a Poisson bivector, transforms a covector (a gradient of a potential) into a vector. From the physical point of view, L expresses kinematics of the state variables x. In the particular case of classical mechanics of particles (the state variables in this case are $x = (p, q)$, where q are position vectors and p the momenta of the particles), $L = \begin{pmatrix} 0 & 1 \\ -1 & 0 \end{pmatrix}$. This is the Poisson bivector transforming in classical mechanics the gradient of energy $E(q, p)$ into a vector field. In the general setting, L is required to satisfy the following properties: $\{A, B\} =< A_x, LB_x >$ is a Poisson bracket, i.e. $\{A, B\} = -\{B, A\}$, and satisfies the Jacobi identity $\{A, \{B, C\}\} + \{B, \{C, A\}\} + \{C, \{A, B\}\} = 0$; A, B, C are sufficiently regular real valued functions of x, $<, >$ denotes the inner product.

Dissipation: $\Xi(\Phi_x)$, called a dissipation potential, is a sufficiently regular real valued function of Φ_x satisfying the following properties: (i) $\Xi(0) = 0$, (ii) Ξ reaches its minimum at 0, (iii) Ξ is concave in a neighborhood of 0.

The properties required from L, Ξ appearing in (2.2) imply that solutions to (2.2) satisfy

the following inequality:

$$\frac{d\Phi}{dt} \leq 0 \tag{2.3}$$

The free energy Φ thus remains unchanged or decreases during the time evolution (2.3): $\frac{d\Phi}{dt} =< \Phi_x, L\Phi_x > - < \Phi_x, \frac{\partial \Xi}{\partial \Phi_x} >\leq 0$. The last inequality follows from $< \Phi_x, L\Phi_x >= 0$ and from the properties required from the dissipation potential Ξ. The inequality (2.3) together with the thermodynamic stability requirement (i.e. Φ is a convex function of x) allows us to consider Φ as a Lyapunov function. This then means that solutions to (2.2) tend, as $t \rightarrow \infty$, to states that minimize the free energy (i.e. the states, called equilibrium states, that are solutions of $\Phi_x = 0$).

We now compare the framework (2.2) with the more familiar framework

$$\dot{x} = -div\boldsymbol{J}(x) \tag{2.4}$$

used extensively in classical hydrodynamics. The equations (2.4) are called balance laws (or local conservation laws), x are assumed to be functions of $\boldsymbol{r}$, $div\boldsymbol{J} = \frac{\partial J_i}{\partial r_i}$, the summation convention is used throughout this thesis, $\boldsymbol{J}$ denotes a flux. A specification of $\boldsymbol{J}$ is called in classical hydrodynamics a constitutive relation.

The framework (2.4) itself (i.e. irrespectively of the choice of $\boldsymbol{J}$) guarantees the global conservation (i.e. $\int d\boldsymbol{r}x(\boldsymbol{r})$ does not change in time). In the case of incompressible and isothermal fluids to which we limit ourselves in this thesis the only classical hydrodynamic field is the momentum field $\boldsymbol{u}(\boldsymbol{r})$. With $x = \boldsymbol{u}(\boldsymbol{r})$, the framework (2.4) guarantees conservation of the total momentum $\boldsymbol{U} = \int d\boldsymbol{r}\boldsymbol{u}(\boldsymbol{r})$. If we now think of applying the framework (2.4) to PLS nanocomposites, the following questions come into mind.

Question 1. Does the framework (2.4) guarantee the compatibility with thermodynamics?

Question 2. Does the framework (2.4) guarantee the compatibility with mechanics?

Question 3. How to use the framework (2.4) for fields x that are not required to be globally conserved?

The first question has been extensively studied in nonequilibrium thermodynamics. It has been shown that by appropriately augmenting the fields x, the framework (2.4) adopts

a local version of the inequality (2.3). This then answers the first question.

As for the second question, it is well known that the balance law of the local momentum $\boldsymbol{u}(\boldsymbol{r})$ can also be physical interpreted as a continuum version of Newton's law. This alternative viewpoint provides the momentum flux with the interpretation of a force acting on a surface. The compatibility with mechanics is thus clear but only if we choose x to be the momentum field $\boldsymbol{u}(\boldsymbol{r})$.

When dealing with complex fluids, for instance with PLS nanocomposites, we have to include into the state variables x also fields characterizing the internal structure. Such fields are typically not associated with a global conservation laws. This means that the framework (2.4) is not anymore applicable. If we however insist on applying it also for complex fluids then we have to limit x only to $x = \boldsymbol{u}(\boldsymbol{r})$ and leave the introduction of the other fields as well as the equations governing their time evolution to the constitutive relation (i.e. to the specification of the momentum flux). The framework (2.4) does not provide any guidance for discussing this problem.

Now we return to the framework (2.2). The conservation of the total momentum guaranteed by the framework (2.4) is not automatically guaranteed by the framework (2.2). First of all, in order to discuss the momentum conservation, we have to include the local momentum $\boldsymbol{u}(\boldsymbol{r})$ into the state variables x. An appropriate choice of kinematics and dissipation is then shown to imply the momentum conservation.

Next, we turn to the three questions asked above in the context of the framework (2.4) and answer them in the context of the framework (2.2).

The compatibility with thermodynamics is guaranteed since the framework (2.2) implies the inequality (2.3). The compatibility with mechanics is guaranteed by the fact that the operator L expressing mathematically the kinematics is a Poisson bivector. Most importantly, the compatibility with mechanics is manifested for any choice of x. We recall that for the framework (2.4) the compatibility with mechanics appeared only for the choice $x = \boldsymbol{u}(\boldsymbol{r})$.

The most obvious advantage of the framework (2.2) is that we can use it for any set x of state variables. When dealing with complex fluids it is indeed very important to be very

flexible with choosing the state variables characterizing the internal structure. The framework (2.2) does provide a guidance for writing the equations governing the time evolution of any set x.

CHAPTER 3

ORGANIZATION OF THE ARTICLES

An introduction and objective of this thesis as well as a brief summary of the literature about PLS nanocomposites have been given in the two previous chapters. The rest of this thesis is organized as follow:

In chapter 4, a mesoscopic level of description is chosen to formulate a rheological model of isothermal and incompressible suspensions of clay lamellae in polymer melts. Clay lamellae are assumed in this chapter to be completely exfoliated and homogeneously dispersed in a viscoelastic polymer matrix. The model takes into account the polymer-lamella and lamella-lamella interactions. Two microstructural state variables are chosen to be: a conformation tensor $\boldsymbol{c}$ (second moment of the distribution of the end-to-end vectors of the macromolecules) characterizing the polymer macromolecules, and another conformation tensor $\boldsymbol{a}$ (second moment of the distribution of the vectors perpendicular to the lamellae) characterizing the suspended lamellae. Having chosen the state variables, the model is constructed in the thermodynamic (GENERIC) framework as an extension of the familiar FENE-P model for polymer melts. Predictions of the model, obtained by solving numerically its governing equations, are responses of the suspension to transient (start-up and relaxation) and steady shear flows. The calculated rheological data for steady and transient shear flows are compared with

experimental data reported in the literature.

In chapter 5, we consider only polymer melts. Our objective is to take a more realistic physical picture of polymer macromolecules (i.e. reptation hypothesis) composing it. The macromolecules are modeled as worm-like chains that only locally are either FENE-P or inextensible dumbbells. On the mesoscopic level of description employed in this chapter, a one parameter (a coordinate s on the backbone of the chain) family $\boldsymbol{c}(s)$ conformation tensors replaces the one conformation tensor $\boldsymbol{c}$ as a state variable characterizing the polymer macromolecules. Following GENERIC framework, this level is considered as an autonomous level and some basic elements of the reptation physics (introduced originally on kinetic theory level) are formulated on it. In the formulation of the model, the polymer melts under consideration are assumed to be incompressible homogeneous and isothermal fluids. Model predictions are then compared with experimental data reported in the literature.

In chapter 6, both models developed in chapters 4 and 5 are combined. As a result we arrive at a rheological model of isothermal suspensions of completely exfoliated silicate lamellae in polymer melts. The model predicts all linear and nonlinear rheological material functions with a single set of material parameters. The chain view of macromolecules becomes particularly important in low shear rates and low frequencies. The tube constraining the motion of chains is composed of both surrounding macromolecular chains and the lamellae. The complexity brought by the presence of the silicate layers makes the kinetic theory based rheological models (on which distribution functions rather than conformation tensors are used as microstructural state variables) are practically unusable due to the mathematical difficulty of solving the governing equations. Predicted rheological material functions for steady, transient and oscillatory shear flows are compared with experimental data. Particular attention is paid to the region of low shear rate and low frequency.

In chapter 7, the linear and nonlinear melt-state viscoelastic properties of PLS nanocomposites prepared by direct melt mixing of poly[butylene succinate-co-adipate] (PBSA) and organically modified montmorillonite (Cloisite 30B) are investigated experimentally. The morphology of the nanocomposites is investigated by means of WAXD and TEM observa-

tion. A new set of experimental data for polymer/layered silicate nanocomposites together with their evaluation made with the help of two mesoscopic models that we have developed previously (introduced in chapters 4 and 6) is reported. The experimental data contribute to the large pool of the data existing in literature for PLS nanocomposites by an original choice of the polymer (of particular interest due to its biodegradability) and by their completeness (that we need for the comparison with model predictions). We report results of both linear and nonlinear (in both steady and transient shear flows) rheological measurements.

In chapter 8, flow reversal experiment is employed to evaluate the microstructure of PLS nanocomposites prepared by melt mixing of PBSA and organically modified montmorillonite under flow and at rest. In the experimental rheological data that can be found in the literature about polymer nanocomposites, less attention has been paid to transient normal stress difference and its overshoot in reverse start-up flow. In this chapter, structure recovery during rest time and reappearance of overshoots on both the shear stress and the normal stress difference are systematically studied. Polymer-particle and particle-particle interactions are expected to play an important role in determining flow properties of suspensions with large number concentration of particles. In nanocomposites, the number density of silicate lamellae becomes large even with small silicate weight concentration. Consequently the polymer-lamellae and lamellae-lamellae interactions are always very important in nanocharge suspensions. Since the models developed in the previous chapters include explicitly this type of interactions, comparison with model predictions is used to suggest an explanation for the phenomena seen in the forward and reverse start-up flows and in the structure build-up at rest.

CHAPTER 4

A MESOSCOPIC RHEOLOGICAL MODEL OF POLYMER/LAYERED SILICATE NANOCOMPOSITES

Hassan Eslami[a], Miroslav Grmela[a1] , Mosto Bousmina[b,c]

[a] Center for Applied Research on Polymers and Composites (CREPEC)
Ecole Polytechnique de Montreal, C.P.6079 suc. Centre-ville,
Montreal, H3C 3A7, Quebec, Canada

[b] Canada Research Chair on Polymer Physics and Nanotechnology
and Center for Applied Research on Polymers and Composites (CREPEC)
Department of Chemical Engineering, Laval University, Ste-Foy,
G1K 7P4, Quebec, Canada

[c] Hassan II Academy of Sciences and Technology, Rabat, Marocco

J. Rheol. 51(6), 1189-1222 November/December (2007)

[1]corresponding author: e-mail: miroslav.grmela@polymtl.ca

Abstract

A mesoscopic rheological model is proposed for polymer/layered silicate nanocomposites. The conformation tensors $\boldsymbol{c}$ and $\boldsymbol{a}$ are chosen to characterize states of macromolecules and silicate layers (plates) respectively. In the absence of the plates, the model reduces to the well known FENE-P model. The predictions of the model are shown to agree with thermodynamics. Other predictions of the model, obtained by solving numerically its governing equations, are responses of the suspension to transient (start-up and relaxation) and steady shear flows. The results show that the model predictions cover a wide range of the rheological behavior generally observed for polymer/layered silicate nanocomposites.

4.1 Introduction

Due to their nanometric size and high aspect ratio (square root of the surface area over the thickness), incorporation of small amount (2-6 wt %) of clay lamellae within polymer matrixes imparts the obtained polymer/layered silicate (PLS) nanocomposites with enhanced dimensional and thermal stability, increased UV resistance and barriers properties, enhanced surface finishing and surface printability, and to some extent enhanced mechanical properties [Sinha Ray and Okamoto (2003b); Sinha Ray and Bousmina (2005a)]. The majority of these properties are obtained through exfoliation of the individual lamellae and their homogeneous distribution within the polymer matrix. Such operation can be obtained in solvent medium or alternatively in molten state where the mixing process is highly governed by the rheology of the system [Bousmina (2006)]. Although the subject is relatively new, the literature is very abundant with various experimental data including rheology [Solomon et al. (2001); Sinha Ray (2006); Sinha Ray and Bousmina (2005a,b); Zhao et al. (2005); Krishnamoorti and Giannelis (1997); Wu et al. (2005); Krishnamoorti et al. (2001); Ayyer and Leonov (2004); Tung et al. (2005)]. However, little effort has been devoted to modeling. Some modeling and simulation efforts have been devoted to thermodynamics and phase behavior of PLS nanocomposites [Kim et al. (2004); Hooper and Schweizer (2006)], but the subject is

still virgin in terms of modeling of their rheological behavior. Rheological characterization is quantitative and very sensitive to structure and its evolution during flow. To understand the melt-processing of such PLS nanocomposites it is then of importance to quantitatively understand their behavior by working out reliable predictive models.

The objective of this paper is to develop a mesoscopic rheological model (providing transition between the microstructure and the nonlinear flow behavior) of isothermal and incompressible suspensions of clay lamellae within polymer melts. In this first paper we consider only the suspensions in which the lamellae are completely exfoliated and homogeneously dispersed in the viscoelastic polymer matrix. The model takes into account the polymer-lamella and lamella-lamella interactions. The full set of the governing equations in dimensionless form is presented at the beginning of Section 4.3. Predictions of the model are compared to some available rheological data found in the literature. The comparison is made for both steady and transient shear flows.

4.2 Formulation of the model

The rheological model for suspensions of clay lamellae in polymer melts is constructed first bottom-up. We begin with the familiar FENE-P model for polymers, reformulate it into a form that is convenient for further generalizations, and finally extend it to suspensions of clay lamellae in polymer melts. The top-down (i.e. starting with the GENERIC framework) construction of the same model is presented in Appendix.

4.2.1 FENE-P model

In the absence of clay lamellae, the rheological model for the nanocomposites that we shall develop in this paper reduces to the well known FENE-P model. We thus begin with this familiar model. First, we just recall it from the literature [Bird et al. (1980)] (Section 4.2.1.1). Then, we reformulate it into two new forms. It is important to emphasize that the FENE-P model remains exactly the same before and after the reformulations. The advantage of the

reformulations is that the mesoscopic physics that is behind the FENE-P model becomes more transparent in the new forms (in Section 4.2.1.2 it is the physics related to the dissipation and in Section 4.2.1.3 it is the physics related to the extra stress tensor) and moreover, in the new forms the FENE-P model can easily be extended and combined with other models (Sections 4.2.2 and 4.2.3).

4.2.1.1 Standard formulation

The fluid under consideration in this section is composed of polymer macromolecules. To describe its internal structure, we shall use two quantities: the conformation tensor $\boldsymbol{c}$, and the distribution function $\psi(\boldsymbol{Q})$. The former has the physical meaning of an internal deformation tensor, the latter is one molecule configuration space distribution function of polymer molecules regarded as dumbbells with the end-to-end vector $\boldsymbol{Q}$. The quantities $\boldsymbol{c}$ and $\psi(\boldsymbol{Q})$ are related by

$$c_{\alpha\beta} = \int d\boldsymbol{Q} Q_\alpha Q_\beta \psi(\boldsymbol{Q}) \tag{4.1}$$

where, $\alpha, \beta = 1, 2, 3$. The level of description on which $\boldsymbol{c}$ (respectively $\psi(\boldsymbol{Q})$) is used as one of the state variables will be referred to as $\boldsymbol{c}$-level (respectively ψ-level). The conformation tensor $\boldsymbol{c}$ as well as the distribution function ψ can depend on the position coordinate $\boldsymbol{r}$ but in this paper we shall concentrate mainly on homogeneous systems in which $\boldsymbol{c}$ is independent of $\boldsymbol{r}$. As it is seen from (4.1), the ψ-level is more microscopic since the distribution function contains more details than its second moment. On the other hand, the symmetric positive definite tensor $\boldsymbol{c}$ has an autonomous existence. It can have physical interpretations that are different from the one seen in (4.1). In this section and in the whole paper, we shall think and express ourselves solely on the $\boldsymbol{c}$-level. Only occasionally, in order to clarify the physical meaning of some quantities entering our analysis, we shall use the ψ-level. The full set of state variables (denoted by the symbol x in this paper) will always include one or more conformation tensors but it also may include other quantities. In the standard formulation of the FENE-P theory,

$$x = \boldsymbol{c} \tag{4.2}$$

The FENE-P model [Bird et al. (1980)] provides the following equation governing the time evolution of $\boldsymbol{c}$:

$$\begin{aligned}\frac{d\boldsymbol{c}}{dt} &= -\frac{1}{2}(\boldsymbol{\Omega}\cdot\boldsymbol{c}-\boldsymbol{c}\cdot\boldsymbol{\Omega})+\frac{1}{2}(\dot{\boldsymbol{\gamma}}\cdot\boldsymbol{c}+\boldsymbol{c}\cdot\dot{\boldsymbol{\gamma}}) \\ &\quad +\frac{4k_BT}{\zeta}\boldsymbol{\delta}-\frac{4H}{\zeta}\frac{\boldsymbol{c}}{(1-tr(\boldsymbol{c}/Q_0^2))}\end{aligned} \tag{4.3}$$

and the following expression for the extra stress tensor $\boldsymbol{\sigma}$:

$$\boldsymbol{\sigma} = -n_c\frac{H}{1-tr(\boldsymbol{c}/Q_0^2)}+n_ck_BT\boldsymbol{\delta} \tag{4.4}$$

Equation (4.3) has been derived originally [Bird et al. (1980, 1987b)] by, first, writing down the time evolution equation for $\psi(\boldsymbol{Q})$ (as the Liouville equation corresponding to the Newtonian dynamics - in the inertialless approximation - of two beads of a dumbbell), and second, by using (4.1) and an appropriate closure -Peterlin closure -, to transform the kinetic equation into the time evolution equation for $\boldsymbol{c}$. The expression (4.4) for the extra stress tensor $\boldsymbol{\sigma}$ has been derived by calculating the force acting on a surface element (i.e. by using the physical interpretation of $\boldsymbol{\sigma}$ revealed in the role it plays in the time evolution equation for the velocity $\boldsymbol{v}$).

The symbols appearing in (4.3) have the following meaning: $\dot{\gamma}_{\alpha\beta}=\frac{\partial v_\alpha}{\partial r_\beta}+\frac{\partial v_\beta}{\partial r_\alpha}$ and $\boldsymbol{\Omega}_{\alpha\beta}=\frac{\partial v_\alpha}{\partial r_\beta}-\frac{\partial v_\beta}{\partial r_\alpha}$, $\boldsymbol{v}(\boldsymbol{r})$ is the overall velocity field, k_B is the Boltzmann constant, T is the temperature, Q_0 is the largest extension of the dumbbell, H is the elastic modulus of the dumbbell spring, ζ is the friction (bead-fluid) coefficient, n_c is the number density of the polymer macromolecules, $\boldsymbol{\delta}$ is the identity tensor, and tr is the trace.

Judging from the original derivation of the kinetic equation that eventually leads to (4.3), the domain of applicability of (4.3) are dilute solutions of polymer molecules in a Newtonian fluid. However, already the fact the FENE-P model is formulated on a more macroscopic $\boldsymbol{c}$-level, and another fact that the Peterlin closure transforms the kinetic equation, that is linear in ψ, into (4.3) that is nonlinear in $\boldsymbol{c}$, indicates that the FENE-P model may have a much larger domain of applicability. Indeed, the FENE-P model has been applied to polymer melts and concentrated polymer solutions in [Guo et al. (2005); Ramazani et al. (2001)].

Regarding the problem of estimating the physical domain of applicability of a mesoscopic theory from the way it is derived from a more microscopic theory, it is useful to recall the well known derivation of classical hydrodynamics from the Boltzmann kinetic theory. The larger domain of validity of classical hydrodynamics (recall that the Boltzmann kinetic theory is valid only for dilute gases) becomes apparent only in its another derivation, namely the phenomenological derivation (recalled in Appendix). This observation represents in fact one of the argument indicating the importance of developing a general framework for mesoscopic theories that is based mainly on their more macroscopic consequences. Their microscopic origins take the principal role only in the next stage consisting of filling up the framework. The framework will be gradually emerging in the rest of Section 4.2.1 and it will be recalled in a general setting in Appendix.

4.2.1.2 Formulation with the free energy

The first two terms on the right hand side of (4.3) represent advection of $\boldsymbol{c}$ by the overall flow field $\boldsymbol{v}$. We note that if we reverse the sign of $\boldsymbol{v}$ then these two terms change their sign and consequently we see that the transformation $\boldsymbol{v} \to -\boldsymbol{v}$ compensates the inversion of time (i.e. the transformation $t \to -t$ made on the left hand side of (4.3)). Because of this property, the first two terms on the right hand side of (4.3) represent the time reversible part of the time evolution. We shall return to the advection part of the time evolution in Section 4.2.2 and then also in Appendix.

Now, we turn our attention to the last two terms on the right hand side of (4.3). We note that these two terms are time irreversible (i.e. they do not change their signs by changing the sign of $\boldsymbol{v}$) and their main role is to bring dissipation to the time evolution. In order to manifestly display this property, we rewrite (4.3) into a new form

$$\begin{aligned} \frac{d\boldsymbol{c}}{dt} &= -\frac{1}{2}\left(\boldsymbol{\Omega}\cdot\boldsymbol{c}-\boldsymbol{c}\cdot\boldsymbol{\Omega}\right)+\frac{1}{2}\left(\dot{\boldsymbol{\gamma}}\cdot\boldsymbol{c}+\boldsymbol{c}\cdot\dot{\boldsymbol{\gamma}}\right) \\ &\quad -\frac{\partial\Xi}{\partial\Phi^{c}_{\boldsymbol{c}}} \end{aligned} \tag{4.5}$$

where Ξ, called a dissipation potential, is given by

$$\Xi = \Phi^c_{\boldsymbol{C}} \cdot \boldsymbol{\Lambda}^{cc} \cdot \Phi^c_{\boldsymbol{C}} \tag{4.6}$$

$$\begin{aligned} \Phi^c &= E^c - k_B T S^c \\ E^c &= -\frac{1}{2} n_c H Q_0^2 \ln\left(1 - tr(\boldsymbol{c}/Q_0^2)\right) \\ S^c &= \frac{1}{2} n_c \ln(\det(\boldsymbol{c}/Q_0^2)) \end{aligned} \tag{4.7}$$

$\Phi^c_{\boldsymbol{C}} = \frac{\partial \Phi^c}{\partial \boldsymbol{C}}$, and the mobility tensor $\boldsymbol{\Lambda}^{cc} = \frac{2}{n_c \zeta} \boldsymbol{c}$. The same symbols appearing in (4.5) and in (4.3) have the same meaning. By simply performing the calculations involved in (4.5) (we recall the identity $\partial(\ln \det \boldsymbol{c})/\partial \boldsymbol{c} = \boldsymbol{c}^{-1}$), we easily convince ourselves that Eq.(4.5) is indeed exactly the same as Eq.(4.3). This means that (4.5) is only an equivalent reformulation of (4.3).

The advantage of (4.5) over (4.3) is that a new macroscopic physics is revealed in (4.5):

(i) We have identified the potential Φ^c that has the physical interpretation of the free energy, E^c is the FENE-P intramolecular energy, and S^c is the entropy. As for the energy, we indeed see that in the case of small deformations (i.e. small $tr\boldsymbol{c}$) the FENE-P energy is well approximated by $E^c = H\, tr\boldsymbol{c}$ which is the familiar Hooke elastic energy and $E^c \to \infty$ as $tr\boldsymbol{c} \to Q_0^2$ which guarantees the finite extensibility. As for the entropy [Sarti and Marrucci (1973)], it arises directly by maximizing the Boltzmann entropy $S_{Boltzmann} = -k_B \int d\boldsymbol{Q} \psi(\boldsymbol{Q}) ln \psi(\boldsymbol{Q})$ subjected to the constraint (4.1).

(ii) We can prove easily the dissipation property

$$\frac{d\Phi^c}{dt} < 0 \tag{4.8}$$

of solutions to (4.5). The proof of (4.8) is made in two steps. First, we prove it for (4.5) with the first two terms on its right hand side missing , and second, we prove that Φ^c remains unchanged if the third term on the right hand side of (4.5) is missing. The second step is made below in Section 4.2.1.3. The first step is straightforward: $\frac{d\Phi^c}{dt} = \Phi^c_{\boldsymbol{C}} \cdot \frac{d\boldsymbol{C}}{dt} = -2\Phi^c_{\boldsymbol{C}} \cdot \Lambda^{cc} \cdot \Phi^c_{\boldsymbol{C}} < 0$. The last inequality follows from the fact that the mobility tensor

$\boldsymbol{\Lambda}^{cc} = \frac{2}{n_c\zeta}\boldsymbol{c}$ is positive definite. The physical significance of the inequality (4.8) will be explained in the last paragraph of Section 4.2.1.3.

(iii) We have established a relation to nonequilibrium thermodynamics. The term $\Phi^c_{\boldsymbol{c}}$ arising in (4.6) is, if the terminology of nonequilibrium thermodynamics is used, a thermodynamic force and the dissipation potential is directly related to the entropy production (in our case, due to our limitation to isothermal fluids, to the production of the free energy).

(iv) The time evolution equation (4.5) can be easily adapted to different physical systems and situations by introducing into the free energy new terms expressing new physics, and by appropriately modifying the mobility tensor $\boldsymbol{\Lambda}^{cc}$. For example, if we replace $\boldsymbol{\Lambda}^{cc} = \frac{2}{n_c\zeta}\boldsymbol{c}$ arising in the classical FENE-P model by $\Lambda_0^{cc}\left(\widehat{\boldsymbol{c}\boldsymbol{\delta}} + \widehat{\boldsymbol{c}\boldsymbol{c}}\right)$, where $\widehat{\ }$ denotes the symmetrization in the four indices, then the second normal stress difference (that is always zero in the classical FENE-P model) becomes different from zero. We shall use this modification in the calculations reported in Section 4.3.

Summing up, the reformulation (4.5) helped us to see the role of the last term on the right hand side of (4.3) in the time evolution. It did not bring however any clarification to the expression (4.4) for the extra stress tensor $\boldsymbol{\sigma}$. Such clarification will emerge in the next section.

4.2.1.3 Formulation with the free energy and the momentum equation

We begin by extending the state variables (4.2). The new state variables are

$$x = (\boldsymbol{u}(\boldsymbol{r}), \boldsymbol{c}(\boldsymbol{r})) \tag{4.9}$$

where $\boldsymbol{u}(\boldsymbol{r})$ is the momentum field of the fluid per unit volume. In this section we are thus adopting the momentum field into the set of the state variables. The equations governing the time evolution of (4.9) are the following:

$$\begin{aligned}
\frac{\partial \boldsymbol{u}}{\partial t} &= -\nabla\cdot(\boldsymbol{u}\Phi_{\boldsymbol{u}}) - \nabla p - \nabla\cdot\boldsymbol{\sigma} \\
\frac{\partial \boldsymbol{c}}{\partial t} &= -\nabla(\boldsymbol{c}\cdot\Phi_{\boldsymbol{u}}) - \frac{1}{2}(\boldsymbol{\Omega}\cdot\boldsymbol{c} - \boldsymbol{c}\cdot\boldsymbol{\Omega}) + \frac{1}{2}(\dot{\boldsymbol{\gamma}}\cdot\boldsymbol{c} + \boldsymbol{c}\cdot\dot{\boldsymbol{\gamma}}) \\
&\quad -\frac{\partial \Xi}{\partial \Phi_{\boldsymbol{c}}}
\end{aligned} \tag{4.10}$$

where p is the scalar hydrostatic pressure, $\boldsymbol{\sigma}$ is the extra stress tensor, $\Phi(\boldsymbol{u}, \boldsymbol{c})$ is the free energy

$$\Phi(\boldsymbol{u}, \boldsymbol{c}) = \frac{1}{V} \int d\boldsymbol{r} \frac{u^2}{\rho} + \Phi^c(\boldsymbol{c}) \tag{4.11}$$

V is the volume of the fluid, ρ is the mass per unit volume, and Φ^c is given in (4.7). The first term on the right hand side of (4.11) (i.e. the new term arising due to the use of (4.9) instead of (4.2) as state variables) has the physical interpretation of the kinetic energy. Note that $\Phi_{\boldsymbol{u}} = \frac{\boldsymbol{u}}{\rho} = \boldsymbol{v}$ is the velocity field. We have added the term $-\nabla(\boldsymbol{c} \cdot \Phi_{\boldsymbol{u}})$ to the right hand side of the second equation in (4.10) in order to include also the case when $\boldsymbol{c}$ depends on the position coordinate $\boldsymbol{r}$.

We turn now our attention to the time evolution of Φ given in (4.11). First, we split the time evolution of x into reversible and irreversible parts: $\frac{\partial x}{\partial t} = \left(\frac{\partial x}{\partial t}\right)_{revrsible} + \left(\frac{\partial x}{\partial t}\right)_{irrevrsible}$. The reversible part of (4.10) is the part that is invariant with respect to the transformation ($t \to -t$; $\boldsymbol{u} \to -\boldsymbol{u}$). The remaining part is the time irreversible part. It is easy to see that (4.10) with the term involving the dissipation potential Ξ missing generates the time reversible evolution provided p and $\boldsymbol{\sigma}$ remain invariant under the transformation $\boldsymbol{u} \to -\boldsymbol{u}$. Equation (4.10) with all terms missing except the term involving Ξ generates the time irreversible evolution.

We shall now require that

$$\left(\frac{d\Phi}{dt}\right)_{reversible} = 0 \tag{4.12}$$

and

$$\left(\frac{d\Phi}{dt}\right)_{irreversible} < 0 \tag{4.13}$$

which, if put together, implies

$$\frac{d\Phi}{dt} = \left(\frac{d\Phi}{dt}\right)_{reversible} + \left(\frac{d\Phi}{dt}\right)_{irreversible} \leq 0 \tag{4.14}$$

The inequality (4.13) has already been proven in Section 4.2.1.2. We turn now to (4.12). We shall show that (4.12) holds provided

$$p = -\varphi + \rho\Phi_\rho + \boldsymbol{u} \cdot \Phi_{\boldsymbol{u}} + \boldsymbol{c} : \Phi_{\boldsymbol{c}} \tag{4.15}$$

where φ is defined by $\Phi = \frac{1}{V}\int d\boldsymbol{r}\varphi$ and

$$\boldsymbol{\sigma} = -2\,\boldsymbol{c}\cdot\Phi_{\boldsymbol{c}} \tag{4.16}$$

The relation (4.15) tells us that p has the physical meaning of the local pressure and (4.16) is an expression for the extra stress tensor. By inserting the free energy (4.11) into (4.16) we see that (4.16) is indeed the same as (4.4). The idea to obtain expression for the extra stress tensor from the requirement (4.12) has been introduced first in Grmela (1985).

To prove that (4.15) and (4.16) are consequences of (4.12), we simply write $\left(\frac{d\Phi}{dt}\right)_{reversible} = +\int d\boldsymbol{r}\Phi_\rho\left(\frac{\partial\rho}{\partial t}\right)_{reversible} + \int d\boldsymbol{r}\Phi_{\boldsymbol{u}}\left(\frac{\partial\boldsymbol{u}}{\partial t}\right)_{reversible} + \Phi_{\boldsymbol{c}}\left(\frac{\partial\boldsymbol{c}}{\partial t}\right)_{reversible} = 0$ and insert into it the reversible time evolution equations. To make the calculations easier we have adopted $\rho(\boldsymbol{r})$ (together with the equation $\frac{\partial\rho}{\partial t} = -div(\rho\Phi_{\boldsymbol{u}})$ governing its time evolution) to the full set of state variables. In other words, the fluid is considered compressible in the proof.

The inequality (4.14) is the mathematical formulation of the compatibility of the time evolution equations (4.10) with thermodynamics. We have proven (the inequality (4.14) allows us to regard the free energy as a Lyapunov function) that solutions to the governing equations of the FENE-P model (i.e. Eqs.(4.10) and (4.16)) agree with the experimentally observed compatibility with thermodynamics, namely, with the observation that fluids, if left undisturbed sufficiently long time, reach a state, called an equilibrium state (the state at which the free energy reaches its minimum), at which its behavior is found to be well described by classical equilibrium thermodynamics with the fundamental thermodynamic relation given by $-\frac{P}{T} = \Phi|_{equilibrium\ states}$, P is the thermodynamic pressure and T is the temperature.

4.2.2 Lamellae

In this section we replace the polymer macromolecules with lamellae. The resulting fluid is a complex fluid for which we want to formulate a rheological model. We cannot rely anymore on a well established model as we did in the previous section. We turn therefore directly to the viewpoint that emerged in Section 4.2.1.3.

First, we have to decide what are the variables that we shall use to describe states of the lamellae. In this paper we make the simplest choice. Let $\boldsymbol{n}$ be a unit vector perpendicular to the lamella. The distribution of the lamellae (we again restrict ourselves in this paper to spatially homogeneous distribution) is described by the distribution function $\psi(\boldsymbol{n})$. Its second moment is a tensor denoted by the symbol $\boldsymbol{a}$ (i.e. $a_{\alpha\beta} = \int d\boldsymbol{n} n_\alpha n_\beta \psi(\boldsymbol{n})$). The constraint $|\boldsymbol{n}| = 1$ is expressed on the $\boldsymbol{a}$-level as $tr\boldsymbol{a} = A_0$ where A_0 is the surface area of the lamella. The full set of state variables is thus

$$x = (\boldsymbol{u}(\boldsymbol{r}), \boldsymbol{a}(\boldsymbol{r})); \;\; tr\boldsymbol{a} = A_0. \tag{4.17}$$

where $\boldsymbol{u}$ has the same meaning as in the preceding section (i.e. $\boldsymbol{u}$ is the field of the overall momentum).

Next, we have to address the problem of how the lamellae are advected by the overall flow $\boldsymbol{u}$. In the FENE-P model, the advection (expressed in the first two terms on the right hand side of (4.3)) emerged from the kinetic equation (i.e. from the passive advection of two beads of the dumbbell). If we look at (4.3) solely on the $\boldsymbol{c}$-level, we note that it is a Lie derivative of the tensor $\boldsymbol{c}$ along the vector field $\boldsymbol{u}$. In the terminology used in rheology, the first two terms on the right hand side of (4.3)), together with $\frac{\partial \boldsymbol{c}}{\partial t}$ and the first term on the right hand side of the second equation in (4.10) (that has to be added if $\boldsymbol{c}$ depends on $\boldsymbol{r}$) is called an upper convected time derivative. The "first principle" microhydrodynamic [Kim and Karilla (1991)] approach to the advection of lamellae consists of formulating and solving (e.g. following Eshelby (1957, 1959)) the corresponding Stokes problem. The advection arising in this way (as it is well known in particular form the advection of fibers [Jeffery (1922)]) is not passive (see also Appendix). In order to keep our model simple, we shall be content in this paper with the advection of lamellae obtained by making only a straightforward adaptation of the upper convected advection of the dumbbells. The adaptation consists of: (a) replacement of the upper convected derivative by the lower convected derivative, (b) modification that guarantees $\frac{dtr\boldsymbol{a}}{dt} = 0$, and (c) the Gordon-Schowalter modification [Gordon and Schowalter (1972)] accounting, phenomenologically, for the active part of the advection. After making

the modifications, the governing equations become

$$\begin{aligned}\frac{\partial \boldsymbol{u}}{\partial t} &= -\nabla\cdot(\boldsymbol{u}\Phi_{\boldsymbol{u}}) - \nabla p - \nabla\cdot\boldsymbol{\sigma}\\ \frac{\partial \boldsymbol{a}}{dt} &= -\nabla(\boldsymbol{a}\cdot\Phi_{\boldsymbol{u}}) - \frac{1}{2}(\boldsymbol{\Omega}\cdot\boldsymbol{a} - \boldsymbol{a}\cdot\boldsymbol{\Omega}) + \xi\left(-\frac{1}{2}(\dot{\gamma}\cdot\boldsymbol{a} + \boldsymbol{a}\cdot\dot{\gamma}) + \frac{1}{A_0}tr(\boldsymbol{a}\,.\,\dot{\gamma})\boldsymbol{a}\right)\\ &\quad -\frac{\partial\Xi}{\partial\Phi_{\boldsymbol{a}}}\end{aligned} \tag{4.18}$$

The term involving $tr(\boldsymbol{a}\cdot\dot{\gamma})$ guarantees the preservation of the constraint $tr\boldsymbol{a} = A_0$ for the time reversible evolution (i.e. for (4.18) without term involving Ξ), ξ is the Gordon-Schowalter phenomenological parameter (note that in the particular case $\xi = 1$, the advection becomes exactly lower convected), and Ξ, Φ denote dissipation potential and free energy (both will be specified below). The same argument that lead us in Section 4.2.1.3 to the expression for the extra stress tensor (4.16) leads us now to

$$\boldsymbol{\sigma} = 2\,\xi\,\boldsymbol{a}\cdot\Phi_{\boldsymbol{a}} - \frac{2}{A_0}\,\xi\,\boldsymbol{a}\,tr(\boldsymbol{a}\cdot\Phi_a) \tag{4.19}$$

We note here the appearance of the Gordon-Schowalter parameter ξ in the expression for the extra stress tensor. The realization that a modification of the advection has to be always accompanied by a corresponding modification of the expression for the extra stress tensor can easily be missed if the extra stress tensor is discussed in the same way as in the standard presentation of the FENE-P model (see Section 4.2.1.1).

The argument supporting the first modification of the advection of lamellae (i.e. replacement of the upper convected by the lower convected derivative) goes as follows. Let $\boldsymbol{m}$ be a vector lying in the plane of the lamella. Since $\boldsymbol{n}$ has been chosen to be perpendicular to the lamella, we have $<\boldsymbol{n},\boldsymbol{m}>= 0$ (where $<,>$ denotes the inner product), and also $\frac{d}{dt}<\boldsymbol{n},\boldsymbol{m}>= 0$ since the vectors $\boldsymbol{n}$ and $\boldsymbol{m}$ remain perpendicular during the time evolution. We let the vector $\boldsymbol{m}$ to be advected in the same way as the vector $\boldsymbol{Q}$ in the previous section (to shorten the notation, we write $\frac{d\boldsymbol{m}}{dt} = \mathcal{L}^{upper}\boldsymbol{m}$, where the upper index refers to "upper convected derivative"). Consequently, $\frac{d}{dt}<\boldsymbol{n},\boldsymbol{m}>=<\frac{d\boldsymbol{n}}{dt},\boldsymbol{m}> + <\boldsymbol{n},\frac{d\boldsymbol{m}}{dt}>=<\frac{d\boldsymbol{n}}{dt},\boldsymbol{m}> + <\boldsymbol{n},\mathcal{L}^{upper}\boldsymbol{m}>=<\frac{d\boldsymbol{n}}{dt},\boldsymbol{m}> + <(\mathcal{L}^{upper})^T\boldsymbol{n},\boldsymbol{m}>= 0$. This then implies that $\boldsymbol{n}$ is advected by the lower convected time derivative $\frac{d\boldsymbol{n}}{dt} = -(\mathcal{L}^{upper})^T\boldsymbol{n} = \mathcal{L}^{lower}\boldsymbol{n}$. In the absence

of the constraint $|\boldsymbol{n}| = 1$, this time evolution of $\boldsymbol{n}$, translated first into the time evolution of the distribution function $\psi(\boldsymbol{n})$, projects exactly on the lower convected time evolution of the second moment $\boldsymbol{a} = \int d\boldsymbol{n}\, \boldsymbol{n}\boldsymbol{n}\psi(\boldsymbol{n})$. This is not however the case in the presence of the constraint $|\boldsymbol{n}| = 1$. Higher order moments remain in the projected equation. They have to be expressed in terms of the second moment, or in other words, the projected equations have to be closed. All these problems, that arise if the advection of $\boldsymbol{a}$ is seen as a projection of an advection formulated first on the ψ-level, are solved in this paper by making the three simple modifications (a)-(c) of the upper convected derivative. More thorough analysis of this aspect of the model is under investigation [Gu and Grmela (2008)] (see also Appendix).

It remains to specify the dissipation potential Ξ and the free energy Φ. We begin with Ξ. We shall choose it in the same way as in the context of the FENE-P model:

$$\Xi = \boldsymbol{A} \cdot \boldsymbol{\Lambda}^{aa} \cdot \boldsymbol{A} \tag{4.20}$$

where $\boldsymbol{\Lambda}^{aa}$ is a phenomenological mobility tensor and $\boldsymbol{A}$ is a quantity depending on $\Phi_{\boldsymbol{a}}$ in such a way that the constraint $tr\boldsymbol{a} = A_0$ is preserved during the dissipative time evolution (i.e. that $tr\left(\Xi_{\Phi_{\boldsymbol{a}}}\right) = 0$ holds). It is easy to see (see also Edwards et al. (2003)) that if we choose

$$\boldsymbol{A} = \Phi_{\boldsymbol{a}} - \frac{1}{3} tr\Phi_{\boldsymbol{a}}\boldsymbol{\delta} \tag{4.21}$$

then indeed $\frac{dtr\left(\Xi_{\Phi_{\boldsymbol{a}}}\right)}{dt} = 0$.

Next, we turn to the free energy Φ. We choose it as follows:

$$\Phi(\boldsymbol{u}, \boldsymbol{a}) = \frac{1}{V}\int d\boldsymbol{r}\frac{u^2}{\rho} + \Phi^a(\boldsymbol{a}) \tag{4.22}$$

where

$$\begin{aligned}
\Phi^a &= E^a - k_B T S^a \\
E^a &= 0 \\
S^a &= \frac{1}{2} n_a \frac{G}{k_B T} A_0 tr\left(\frac{\boldsymbol{a}}{A_0}\right) + \frac{1}{2} n_a \left(1 - K_{flex}\right) \ln(\det\left(\frac{\boldsymbol{a}}{A_0}\right)) \\
&\quad - \frac{1}{2} n_a K_{flex} tr\left(A_0 \boldsymbol{a}^{-1}\right) + \frac{1}{2} n_a^2 \kappa \left(tr\left(\frac{\boldsymbol{a}}{A_0} \cdot \frac{\boldsymbol{a}}{A_0}\right) - (tr\frac{\boldsymbol{a}}{A_0})^2\right)
\end{aligned} \tag{4.23}$$

where n_a is the number density of plates ($n_a = \frac{1}{A_0 h}$; A_0 is the surface area of the lamella and h its thickness), κ and K_{flex} are phenomenological parameters whose physical interpretation is explained below.

The first term in the entropy expresses the constraint $tr\boldsymbol{a} = A_0$. The parameter G is the Lagrange coefficient that will be determined later (see the text following Eq.(4.32)). The following two terms represent a linear combination of the classical entropy appearing already in (4.7) and the Khokhlov-Semenov entropy [Khokhlov and Semenov (1985)] accounting for the flexibility of the plates (K_{flex} a parameter characterizing the flexibility of plates). The fourth term is the Maier-Saupe type entropy [Maier and Saupe (1960)] accounting for the topological interactions among the plates. By the topological interaction we mean the constraint that the presence of other plates represent for the placement of the plate described by the conformation tensor $\boldsymbol{a}$. This type of interactions is also known as excluded volume interactions if the shape of the particles involved in the interactions does not play any role (as it is for example in the case of solid spherical particles).

The energy part E^a (e.g. energies associated with possible bending and stretching of lamellae or van der Walls type lamella-lamella interactions) of the free energy Φ^a is neglected. However, at least the part of the interaction energy that can be expressed in terms of the second invariant of $\boldsymbol{a}$ could be seen to be included in the entropy term. The phenomenological parameter κ measures thus the intensity of the topological plate-plate interactions and also interactions depending on the second invariant. The distinction between the energy and the entropy part will manifest itself in the temperature dependence of κ.

The free energy Φ as well as the dissipation potential Ξ and the advection have been introduced above by using arguments belonging solely to the conformation tensor level. The quantities $\xi, \boldsymbol{\Lambda}^{aa}, K_{flex}$ and κ, serving as material parameters on the conformation tensor level, have a clear physical meaning inside the conformation tensor level but their relation to microscopic (molecular) material parameters has not been established. We regard $(\xi, \boldsymbol{\Lambda}^{aa}, K_{flex}, \kappa)$ as phenomenological quantities whose values are determined by comparing consequences of the model with results of experimental observations and/or with consequences of other mod-

els. A theoretical way of establishing a relation between $(\xi, \mathbf{\Lambda}^{aa}, K_{flex}, \kappa)$, and microscopic materials parameters consists of constructing first a microscopic theory involving the microscopic material parameters and then reducing it to the conformation-tensor level. We do not follow this route in this paper.

Below, we shall only outline the ψ-level origin of the free energy (4.23). The ψ-level physical explanation of the classical entropy has already been given in the text following (4.7). We shall now provide a similar clarification for the remaining two parts of the entropy.

Khokhlov and Semenov (1985) discussed flexible macromolecules on the ψ-level. Their analysis leads to the following expression for the entropy: $S \sim \int d\boldsymbol{n} \frac{1}{4\psi(\boldsymbol{n})} \left(\frac{\partial \psi(\boldsymbol{n})}{\partial \boldsymbol{n}} \cdot \frac{\partial \psi(\boldsymbol{n})}{\partial \boldsymbol{n}} \right)$. If $\psi(\boldsymbol{n}) \approx (2\pi)^{-\frac{2}{3}} (det \boldsymbol{a}^{-1})^{\frac{1}{2}} \; exp(-\boldsymbol{n} \cdot \boldsymbol{a}^{-1} \cdot \boldsymbol{n})$ is inserted into this expression, the expression representing the Khokhlov-Semenov entropy in (4.23) (i.e. the third term) appears.

Due to the plate-plate topological interactions, the plates have a tendency to arrange themselves into parallel formations. The analogical situation arising if the plates are replaced by rigid rods has been discussed on the ψ-level by Onsager (1949). The new term in the entropy, expressing the topological interactions among rods, has the form $S \sim \int d\boldsymbol{n} \int d\boldsymbol{n}' |\boldsymbol{n} \times \boldsymbol{n}'| \psi(\boldsymbol{n}) \psi(\boldsymbol{n}')$, where $\boldsymbol{n}$ is the unit vector along the rod. We suggest now to use the same expression for plates with $\boldsymbol{n}$ being the unit vector perpendicular to them. Moreover, we note (this observation has been made in Grmela (1990)) that if we replace $|\boldsymbol{n} \times \boldsymbol{n}'|$ in the Onsager entropy by $|\boldsymbol{n} \times \boldsymbol{n}'|^2$ (note that with this replacement the Onsager entropy still keeps its physical interpretation) then the Onsager entropy becomes exactly equal to the Maier-Saupe entropy $S \sim (tr(\boldsymbol{a} \cdot \boldsymbol{a}) - (tr \boldsymbol{a})^2)$ [Maier and Saupe (1960)] expressing the topological interaction on the $\boldsymbol{a}$-level.

4.2.3 FENE-P dumbbells and lamellae

The fluid under consideration is now composed of both FENE-P dumbbells and lamellae. As in Section 4.2.2, we shall formulate the rheological model of such fluid directly in the setting that emerged in Section 4.2.1.3.

The full set of state variables is

$$x = (\boldsymbol{u}(\boldsymbol{r}), \boldsymbol{c}(\boldsymbol{r}), \boldsymbol{a}(\boldsymbol{r})); \;\; tr\boldsymbol{a} = A_0. \tag{4.24}$$

where the symbols appearing in (4.24) have the same meaning as in in Sections 4.2.1.1. and 4.2.1.2.

Coupling between FENE-P dumbbells and lamellae will be introduced only in the dissipation potential Ξ and the free energy Φ. We shall assume that the advection of a macromolecule is not affected by the presence of lamellae, and conversely, the advection of a lamella is not affected by the presence of the polymer macromolecules. Consequently, the equations governing the time evolution of (4.24) are the following:

$$\begin{aligned}
\frac{\partial \boldsymbol{u}}{\partial t} &= -\nabla \cdot (\boldsymbol{u}\Phi_{\boldsymbol{u}}) - \nabla p - \nabla \cdot \boldsymbol{\sigma} \\
\frac{\partial \boldsymbol{c}}{\partial t} &= -\nabla(\boldsymbol{c} \cdot \Phi_{\boldsymbol{u}}) - \frac{1}{2}(\boldsymbol{\Omega} \cdot \boldsymbol{c} - \boldsymbol{c} \cdot \boldsymbol{\Omega}) + \frac{1}{2}(\dot{\gamma} \cdot \boldsymbol{c} + \boldsymbol{c} \cdot \dot{\gamma}) \\
&\quad -\frac{\partial \Xi}{\partial \Phi_{\boldsymbol{c}}} \\
\frac{\partial \boldsymbol{a}}{\partial t} &= -\nabla(\boldsymbol{a} \cdot \Phi_{\boldsymbol{u}}) - \frac{1}{2}(\boldsymbol{\Omega} \cdot \boldsymbol{a} - \boldsymbol{a} \cdot \boldsymbol{\Omega}) + \xi\left(-\frac{1}{2}(\dot{\gamma} \cdot \boldsymbol{a} + \boldsymbol{a} \cdot \dot{\gamma}) + \frac{1}{A_0} tr(\boldsymbol{a} \,.\, \dot{\gamma})\boldsymbol{a}\right) \\
&\quad -\frac{\partial \Xi}{\partial \Phi_{\boldsymbol{a}}}
\end{aligned} \tag{4.25}$$

where

$$\boldsymbol{\sigma} = -2\,\boldsymbol{c} \cdot \Phi_{\boldsymbol{c}} + 2\,\xi\,\boldsymbol{a} \cdot \Phi_{\boldsymbol{a}} - \frac{2}{A_0}\,\xi\,\boldsymbol{a}\,tr(\boldsymbol{a} \,.\, \Phi_a) \tag{4.26}$$

Here we want to stress again that we have obtained the expression for the extra stress tensor $\boldsymbol{\sigma}$ automatically as a part of the governing equations. This has at least three advantages: First, we are certain that the expression for $\boldsymbol{\sigma}$ is compatible with the time evolution of the internal structure, second, we do not need any new physical considerations and new approximations to arrive at the expression for $\boldsymbol{\sigma}$, and third, the expression (4.26) is in fact a family of expressions, a new physics expressed in new free energy implies automatically a new expression for $\boldsymbol{\sigma}$.

Next, we turn our attention to the dissipation potential. We shall choose it as follows:

$$\Xi = (\Phi_{\boldsymbol{C}}, \boldsymbol{A}) \begin{pmatrix} \boldsymbol{\Lambda}^{cc} & \boldsymbol{\Lambda}^{ca} \\ \\ \boldsymbol{\Lambda}^{ca} & \boldsymbol{\Lambda}^{aa} \end{pmatrix} \begin{pmatrix} \Phi_{\boldsymbol{C}} \\ \boldsymbol{A} \end{pmatrix} \tag{4.27}$$

The terms proportional to the mobility tensor $\boldsymbol{\Lambda}^{ca}$ represents the coupling. All three mobility tensors $\boldsymbol{\Lambda}^{cc}$, $\boldsymbol{\Lambda}^{aa}$, and $\boldsymbol{\Lambda}^{ca}$ are phenomenological parameters. The first one,$\boldsymbol{\Lambda}^{cc}$, is specified by requiring that in the absence of lamellae our model is identical with the FENE-P model. This requirement, as we have already seen in Section 4.2.1.1, implies that $\boldsymbol{\Lambda}^{cc}$ is proportional to $\boldsymbol{c}$. To specify the remaining two mobility tensors, we follow Beris and Edwards (1990, 1994) and assume that they are polynomial functions of $\boldsymbol{c}$ and $\boldsymbol{a}$:

$$\begin{aligned} \boldsymbol{\Lambda}^{cc} &= \Lambda_0^{cc} \left(\widehat{\boldsymbol{c}\boldsymbol{\delta}} + \widehat{\boldsymbol{c}\boldsymbol{c}} \right) \\ \boldsymbol{\Lambda}^{aa} &= \Lambda_0^{aa} \left(f_1 \widehat{\boldsymbol{a}\boldsymbol{\delta}} + f_2 \widehat{\boldsymbol{a}\boldsymbol{a}} + f_3 \widehat{\boldsymbol{a}\boldsymbol{a}\boldsymbol{a}} \right) \\ \boldsymbol{\Lambda}^{ca} &= \Lambda_0^{ca} \widehat{\boldsymbol{c}\boldsymbol{a}} \end{aligned} \tag{4.28}$$

where $\boldsymbol{\Lambda}$ are all fourth order tensors,$\widehat{\ }$ means symmetrization in the four indices, and Λ_0^{cc}, Λ_0^{aa} and Λ_0^{ca} are phenomenological parameters. The coefficients f_1, f_2, f_3 equal either 0 or 1. We are introducing them in order to explore (in Section 4.3) the influence of higher order terms in the mobility. If $(f_1 = 1, f_2 = 0, f_3 = 0)$ (resp. $(f_2 = 1, f_1 = 0, f_3 = 0)$ or $(f_3 = 1, f_1 = 0, f_2 = 0)$), we call $\boldsymbol{\Lambda}^{aa}$ a first order (resp. the second or third order) mobility tensor.

The physical interpretation of the coefficients Λ_0 is: $(\Lambda_0)^{-1} \sim \lambda_0$ where λ_0 are relaxation times. In the two component fluid under consideration (polymers and lamellae), we need a mixing rule for the relaxation times. We choose the simplest one. We shall pass from λ_0^{cc} to $(1-\alpha)\lambda_0^{cc}$, from λ_0^{aa} to $\alpha\lambda_0^{aa}$, and from λ_0^{ca} to $\alpha(1-\alpha)\lambda_0^{ca}$, where α is the volume fraction of the lamellae. It is related to the weight fraction w by $\alpha = \rho_c w/(\rho_a - (\rho_a - \rho_c)w)$, where ρ_c (resp. ρ_a) is a mass density of the polymer (resp. lamellae). The other place where the volume fraction α enters the governing equations (4.25) is in the free energy discussed below.

We turn now to the free energy $\Phi(\boldsymbol{u}, \boldsymbol{c}, \boldsymbol{a})$. Here we have to face a problem that is inherent to all mesoscopic considerations. While such considerations have many obvious advantages (e.g. a relative simplicity of the resulting governing equations and a large domain of applicability due to a possibility to interpret in many different ways the mesoscopic state variables), they also have disadvantages. The microscopic constituents of the fluids under investigations present themselves in mesoscopic analyses only through their effective, averaged (renormalized) representatives. This is not a serious problem if only one kind of microscopic constituents is present in the fluid (the case discussed in Sections 4.2.1 and 4.2.2), but it becomes a more serious problem if the fluid is composed of more than one kind of such constituents (polymer macromolecules and clay lamellae in this section). Their mesoscopic representatives have to be put on the same level so that their binary interactions represent faithfully the interactions taking place on the microscopic level. In the fluid discussed in this paper, one lamellae will very likely interact simultaneously (due to their large surface area) with many polymer macromolecules. The simplest way to harmonize our mesoscopic analysis presented in Section 4.2.1 and 2.2, is to rescale n_c and n_a. We shall do it by introducing a renormalized number density, $n_a^{(renormalized)} = \chi n_a$ of the lamellae. Hereafter, the number density n_a is the renormalized number density.The dimensionless coefficient χ is, roughly speaking, a number of polymer macromolecules that are in contact with a single plate. For example, for a constant clay loading, the larger is the plate surface the larger is χ. In the sequel, we regard however the parameter χ as a phenomenological parameter obtained by fitting experimental data. We shall see in Section 4.3 that $\chi \sim 2 \times 10^2$. The only way to avoid the necessity of the phenomenological rescaling is to step up on a more microscopic level on which we could discuss microscopic details of the polymer-lamellae interactions. A step in this direction is made in a paper under preparation in which we consider polymer molecules as chains (i.e. the conformation tensor depends in this analysis on the location on the chain).

The free energy that we choose for the model investigated in this paper is the following:

$$\Phi(\boldsymbol{u},\boldsymbol{c},\boldsymbol{a}) = \frac{1}{V}\int d\boldsymbol{r}\frac{\boldsymbol{u}^2}{2\rho} + \Phi^c + \Phi^a + \Phi^{ca} \tag{4.29}$$

where Φ^c is given in (4.7), Φ^a in (4.23) and

$$\begin{aligned} \Phi^{ca} &= E^{ca} - k_B T S^{ca} \\ E^{ca} &= 0 \\ S^{ca} &= -\frac{1}{2} n_c n_a \kappa' tr\left(\frac{\boldsymbol{c}}{Q_0^2}\cdot\frac{\boldsymbol{a}}{A_0}\right) \end{aligned} \tag{4.30}$$

κ' is a phenomenological parameter measuring the polymer-plate interaction. Similarly as in the case of E^a and S^a (see Section 4.2.2), we can assume that a part of the polymer-plate interaction (the part expressible in terms of the scalar product of $\boldsymbol{c}$ and $\boldsymbol{a}$) is included in S^{ca}. This requires however a reinterpretation of the parameter κ' and its appropriate dependence on the temperature. By n_c we denote the number density of polymers, $n_c = \frac{(1-\alpha)\rho_c N_A}{M_c}$; $n_a = \frac{\alpha}{A_0 h}$, N_A is the Avogadro number, M_c is the molecular weight of the polymer, ρ_c is the mass density of the polymer. The expression in (4.30) is the Onsager entropy [Onsager (1949)] (see Section 4.2.1.2) adapted to the plate-molecule interactions expressed in terms of the conformation tensors rather than the distribution functions: $\int d\boldsymbol{Q}\int d\boldsymbol{n}(\boldsymbol{Q}\cdot\boldsymbol{n})^2\psi(\boldsymbol{Q})\psi(\boldsymbol{n}) = tr(\boldsymbol{c}\cdot\boldsymbol{a})$. We have replaced the vector product appearing in the Onsager expression by the scalar product since the vectors $\boldsymbol{Q}$ and $\boldsymbol{n}$ tend to be perpendicular rather than parallel as it is in the case of the Onsager entropy.

The choice of the parameters entering the free energy (4.29) is restricted by requiring the thermodynamic stability, i.e. by requiring that its second derivative is positive definite.

At this point we have completed the formulation of the governing equations of the model. In the next sections we turn to their solutions.

4.3 Results and discussion

Now we turn to numerical solutions of the governing equations. We begin by transforming them to a dimensionless form. The dimensionless variables are chosen to be:

$$\boldsymbol{c}^* = \frac{H}{k_B T}\,\boldsymbol{c} \quad ; \quad \boldsymbol{a}^* = \frac{G}{k_B T}\,\boldsymbol{a} \quad ; \quad t^* = \frac{t}{\lambda} \quad ; \quad \dot{\gamma}^* = \dot{\gamma}\lambda \quad ; \quad \Omega^* = \Omega\lambda \tag{4.31}$$

Next, we define the dimensionless parameter b that is familiar from the dimensionless form of the governing equations of the FENE-P model and the corresponding dimensionless parameter b' for the lamellae:

$$b = \frac{HQ_0^2}{k_B T} \quad ; \quad b' = \frac{GA_0}{k_B T} \tag{4.32}$$

The value of b will be chosen as in the calculations with the FENE-P model [Bird et al. (1987b)], the value of b' is completely determined by the constraint $tr\boldsymbol{a} = A_0$: $b' = 3$.

In the variables (4.31), and with the choice (4.28) of the mobility tensors, the time evolution equations become:

$$\begin{aligned}
\frac{d\boldsymbol{c}}{dt} &= -\frac{1}{2}\left(\boldsymbol{\Omega}\cdot\boldsymbol{c} - \boldsymbol{c}\cdot\boldsymbol{\Omega}\right) + \frac{1}{2}\left(\dot{\boldsymbol{\gamma}}\cdot\boldsymbol{c} + \boldsymbol{c}\cdot\dot{\boldsymbol{\gamma}}\right) \\
&\quad -\frac{8\,\Lambda_0^{cc}}{(1-\alpha)}\left(\frac{1}{2b}\left(\boldsymbol{c}\cdot\Phi_c + \Phi_c\cdot\boldsymbol{c}\right) + \frac{1}{b^2}\boldsymbol{c}\cdot\Phi_c\cdot\boldsymbol{c}\right) \\
&\quad -\frac{4\,\Lambda_0^{ca}}{\alpha(1-\alpha)\,b}\left(\frac{1}{6}(\boldsymbol{c}\,.\,\Phi_a\,.\,\boldsymbol{a} + \boldsymbol{a}\,.\,\Phi_a\,.\,\boldsymbol{c})\right. \\
&\quad \left. +\frac{1}{18}(\boldsymbol{a}\,.\,\boldsymbol{c} + \boldsymbol{c}\,.\,\boldsymbol{a})\,tr\Phi_a)\right)
\end{aligned} \tag{4.33}$$

$$\begin{aligned}
\frac{d\boldsymbol{a}}{dt} &= -\frac{1}{2}\left(\boldsymbol{\Omega}\cdot\boldsymbol{a} - \boldsymbol{a}\cdot\boldsymbol{\Omega}\right) + \xi\left(-\frac{1}{2}\left(\dot{\boldsymbol{\gamma}}\cdot\boldsymbol{a} + \boldsymbol{a}\cdot\dot{\boldsymbol{\gamma}}\right) + \frac{1}{3}tr(\boldsymbol{a}\,.\,\dot{\boldsymbol{\gamma}})\boldsymbol{a}\right) \\
&\quad -\frac{8\,\Lambda_0^{aa}}{\alpha}\left[\frac{f_1}{3}\left(\frac{1}{2}(\boldsymbol{a}\cdot\Phi_a + \Phi_a\cdot\boldsymbol{a}) - \frac{1}{3}\boldsymbol{\delta}tr(\boldsymbol{a}\cdot\Phi_a) - \frac{1}{3}\boldsymbol{a}tr\Phi_a + \frac{1}{9}\boldsymbol{\delta}tr\boldsymbol{a}tr\Phi_a\right)\right. \\
&\quad +\frac{f_2}{9}\left(\boldsymbol{a}\cdot\Phi_a\cdot\boldsymbol{a} - \frac{1}{3}\boldsymbol{\delta}tr(\boldsymbol{a}\cdot\Phi_a\cdot\boldsymbol{a}) - \frac{1}{3}\boldsymbol{a}\cdot\boldsymbol{a}tr\Phi_a + \frac{1}{9}\boldsymbol{\delta}tr(\boldsymbol{a}\cdot\boldsymbol{a})tr\Phi_a\right) \\
&\quad +\frac{f_3}{27}\left(\frac{1}{2}(\boldsymbol{a}\cdot\Phi_a\cdot\boldsymbol{a}\cdot\boldsymbol{a} + \boldsymbol{a}\cdot\boldsymbol{a}\cdot\Phi_a\cdot\boldsymbol{a}) - \frac{1}{3}\boldsymbol{\delta}tr(\boldsymbol{a}\cdot\boldsymbol{a}\cdot\Phi_a\cdot\boldsymbol{a})\right. \\
&\quad \left.\left. -\frac{1}{3}\boldsymbol{a}\cdot\boldsymbol{a}\cdot\boldsymbol{a}tr\Phi_a + \frac{1}{9}\boldsymbol{\delta}tr(\boldsymbol{a}\cdot\boldsymbol{a}\cdot\boldsymbol{a})tr\Phi_a\right)\right] \\
&\quad -\frac{4\,\Lambda_0^{ca}}{\alpha(1-\alpha)\,b}\left(\frac{1}{6}(\boldsymbol{c}\,.\,\Phi_c.\boldsymbol{a} + \boldsymbol{a}\,.\,\Phi_c\,.\,\boldsymbol{c}) - \frac{1}{9}\,\boldsymbol{\delta}\,tr(\boldsymbol{c}\,.\,\Phi_c\,.\,\boldsymbol{a})\right)
\end{aligned} \tag{4.34}$$

and

$$\sigma = -2\,\boldsymbol{c}\,.\,\Phi_c + 2\,\xi\,\left(\boldsymbol{a}.\Phi_a - \frac{1}{3}\,\boldsymbol{a}\,tr(\boldsymbol{a}\,.\,\Phi_a)\right) \tag{4.35}$$

The derivatives of the free energy Φ_c and Φ_a are given by

$$\Phi_c = \frac{1}{2}\,n_c\,k_B\,T\,\left(\frac{\boldsymbol{\delta}}{1-tr\boldsymbol{c}/b} - \boldsymbol{c}^{-1}\right) + \frac{1}{6\,b}\,n_c\,n_a\,k_B\,T\,\kappa'\,\boldsymbol{a} \tag{4.36}$$

$$\begin{aligned}\Phi_a &= \frac{1}{2}\,n_a\,k_B\,T\,\left(\boldsymbol{\delta} - (1-K_{flex})\,\boldsymbol{a}^{-1} - 3\,K_{flex}\,\boldsymbol{a}^{-2} + \frac{2}{9}n_a\kappa\,(\boldsymbol{\delta}\,tr\boldsymbol{a} - \boldsymbol{a})\right)\\ &+\frac{1}{6\,b}\,n_c\,n_a\,k_B\,T\,\kappa'\,\boldsymbol{c}\end{aligned} \tag{4.37}$$

To simplify the notation, we have omitted the stars. All quantities appearing in this section are dimensionless.

The imposed flow is chosen to be the simple shear flow

$$\dot{\boldsymbol{\gamma}} = \dot{\gamma}_{(t)}\begin{pmatrix} 0 & 1 & 0\\ 1 & 0 & 0\\ 0 & 0 & 0\end{pmatrix} \quad ; \quad \boldsymbol{\Omega} = \dot{\gamma}_{(t)}\begin{pmatrix} 0 & -1 & 0\\ 1 & 0 & 0\\ 0 & 0 & 0\end{pmatrix} \tag{4.38}$$

We look for solutions of (4.33) and (4.34) in the form

$$\boldsymbol{c} = \begin{pmatrix} c_{11} & c_{12} & 0\\ c_{12} & c_{22} & 0\\ 0 & 0 & c_{33}\end{pmatrix} \quad ; \quad \boldsymbol{a} = \begin{pmatrix} a_{11} & a_{12} & 0\\ a_{12} & a_{22} & 0\\ 0 & 0 & a_{33}\end{pmatrix} \tag{4.39}$$

The initial conditions are the equilibrium states (i.e. the states at which the free energy reaches its minimum): $\boldsymbol{c}_{eq} = \frac{b}{b+3}\,\boldsymbol{\delta}$ and $\boldsymbol{a}_{eq} = \boldsymbol{\delta}$.

From the mathematical point of view, Eqs.(4.33),(4.34) represent a system of ordinary differential equations. We solve them numerically by using the MATHEMATICA software package [Wolfram (1991)].

The parameters $\mathcal{P}$ entering the governing equations (4.33) and (4.34) are:

$$\mathcal{P} = (b,\ \xi,\ \kappa,\ \kappa',\ K_{flex},\ \chi,\ \Lambda_0^{cc},\ \Lambda_0^{aa},\ \Lambda_0^{ca}) \tag{4.40}$$

It is in $\mathcal{P}$ where we are expressing in the model the individual nature of the suspension. The parameters $\mathcal{P}$ are the material parameters. We turn now to a systematic investigation of the mapping

$$\mathcal{P} \rightarrow \textit{thermodynamic and rheological behavior in transient and steady flows} \quad (4.41)$$

where the "*thermodynamic and rheological behavior in transient and steady flows*" represent in this paper results of rheological measurements under imposed simple shear flows.

Before engaging ourselves in this investigation, we make a comment about the problem of identifying material parameters in the context of rheological models whose point of departure is a microscopic level (for example the level of quantum mechanics or the level of microhydrodynamics [Kim and Karilla (1991)] if we are dealing with suspensions in simple fluids). The material parameters $\mathcal{P}_{micro}$ in such models belong to the microscopic level and can be identified, at least in principle, by making microscopic-level measurements. The rheological model provides then, at least in principle, a passage from the microscopic level to the macroscopic level on which the rheological measurements are made. In other words, the rheological model provides the mapping $\mathcal{P}_{micro} \rightarrow$ "*thermodynamic and rheological behavior in transient and steady flows*". The predictions of the macroscopic behavior do not involve any "adjustable parameter".

The model that we have formulated in this paper is different in that the material parameters $\mathcal{P}$ entering it do not belong to any microscopic level and their values cannot be therefore found by making microscopic-level measurements. The advantage of our model is that the mapping (4.41) is not only obtainable "in principle" but it arises as a result of routine and straightforward numerical calculations. Moreover, the mapping $\mathcal{P} \rightarrow$ "*equilibrium thermodynamic behavior*" is found analytically. It is in fact manifestly displayed in the governing equations of the model. While the material parameters $\mathcal{P}$ in our model do not belong to a more microscopic level, they still represent microscopic quantities (even if "averaged" - see the paragraph preceding Eq. (4.29)). The mapping (4.41) thus still addresses the micro-macro relation even if not in such a fundamental way as if we were starting the

modeling on, say, the level of quantum mechanics. We shall not investigate the mapping (4.41) by turning to more microscopic levels for help. We shall proceed as follows. First, we attempt to identify a subset $\mathcal{M}$ of "*thermodynamic and rheological behavior in transient and steady flows*" that will serve us as a family of rheological measurements. By inverting the mapping $\mathcal{P} \rightarrow \mathcal{M}$ we obtain values of the material parameters $\mathcal{P}$. With known material parameters we then predict the rest of "*thermodynamic and rheological behavior in transient and steady flows*" and compare them with results of their experimental observations.

The model of clay lamellae nanocomopsites has been introduced in this paper as an extension of the FENE-P model. It is therefore natural to start also the investigation of the mapping (4.41) with this familiar model. If the lamellae are absent, the fluid under investigation is composed of only polymer molecules, the rheological model reduces to the FENE-P model, and the material parameters are

$$\mathcal{P}_{FENE-P} = (b, \Lambda_0^{cc}) \tag{4.42}$$

One observation that we include into $\mathcal{M}_{FENE-P}$ is the observation of the zero shear viscosity η_0 since, as we easily see from the FENE-P governing equations, $\eta_0 = \frac{b^2}{4\Lambda_0^{cc}(b+4)}$. For the extended FENE-P model with $\mathbf{\Lambda}^{cc}$ involving terms that are quadratic in $\boldsymbol{c}$ (see (4.28)) we can show that $\frac{\Psi_{20}}{\Psi_{10}} = -\frac{1}{2(b+4)}$. Measurements of the zero shear limits of the viscosity coefficient and of the first and the second normal stress differences thus provide, in the context of the extended FENE-P model, the material parameters (b, Λ_0^{cc}). To the best of our knowledge, there is no measurement that, if combined with the measurement of η_0, would give values to both parameters b and Λ_0^{cc} in the context of the classical FENE-P model. This is mainly because there is a universal (i.e. independent of $\mathcal{P}$) mapping $\eta(\dot{\gamma}) \rightarrow ((\Psi_1(\dot{\gamma}), \eta_E(\dot{\epsilon}));\ \Psi_2(\dot{\gamma}) = 0$. This result was proven in Grmela and Carreau (1987) for a family of models of which the classical FENE-P model is a special case but the extended FENE-P model is not. The role of the second observation that we include into $\mathcal{M}_{FENE-P}$ in the context of the classical FENE-P model has to be therefore taken by a feature or features of the curves $\eta(\dot{\gamma})$ or $\eta^{\pm}$ (e.g. the

length of the Newtonian plateau or the location and intensity of the overshoot) for which we do not have an analytical expressions. This way of determining the material parameters $\mathcal{P}_{FENE-P}$ is then known as "finding the material parameters by fitting experimental data".

We shall adopt the same strategy for the model developed in Section 4.2. In order to identify the most appropriate features of the observed rheological behavior that could serve as the measurements $\mathcal{M}$, we shall systematically investigate how the predictions of the model depend on the material parameters $\mathcal{P}$.

Due to the lack of experimental data regarding the second normal stress differences coefficient, its values predicted by the model are not presented. We just mention that the model predicts negative values for Ψ_2 over the whole range of time and shear rates and it also predicts that the ratio $(-\Psi_2/\Psi_1)_{t\longrightarrow\infty}$ decreases with increasing shear rate in the case of the pure polymers and also the nanocomposites in which the mobility of lamellae is chosen to have linear and quadratic dependence on $\boldsymbol{a}$. For higher order mobility tensors, the ratio shows a maximum.

In the following five subsection we shall explore how the parameters included in $\mathcal{P}$ influence the rheological behavior. Let us think of $\mathcal{P}$ as of a nine dimensional space (we shall call it a parameter space). To every point in the parameter space we can attach rheological properties found by solving numerically Eqs.(4.33),(4.34). The exploration of the parameter space reported below proceeds as follows: First, we choose a fixed point P_0 in the parameter space, and second, we explore its neighborhood by changing $\dot{\gamma}$ (in Section 4.3.1), $\Lambda_0^{cc}, \Lambda_0^{aa}, \Lambda_0^{ca}$ (in Section 4.3.2), α (in Section 4.3.3), f_1, f_2, f_3 (in Section 4.3.4), and κ, κ', b, χ (in Section 4.3.5).

The point P_0 is chosen as follows: η_0 for pure polymer is $\eta_0 = 30000$ Pa.s, $b = 50, \xi = 0.98, \kappa = 2 \times 10^{-24}, \kappa' = 5 \times 10^{-24}, K_{flex} = 0.1, \chi = 200, \Lambda_0^{aa} = 5 \times 10^{-7}, \Lambda_0^{ca} = 10^{-6}, f_1 = f_1 = 0$ and $f_3 = 1$. Prediction of transient material functions is made at $\dot{\gamma} = 0.1s^{-1}$ and clay loading is considered to be 5 wt %. The following considerations lead us to this choice of P_0. The zero shear viscosity coefficient η_0 and b are taken to be those arising in the FENE-P model. The mobility parameters Λ_0 essentially determine the zero shear viscosity of the

suspension. We choose them to provide the values seen in experiments. The choice 0.1 for the parameter K_{flex} means that we assume the lamellae to be more rigid than flexible. The value of the parameter χ is made on the basis of the considerations shown in Section 4.2.3. The parameters κ and κ' are those that make the terms in the free energy of the same order.

4.3.1 Effects of the shear rate on transient material functions

Figures 4.1(a) and 4.1(b) display the effects of shear rate on the transient material functions, $\eta^{\pm}$ and $\Psi_1^{\pm}$. The results show that for small shear rates, the viscosity reaches its steady state value monotonically. As the shear rate increases, the curve of viscosity versus time shows an overshoot. The size of this overshoot increases and the time at which the overshoot appears decreases when shear rate increases. Relaxation data (displayed on different x and y scales for clarity) show that the viscosity relaxes monotonically to zero in low shear rate and then it relaxes more rapidly as the shear rate increases. Similar results are obtained for start-up and relaxation of the first normal stress difference coefficient (see Figure 4.1(b)). As seen on Figures 4.1(a) and 4.1(b) and on many other results that are not presented (for the sake of brevity) in this paper, the overall qualitative features of the curves are essentially the same as the ones seen in the experimental data collected for pure polymers, miscible polymer blends [Bird et al. (1987a); Eslami et al. (2003, 2004)] and also for polymer nanocomposites [Wu et al. (2005); Ayyer and Leonov (2004)].

4.3.2 Effects of the mobility coefficients on transient material functions

Figures 4.2(a) and 4.2(b) show the influence of polymer mobility coefficient (Λ_0^{cc}) on the transient material functions, $\eta^{\pm}$ and $\Psi_1^{\pm}$ respectively. As seen on Figure 4.2(a), both the stationary value and the size of the overshoot increase with decreasing Λ_0^{cc}. Figure 4.2(b) indicates that similarly as the viscosity coefficient, the stationary values of Ψ_1^{+} increase with decreasing Λ_0^{cc}. However, Ψ_1^{+} is less sensitive to increasing the size of the overshoot than η^{+}

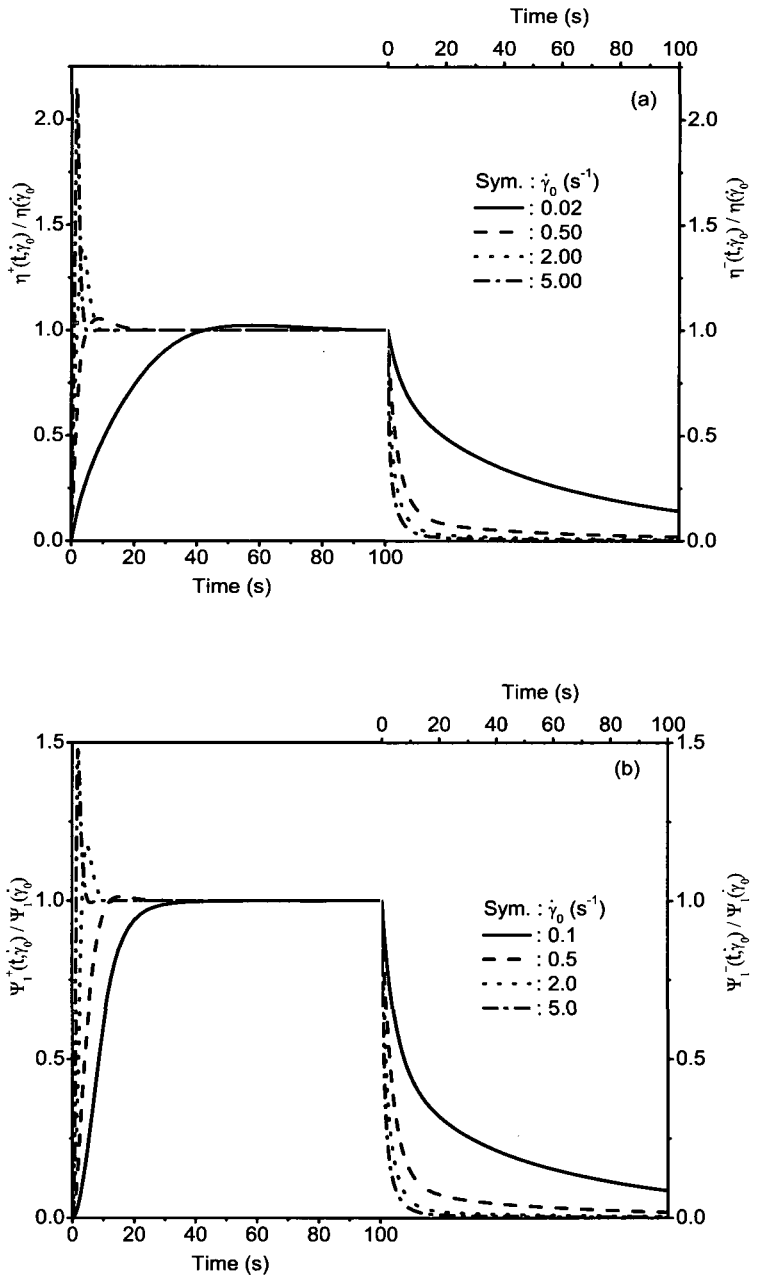

Figure 4.1: Effect of the shear rate on the stress growth and relaxation of the material functions: (a) viscosity and (b) first normal stress coefficient.

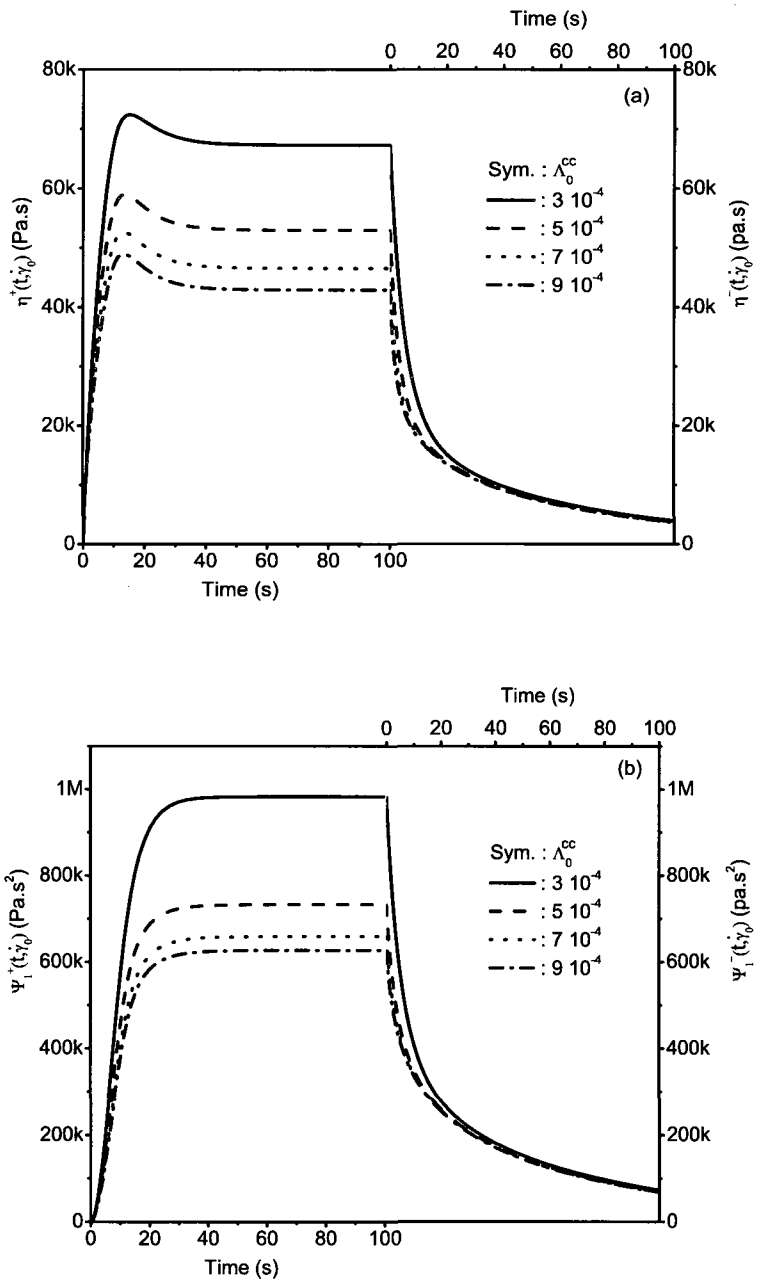

Figure 4.2: Effect of the mobility coefficient of polymer Λ_0^{cc} on the stress growth and relaxation of the material functions: (a) viscosity and (b) first normal stress coefficient.

(the size of overshoots becomes visible more clearly if one draws the curves in the normalize form as it is done in Figure 4.1).

Figures 4.3(a) and 4.3(b) present the influence of the plate mobility coefficient Λ_0^{aa} on the transient rheological properties. Regarding the stationary values, the effects are the same as the effect of Λ_0^{cc} on the material functions. But these effects are more pronounced at low shear rates. This means that one can see the effect of the mobility of polymer at high shear rates and the effect of the mobility of plates at low shear rates. We also note that Ψ_1 is more sensitive to changing Λ_0^{aa} than η. These observations are very useful for reversing the mapping identifying the measurements $\mathcal{M}$.

The effects of the interaction mobility coefficient Λ_0^{ca} on the material functions are presented in Figures 4.4(a) and 4.4(b). In general, the rheological properties are found to depend very sensitively on Λ_0^{ca}. At low shear rates the steady state value of the viscosity coefficients and the first normal stress difference coefficients decrease as Λ_0^{ca} decreases. At high shear rates (the results are not shown), the dependence is inverse. As for the overshoot, its size in η^+ is more sensitive to the change in Λ_0^{ca} than in Ψ_1^+.

4.3.3 Effects of the nano-particle loading on material functions

The transient viscosity and the first normal stress differences coefficient of polymer nanocomposites at different contents of nano-particle are presented on Figures 4.5(a) and 4.5(b). As mentioned earlier, the volume fraction of nano-particle α is introduced in both the dissipation potential and the free energy function. The steady state predictions are also shown on Figures 4.6(a) and 4.6(b) for a wide range of shear rates and different nano-particle contents. As expected, the rheology of polymer nanocomposites is significantly influenced by nano-particle content.

As the nano-particle loading increases i.e. α increases, the effects become more significant. The results presented in transient flow show that both the stationary values and the size of the overshoots increase with increasing nano-particle loading. The dependence of overshoots on α is stronger in η^+ than in Ψ_1^+. The stationary values of Ψ_1^+ (i.e. $\Psi_1^+|_{t\to\infty}$) depends

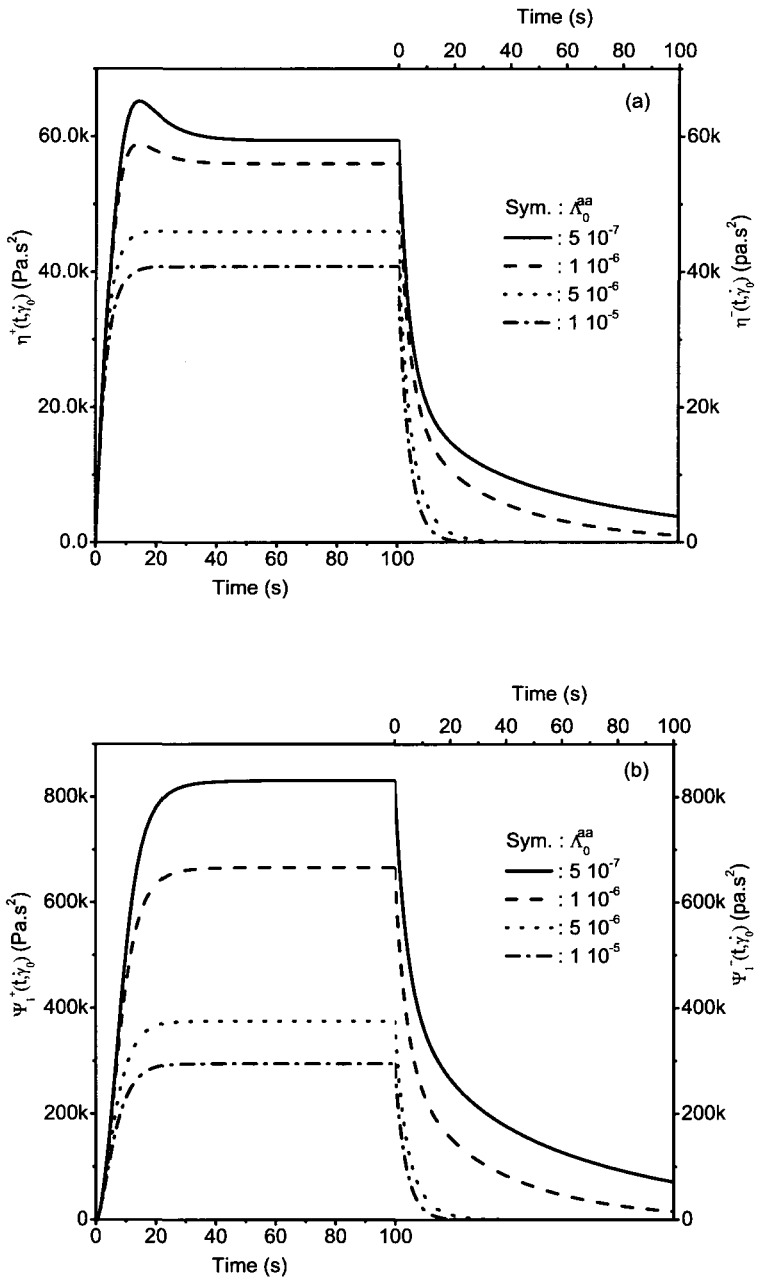

Figure 4.3: Effect of the mobility coefficient of plate Λ_0^{aa} on the stress growth and relaxation of the material functions: (a) viscosity and (b) first normal stress coefficient.

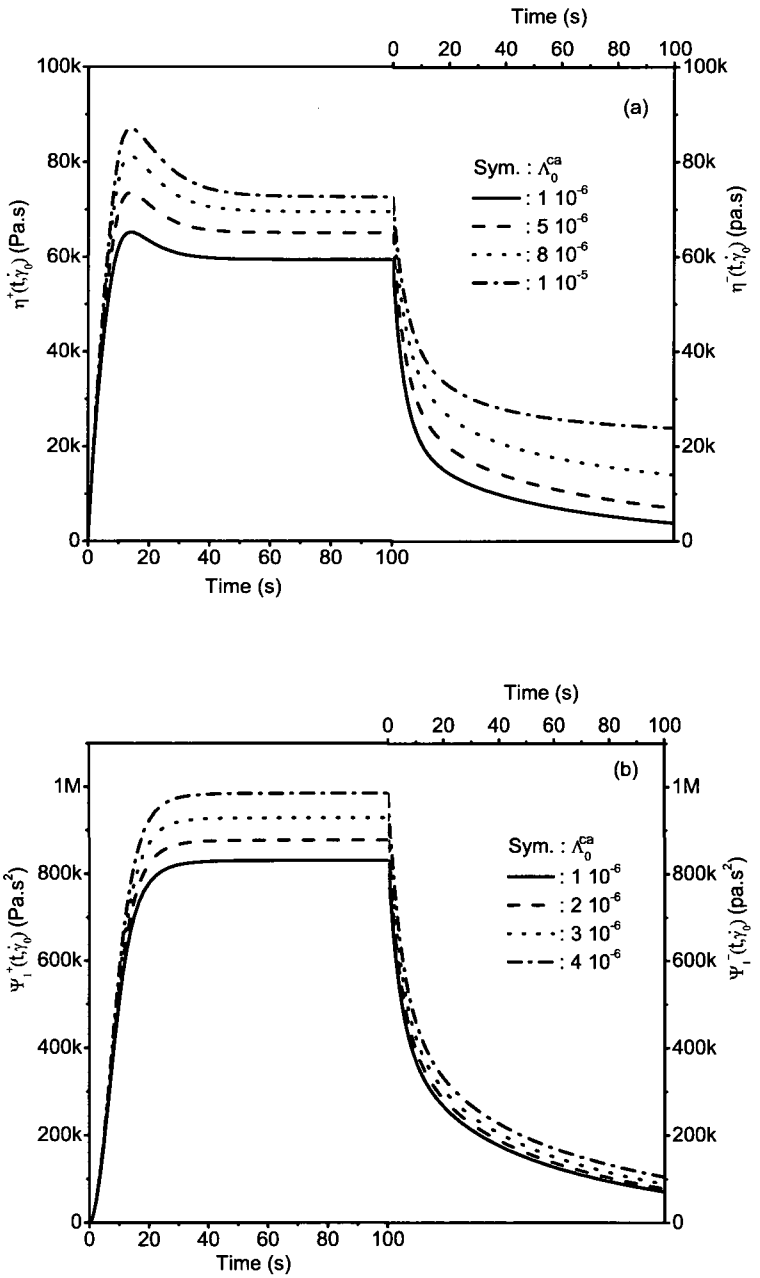

Figure 4.4: Effect of the interaction mobility coefficient Λ_0^{ca} on the stress growth and relaxation of the material functions: (a) viscosity and (b) first normal stress coefficient.

more sensitively on α than the stationary value of the viscosity coefficients. Relaxation data indicate that the viscosity decreases monotonically with time at different contents of nano-particle loading. As α increases, the time required for the viscosity to reach zero increases. This means that increasing nano-particle content causes a delay in relaxation phenomena. Similar results are obtained for relaxation of the first normal stress coefficients (see Figure 4.5(b)).

The steady material functions are also affected by α. An increase of α results in an increase in viscosity at low shear rates and a very small change at high shear rates. In other words, when α increases the behavior for all ranges of shear rates becomes non-Newtonian (shear thinning). For pure polymer as well as for nanocomposites with small amount of clay, the Newtonian behavior at low shear rates and the shear thinning behavior in higher shear rates has been observed experimentally [Sinha Ray (2006)]. In our model, we can also see this behavior in the case of lower order mobility tensor of lamellae (see Figure 4.7(a)) (see also the second paragraph in Section 4.3.4). Model predictions show that at high shear rates the viscosity is almost independent of the silicate loading and is comparable to that of the polymer matrix. This is because at high shear rates the plates are all oriented in the direction of the flow and the viscosity of the suspension is dominated by the polymer matrix. In general, the model predictions are consistent with experimental data for PLS nanocomposites [Sinha Ray (2006); Sinha Ray and Okamoto (2003b); Sinha Ray and Bousmina (2005a,b); Ayyer and Leonov (2004); Krishnamoorti et al. (2001)]. The same results are observed in Figure 4.6(b) where the effect of α on the first normal stress coefficients is presented.

4.3.4 Effects of the mobility tensors on material functions

As mentioned earlier, we have followed Beris and Edwards (1990, 1994) in the choice of the mobility tensors. We have used polynomial functions in $\boldsymbol{c}$ and $\boldsymbol{a}$ (see Eq.(4.28)). In the absence of lamellae, the FENE-P model is recovered with the first order mobility tensor. As shown in Grmela and Carreau (1987) this then implies (provided the free energy depends only on $tr\boldsymbol{c}$) that the slope in the shear thinning region is $-2/3$. In this paper we are extending

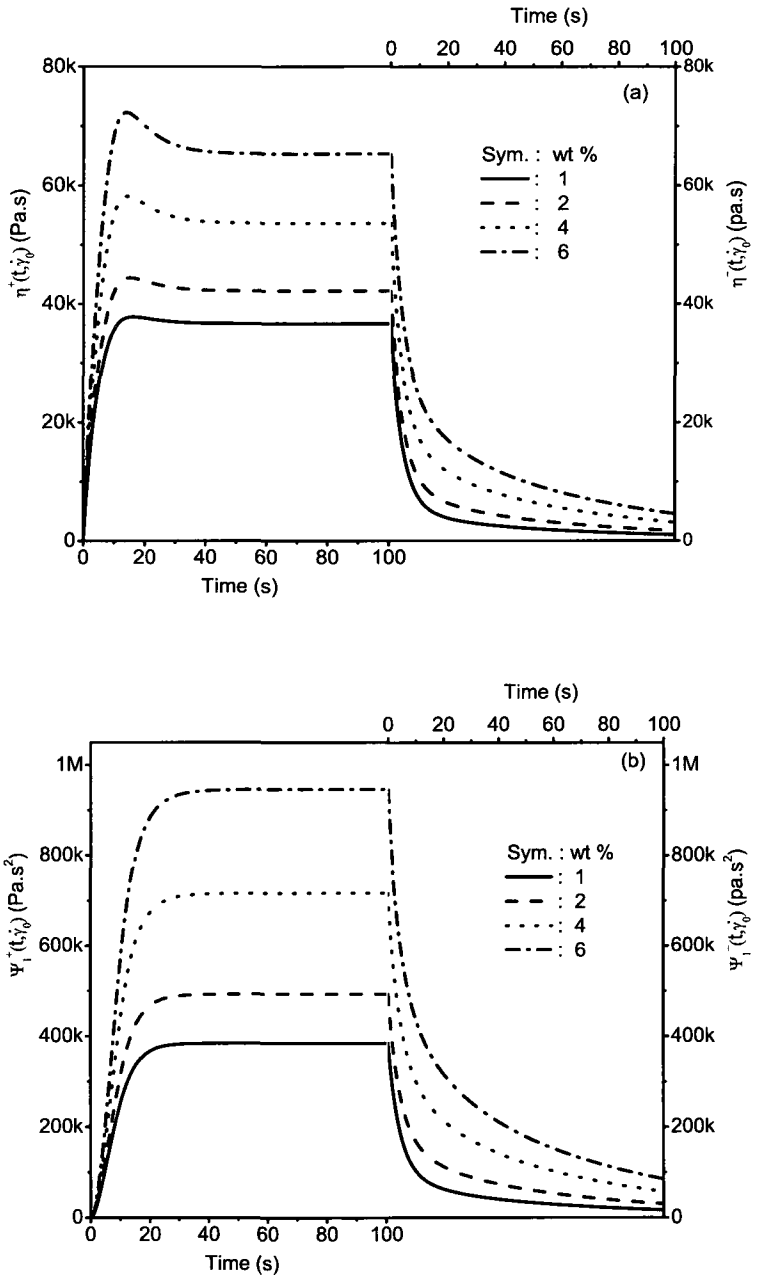

Figure 4.5: Effect of the nano-particle weight fraction on the stress growth and relaxation of the material functions: (a) viscosity and (b) first normal stress coefficient.

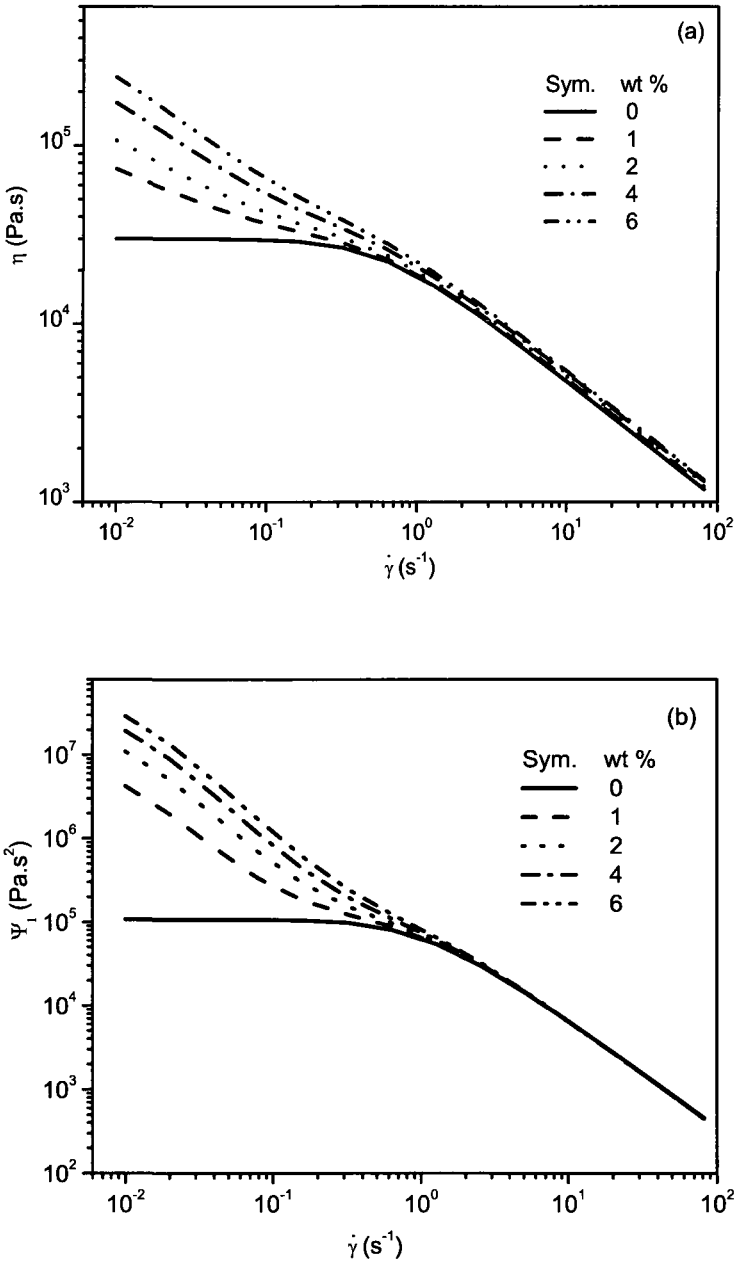

Figure 4.6: Effect of the nano-particle weight fraction on the steady shear flow material functions: (a) viscosity and (b) first normal stress coefficient.

the classical FENE-P model by considering the mobility tensor that is a combination of the first and the second order (see Eq.(4.28)). With this modification, we can slightly change the slope. Another way of changing it is to choose a more general free energy (for more information see Eslami et al. (2003, 2004)).

The effects of the mobility tensor of lamellae on the material functions have also been investigated in steady and transient shear flows. Figures 4.7(a) and 4.7(b) show the effect of different mobility expressions of lamellae on the steady material functions η and Ψ_1. The results indicate that the choice of this parameter has a strong effect on the viscosity in low shear rates. Changing Λ^{aa} in Eq.(4.28) results in a change of the slope of the viscosity-shear rate curve in low shear rate region. The value of this slope increases with increasing the dependency of Λ^{aa} on $\boldsymbol{a}$. For the expression involving the third-order terms in $\boldsymbol{a}$, one can see non-Newtonian behavior for all shear rates. This additional flexibility in changing the viscosity curves allows a better fit between experimental data and model predictions. The same flexibility is observed also for the normal stress coefficients (see Figure 4.7(b)). No effect of changing Λ^{aa} is observed in the region of high shear rates. The effect of Λ^{aa} has also been investigated for the transient material functions. The results (not presented here for the sake of brevity) show that the stress overshoot increases with increasing the dependency of Λ^{aa} on $\boldsymbol{a}$. In other words, third order mobility tensor shows the highest overshoot. Its effect is less pronounced in $\Psi_1^{\pm}$.

4.3.5 Sensitivity of the model to other parameters

The sensitivity of the model to the remaining parameters included in $\mathcal{P}$ has also been studied. Figure 4.8 shows the effect of the parameter b on the stress growth viscosity. The results show that with b increasing, both the stationary values and the size of overshoot decrease. Relaxation data show that η^- relaxes more rapidly than Ψ_1^- (prediction regarding $\Psi_1^{\pm}$ is not presented here for the sake of brevity).

Figure 4.9 shows the effect of polymer plate interaction parameter κ' on $\eta^{\pm}$. When κ' increases, the stationary values in the viscosity decrease and the size of the overshoots

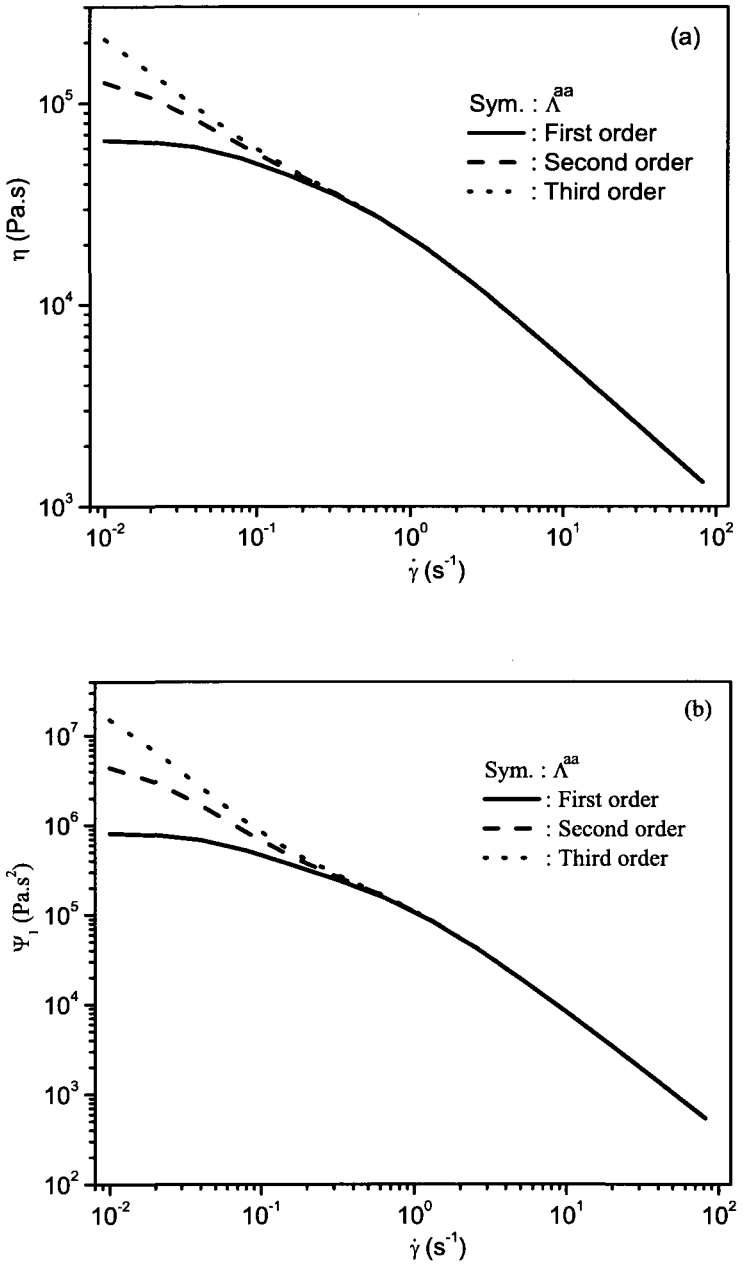

Figure 4.7: Effect of the mobility tensor of plates, Λ^{aa} on the steady shear material functions: (a) viscosity and (b) first normal stress coefficient.

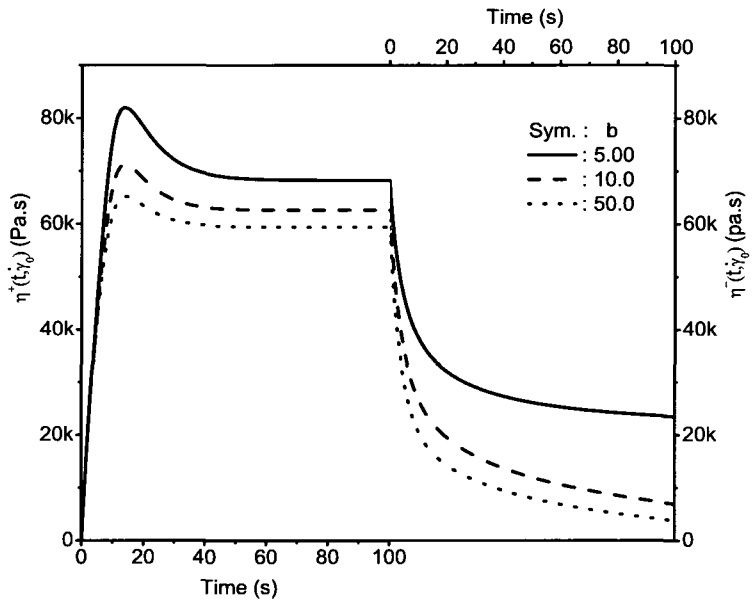

Figure 4.8: Effect of the parameter b on the stress growth and relaxation viscosity.

increases. The same results are seen for Ψ_1. The parameter κ' has a more pronounced effect on η^+ than on Ψ_1^+. Relaxation data show that Ψ_1^- relaxes more rapidly than η^- (again, prediction regarding $\Psi_1^\pm$ is not presented here for the sake of brevity).

As mentioned earlier, we had to address the disparity of shapes and sizes (polymer macromolecules versus plates). In order to solve this difficulty we have to render layered silicates to the size of polymer chains. Hence we consider a scaling parameter χ. We replace the number density n_a of the plates by χn_a (see the third paragraph after Eq.(4.28)). Due to the large area and the rigidity of the lamellae, a single lamella interacts with a group of macromolecules. We thus expect χ to be greater than one. The effect of χ on $\eta^\pm$, is shown on Figure 4.10. From our calculations we see that, in general, χ affects strongly all rheological material functions. Figure 4.10 shows that both steady state viscosity and the size of the related overshoots increase with increasing χ. The same is observed for Ψ_1^+, but Ψ_1^+ is more sensitive to change in χ than η^+ (again, prediction regarding $\Psi_1^\pm$ is not presented here for the sake of

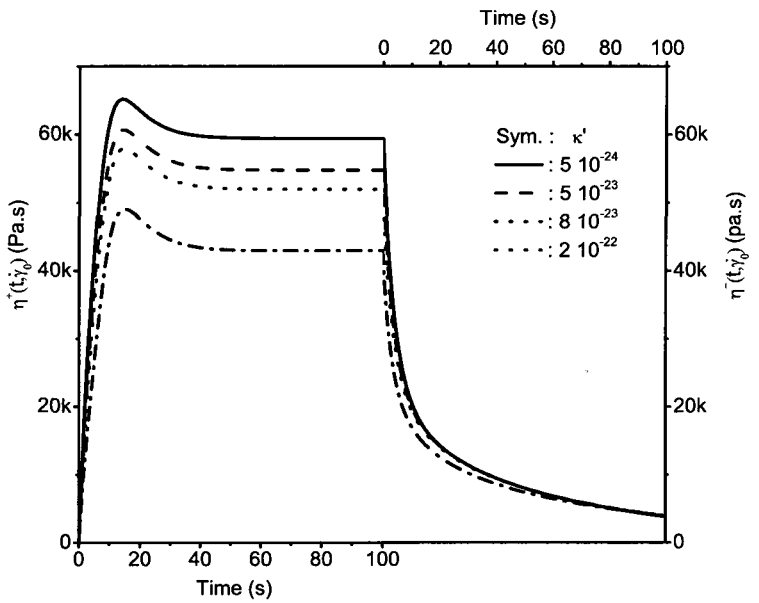

Figure 4.9: Effect of the polymer-plate interaction κ' on the stress growth and relaxation viscosity.

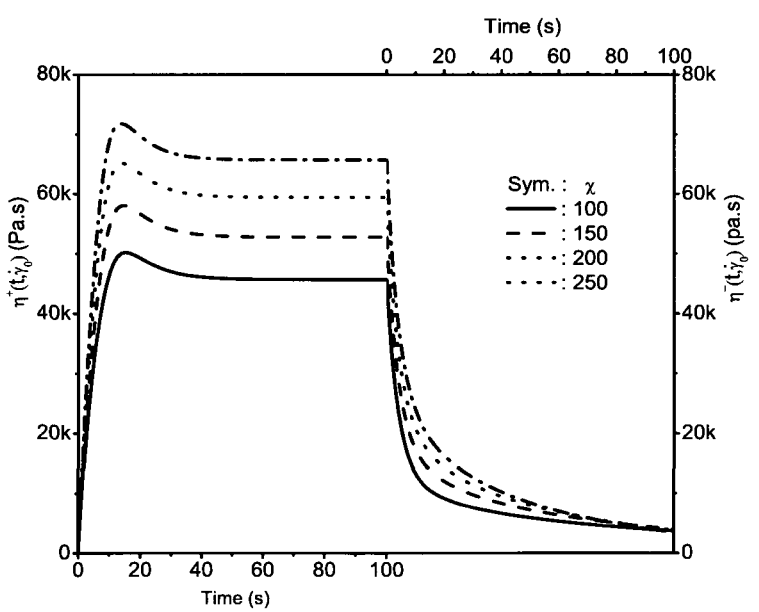

Figure 4.10: Effect of the scaling parameter χ on the stress growth and relaxation viscosity.

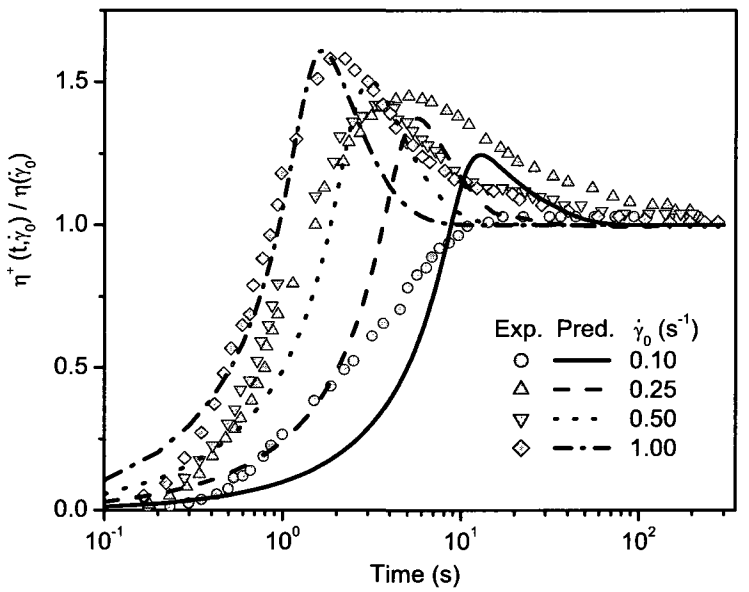

Figure 4.11: Model predictions and comparison with experimental data in transient shear flow. Data are taken from Wu et al. (2005).

brevity). Relaxation data show the same type of dependency for all material functions. All relaxation material functions relax more rapidly at small values of χ and they relax more slowly as χ increases. We note in addition that the the influence of the parameters κ, κ' and χ is interrelated.

4.3.6 Comparison with experimental data

Results of rheological measurements (taken from Wu et al. (2005); Ayyer and Leonov (2004)) in transient shear flows at the constant temperature $T_0 = 230°C$ are presented in Figure 4.11 and at the constant temperature $T_0 = 250°C$ in Figure 4.12. Model parameters are chosen to be: $b = 50, \kappa = 5 \times 10^{-23}, \kappa' = 1.5 \times 10^{-23}, K_{flex} = 0.5, \chi = 200, \xi = 0.98, \Lambda_0^{cc} = 5 \times 10^{-3}, \Lambda_0^{aa} = 2 \times 10^{-7}, \Lambda_0^{ca} = 3 \times 10^{-5}$ and 6 wt % clay in Figure 4.11 and $b = 7, \kappa = 5 \times 10^{-24}, \kappa' = 5.8 \times 10^{-23}, K_{flex} = 0.15, \chi = 200, \xi = 0.95, \Lambda_0^{cc} = 8 \times 10^{-3}, \Lambda_0^{aa} = 3.4 \times 10^{-4}$

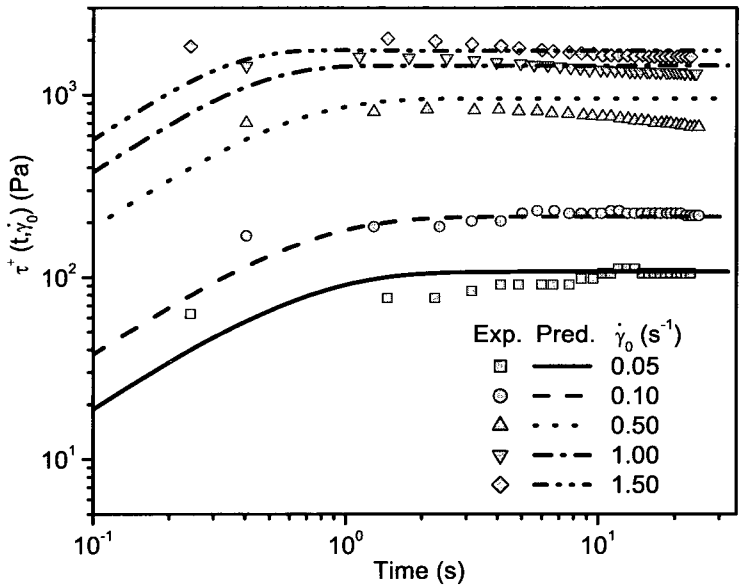

Figure 4.12: Model predictions and comparison with experimental data in transient shear flows. Data are taken from Ayyer and Leonov (2004).

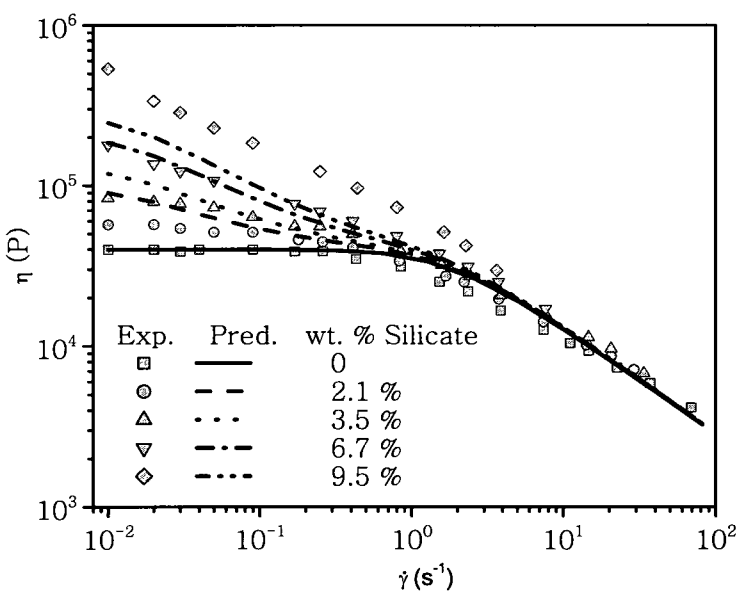

Figure 4.13: Model predictions and comparison with experimental data in steady shear flow. Data are taken from Krishnamoorti et al. (2001).

and $\Lambda_0^{ca} = 5 \times 10^{-4}$ in Figure 4.12. Figure 4.11 shows that at high shear rate the model predictions are in agreement with the start-up experimental data but at low shear rate the agreement is less satisfactory. Figure 4.12 shows also a good agreement of model predictions with the experimental data.

Figure 4.13 shows the effect of nano-particle weight fraction on the steady state viscosity. The experimental data, taken from Krishnamoorti et al. (2001), have been collected at the temperature $T_0 = 85°C$ for a wide rage of shear rates. Model prediction are also compared with this set of experimental data and model parameters are chosen to be: $b = 30, \kappa = 3 \times 10^{-24}, \kappa' = 10^{-24}, K_{flex} = 0.15, \chi = 200, \xi = 0.98, \Lambda_0^{aa} = 1.3 \times 10^{-6}$ and $\Lambda_0^{ca} = 5 \times 10^{-7}$. The results show that this set of experimental data are in a rather good agreement with model prediction specially in low nano-particle loading. The reasons for less satisfactory agreement (especially at low shear rates and high silicate loading) may be partially due to the fact that the silicate lamellae in experimentally prepared suspensions are rarely completely exfoliated and consequently some new physical processes, that are not included in our model, become important.

4.4 Concluding remarks

A rheological model of a spatially homogeneous and isothermal suspension of completely exfoliated clay lamellae (nanoparticles) in polymer melts is formulated. The mesoscopic level of description chosen for the theoretical analysis is the one on which states of the macromolecules composing the polymer melt are characterized by a conformation tensor and states of the clay lamellae by another conformation tensor. Having chosen the state variables, the model is formulated by, first, writing down a framework for the governing equations (guaranteeing the compatibility with thermodynamics) and second, filling the framework by specifying the kinematics of the state variables, the free energy, and the dissipation potential. The framework emerges in the paper in reformulations of the familiar FENE-P model. The reformulations reveal the physics, expressed solely in terms of the conformation tensor, that

is behind the model.

An alternative mesoscopic level of description which we could have chosen to develop our theoretical analysis is the more microscopic level on which states are described by one particle configuration space distribution function (ψ-level). Many of the problems that we discuss in this paper on the conformation tensor level have been discussed on the ψ-level in [Forest and Wang (2003, 2005); Singh and Rey (1998)]. If we regard the conformation tensor as the second moment of the distribution function then, in principle, the conformation-tensor theory developed in this paper can be reduced from the distribution-function theory. However, the reduction process is, in general, very complex. It requires a detailed knowledge of solution of the governing equations on the ψ-level. Alternatively, to make the reduction feasible, one often introduces empirically chosen "closures", i.e. formulas expressing higher order moments (remaining still in the ψ-level governing equations after they have been projected on the second moment) in terms of the second moment. We have avoided the arbitrariness of closures by formulating the governing equations directly on the conformation tensor level. We have constructed the equations governing the time evolution of the conformation tensors by expressing in them the same type of physics as the one expressed in [Forest and Wang (2003, 2005); Singh and Rey (1998)] on the ψ-level and not by, first, constructing the equations governing the time evolution of distribution functions, and second, reducing them to second moments. Another advantage of considering the conformation tensor level of description as autonomous is that we do not have to regard the conformation tensor only as the second moment of one particle distribution function but we can give it other interpretations (e.g. as the deformation tensor of a network of internal entanglements). The disadvantage is, of course, that the parameters that we use on the conformation tensor level to characterize the fluids are more phenomenological than those used on the ψ-level.

The mesoscopic level of description chosen in this paper appears to be a good compromise between microscopic details and overall simplicity of the governing equations. We are able to express in the model important features of the physics involved (like for example polymer-plate and plate-plate interactions) and on the other hand, the governing equations are easily

solved numerically by standard software packages. The calculated rheological data for steady and transient shear flows are compared with experimental data reported in the literature. The results show a good agreement for start-up flows at higher shear rates and less satisfactory agreement at lower shear rates. For steady shear flow, model predictions and experimental data are in good agreement specially in the case of small content of the nano-particles.

In general, we note that the agreement of model predictions with the experimentally observed rheological behavior is less satisfactory at low shear rates and high silicate loading. The challenge is to identify the physical processes that become important in these situations and to express them in the model. The framework of the model will remain unchanged since we shall again require the agreement of model predictions with the observed compatibility with thermodynamics.

4.5 Appendix: GENERIC

The standard formulation of classical hydrodynamics (recalled below) is top down. The point of departure is a general principle that provides a framework for the governing equations. The framework is then filled (or in other words, constitutive relations are specified) in the second stage. The question arises as to whether the same strategy can be used to construct mesoscopic dynamical theories of complex fluids.

4.5.1 Classical hydrodynamics: Standard formulation

The state variables of classical hydrodynamics are classical hydrodynamic fields

$$x = (\rho(\boldsymbol{r}), \boldsymbol{u}(\boldsymbol{r}), e(\boldsymbol{r})) \tag{4.43}$$

We require that the total mass $\int d\boldsymbol{r}\rho(\boldsymbol{r})$, the total momentum $\int d\boldsymbol{r}\boldsymbol{u}(\boldsymbol{r})$, and the total energy $\int d\boldsymbol{r}e(\boldsymbol{r})$ are preserved during the time evolution. This implies (assuming that the hydrodynamic fields are sufficiently regular) that the time evolution equations have the form

of local conservation laws

$$\frac{\partial x}{\partial t} = -divJ(x) \tag{4.44}$$

where $J(x)$ are unspecified fluxes. Their specification, called a constitutive relation, consists of the second stage of the modeling.

We make four observations.

(i) The obvious advantage of the above construction is the modular nature of the modeling. The general framework (4.44) remains the same for all fluids. The individual nature of the fluids is expressed only in the constitutive relations.

(ii) Nonequilibrium thermodynamics has complemented the general framework (4.44) by considering also the time evolution of the total entropy $\int d\boldsymbol{r} s(\rho, \boldsymbol{u}, e; \boldsymbol{r})$, where s is the local entropy and the relation between $(\rho(\boldsymbol{r}), \boldsymbol{u}(\boldsymbol{r}), e(\boldsymbol{r}))$ and $(\rho(\boldsymbol{r}), \boldsymbol{u}(\boldsymbol{r}), s(\boldsymbol{r}))$ is one-to-one. The total entropy is required to be conserved during the reversible time evolution (for the definition of the time reversibility and irreversibility see Section 4.2.1.3) and to grow during the irreversible time evolution. These new requirements restrict then the freedom of choice of the constitutive relations (for example, the hydrodynamic pressure p appearing in the flux of momentum is found to be the local pressure and the coefficients of heat conductivity and viscosity are positive).

(iii) In this paper we have restricted ourselves to isothermal fluids. Under this restriction, the state variables (4.43) reduce to $(\rho(\boldsymbol{r}), \boldsymbol{u}(\boldsymbol{r}))$ and the entropy is replaced by the free energy $\int d\boldsymbol{r} \varphi(\rho, \boldsymbol{u}; \boldsymbol{r})$.

(iv) We note that the global conservation laws serving us as the general principle imply a universal framework (4.44) for the time evolution only if the state variables are the classical hydrodynamic fields (4.43). Since complex fluids require more general state variables, the top down approach sketched above cannot be applied in their investigations. Are there other general principles that could provide a universal framework for the time evolution of a general set of state variables? An attempt to answer this question is briefly recalled below.

4.5.2 GENERIC: Complex fluids

Because the whole paper is restricted to isothermal systems, also the structure of GENERIC is presented below only for such systems. Let x denote the full set of state variables and $\Phi(x)$ be the free energy. The time evolution of x is governed by

$$\frac{\partial x}{\partial t} = L\Phi_x - \frac{\partial \Xi}{\partial \Phi_x} \tag{4.45}$$

(we use the notation: $\Phi_x = \frac{\partial \Phi}{\partial x}$). The top down construction consists of the universal framework (4.45) and the "constitutive relations" (i.e. a specification of Φ, L, and Ξ). Now, we explain the physical principles expressed in (4.45).

Without the second term on the right hand side, the time evolution equation (4.45) is reversible and L is a Poisson bivector expressing kinematics of x. We say that L is a Poisson bivector if $\{A, B\} =< A_x, LB_x >$ is a Poisson bracket (i.e. $\{A, B\} = -\{B, A\}$ and the Jacobi identity holds); $A(x), B(x)$ are sufficiently regular real valued functions of x, $<,>$ denotes the inner product. We thus see immediately that $\left(\frac{d\Phi}{dt}\right)_{reversible} = \{\Phi, \Phi\} = 0$ holds for the reversible time evolution. The physical hypothesis (the principle) of which $\frac{\partial x}{\partial t} = L\Phi_x$ is a consequence is that the reversible time evolution taking place on mesoscopic levels inherits the Hamiltonian nature from its microscopic origins, and that the potential generating it is the free energy.

It is useful to regard the Poisson bivector L as an appropriate extension to general state variables x of $L = \begin{pmatrix} 0 & 1 \\ -1 & 0 \end{pmatrix}$ (or equivalently $\{A, B\} = A_q B_p - B_q A_p$) arising in classical mechanics in which $x = (q, p)$; q is the position coordinate and p the momentum of the particle. From the physical point of view, we are expressing in L the fact that the space with q and p as coordinates is not just a two dimensional space but a two dimensional space equipped with a structure expressing kinematics of classical mechanics. The structure is the following: p is not completely independent of q. p is the dual of the time derivative of q, or, if we use the mathematical terminology, the space with q and p as coordinates is a two dimensional space equipped with the structure of the cotangent bundle; q is the coordinate

in the base space and p is the coordinate in the cotangent space attached to the base space at the point with the coordinate q.

Without the first term on the right hand side, the time evolution equation (4.45) is irreversible. The potential $\Xi(\Phi_x)$, called dissipation potential, is required to have the following properties: $\Xi(0) = 0$, Ξ reaches its minimum at 0, and Ξ is a convex function in a neighborhood of 0. This then implies $\left(\frac{d\Phi}{dt}\right)_{irreversible} = - < \Phi_x, \frac{\partial \Xi}{\Phi_x} > < 0$ The physical hypothesis of which $\frac{\partial x}{\partial t} = -\frac{\partial \Xi}{\partial \Phi_x}$ is a consequence is that the free energy is required to decrease during the irreversible time evolution. If Φ_x is not too large (i.e. if the states under investigations are not too far from equilibrium at which $\Phi_x = 0$) then the dissipation potential Ξ satisfying the properties listed above is well approximated by the quadratic function: $\Xi(\Phi_x) =< \Phi_x \Lambda \Phi_x >$, where $\Lambda > 0$. This quadratic approximation appears to be sufficient in many applications (including the model presented in this paper).

We make two comments.

(i) The first one is about the terminology. In the mathematical literature, "Poisson" is more general than "Hamiltonian". In the Poisson structure the operator L (that we call Poisson bivector) can be degenerate. In fact, in mesoscopic theories L is always degenerate. In the Hamiltonian structure the operator L must be nondegenerate (as it is for example for L arising in classical mechanics).

(ii) In the second comment, we give a few references where the interested reader can find the history of (4.45), more details and many additional references: [Grmela (1984, 1986, 1991, 2002); Beris and Edwards (1994); Grmela and Ottinger (1997); Ottinger and Grmela (1997); Ottinger (2005)].

4.5.3 Examples of particular realizations of GENERIC

In order to illustrate the GENERIC framework, we now present "constitutive relations" (i.e. specifications of Φ, L, Ξ) that, if put into (4.45), lead to classical hydrodynamics, Boltzmann kinetic theory, the model presented in this paper, and the rheological model of fiber suspensions developed in Rajabian et al. (2005).

4.5.3.1 Classical hydrodynamics: GENERIC formulation

We begin with the momentum field $\boldsymbol{u}$. The equation governing its time evolution is not only a local conservation law but also Newton's law. If formulated in the Hamiltonian form, it takes the form

$$\frac{\partial \boldsymbol{u}}{\partial t} = LE_{\boldsymbol{u}} \tag{4.46}$$

where

$$\{A, B\}^{(u)} =< A_{\boldsymbol{u}}, LB_{\boldsymbol{u}} >= \int d\boldsymbol{r} u_\alpha \left(\frac{\partial A_{u_\alpha}}{\partial r_\beta} B_{u_\beta} - \frac{\partial B_{u_\alpha}}{\partial r_\beta} A_{u_\beta} \right) \tag{4.47}$$

and $E = \int d\boldsymbol{r} \frac{\boldsymbol{u}^2}{2\rho}$ is the energy. The bracket (4.47) is indeed a Poisson bracket that expresses mathematically the kinematics of continuum (i.e. the Lie group of transformations $\mathcal{R}^3 \rightarrow \mathcal{R}^3$; $\boldsymbol{r} \in \mathcal{R}^3$). If the two scalar fields $\rho(\boldsymbol{r})$ and $s(\boldsymbol{r})$ are adopted to the full set of state variables, the Poisson bracket (4.47) acquires two new terms: $\int d\boldsymbol{r}\rho \left(\frac{\partial A_\rho}{\partial r_\alpha} B_{u_\alpha} - \frac{\partial B_\rho}{\partial r_\alpha} A_{u_\alpha} \right)$ and $\int d\boldsymbol{r} s \left(\frac{\partial A_s}{\partial r_\alpha} B_{u_\alpha} - \frac{\partial B_s}{\partial r_\alpha} A_{u_\alpha} \right)$ expressing their kinematics (i.e. their passive advection by $\boldsymbol{u}$). The conservations of the total mass, momentum, and energy in the reversible time evolution (one of the starting hypotheses in the standard formulation) appear now as consequences of the Hamiltonian formulation.

For the GENERIC formulation of the dissipative part of the time evolution (corresponding to the Navier-Stokes-Fourier constitutive relations) we refer to Grmela (2002) where the interested reader will find also additional explanations and references.

4.5.3.2 Kinetic theory (Boltzmann equation)

The universal GENERIC framework (4.45) is applicable not only to the state variables x composed of classical hydrodynamic fields and some additional fields characterizing the internal structure but also to x composed of distribution functions. For example, the Boltzmann kinetic equation governing the time of one particle phase space distribution function $f(\boldsymbol{r}, \boldsymbol{v})$ is also a particular realization of (4.45). The Poisson bracket expressing kinematics of $f(\boldsymbol{r}, \boldsymbol{v})$ is $\int d\boldsymbol{r} \int d\boldsymbol{v} f \left(\frac{\partial A_f}{\partial r_\alpha} \frac{\partial B_f}{\partial v_\alpha} - \frac{\partial B_f}{\partial r_\alpha} \frac{\partial A_f}{\partial v_\alpha} \right)$, and the the entropy is the Boltzmann entropy $-k_B T \int d\boldsymbol{r} \int d\boldsymbol{v} f(\boldsymbol{r}, \boldsymbol{v}) ln\, f(\boldsymbol{r}, \boldsymbol{v})$. Details of the GENERIC formulation of the Boltzmann

equation can be found in Grmela (2002).

4.5.3.3 The rheological model developed in this paper

The Poisson bracket expressing the kinematics of the state variables $x = (\boldsymbol{u}, \boldsymbol{c}, \boldsymbol{a})$ (see (4.24)) is

$$\begin{aligned}
\{A, B\} &= \{A, B\}^{(u)} + c_{\alpha\beta}\left(A_{c_{\beta\gamma}}\frac{\partial B_{u_\gamma}}{\partial r_\alpha} - B_{c_{\beta\gamma}}\frac{\partial A_{u_\gamma}}{\partial r_\alpha}\right) \\
&+c_{\alpha\gamma}\left(A_{c_{\beta\gamma}}\frac{\partial B_{u_\beta}}{\partial r_\alpha} - B_{c_{\beta\gamma}}\frac{\partial A_{u_\beta}}{\partial r_\alpha}\right) \\
&-a_{\alpha\beta}\left(A_{a_{\beta\gamma}}\frac{\partial B_{u_\alpha}}{\partial r_\gamma} - B_{a_{\beta\gamma}}\frac{\partial A_{u_\alpha}}{\partial r_\gamma}\right) \\
&-a_{\alpha\gamma}\left(A_{a_{\beta\gamma}}\frac{\partial B_{u_\alpha}}{\partial r_\beta} - B_{a_{\beta\gamma}}\frac{\partial A_{u_\alpha}}{\partial r_\beta}\right) \\
&+2a_{\alpha\beta}a_{\gamma\delta}\left(A_{a_{\gamma\delta}}\frac{\partial B_{u_\beta}}{\partial r_\alpha} - B_{a_{\gamma\delta}}\frac{\partial A_{u_\beta}}{\partial r_\alpha}\right)
\end{aligned} \tag{4.48}$$

where $\{A, B\}^{(u)}$ is given in (4.47). Equation $\frac{\partial x}{\partial t} = L\Phi_x$ where L corresponds to (4.48) by $\{A, B\} =< A_x, LB_x >$ are indeed Eqs.(4.18) and (4.26) with $\xi = 1$. The bracket (4.48) expresses the classical kinematics of $\boldsymbol{u}$ and the passive advection of $\boldsymbol{c}$ and $\boldsymbol{a}$ by $\boldsymbol{u}$: the upper convected advection of $\boldsymbol{c}$ and the lower convected advection of $\boldsymbol{a}$ that, in addition, takes into account the constraint $tr\boldsymbol{a} = const.$. If $\xi \neq 1$ then the advection is not anymore passive and it cannot be put into the Hamiltonian form.

The other elements of the GENERIC structure, namely the free energy and the dissipation potential, are given respectively in (4.29) and (4.27).

In the further development of the model presented in this paper we intend to discuss in a more realistic way the active advection of the lamellae (following the new approach to the active advection introduced recently in Gu and Grmela (2008)) and to replace the FENE-P dumbbells by reptating chains (in preparation).

4.5.3.4 Fiber suspensions

In this subsection we illustrate the modular character of the construction of rheological models that is made possible by the GENERIC structure. Just by appropriately changing

the constitutive relations (i.e. by appropriately changing the specification of L, Φ and Ξ arising in (4.45)), we can adapt a mesoscopic rheological model from one physical system to another. By an appropriate change we mean that the new physics is reflected in new specifications of L, Φ and Ξ. As an example, we replace the lamellae considered in this paper by fibers. Such fiber suspensions have been already discussed in terms of the GENERIC modeling in Rajabian et al. (2005). We shall now recall the differences in the constitutive relations.

First, we decide to choose the same level of description and choose the same state variables (4.24). The physical interpretations of $\boldsymbol{u}$ and $\boldsymbol{c}$ remain the same. The tensor $\boldsymbol{a}$ has however in Rajabian et al. (2005) a different interpretation. In order to characterize states of a fiber, we use one vector, namely the unit vector along the fiber. The tensor $\boldsymbol{a}$ is its second moment. In order to characterize states of a lamella, we also use one, namely the unit vector perpendicular to the plane of the lamellae. The tensor $\boldsymbol{a}$ (used in this paper) is its second moment.

Next, we turn to the advection. The different interpretations of the conformation tensor $\boldsymbol{a}$ imply different advections. We have discussed it already in Section 4.2.2. If we consider only the passive advection then the $\boldsymbol{a}$ representing fibers is upper convected and $\boldsymbol{a}$ representing the lamellae is lower convected. However, the passive advection is only a poor approximation for advections of both fibers and lamellae. This is clearly revealed in the microhydrodynamic approach to advection in which one formulates and solves the corresponding Stokes problem [Jeffery (1922); Kim and Karilla (1991)]. Different strategies for taking into account the active part of the advection are followed in Rajabian et al. (2005) and in this paper. In Rajabian et al. (2005), the modified (nonpassive) advection is obtained by starting with the advection on the level of kinetic theory (i.e. on the ψ-level), projecting it on the second moment $\boldsymbol{a}$, and finally making an appropriate closure (i.e. expressing the fourth moment, that remains in the advection after the projection, in terms of $\boldsymbol{a}$). There is no clear physics on the $\boldsymbol{a}$-level that can be associated with the choice of closures. The arguments for and against certain closures are based solely on the requirement that the final results arising on the ψ-level are well approximated by the results arising on the $\boldsymbol{a}$-level after making the closure. In order

to keep the $\boldsymbol{a}$-level autonomous and to avoid the arbitrariness associated with the choice of closures, we have modified in this paper the passive advection only by following Gordon and Schowalter [Gordon and Schowalter (1972)], and, in the future development of the model, by following the approach introduced recently in [Gu and Grmela (2007)].

The free energy of fibers and lamellae are formally the same. Only the phenomenological coefficients appearing in them distinguish one from the other. However, the part of the free energies S^{ca} (see (4.30)) describing the topological polymer-plate interactions in (4.30) and the topological polymer-fiber interactions in Rajabian et al. (2005) are different. In the polymer-fiber interactions, the fibers tend to be parallel with the polymer chains while in the polymer-plate interactions the plates tend to be parallel with the polymer chains and thus the vectors perpendicular to the plates tend to be perpendicular to the polymer chains. This difference then leads to different expressions for S^{ca}.

Finally, the dissipation potential Ξ chosen in Rajabian et al. (2005) is different from (4.27). The choice made in Rajabian et al. (2005) was inspired by the requirement that the term representing the dissipation resembles as much as possible the terms that have proven in the literature to provide good agreement with experimental observations.

Acknowledgements

The authors acknowledge the financial support provided by the Natural Sciences and Engineering Research Council (NSERC) of Canada.

References

1. Ayyer, R.K. and A.I. Leonov, "Comparative rheological studies of polyamide-6 and its low loaded nanocomposite based on layered silicates," Rheol Acta. **43**, 283-292 (2004).

2. Beris, A.N. and B.J. Edwards, "Thermodynamics of flowing systems," 1 st ed., Oxford University Press, New York, (1994).

3. Beris, A.N. and B.J. Edwards, "Poisson bracket formulation of viscoelastic flow equations of differential type: A unified approach," J. Rheol. **34**, 55-78, (1990).

4. Bird, R.B., P.J. Dotson, N.L. Johnson, "Polymer solution rheolgy based on a finitely extensible bead-spring chain model" J. Non-Newtonian Fluid Mech. **7** 213 (1980).

5. Bird, R.B., O. Hassager, R.C. Armstrong and C.F. Curtiss, "Dynamics of polymeric fluids," **Vol. 2**, Wiley, N.Y. (1987).

6. Bousmina, M. "Study of intercalation and exfoliation processes in polymer nanocomposites," Macromolecules **39**, 4259-4263, (2006).

7. Edwards, B.J., M. Dressler, M. Grmela and A. Ait-Kadi, "Rheological models with microstructural constraints," Rheol. Acta **42**, 64-72, (2003).

8. Eshelby, J.D. "The determination of the elastic field of an ellipsoidal inclusion, and related problems," Proc. R. Soc. Lond. A **241**, 376-396 (1957).

9. Eshelby, J.D., "The elastic field outside of an ellipsoidal inclusion", Proc. R. Soc. London A **252**, 561-569 (1959).

10. Eslami, H., A. Ramazani and H.A. Khonakdar, "Predictions of some internal microstructural models for polymer melts and solutions in shear and elongational flows," Macromol. Theory Simul. **13**, 655-664, (2004).

11. Eslami, H., A. Ramazani and H.A. Khonakdar, "Volume preserving conformational rheological models for multi-component miscible polymer blends using the GENERIC formalism," Macromol. Theory Simul. **12**, 524-530, (2003).

12. Forest, M. G., Q. Wang, "Monodomain response of finite-aspect-ratio macromolecules in shear and related linear flows" Rheol. Acta **42** 20-46 (2003).

13. Forest, M. G., Q. Wang, "Hydrodynamic theories of mixtures of polymers and rodlike liquid crystalline polymers", Phys. Rev. E **72** 041805 (2005).

14. Gordon, R.J. and W.R. Schowalter, Anisotropic fluid theory: A different approach to the dumbbell theory of dilute polymer solutions, Trans. Soc. Rheol. **16**, 79-97 (1972).

15. Grmela, M. "Particle and bracket formulations of kinetic equations", Contemp. Math. **28**, 125-132 (1984).

16. Grmela, M., "Stress Tensor in generalized hydrodynamics", Phys.Letters A, **111**, 41-44 (1985).

17. Grmela, M., "Bracket formulation of diffusion-convection equations," Physica D **21**, 177-212, (1986).

18. Grmela, M., "Thermodynamic and rheological modeling: Polymeric liquid crystals", pp 55-81 , in Polymer Rheology and Processing, A.A. Collyer and L.A. Utracki (eds) Elsevier 1990

19. Grmela, M., "Mesoscopic dynamic and thermodynamic: Application to polymer fluids," Lecture Notes in Physics **381**, 99-126, (1991).

20. Grmela, M. "Reciprocity relations in thermodynamics: Physica A, **309** 304-328 (2002).

21. Grmela, M. and P.J. Carreau, "Conformation tensor rheological models" J. Non-Newtonian Fluid Mech. **23** 271-294 (1987).

22. Grmela, M. and H.C. Ottinger, "Dynamics and thermodynamics of complex fluids. I. Development of a general formalism," Phys. Rev.E **E.55**, 6620-6632, (1997).

23. Gu, J.F. and M. Grmela, "GENERIC model of active advection", J.Non-Newtonian Fluid Mech. (in press)doi:10.1016/j.jnnfm.2007.05.001

24. Guo, R., J. Azaiez, C. Bellehumeur, " Rheology of fiber filled polymer melts: Role of fiber-fiber interactions and polymer-fiber coupling, Polym. Eng. Sci. **45** 385-399 (2005).

25. Herrchen, M. and H.C. Oettinger, "A detailed comparison of various FENE dumbbell models", J. Non-Newtonian Fluid Mech. **68** 17-42 (1997).

26. Hooper, J.B. and K.S., Schweizer, "Theory of Phase Separation in Polymer Nanocomposites," Macromolecules, **39**, 5133-5142, (2006).

27. Jeffery, G.B., "The motion of ellipsoidal particles immersed in a viscous fluid", Proc. R. Soc. Lond. A **102**, 181-179 (1922).

28. Khokhlov, A.R. and A.N. Semenov, "On the theory of liquid-crystalline ordering of polymer chains with limited flexibility," Journal of Stat Phys **38**, 161-182, (1985).

29. Kim, S. and S.J. Karilla, Microhydrodynamics, Butterworth-Heinemann (1991).

30. Kim, K., L.A. Utracki and M. Kamal, "Numerical simulation of polymer nanocomposites using self-consistent mean-field model," J. Chem. Phys **121**, 10766-10777, (2004).

31. Krishnamoorti, R. and E.P. Giannelis, "Rheology of end-tethered polymer layered silicate nanocomposites," Macromolecules **30**, 4097-4102, (1997).

32. Krishnamoorti, R., J. Ren and A.S. Silva, "Shear response of layered silicate nanocomposites," J. Chem. Phys **114**, 4968-4972, (2001).

33. Maier, W. and Saupe, A., Naturforschung **15** 287 (1960).

34. Onsager, L., "The effects of shape on the interaction of colloidal particles," Ann. N.Y. Acad. Sci. **51**, 627-659, (1949).

35. Ottinger, H.C. and M. Grmela, "Dynamics and thermodynamics of complex fluids. II. Illustrations of a general formalism," Phys. Rev.E **E.56**, 6633-6655, (1997).

36. Oettinger,H.C., Beyond equilibrium thermodynamics, Wiley-Interscience (2005).

37. Rajabian, M., C. Dubois, M. Grmela, "Suspension of semiflexible fibers in polymeric fluids: rheology and thermodynamics", Rheol. Acta **44**, 521-535 (2005).

38. Ramazani, A., A. Ait-Kadi, M. Grmela,"Rheology of fiber suspensions in viscoelastic media: Experiments and model predictions" J. Rheol. **45**, 945 (2001).

39. Sarti, G.S. and G. Marrucci, "Thermomechanics of dilute polymer solutions: multiple bead-spring model ," Chem Eng Sci **28**, 1053-1059, (1973).

40. Singh, A.P., A.D. Rey, "Microstrucure constitutive equations for discotic nematic liquid crystalline materials", Rheol. Acta **37** 30-45, 374-386 (1998)

41. Sinha Ray, S.,"Rheology of polymer/layered silicate nanocomposites" J. Ind. Eng. Chem. **12** 811-842 (2006).

42. Sinha Ray, S. and M. Okamoto, "Polymer/layered silicate nanocomposites: a review from preparation to processing," Prog. Polym. Sci. **28**, 1539-1641, (2003).

43. Sinha Ray, S. and M. Bousmina, "Biodegradable polymers and their layered silicate nanocomposites: In greening the 21st century materials world," Prog. Mater Sci. **50**, 962-1079, (2005).

44. Sinha Ray, S. and M. Bousmina, "Poly(butylene sucinate-co-adipate) montmorillonite nanocomposites: effect of organic modifier miscibility on structure, properties, and viscoelasticity," Polymer **46**, 12430-12439, (2005).

45. Solomon, M.J., A.S. Almusallam, K.F. Seefeldt, K. F, A. Somwangthanaroj, and P. Varadan, "Rheology of Polypropylene/Clay Hybrid Materials, " Macromolecules **34**, 1864-1872, (2001).

46. Tung, J., R.K. Gupta, G.P. Simon, G.H. Edward and S.N. Bhattacharya, "Rheological and mechanical comparative study of in situ polymerized and melt-blended nylon 6 nanocomposites," Polymer **46**, 10405-10418, (2005).

47. Wolfram, S., "Mathematica-A system for doing mathematics by computer," 2nd ed., Wesley-VCH, New York, (1991).

48. Wu, D., Ch. Zhou, Z. Hong, D. Mao and Z. Bian, "Study on rheological behaviour of poly(butylene terephthalate)/montmorillonite nanocomposites," European Polymer Journal **41** 2199-2207, (2005).

49. Zhao, J., A.B. Morgan and J.D. Harris, "Rheological characterization of polystyreneclay nanocomposites to compare the degree of exfoliation and dispersion," Polymer, **46**, 8641-8660, (2005).

CHAPTER 5

MESOSCOPIC FORMULATION OF REPTATION

Hassan Eslami and Miroslav Grmela[1]

Center for Applied Research on Polymers and Composites (CREPEC)

Ecole Polytechnique de Montreal, C.P.6079 suc. Centre-ville,

Montreal, H3C 3A7, Quebec, Canada

Rheologica Acta (2008) 47:399-415

[1]corresponding author: e-mail: miroslav.grmela@polymtl.ca

Abstract

Macromolecules stretch and bend. Their motion is moreover constrained (due to the presence of other macromolecules in their neighborhood) to a tube-like region. This well known physical picture is translated into governing equations on a new mesoscopic level of description by following the modular construction provided by GENERIC. Rheological predictions are calculated in both linear and nonlinear domain. A good agreement with results of experimental observations is found.

5.1 Introduction

The first step in rheological modeling, i.e. in an attempt to establish a bridge between microscopic and macroscopic (flow) properties of fluids, is the choice of a microscopic level of description serving as the point of departure. For polymeric fluids composed of macromolecular chains, the choice of one chain kinetic theory level, made by de Gennes [De Gennes (1971)] , Edwards (1976) and Doi and Edwards (1986), gave rise to a very successful theory known as reptation theory [Doi and Edwards (1986); Likhtman and McLeish (2002); McLeish (2002); Marrucci et al. (2001); Marrucci and Grizzuti (1988); Mead and Leal (1995); Mead et al. (1995); Ottinger (1999)].

In this paper we explore a possibility to express the reptation physics on a more macroscopic level. We choose it to be the level on which the second order conformation tensor replaces the one chain distribution function as a state variable. The reason why we are turning to more macroscopic levels (i.e. levels involving less details than the level of one chain kinetic theory) is threefold: (i) we intend to investigate in the future suspensions of nanoparticles in polymeric fluids [Eslami et al. (2007)] and need thus a relatively simple theory of the charge-free matrix fluid, (ii) we want to reduce the effort needed to pass (by solving numerically the governing equations) to the macroscopic level on which the rheological measurements are made, and (iii) by taking a multilevel view of the reptation physics we hope to enrich it.

In order to illustrate the interesting issues that arise in multilevel modeling, we take two well known levels $\mathcal{L}_{ds}$ and $\mathcal{L}_{1kt}$, formulate on them physics of polymeric fluids, and make a few observations.

The level $\mathcal{L}_{ds}$ is the level used in direct molecular simulations. Coordinates of a large number ($\approx 10^5$) of polymer chains serve as state variables. Their time evolution is governed by Newton's equations. The physics enters in the specification of all the forces involved. Collection of trajectories of all chains, obtained by solving (with the assistance of computers) Newton's equations, is the raw material from which the flow behavior observed in experiments is then extracted.

The level $\mathcal{L}_{1kt}$ is the level used in the reptation theory. The state variable is a one chain distribution function. Its time evolution is governed by a kinetic equation expressing the physical insight intrinsic to the reptation theory.

We make now a few observations.

Observation 1:

The two levels are autonomous. Neither of them needs the other to formulate its own physics and to express it in mathematical terms. In spite of the fact that the physical system under consideration (polymeric fluids) is the same on both levels, the physics as well as its mathematical formulation are quite different. The physics on the level $\mathcal{L}_{ds}$ is the classical mechanics of a large number of particles with complex interactions. The physics on the level $\mathcal{L}_{1kt}$ focuses on one chain whose motion is constrained into a tube representing the other chains.

Observation 2:

The level $\mathcal{L}_{ds}$ involves more details and is therefore termed "more microscopic" than the level $\mathcal{L}_{1kt}$. The more macroscopic level $\mathcal{L}_{1kt}$ can be reduced from the level $\mathcal{L}_{ds}$. The reduction consists of extracting a pattern in the collection of trajectories. A new physics, namely the reptation physics, emerges in this pattern recognition process. We note here that this is not however the way the reptation physics has been originally introduced. In fact, the pattern recognition process mentioned above is very difficult and, to the best of our

knowledge, it has yet to be realized. Direct simulations involving some elements of coarse-graining have been reported in Refs.[Padding and Briels (2001); Kindt and Briels (2007)]. The original introduction of the reptation physics has been made independently of other levels of description (see Observation 1 above).

We note that in spite of the fact that the level $\mathcal{L}_{ds}$ is more detailed and thus more fundamental than the level $\mathcal{L}_{1kt}$, it is not useful to regard it as being superior to the level $\mathcal{L}_{1kt}$. It is true that some details seen on the level $\mathcal{L}_{ds}$ are not seen on the level $\mathcal{L}_{1kt}$ but it is also true that there are things on the level $\mathcal{L}_{1kt}$ that are not seen on the level $\mathcal{L}_{ds}$. It is useful to regard both levels as having the same status and being complementary one to the other.

Observation 3:

Both levels should imply the same macroscopic (thermodynamic and rheological) behavior. The same macroscopic behavior means the same properties of solutions of the governing equations and consequently the same mathematical structure guaranteeing their existence. Indeed, such mathematical structure has been identified [Grmela (1984, 1986); Beris and Edwards (1994); Grmela and Ottinger (1997); Ottinger and Grmela (1997); Ottinger (2005)]. It has been termed (in Grmela and Ottinger (1997); Ottinger and Grmela (1997)) GENERIC. This structure has been found very useful in expressing physical insights in governing equations on all levels.

It is very interesting to attempt to make similar type of observations also about different pairs of levels (e.g. the pair consisting of level of one particle kinetic theory and the level of classical hydrodynamics, or the pair consisting of the level of classical mechanics of particles and the level of classical thermodynamics). In the rest of this paper we shall put ourselves on the level on which states of polymeric fluids are characterized by second order symmetric and positive definite tensors (termed conformation tensors). We shall denote the level by the symbol $\mathcal{L}_{ct}$. Following GENERIC, we consider the level $\mathcal{L}_{ct}$ as an autonomous level and formulate on it some basic elements of the reptation physics (introduced originally on the level $\mathcal{L}_{1kt}$). Equations governing the time evolution of conformation tensors have arisen in the reptation physics before but only as reduced forms of kinetic equations. The conformation

tensor is in these reduced kinetic equations a second moment of the distribution function. The reductions are made in order to bring the kinetic equations to a form in which they can be solved more easily. The two ways of introducing the governing equations on the $\mathcal{L}_{ct}$ level, one followed in this paper (a new realization of the reptation physics), and the other one used in the kinetic theory (reduction of the governing equations on the $\mathcal{L}_{1kt}$ level) are different. We shall discuss briefly their relation in Section 5.2.2.3.

The paper is organized as follows: In Section 5.2 we derive the governing equation of the model by following the framework provided by GENERIC. The framework is first recalled on the example of the familiar rigid or FENE-P model (in Section 5.2.1). Then, in Section 5.2.2, we formulate the reptation model as a straightforward extension of the rigid and FENE-P models. Solutions of the governing equations representing the linear and nonlinear rheological responses are then presented in Section 5.3.

5.2 Model formulation

We assume that the polymer melts under consideration are incompressible homogeneous and isothermal fluids. In Section 5.2.1 we model the macromolecules composing the polymer melt as dumbbells. Their states are chosen to be characterized by the conformation tensor, $\boldsymbol{c}$, that is interpreted physically as an internal deformation tensor. Alternatively, we can regard $\boldsymbol{c}$ as a second moment of the distribution function $\psi(\boldsymbol{Q})$ ($c_{ij} = \int d\boldsymbol{Q} Q_i Q_j \psi(\boldsymbol{Q})$; $i, j = 1, 2, 3$) of dumbbells ($\boldsymbol{Q}$ is the end-to-end vector of the dumbbell). From the mathematical point of view, $\boldsymbol{c}$ is a symmetric and positive definite matrix. Hereafter, we consider $\boldsymbol{c}$ to be dimensionless ($tr\boldsymbol{c} = 1$ if the dumbbell reaches its maximal extension Q_0 introduced in (5.3) below). In Section 5.2.2 we take a more detailed (more microscopic) viewpoint of the polymer melts. The macromolecules composing them are modeled as worm-like chains that only locally are regarded as dumbbells. We shall systematically consider both the finitely extensible FENE-P dumbbells and inextensible rigid dumbbells. The variable characterizing states of the chains are conformation tensors $\boldsymbol{c}(s)$, where $-1 < s < 1$ is the coordinate along

the backbone of the chain. The passage from a dumbbell to a local dumbbell (i.e. a dumbbell depending on the coordinate s) allows us to introduce two new features: (i) a new dissipative mechanism (namely the reptation, i.e. the diffusion along the chain), and (ii) a new type of energy, namely the energy associated with nonlocal intrachain interactions.

5.2.1 Rigid or FENE-P dumbbell

The role of this subsection is to recall the familiar FENE-P and rigid model and to cast its governing equations into the GENERIC form in which they are then extended in Section 5.2.2.

We begin with the FENE-P model. The point of departure of Bird et al. (1980) derivation of equations governing the time evolution of $\boldsymbol{c}$ is Newton's equation for the motion of two beads of an isolated dumbbell. The forces acting on the beads are of three types: the intramolecular elastic force guaranteeing the finite extensibility of the dumbbell, the frictional Stokes force, and the Brownian force. The Liouville equation corresponding the inertialless approximation of these equations is the kinetic equation governing the time evolution of the distribution function $\psi(\boldsymbol{Q})$. Its projection on the second moment $\boldsymbol{c}$ together with application of the Peterlin closure approximation leads then to the equation governing the time evolution of $\boldsymbol{c}$. Below, we write it in the form (the GENERIC form) in which we shall discuss its extension in Section 5.2.2:

$$\begin{aligned}
\frac{\partial u_\alpha}{\partial t} &= -\partial_\beta\left(\frac{u_\alpha u_\beta}{\rho}\right) - \partial_\alpha p - \partial_\beta \sigma_{\alpha\beta} \\
\frac{dc_{\alpha\beta}}{dt} &= -\frac{1}{2}\left(\boldsymbol{\Omega}\cdot\boldsymbol{c} - \boldsymbol{c}\cdot\boldsymbol{\Omega}\right)_{\alpha\beta} + \frac{1}{2}\left(\dot{\boldsymbol{\gamma}}\cdot\boldsymbol{c} + \boldsymbol{c}\cdot\dot{\boldsymbol{\gamma}}\right)_{\alpha\beta} \\
&\quad - \frac{\partial \Xi}{\partial \Phi_{c_{\alpha\beta}}}
\end{aligned} \tag{5.1}$$

where $\partial_\alpha = \frac{\partial}{\partial r_\alpha}$, $\boldsymbol{u}(\boldsymbol{r})$ is the momentum field, $\boldsymbol{r}$ is the position vector, ρ is the mass density of the fluid (a constant independent of $\boldsymbol{r}$), p is the hydrostatic pressure given by

$$p = -\varphi + u_\beta \Phi_{u_\beta} + c_{\alpha\beta}\Phi_{c\alpha\beta}, \tag{5.2}$$

$\Phi(\boldsymbol{u}, \boldsymbol{c}) = \int d\boldsymbol{r}\varphi$ is the free energy

$$\begin{aligned}\Phi &= \frac{1}{V}\int d\boldsymbol{r}\frac{\boldsymbol{u}^2}{2\rho} \\ &+\frac{1}{V}\int d\boldsymbol{r}\left[-nHQ_0^2\ln\left(1-tr\ \mathbf{c}\right)-\frac{1}{2}nk_BT\ln(\det\mathbf{c})\right]\end{aligned} \tag{5.3}$$

V is the volume of the fluid, Ξ is the dissipation potential

$$\Xi = \Phi_{c_{ij}}\Lambda_{ijkl}\Phi_{c_{kl}} \tag{5.4}$$

and $\boldsymbol{\sigma}$ is the extra stress tensor given by

$$\sigma_{\alpha\beta} = -2c_{\alpha\varepsilon}\Phi_{c_{\varepsilon\beta}} \tag{5.5}$$

We explain now the meaning of the symbols appearing in the above equations. We use $i, j, k, ... = 1, 2, 3$ or alternatively the Greek letters $\alpha, \beta, \gamma, ... = 1, 2, 3$ to denote indices. We also use through the paper the summation convention (summation over repeated indices). By Φ_{u_α} we denote $\frac{\delta\Phi}{\delta u_\alpha}$ and similarly, $\Phi_{c_{\alpha\beta}} = \frac{\delta\Phi}{\delta c_{\alpha\beta}}$, δ/δ we denote the variational functional derivatives. Note that due to the form of the free energy given in (5.3), $\Phi_{u_\alpha} = u_\alpha/\rho$ is the velocity. By $\dot{\gamma}_{\alpha\beta} = \partial_\beta\Phi_{u_\alpha} + \partial_\alpha\Phi_{u_\beta}$ and $\Omega_{\alpha\beta} = \partial_\beta\Phi_{u_\alpha} - \partial_\alpha\Phi_{u_\beta}$ we denote the strain rate and the vorticity tensor respectively. By the symbol n we denote the number density of the polymer ($n = \frac{\rho N_A}{M}$, N_A is the Avogadro number, ρ is density of the polymer and M its molecular weight), Q_0 is their maximal extensibility of the dumbbell, H is the elastic modulus, k_B is the Boltzmann constant, T is a (constant) temperature, $\boldsymbol{\Lambda}$ is the mobility tensor, $\boldsymbol{\Lambda} = \frac{2}{n\zeta}\widehat{\boldsymbol{c}\boldsymbol{\delta}}$, the symbol $\widehat{}$ denotes the symmetrization in the four indices, ζ is the friction constant, $\boldsymbol{\delta}$ is the unit tensor.

By simply performing the operations involved in Eqs.(5.1)-(5.5) we prove that these equations are indeed equivalent to the equations appearing in Bird et al. (1980). The advantages of the formulation (5.1)-(5.5) over the original formulation [3] are the following:

(a) We have identified the free energy $\Phi = E - k_BTS$. The first term in (5.3) is the kinetic energy, the second term is the intramolecular energy (note that if the deformations are small,

i.e. $tr\boldsymbol{c}$ is small, then the intramolecular energy is well approximated by the Hook energy $HQ_0^2 tr\boldsymbol{c}$, and when $tr\boldsymbol{c} \to 1$ then the intramolecular energy $\to \infty$ which guarantees the finite extensibility), and the third term represent the entropy S multiplied by the temperature T.

(b) Without the term involving Ξ, the time evolution equations (5.1) together with (5.2) and (5.5) are: (i) time reversible, i.e. the transformation $\boldsymbol{u} \to -\boldsymbol{u}$ compensates the inversion of the time $t \to -t$), (ii) nondissipative, i.e. $\frac{d\Phi}{dt} = 0$, and (iii) Hamiltonian, i.e. Eqs. (5.1),(5.2) and (5.5) can be cast into the from

$$\frac{d}{dt}\begin{pmatrix} \boldsymbol{u} \\ \boldsymbol{c} \end{pmatrix} = L \begin{pmatrix} \Phi_{\boldsymbol{u}} \\ \Phi_{\boldsymbol{c}} \end{pmatrix} \tag{5.6}$$

where L is given by

$$\begin{aligned} \{A, B\} &= \int d\boldsymbol{r} \begin{pmatrix} A_{\boldsymbol{u}} & A_{\boldsymbol{c}} \end{pmatrix} L \begin{pmatrix} B_{\boldsymbol{u}} \\ B_{\boldsymbol{c}} \end{pmatrix} \\ &= \int d\boldsymbol{r} u_i(\partial_j \left(A_{u_i}\right) B_{u_j} - \partial_j(B_{u_i}) A_{u_j}) \\ &+ c_{ij} \left(\partial_m(A_{c_{ij}}) B_{u_m} - \partial_m(B_{c_{ij}}) A_{u_m}\right) \\ &+ c_{ki} \left(A_{c_{im}} \partial_k(B_{u_m}) - B_{c_{im}} \partial_k(A_{u_m})\right) \\ &+ c_{km} \left(A_{c_{im}} \partial_k(B_{u_i}) - B_{c_{im}} \partial_k(A_{u_i})\right) \end{aligned} \tag{5.7}$$

A and B are sufficiently regular real valued functions of $(\boldsymbol{u}, \boldsymbol{c})$. The bracket $\{A, B\}$ appearing in (5.7) is a Poisson bracket (i.e. $\{A, B\} = -\{B, A\}$ and $\{\{A, B\}, C\} + \{\{C, A\}, B\} + \{\{B, C\}, A\} = 0$). The expression for the hydrostatic pressure (5.2) and the extra stress tensor (5.5) appear as necessary conditions for (5.1) being Hamiltonian. Alternatively, (5.2) and (5.5) can also be derived [Doi and Edwards (1986)] from the requirement of the nondissipativity (i.e. the requirement that $\frac{d\Phi}{dt} = 0$). The nondissipativity of the time evolution governed by (5.6) follows from $\frac{d\Phi}{dt} = \{\Phi, \Phi\} = 0$. The last equality is a direct consequence of the antisymmetry of the Poisson bracket.

(c) The last term on the right hand side of the second equation in (5.1) (i.e. the term involving Ξ) represents the dissipation. With this term, the time evolution equation (5.6)

takes the form

$$\frac{d}{dt}\begin{pmatrix} \boldsymbol{u} \\ \boldsymbol{c} \end{pmatrix} = L\begin{pmatrix} \Phi_{\boldsymbol{u}} \\ \Phi_{\boldsymbol{c}} \end{pmatrix} - \begin{pmatrix} \frac{\partial \Xi}{\partial \Phi_{\boldsymbol{u}}} \\ \frac{\partial \Xi}{\partial \Phi_{\boldsymbol{c}}} \end{pmatrix} \tag{5.8}$$

The potential $\Xi(\Phi_u, \Phi_c)$ is called a dissipation potential. By using the result (ii) proven in the previous paragraph, we see immediately that $\frac{d\Phi}{dt} = -\Phi_{\boldsymbol{c}}\frac{\partial \Xi}{\partial \Phi_{\boldsymbol{c}}} = -2\Phi_{\boldsymbol{c}}\boldsymbol{\Lambda}\Phi_{\boldsymbol{c}} < 0$ The last inequality is a consequence of $\boldsymbol{\Lambda}$ being positive definite. The role of the dissipation is thus to bring, by following the time evolution, the fluid to equilibrium states at which the thermodynamic potential Φ reaches its minimum. By using the terminology of the classical nonequilibrium thermodynamics, $\Phi_{\boldsymbol{c}}$ is called a dissipative thermodynamic force. It drives the fluid to the equilibrium at which the force disappears (indeed, $\Phi_{\boldsymbol{c}} = 0$ at equilibrium).

(d) A new physics can be easily incorporated into the governing equations by simply changing appropriately the free energy and the dissipation potential. This will be done in the next section.

(e) The above GENERIC formulation can also be very easily adapted to the rigid dumbbell in which the intramolecular potential is replaced by the constraint $tr\boldsymbol{c} = const.$. The equations governing the time evolution remain to be Eq.(5.8). The quantities L, Φ and Ξ are however modified. The Poisson bracket (5.7) acquires a new term $-2c_{ij}c_{kl}(A_{c_{kl}}\partial_i(B_{u_j}) - B_{c_{kl}}\partial_i(A_{u_j}))$, in the free energy, Φ, the term $-nHQ_0^2 ln(1-tr\boldsymbol{c})$ is replaced by $\lambda tr\boldsymbol{c}$, where λ is the Lagrange multiplier determined by the constraint $tr\boldsymbol{c} = const.$, a new term $+2c_{\alpha\beta}tr(\boldsymbol{c}\cdot\Phi_{\boldsymbol{c}})$ appears on the right hand side of the expression for the extra stress tensor (5.5), and the thermodynamic force $\Phi_{\boldsymbol{c}}$ in the thermodynamic potential (5.4) is replaced by $\Phi_{\boldsymbol{c}} - \frac{1}{3}\boldsymbol{\delta} tr\Phi_{\boldsymbol{c}}$.

5.2.2 Local rigid or FENE-P dumbbell

The classical rigid and FENE-P dumbbell models that we have recalled above will now be adapted (extended) to polymer melts. The main idea behind the extension is to pass from seeing the macromolecules as dumbbells to seeing them as chains [Rouse (1953); Zimm (1956)] that only locally are seen as dumbbells. Basic steps of the extension are the following:

(1) We keep the conformation tensor as (now local) structural state variable.

(2) The chains are considered to be continuous (worm-like) in order to be able to replace a cumbersome discrete algebra with differential calculus.

(3) New types of interactions are introduced. In addition to the elastic extensibility of the local dumbbells, we introduce a nonlocal intrachain interaction (like for example the interactions involved in bending in the locally inextensible chains) and iterchain interactions expressed as tube-like constraints leading to a new diffusion-type (reptation) dissipative mechanism.

While neither of these steps is particularly new, their implementation in the framework of the GENERIC formalism leads to a new rheological model that has an attractive feature of being relatively simple and realistic.

We now proceed to construct the extended model by following closely the construction of the FENE-P model recalled in Section 5.2.1.

We begin with the choice of state variables. States of the molecular chains composing the melt are described by the conformation tensor $\boldsymbol{c}(s,t)$. By s; $-1 < s < +1$ we parametrize the backbone of the chain, $\boldsymbol{c}(s)$ is the second moment of the distribution function $\psi(\boldsymbol{Q},s)$ (i.e. $c_{ij}(s) = \int d\boldsymbol{Q} Q_i Q_j \psi(\boldsymbol{Q},s)$), where $\boldsymbol{Q}$ is the tangent vector to the backbone at s, t denotes the time. We allow local stretching of the chain so that the length of $\boldsymbol{Q}$ is not a constant. The complete set of state variables is thus:

$$
\begin{aligned}
&(\boldsymbol{u}(\boldsymbol{r}),\ \boldsymbol{c}(s,t))\,,\ \ -1 < s < 1 \\
&\boldsymbol{c}(-1,t) = \boldsymbol{c}(1,t) = \chi\boldsymbol{\delta}\ \ for\ \ 0 \le t \le \infty
\end{aligned}
\tag{5.9}
$$

where χ is a coefficient that will be specified later (see (5.13)). The lengths, $\sqrt{tr\boldsymbol{c}(s)}$, of the tangent vectors at $-1 < s < 1$ are, in general, all different. The end points of the chains are assumed to be at equilibrium at all times independently of the imposed flow (this is the physical content of the last line in (5.9)). From the physical point of view, this means that the end points of the chain evolve in time much faster than the whole chain and we thus assume that on the scale on which we observe the fluid and the chains the end points are always at equilibrium. The validity of this assumption has been investigated, from the point

of view of direct molecular simulations, in Kroger and Hess (1993). It would not be difficult to replace the boundary conditions in (5.9) by a relaxation type time evolution of the end points. We shall not explore such modification in this paper. The same state variables as (5.9) have been recently used in [Leygue et al. (2006a,b)] (see also Leygue et al. (2001)). We thus follow [Likhtman and McLeish (2002); Leygue et al. (2006b)] at this point. However, the physics and in particular the way the physics is expressed in the mathematical formulation of the model are different. For example, the weakly nonlocal forces involving higher order derivatives with respect to the chain coordinate s are not included in [Leygue et al. (2006a,b)]. In addition, we use systematically the requirement of the compatibility with thermodynamics to write the governing equations. Consequently, the equations governing the time evolution of (5.9) arising bellow are different from those appearing in [Leygue et al. (2006a,b)].

The first step in formulating the time evolution of the state variables (5.9) is to find their kinematics. We shall assume that the kinematics of an isolated dumbbell (discussed in Section 5.2.1) and a local dumbbell discussed in this section is the same. In the context of discrete chains, this is the standard assumption (used for example in Bird et al. (1980)) that beads of a dumbbell are advected by the imposed flow in the same way independently of their belonging to an isolated dumbbell or a dumbbell imbedded in a chain.

Since the kinematics of $(\boldsymbol{u}, \boldsymbol{c})$ and $(\boldsymbol{u}, \boldsymbol{c}(s))$ is the same, the framework (5.1) for equations governing their time evolution remains also the same. The expressions for the hydrostatic pressure and the extra stress tensor take now the form

$$p = u_\beta \Phi_{u_\beta} + \int_{-1}^{1} ds \, (-\varphi + c_{\alpha\beta} \Phi_{c\alpha\beta}) \tag{5.10}$$

and

$$\sigma_{\alpha\beta} \;=\; -2 \int_{-1}^{1} ds \; c_{\alpha\varepsilon} \Phi_{c_{\varepsilon\beta}} \tag{5.11}$$

The new physics emerging in the passage from an isolated to a local dumbbell enters our formulation only in the free energy Φ (Section 5.2.2.1) and in the dissipation potential Ξ (Section 5.2.2.2).

5.2.2.1 Free energy

Equilibrium statistical mechanics provides us with the physical insight and tools needed to discuss the free energy $\Phi = E - k_B T S$, E is the energy k_B the Boltzmann constant, T the temperature, and S the entropy. We consider first the FENE-P dumbbells.

Since the chains are seen as being locally the same FENE-P dumbbells as the ones discussed in the previous section, we propose the following free energy:

$$\begin{aligned}\Phi &= \frac{1}{V}\int d\boldsymbol{r}\frac{\boldsymbol{u}^2}{2\rho} \\ &+\frac{1}{V}\int d\boldsymbol{r}\int_{-1}^{1} ds\left[-nHQ_0^2\ln\left(1-tr\ \mathbf{c}\right)+Ktr(\boldsymbol{c}_s\cdot\boldsymbol{c}_s)-\frac{1}{2}nk_BT\ln(\det\mathbf{c})\right]\end{aligned} \tag{5.12}$$

By $\mathbf{c}_s$ we denote $\frac{\partial \mathbf{c}}{\partial s}$. The first, the second, and the fourth terms are the same as in (5.3) The third term is new. It represent the energy associated with interactions among the dumbbells that are neighbors on the chain. In the case of locally inextensible dumbbells such interactions are related to bending deformations of the chain. The coefficient K is the modulus associated with this type of interactions.

Equilibrium states are the states at which the free energy reaches its minimum. It is easy to verify that $\boldsymbol{c} = \frac{1}{3+f}\boldsymbol{\delta}$ is a solution to $\Phi_{c_{ij}} = \frac{f}{1-tr\ \mathbf{c}}\delta_{ij} - c_{ij}^{-1} - 2\frac{\partial}{\partial s}\left(Kc_{sij}\right) = 0$ where $f = \frac{2HQ_0^2}{k_BT}$. This means that $c_{ij} = \frac{1}{3+f}\delta_{ij}$ represents an equilibrium state and thus

$$\chi = \frac{1}{3+f} \tag{5.13}$$

where χ is introduced in (5.9).

In the case of rigid local dumbbells, the expression (5.12) is modified in the same way as described in Section 5.2.1.

Following the spirit of the reptation theory [De Gennes (1971)], the interactions among dumbbells belonging to different chains are taken into account in the dissipative processes discussed below.

5.2.2.2 Dissipation potential

Now we turn to the dissipation potential Ξ. The first question we ask is of what are the dissipative thermodynamic forces driving the dissipative processes. In addition to $\Phi_{\boldsymbol{C}}$ used in the context of isolated dumbbells, we shall now introduce $(\Phi_{\boldsymbol{C}})_s = \frac{\partial \Phi_{\boldsymbol{C}}}{\partial s}$ as a new dissipative thermodynamic force. We thus regard the dissipation as being driven first by the force $(\Phi_{\boldsymbol{C}})_s$ to states at which $\Phi_{\boldsymbol{C}}$ is independent of s and then by the force $\Phi_{\boldsymbol{C}}$ to equilibrium states for which $\Phi_{\boldsymbol{C}} = 0$. The two forces $\Phi_{\boldsymbol{C}}$ and $(\Phi_{\boldsymbol{C}})_s$ combine into new dissipation potential

$$\Xi = \left(\Phi_{C_{ij}}\ ,\ (\Phi_{C_{ij}})_s\right) \begin{pmatrix} \Lambda^{11}_{ijkl} & 0 \\ 0 & \Lambda^{22}_{ijkl} \end{pmatrix} \begin{pmatrix} \Phi_{C_{kl}} \\ (\Phi_{C_{kl}})_s \end{pmatrix} \tag{5.14}$$

where $\boldsymbol{\Lambda}^{11}$ and $\boldsymbol{\Lambda}^{22}$ are phenomenological mobility tensors. The new potential (5.14) involving two forces is clearly a natural extension of the potential (5.4) involving only one force. The off diagonal elements in the mobility matrix can be different from zero but we do not expect the coupling between the two forces to play an important role and therefore in this paper, for the sake of simplicity, we neglect them.

If we insert the dissipation potential (5.14) into (5.1), the dissipative part of the time evolution equations (denoted $\left(\frac{\partial}{\partial t}\right)_{dissipative}$) becomes (since the functional derivatives are variational functional derivatives)

$$\left(\frac{\partial \boldsymbol{C}}{\partial t}\right)_{dissipative} = -\frac{\partial \Xi}{\partial \Phi_{\boldsymbol{C}}} + \left(\frac{\partial \Xi}{\partial (\Phi_{\boldsymbol{C}})_s}\right)_s \tag{5.15}$$

The second term on the right hand side of (5.15) represents diffusion along the backbone of the chain. It is thus exactly the term that is introduced in the reptation theory as an expression of constraints put on the motion of the chains by the presence of neighbor chains. It is interesting to note that we have arrived at the diffusion along the chain simply on thermodynamic grounds by introducing $(\Phi_{\boldsymbol{C}})_s$ as a new dissipative thermodynamic force.

We now turn to the specification of the mobility tensors $\boldsymbol{\Lambda}$ arising in (5.14). If we remain on the mesoscopic level on which we are formulating our model, they are phenomenological

coefficients. Their choice is restricted only by the requirement (guaranteeing $d\Phi/dt \leq 0$) that the matrix $\begin{pmatrix} \Lambda^{11}_{ijkl} & 0 \\ 0 & \Lambda^{22}_{ijkl} \end{pmatrix}$ is positive definite. This means that both Λ^{11} and Λ^{22} are positive definite tensors.

Following Beris and Edwards (1994, 1990), we suggest the following polynomial functions of $\boldsymbol{c}$:

$$\boldsymbol{\Lambda}^{11} = \Lambda^{11}_0 \left[\kappa_1 \widehat{\boldsymbol{c}\boldsymbol{\delta}} + \kappa_2 \widehat{\boldsymbol{c}\boldsymbol{c}}\right] \tag{5.16}$$

and

$$\boldsymbol{\Lambda}^{22} = \Lambda^{22}_0 \left(1 + \widetilde{\Lambda^{22}_0} \left(tr\boldsymbol{c} - tr\boldsymbol{c}_{eq}\right)^2\right) \left[\kappa_1 \widehat{\boldsymbol{c}\boldsymbol{\delta}} + \kappa_2 \widehat{\boldsymbol{c}\boldsymbol{c}}\right] \tag{5.17}$$

where Λ^{11}_0, Λ^{22}_0 and $\widetilde{\Lambda^{22}_0}$ are phenomenological coefficients. The coefficients κ_1 and κ_2 appearing in (5.16 and 5.17) equal either 0 or 1. We are introducing them in order to be able to explore in the next sections consequences of choosing linear and/or quadratic dependence on $\boldsymbol{c}$. The symbol $\boldsymbol{c}_{eq}$ arising in (5.16) and (5.17) denotes the conformation tensor $\boldsymbol{c}$ at equilibrium.

In the case of rigid dumbbell, the thermodynamic forces are modified as in Section 5.2.1 and Λ^{22} is modified as follow:

$$\boldsymbol{\Lambda}^{22} = \Lambda^{22}_0 \left(1 + \widetilde{\Lambda^{22}_0} \left(II - II_{eq}\right)^2\right) \left[\kappa_1 \widehat{\boldsymbol{c}\boldsymbol{\delta}} + \kappa_2 \widehat{\boldsymbol{c}\boldsymbol{c}}\right] \tag{5.18}$$

Where $II = (tr\boldsymbol{c})^2 - tr\left(\boldsymbol{c} \cdot \boldsymbol{c}\right)$.

At this point we have completed the formulation of the governing equations of the model. In the next sections we shall solve them. Before doing it, we recall the physics that has been take into account in (5.1) with the free energy Φ given in (5.12) and the dissipation potential Ξ in (5.14).

5.2.2.3 Relation to the level $\mathcal{L}_{1kt}$

As we have already mentioned in Introduction, equations governing the time evolution of the conformation tensor (that is seen as a second moment of the one chain distribution

function) can also be derived by, first, deriving kinetic equations, and then reducing them to second moment equations. In fact, almost all papers introducing reptation kinetic equations introduce also their second moment reductions. The reductions are made as a part of the process of solving the kinetic equations. It is important to keep in mind that there is a significant difference between the two ways of introducing governing equations on the level $\mathcal{L}_{ct}$. The physics put into kinetic equations is, in general, lost in the reduced equations while it is kept, but in a new form that uses the language of the $\mathcal{L}_{ct}$ level, in the equations derived in this paper. The reduction process usually consists of two steps: a projection of the kinetic equation on the second moment, and a closure of the projected equation. All the quantities involving still the distribution function in the projected kinetic equation are expressed in the second step in terms of the second moment. It is in the second step where the line of physical arguments is broken. In principle, the reduction process can keep the physics but only if the reduced theory appears as an emerging pattern in a detailed analysis of solutions of the kinetic equations. The mathematical complexity of kinetic equations makes this type of reduction process practically unfeasible.

The governing equations on the $\mathcal{L}_{ct}$ level have been introduced above in Sections 5.2.2.1 and 5.2.2.2 as new realizations of GENERIC expressing, in terms appropriate to the level $\mathcal{L}_{ct}$, the reptation physics introduced originally on the level $\mathcal{L}_{1kt}$. To construct a realization of GENERIC means to identify the building blocks (advection, the free energy and the dissipation potential) and then arranging them in the way prescribed by the GENERIC structure. Individually, the building blocks can be, of course, searched as reduced versions of the corresponding building blocks arising on the $\mathcal{L}_{1kt}$ level. What is not allowed however, in order to keep the line of physical arguments intact, is to project the complete kinetic equation on the second moment equation and then forget all about its GENERIC structure (i.e. about its compatibility with thermodynamics) and make physically unjustified closure approximations.

We have chosen the building blocks as follows. As for the intramolecular forces, we consider local stretching and weakly nonlocal interactions involving higher order derivatives

with respect to the chain coordinate s. The stretching involves the tangent vectors to the chain and it is assumed to be of the FENE-P type. We however also consider the case of rigid local dumbbells, i.e. the case of no local stretching. The stretching is then also associated with a friction, as it is the case in the FENE-P model [Bird et al. (1980)], that is expressed in (5.14) in the term proportional to Λ^{11}. As for the intermolecular interactions, we consider the tube-like constraint introduced in the reptation theory. The constraint brings a new dissipation expressed as diffusion along the backbone of the chain (expressed in (5.14) in the term proportional to Λ^{22}). The constraint is however assumed to leave the advection unchanged. The advection in (5.1) is completely passive. We hope to discuss this last assumption, in particular in the light of the recent discussion of the active advection in Gu and Grmela (2008), in a future paper.

The question arises as to whether there are some features of the $\mathcal{L}_{1kt}$ level reptation physics that have been in Sections 5.2.2.1 and 5.2.2.2 left out or some new that have appeared.

The most important among the features that have been left out are: (A) double reptation and an anisotropic tube cross section [Des Cloizeaux (1988); McLeish (2002); Ottinger (1999)] and (B) global chain stretching [McLeish (2002); Marrucci et al. (2001); Marrucci and Grizzuti (1988); Mead and Leal (1995); Mead et al. (1995); Ottinger (1999)].

First, we comment about (A). Following Ottinger (1999), we note that to express mathematically (A) means in fact to step up on a more microscopic level on which the one chain distribution function is replaced by two chain (or better chain-tube) distribution function in its role as a state variable. On the level $\mathcal{L}_{ct}$, the corresponding more microscopic level would be a level with state variables consisting of the conformation tensor $\boldsymbol{c}$ used above and additional conformation tensors addressing tube deformations and chain-tube correlations. In this paper we do not pursue this type of extension.

As for (B), we note first that one chain distribution function is in fact a function $f(\boldsymbol{u}(s), t)$ rather than $f(\boldsymbol{u}, s, t)$ used in the reptation theory ($\boldsymbol{u}$ is the unit tangent vector to the chain, $\boldsymbol{u}(s)$ is the unit tangent vector to the chain at the point with the coordinate s on its backbone). The former one chain distribution function characterizes the chains globally, the latter locally.

It is intuitively clear that global aspects play very likely an important role in the topology of chains and consequently in the time evolution and flow properties. One way to extend the (local) reptation towards global one is to adopt some global features of chains as independent state variables. Ottinger (1999) has suggested to use the length of chains for this purpose. We could make again easily the same extension also on the level $\mathcal{L}_{ct}$.

At this point we note that there are however also other ways to extend the local formulation to a global one. Being inspired by Cahn and Hilliard (1958), we make the formulation more global by involving in the free energy derivatives with respect to s. This is what we have done in the formulation developed above. In the context of locally inextensible chains, the terms involving such derivatives have physical interpretation related to the chain curvature and bending. The reptation physics formulated above on the level $\mathcal{L}_{ct}$ includes thus some aspects of the feature (B).

The level $\mathcal{L}_{ct}$ is clearly more macroscopic than the level $\mathcal{L}_{1kt}$. If we compare them, we see a loss of details on the level $\mathcal{L}_{ct}$ (the second moment involves less information than all the moments) but we see also a gain. The gain on a more macroscopic level is always a new possibility to deal with some overall features emerging in the time evolution on the more microscopic level. What do we gain in the particular case of going from $\mathcal{L}_{1kt}$ to $\mathcal{L}_{ct}$? We suggest that the gain comes from the fact that the conformation tensor $\boldsymbol{c}$ can have different physical interpretations. In particular, it can be seen as the second moment of one dumbbell distribution function but it can also be seen as a deformation tensor used as a state variable in the network viewpoint of polymeric fluids. We are thus joining an alternative physics of polymeric fluids and we are in position to combine them and to create in this way a new contribution to physics.

The principal motivation for extending the original reptation physics introduced by de Gennes and Edwards (formulated on the level $\mathcal{L}_{1kt}$) has been an effort to produce a better fit with results of rheological observations and an effort to improve the physical picture by making it more complete and intrinsically consistent. As we shall see in the next section, predictions of the model that we have developed above on the level $\mathcal{L}_{ct}$ agree well with

results of observations. The new types of improvements with which we are able to get closer to experimental results are the following:

(a) Predictions of the nonlinear rheological behavior are improved by making a nonlinear extension of dissipation kinetic coefficients (see (5.16) and (5.17)). This appears to be true for both rigid and FENE-P local dumbbells and the kinetic coefficient arising in both the direct dissipation and the reptation dissipation (i.e. in the diffusion along the backbone of the chain). What can be the physical interpretation of this type of modifications? For example, we can argue as follows. Let ν be a new state variable describing a feature of macromolecular chains that is not described by the conformation tensor and that is expected to be of importance (e.g. a global feature of the chain). Depending on the physical interpretation of ν, it is then argued that the dissipation kinetic coefficients depend in a particular way on ν. Since ν is a state variable, the extended theory has to involve an equation governing its time evolution. We now assume that ν evolves faster than other state variables and ν appearing in the kinetic coefficients can be thus replaced by ν_{stat} that is a solution of the equation governing the time evolution of ν in which $\partial\nu/\partial t = 0$. This stationary solution is, in general, a nonlinear function of the remaining state variables. Consequently, the kinetic coefficients become in this way nonlinearly dependent on the state variables. In this paper we do not attempt to identify an appropriate new state variables.

(b) The terms in the free energy involving derivatives with respect to s (i.e. the expression of nonlocality of reptation in our formulation) appear to influence (in a positive way) mainly the linear viscoelastic behavior especially G'' in high frequencies.

Finally, we make an observation about solutions of the governing equations. Predictions of the model (that can be compared with results of rheological and thermodynamic observations) can be extracted by solving its governing equations. For some types of observations (as for example for many observations made in equilibrium thermodynamics), it is enough to extract some qualitative properties of solutions. This can often be done analytically (as it is for example the case with the governing equations introduced in this paper). To connect with rheological observations requires however a detailed knowledge of solutions that can only be

obtained by solving the governing equations numerically. How do we approach the problem of finding numerical solutions? Essentially, we can follow two routs. On the first route we regard it as a technical problem solvable by an available software with a possible assistance of specialists. On the second route, we regard it as a physical problem. The adaptation of the governing equations (their discretization) that is needed to bring computers into the process is regarded as a reduction to a more macroscopic level. In other words, the discrete version of the governing equations is required to express the same type of physics as the original equations. This is then the best guarantee that the numerical solutions are indeed good approximations of solutions to the original equations. This viewpoint of the inevitable final stage of modeling, namely of the process of finding numerical solutions of the governing equations, is thus always a motivation to formulate more macroscopic versions of the models. In our case, the level $\mathcal{L}_{ct}$ can indeed be seen as an intermediate level on the way to solve the governing equations formulated on the level $\mathcal{L}_{1kt}$.

5.3 Results and discussion

Since we have constructed the governing equations (5.1) in the GENERIC framework, we know that their solutions agree with some important experimental observations. Even without inserting into (5.1) a specific free energy Φ, we know that its solutions have the following properties:

(i) The total momentum $\int d\boldsymbol{r}\boldsymbol{u}(\boldsymbol{r})$ is conserved.

(ii) $\frac{d\Phi}{dt} \leq 0$ which means that in the course of the time evolution the fluid is brought into the equilibrium state at which the free energy Φ reaches its minimum. The fundamental thermodynamic relation at the equilibrium is given by the free energy evaluated at the equilibrium states.

Now, we turn our attention to rheological measurements in which the flow, described by $\boldsymbol{u}$, is imposed from outside. This means that we omit the first equation in (5.1) and the flow $\boldsymbol{u}$ appearing in the second equation is regarded as a parameter.

The calculations involved in making the second equation in (5.1) explicit are straightforward and completely standard:

$$\frac{\partial \boldsymbol{c}}{\partial t} = \left(\frac{\partial \boldsymbol{c}}{\partial t}\right)_{nondissipative} + \left(\frac{\partial \boldsymbol{c}}{\partial t}\right)_{dissipative} \tag{5.19}$$

The nondissipative part $(\partial \boldsymbol{c}/\partial t)_{reversible}$ is written explicitly already in (5.1)

$$\left(\frac{\partial \boldsymbol{c}}{\partial t}\right)_{nondissipative} = -\frac{1}{2}\left(\boldsymbol{\Omega}\cdot\boldsymbol{c} - \boldsymbol{c}\cdot\boldsymbol{\Omega}\right) + \frac{1}{2}\left(\dot{\gamma}\cdot\boldsymbol{c} + \boldsymbol{c}\cdot\dot{\gamma}\right) \tag{5.20}$$

(recall that $\Phi_{\boldsymbol{u}}$ is the velocity field). The dissipative part (5.15) is made explicit if we insert into (5.15) the thermodynamic potential Ξ given in (5.14), (5.16), and (5.17):

$$\begin{aligned}
\left(\frac{\partial \boldsymbol{c}}{\partial t}\right)_{dissipative} &= -\frac{\partial \Xi}{\partial \Phi_c} + \left(\frac{\partial \Xi}{\partial (\Phi_{\boldsymbol{c}})_s}\right)_s \\
&= -4\Lambda_0^{11}\left[\kappa_1\left(\boldsymbol{c}\cdot\Phi_{\boldsymbol{c}} + \Phi_{\boldsymbol{c}}\cdot\boldsymbol{c}\right) + 2\,\kappa_2\,\boldsymbol{c}\cdot\Phi_{\boldsymbol{c}}\cdot\boldsymbol{c}\right] \\
&\quad +4\,\Lambda_0^{22}\left(1 + \widetilde{\Lambda_0^{22}}\left(tr\boldsymbol{c} - tr\boldsymbol{c}_{eq}\right)^2\right) \\
&\quad \left[\kappa_1\left(\boldsymbol{c}\cdot(\Phi_{\boldsymbol{c}})_s + (\Phi_{\boldsymbol{c}})_s\cdot\boldsymbol{c}\right) + 2\,\kappa_2\left(\boldsymbol{c}\cdot(\Phi_{\boldsymbol{c}})_s\cdot\boldsymbol{c}\right)\right]_s
\end{aligned} \tag{5.21}$$

where

$$\Phi_{\boldsymbol{c}} = \frac{1}{2}nk_BT\left(\frac{f}{1-tr\boldsymbol{c}}\boldsymbol{\delta} - \boldsymbol{c}^{-1}\right) - 2\,K\boldsymbol{c}_{ss} \tag{5.22}$$

By inserting (5.22) into (5.11) we obtain

$$\begin{aligned}
\boldsymbol{\sigma} &= -2\int_{-1}^{1} ds\left(\boldsymbol{c}\cdot\frac{\partial\Phi}{\partial\boldsymbol{c}} - \boldsymbol{c}\cdot\left(\frac{\partial\Phi}{\partial\boldsymbol{c}_s}\right)_s\right) \\
&= -nk_BT\int_{-1}^{1}\left(\frac{f}{1-tr\boldsymbol{c}}\boldsymbol{c} - \boldsymbol{\delta}\right)ds + 2\,K\int_{-1}^{1}\left(\boldsymbol{c}\cdot\boldsymbol{c}_{ss} + \boldsymbol{c}_{ss}\cdot\boldsymbol{c}\right)ds
\end{aligned} \tag{5.23}$$

After making the modifications (described in Sections 5.2.1 and 5.2.1) needed to transform the governing equations from the FENE-P local dumbbells to the case of rigid local dumbbells, the same type of calculation that lead us to (5.21) and (5.23) will lead us to equations describing the time evolution of chains composed of locally rigid dumbbells. We shall not write them explicitly.

The imposed flows are considered to be steady, start up, and oscillatory shear flows for which $u_1 = \dot{\gamma}_{(t)} x_2$, $u_2 = u_3 = 0$. The absolute value of $\dot{\gamma}_{(t)}$ is called a shear rate. We use the standard notation for the viscosity coefficient η and the first and the second normal stress difference coefficients Ψ_1 and Ψ_2. Our results will include both linear and nonlinear rheology.

From the mathematical point of view, Eqs.(5.19),(5.20), and (5.21) represent a system of six partial differential equations for six unknown functions $c_{ij}; i \leq j, = 1,2,3$ of two independent variables s and t, $-1 \leq s \leq 1$, $t \geq 0$. The equations involve first order derivative in t and up to fourth order derivatives in s. The initial conditions are the equilibrium solutions (i.e. solutions of Eq.(5.1) in the absence of $\boldsymbol{u}$) that are solutions to $\Phi_c = 0$. As for the boundary conditions, we use the symmetry involved in the problem and reduce the domain of s to the interval $0 \leq s < 1$. Moreover, we use:

$$\mathbf{c}(t,1) = \mathbf{c}_{\mathbf{ss}}(t,1) = \frac{1}{3+f}\,\delta \quad ; \quad \mathbf{c}_{\mathbf{s}}(t,0) = \mathbf{c}_{\mathbf{sss}}(t,0) = 0 \tag{5.24}$$

By $\mathbf{c}_{\mathbf{ss}}$ and $\mathbf{c}_{\mathbf{sss}}$ we denote $\frac{\partial^2 \mathbf{c}}{\partial s^2}$ and $\frac{\partial^3 \mathbf{c}}{\partial s^3}$ respectively. We solve Eq.(5.19),(5.20),(5.21)) numerically by using the MATHEMATICA software package [Wolfram (1991)].

If the fluid under consideration is submitted to oscillatory imposed flows (i.e. the shear rate is given by $\gamma(t) = \gamma_0 \, sin\, \omega t$, where ω is the angular frequency), we limit ourselves only to linear (in γ_0) responses. In order to arrive at the linearized governing equations, we assume that the conformation tensor $\boldsymbol{c}$ has the form:

$$\mathbf{c} = \frac{1}{f}\,\delta + \gamma_0\,\omega\,\mathbf{a}\,cos\,\omega t + \gamma_0\,\omega\,\mathbf{b}\,sin\,\omega t \tag{5.25}$$

where $\mathbf{a}$ and $\mathbf{b}$ are unknown tensors. Substituting Eq.(5.25) to (5.19) and (5.23), we obtain (keeping only the terms up to the first order in $\dot{\gamma}_0$)

$$\begin{aligned} \omega\, a_{12} &= 4nk_BT(\kappa_1 f + \kappa_2)\left(\Lambda_0^{11}\, b_{12} - \Lambda_0^{22}\, b_{ss_{12}}\right) \\ &\quad - \frac{16K}{f^2}(\kappa_1 f + \kappa_2)\left(\Lambda_0^{11}\, b_{ss_{12}} - \Lambda_0^{22}\, b_{ssss_{12}}\right) \end{aligned} \tag{5.26}$$

$$\begin{aligned} \omega\, b_{12} &= \frac{1}{f} - 4nk_BT(\kappa_1 f + \kappa_2)\left(\Lambda_0^{11}\, a_{12} - \Lambda_0^{22}\, a_{ss_{12}}\right) \\ &\quad + \frac{16K}{f^2}(\kappa_1 f + \kappa_2)\left(\Lambda_0^{11}\, a_{ss_{12}} - \Lambda_0^{22}\, a_{ssss_{12}}\right) \end{aligned} \tag{5.27}$$

$$\sigma_{12} = \frac{1}{f}\gamma_0\omega\left[(nk_BTf^2a_{12} - 4Ka_{ss_{12}})cos\,\omega t + (nk_BTf^2b_{12} - 4Kb_{ss_{12}})sin\,\omega t\right] \tag{5.28}$$

If we use the form $\sigma(t) = \gamma_0\,(G'\,sin\,\omega t + G''\,cos\,\omega t)$, where G' and G'' are the storage and loss moduli, respectively [4]. From the stress tensor (5.28), we obtain:

$$G' = nk_BTf\omega b_{12} - \frac{4K}{f}\omega b_{ss_{12}} \tag{5.29}$$

$$G'' = nk_BTf\omega a_{12} - \frac{4K}{f}\omega a_{ss_{12}} \tag{5.30}$$

5.3.1 Model predictions and comparison with experimental data

It is useful to regard rheological models as an input-output systems. The input is the microscopic or mesoscopic physics used in its formulation, the outputs are predictions of the observed rheological behavior. Both input and output have many components. In the input they are the particular physical features involved (e.g. the local extensibility, the constraints, etc.) and in the output they are the features of the observed behavior (e.g. the length of the plateau in the curve η versus $\dot{\gamma}$, the slope of this curve as $\dot{\gamma} \to \infty$, etc.). The passage between the input and the output is made by solving the (in general very nonlinear) governing equations of the model. An understanding gained by the model is often measured by the success in establishing direct passages between individual components of the input and individual components of the output. For example, as we shall see below, the nonlinear dependence of the dissipative kinetic coefficients is seen to influence mainly the length of the plateau, the nonlocal intramolecular interactions influence mainly the linear rheological behavior, etc.). A word of caution is in order. The input-output passage involves solutions of complex nonlinear equations. In general, the input-output relation is very complex and simple passages between single components of the input and the output do not exist. Having this in mind, we proceed to investigate the input-output passage of the model presented in this paper.

Since the overall qualitative predictions of the two models involving locally extensible

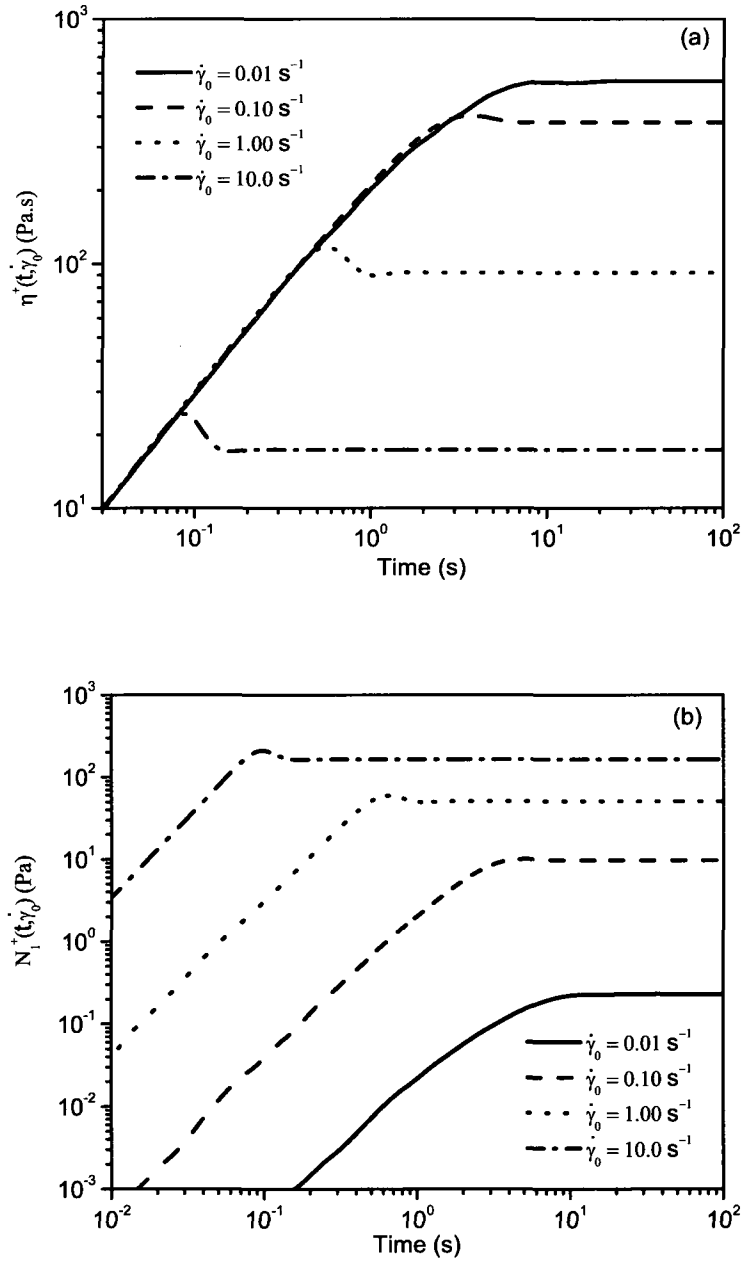

Figure 5.1: Effect of the shear rate on the stress growth (a) viscosity and (b) first normal stress.

and inextensible chains are the same, we show them therefore only for the locally extensible (FENE-P) chains. As for the locally rigid chains, we report the predictions in the section in which we make the comparison with experimental data. In the following calculations of model predictions, the model parameters (in appropriate SI units) are chosen as follows: $\Lambda_0^{11} = 5 \times 10^{-6}, \Lambda_0^{22} = 5 \times 10^{-5}, \widetilde{\Lambda_0^{22}} = 6 \times 10^5, b = 20, K = 1000, \kappa_1 = 1$ and $\kappa_2 = 0$. Prediction of transient material functions is made at $\dot{\gamma} = 0.1 s^{-1}$.

5.3.1.1 Effects of the shear rate on transient material functions

Figures 5.1(a) and 5.1(b) show the effect of the shear rate on the transient material functions, η^+ and N_1^+ respectively. For the small shear rate, the viscosity reaches its steady state value monotonically. As the shear rate increases, the curve of viscosity versus time shows an overshoot. The size of this overshoot increases and the time at which the overshoot appears decreases when shear rate increases. Similar results are obtained for the first normal stress difference (see Figure 5.1(b)). The overall qualitative features of the curves are essentially the same as the ones seen in the experimental and theoretical data collected for polymer melts and solutions [Bird et al. (1987a); Eslami et al. (2004)].

5.3.1.2 Effects of mobility coefficients on material functions

Figures 5.2(a) and 5.2(b) show the influence of the local mobility coefficient Λ_0^{11} on the transient material functions η^+ and N_1^+ respectively. As seen on Figure 5.2(a), both the stationary value and the size of overshoot increase with decreasing Λ_0^{11}. Figure 5.2(b) indicates that similarly as the viscosity coefficient, the stationary values of N_1^+ increase with decreasing Λ_0^{11}.

Figures 5.3(a) and 5.3(b) present the influence of the reptation mobility coefficient Λ_0^{22}, which is related to the diffusion process along the backbone of the chain, on the transient rheological properties. Both stationary value and size of overshoot appear to be more sensitive to changes in Λ_0^{22} than to changes in Λ_0^{11}. Since Λ_0^{22} is the kinetic coefficient associated with the reptation, we thus see that the reptation influences the transient material functions more

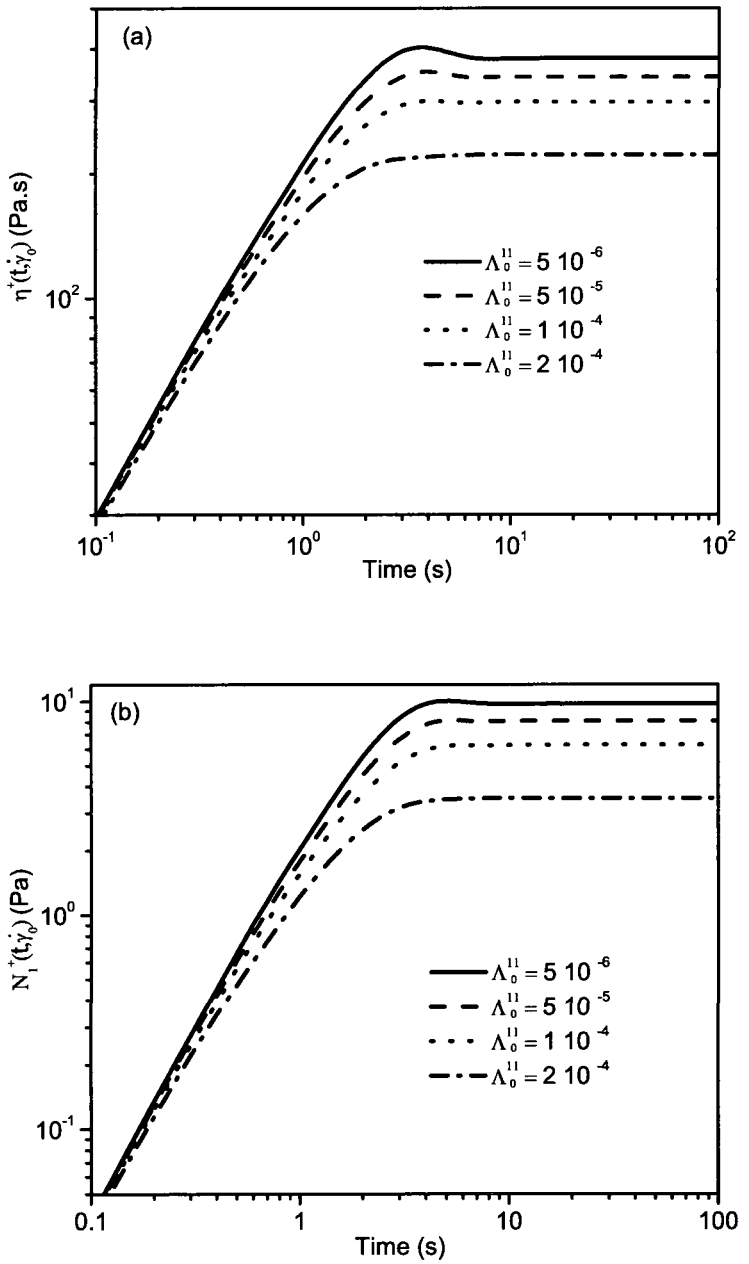

Figure 5.2: Effect of the local mobility coefficient Λ_0^{11} on the stress growth (a) viscosity and (b) first normal stress.

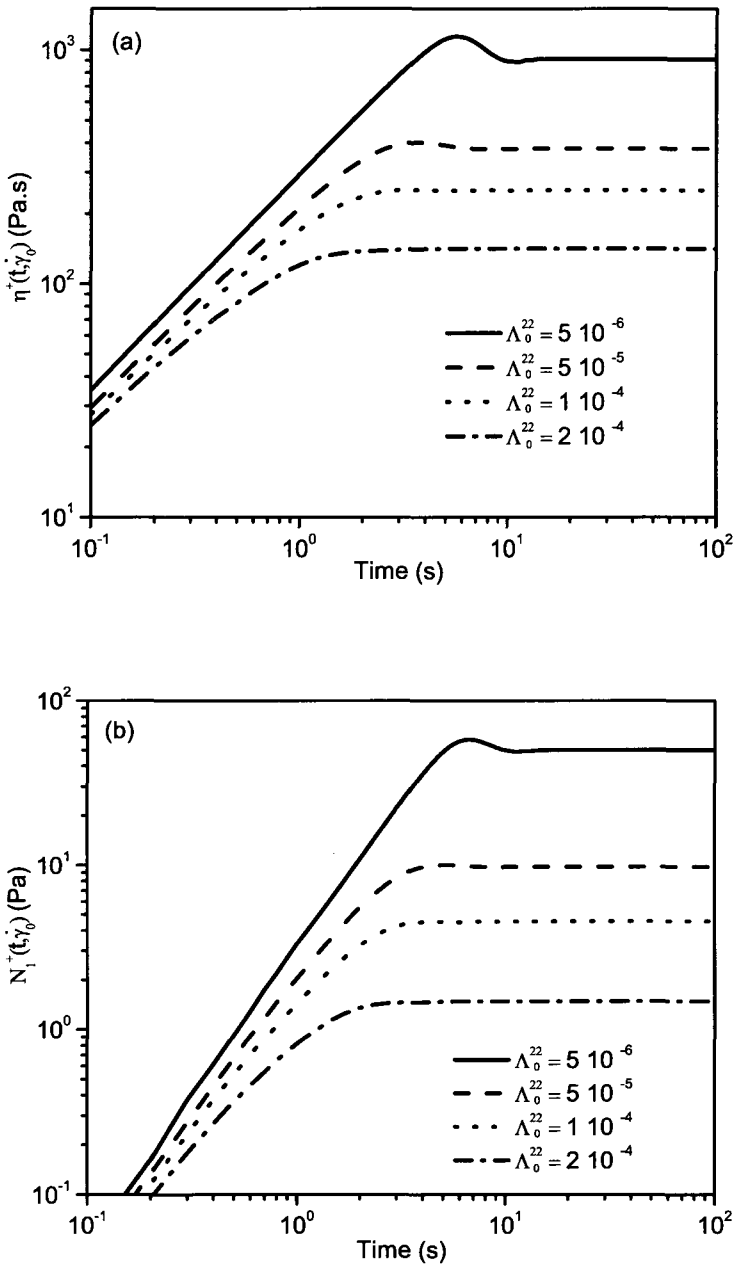

Figure 5.3: Effect of the reptation mobility coefficient Λ_0^{22} on the stress growth (a) viscosity and (b) first normal stress.

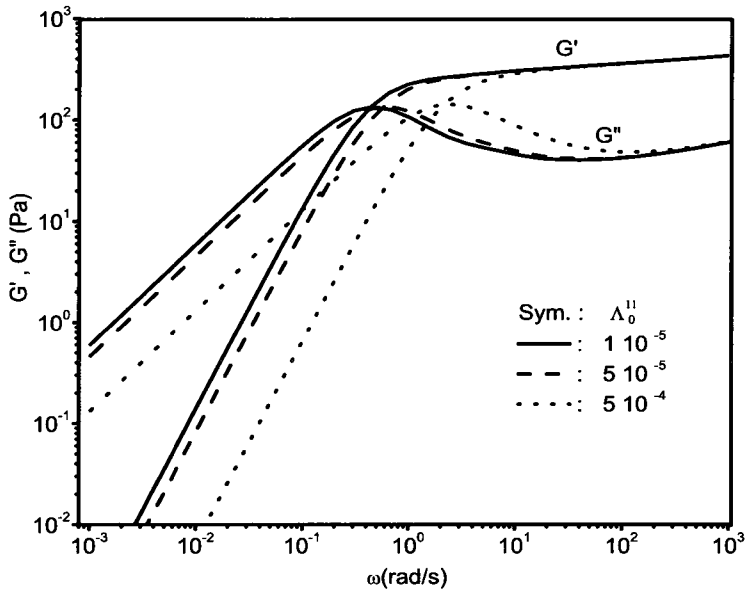

Figure 5.4: Effects of the local mobility coefficient Λ_0^{11} on the storage and loss modulus.

than the local dissipation. Among the material functions, we see that the overshoots in the first normal stress difference N_1^+ are less sensitive to the changes in Λ_0^{22} than the overshoots in η^+ (the size of overshoots becomes visible more clearly if one draws the curves in the normalized form). The overshoot in N_1^+ reflecting changes in Λ_0^{22} are however still clearly visible on Figure 5.3(b). This is the place where the reptation plays the most significant role in predictions of transient material functions.

The effect of the mobility coefficient Λ_0^{11} on the storage and loss moduli are displayed on Figure 5.4. The results show that the cross over point (i.e. the point where $G' = G''$) is shifted to higher frequency with increasing Λ_0^{11}. The results also show that with increasing Λ_0^{11} the storage and the loss modulus decreases at low frequencies while at higher frequencies the loss modulus increases and the storage modulus remains almost unchanged. These observations are very useful for finding the model parameters.

Figure 5.5 shows the effect of the reptation mobility coefficient Λ_0^{22} on the storage and

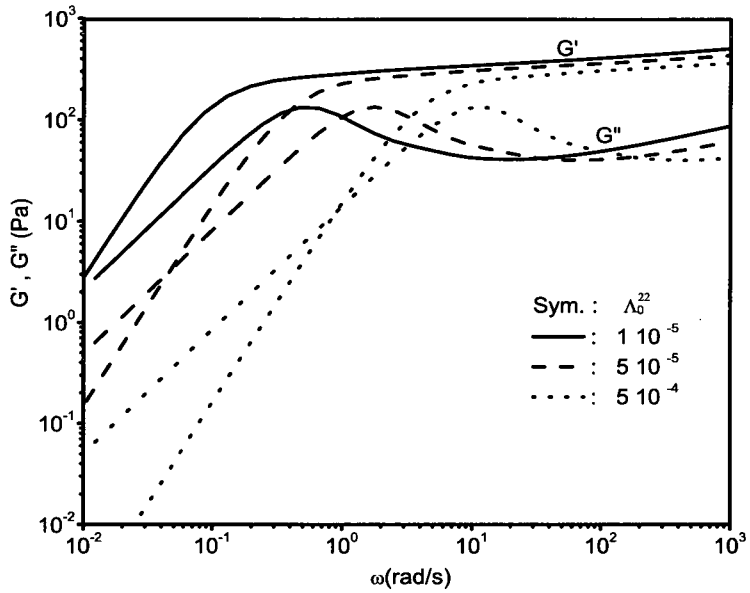

Figure 5.5: Effects of the reptation mobility coefficient Λ_0^{22} on the storage and loss modulus

loss moduli. Although the trends are qualitatively the same as seen on Figure 5.4, the overall features of the curves are more sensitive to changes in Λ_0^{22} than to changes in Λ_0^{11}. For example, the cross over point is shifted faster to higher frequencies with changes in Λ_0^{22} than with changes in Λ_0^{11}. Moreover, at high frequencies the storage modulus slightly decreases with increasing Λ_0^{22} while its value remains almost unchanged when Λ_0^{11} changes. These new features which come from the reptation type dissipation are also very useful for fitting model predictions with experimental data.

5.3.1.3 Sensitivity of the model to other parameters

Figure 5.6 shows the effect of the parameter K (i.e. the bending modulus in the case of locally inextensible chains) on the storage and loss modulus. The storage modulus slightly increases with increasing K at high frequency while its value remains almost unchanged at low frequency range. As for the loss modulus, changes in K do not change its value at low

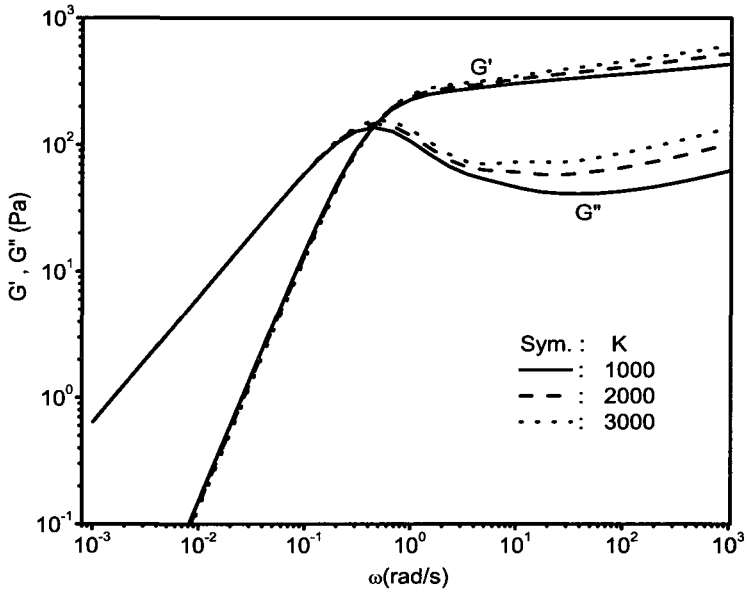

Figure 5.6: Effects of the parameter K on the storage and loss modulus.

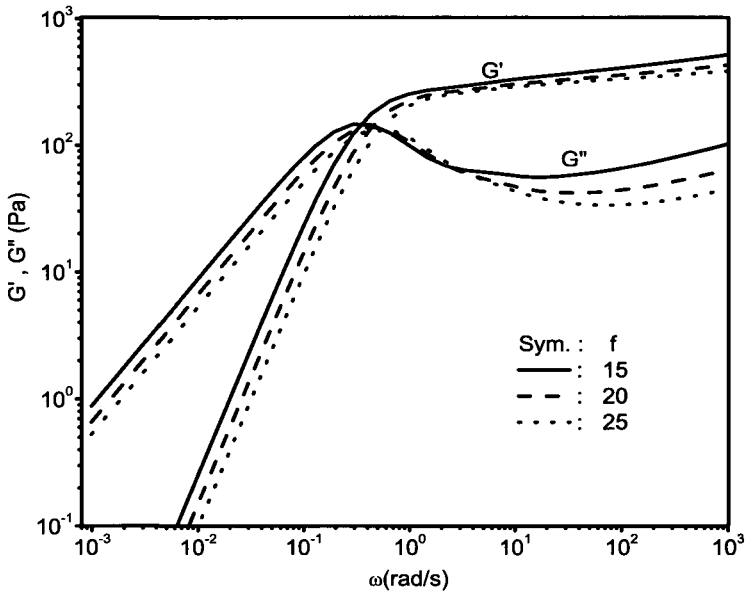

Figure 5.7: Effects of the parameter f on the storage and loss modulus

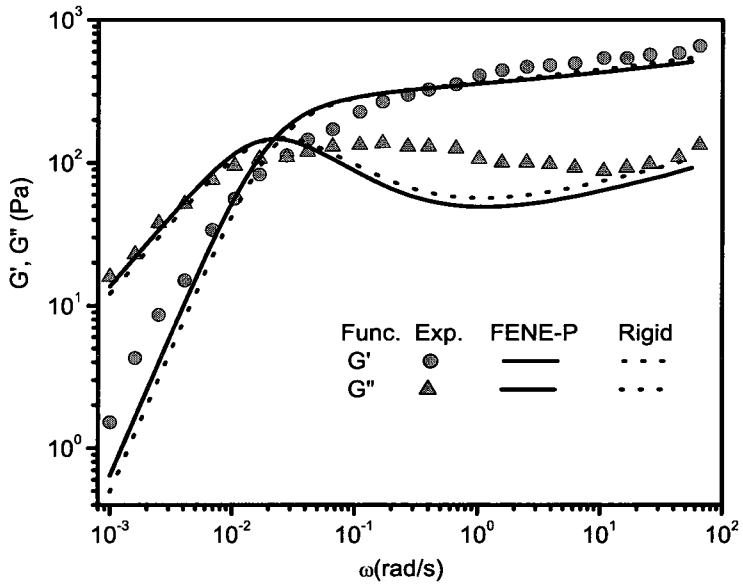

Figure 5.8: Model predictions and comparison with experimental data in small angle oscillatory shear flows: the storage and the loss modulus.

frequency but the effect at high frequencies is dramatic. In fact, this is the main reason why we have included this kind of energy in our model.

Figure 5.7 shows the effect of the parameter f on the storage and loss modulus. The results show that both the storage and the loss modulus increases with decreasing f. The cross over point also slightly shifts to higher frequency with increasing f.

5.3.1.4 Comparison with experimental data

Model predictions are compared with two sets of experimental data taken from Pattamaprom and Larson (2001) for both linear and nonlinear rheological functions. As we mentioned earlier, we make the comparison with predictions of both locally rigid and FENE-P dumbbell models.

For the first set of experimental data (Figures 5.8 and 5.9), the model parameters for

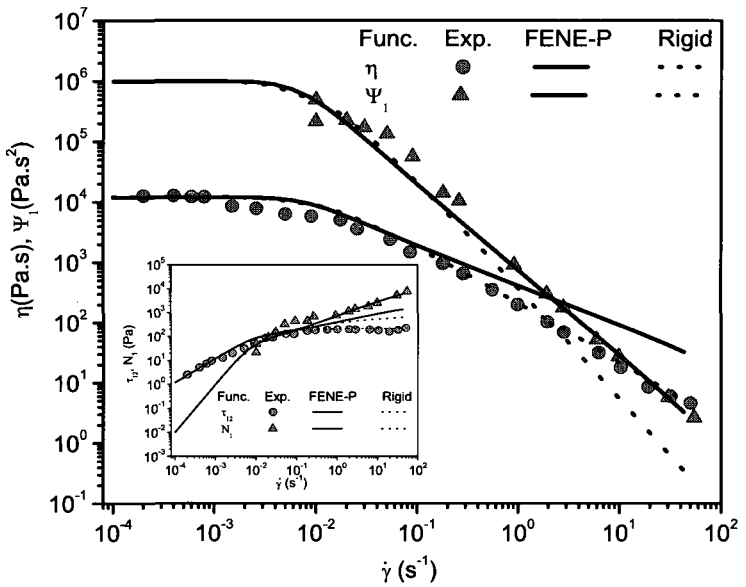

Figure 5.9: Model predictions and comparison with experimental data in steady shear flow.

locally FENE-P dumbbell model are chosen to be (in appropriate SI units): $\Lambda_0^{11} = 5 \times 10^{-6}, \Lambda_0^{22} = 5 \times 10^{-7}, \widetilde{\Lambda_0^{22}} = 4 \times 10^5, b = 20, K = 1000, \kappa_1 = 1$ and $\kappa_2 = 0$ and for locally rigid dumbbell model are chosen to be: $\Lambda_0^{11} = 2.3 \times 10^{-5}, \Lambda_0^{22} = 9.5 \times 10^{-6}, \widetilde{\Lambda_0^{22}} = 5 \times 10^4, K = 30, \kappa_1 = 1$ and $\kappa_2 = 0$. As for the second set of experimental data (Figures 5.10-5.13), the values of model parameters for locally FENE-P dumbbell model are also chosen to be: $\Lambda_0^{11} = 4 \times 10^{-4}, \Lambda_0^{22} = 5 \times 10^{-5}, \widetilde{\Lambda_0^{22}} = 10^4, b = 5, K = 200, \kappa_1 = 1$ and $\kappa_2 = 0$ and for locally rigid dumbbell model are chosen to be: $\Lambda_0^{11} = 1.5 \times 10^{-4}, \Lambda_0^{22} = 3.5 \times 10^{-4}, \widetilde{\Lambda_0^{22}} = 10^2, K = 150, \kappa_1 = 1$ and $\kappa_2 = 0$

Figures 5.8 and 5.10 show that at low frequencies the model predictions are in good agreement with the experimental data for both G' and G'' while at high frequencies the agreement is less satisfactory especially for G''. The predictions of the locally rigid dumbbell model seem to be better at high frequency. The local rigidity appears thus to be a better hypothesis than the local extensibility if the focus is put on high frequency.

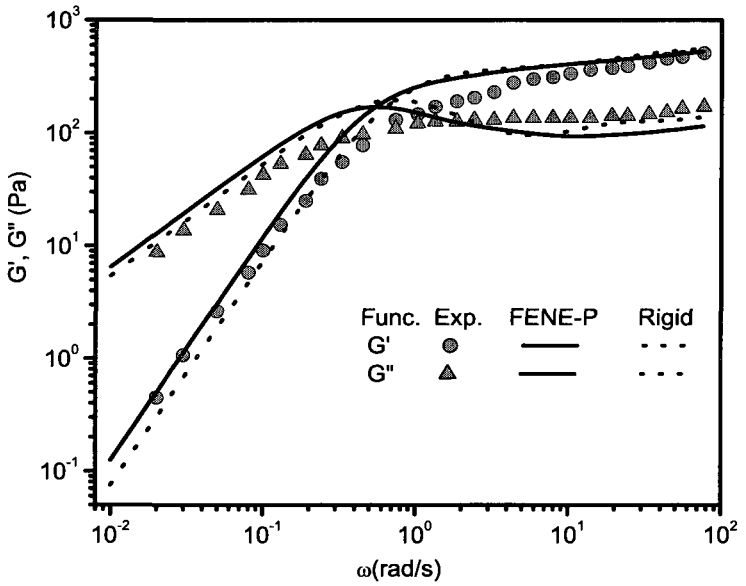

Figure 5.10: Model predictions and comparison with experimental data in small angle oscillatory shear flows: the storage and the loss modulus.

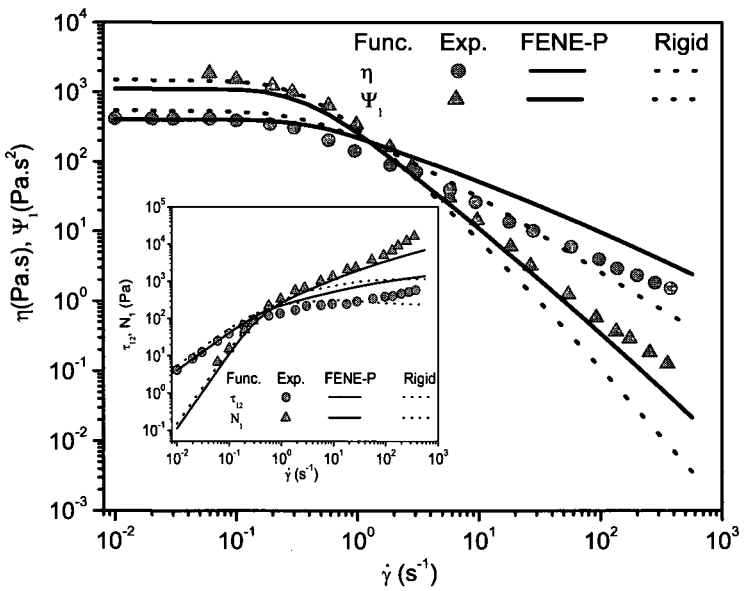

Figure 5.11: Model predictions and comparison with experimental data in steady shear flow.

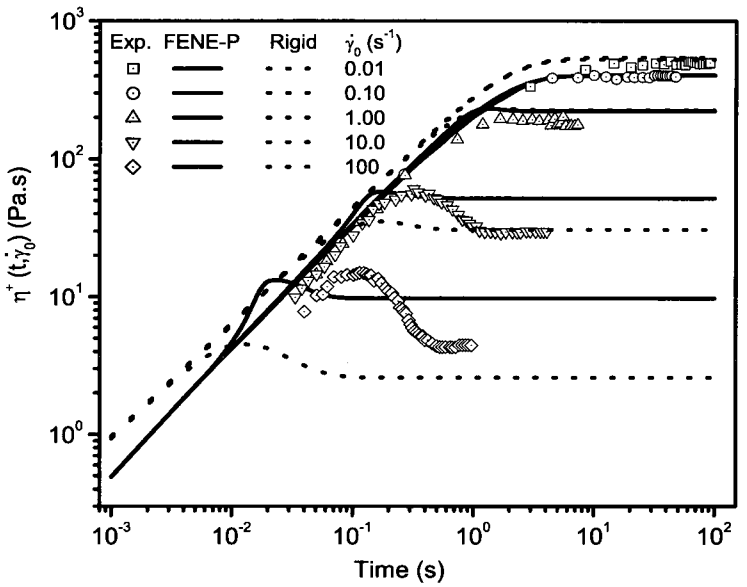

Figure 5.12: Model predictions and comparison with experimental data in transient shear flows.

Figures 5.9 and 5.11 show also a good agreement of the model predictions with the steady experimental data. The agreement is less good for the viscosity in the case of FENE-P dumbbells at hight shear rates, and for the first normal stress difference in the case of locally rigid dumbbells. For the sake of clarity, we present on Figures 5.9 and 5.11 all the data concerning the viscosity, the first normal stress differences. As one can see on these figures (in particular on Figure 5.11) the locally rigid dumbbell model predicts more shear thinning (especially for Ψ_1). We expect that an explicit consideration of the global stretching would bring the predictions closer to the observed behavior.

Figures 5.12 and 5.13 also show good agreement of the model predictions with the transient experimental data at low shear rate and less satisfactory agreement at high shear rate. FENE-P model predictions are in better agreements with experimental data then rigid dumbbell model.

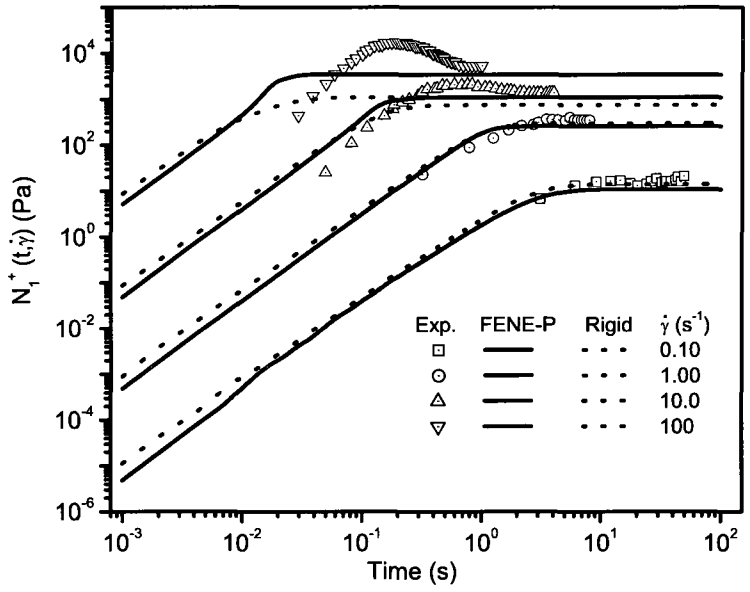

Figure 5.13: Model predictions and comparison with experimental data in transient shear flow.

In general, the reasons for less satisfactory agreement (especially at high frequencies and high shear rates) may be partially due to the fact that we do not consider in our model the influence of the tube-like constraint on the advection and the influence of the global stretching. We hope to address these two points in the future.

5.4 Concluding remarks

Rheological models formulated on the level $\mathcal{L}_{ct}$ (i.e. with the conformation tensor chosen to characterize the microstructure) are very popular among rheologists because their governing equations can be easily solved. On the other hand, the most popular language in terms of which the physics serving as an input of the model is expressed is the one used on the level $\mathcal{L}_{1kt}$ (i.e. with the one particle configuration space distribution serving as the morphological state variable). The passage from the kinetic equation in which the physics is expressed to

the equation that is actually solved involves a projection (the conformation tensor is seen as the second moment of the distribution function) and closure approximations needed in the projected equation to transform it into an equation involving only the second moment. The original physical insight is seriously blurred in the passage mainly because of the arbitrariness in the choice of the closure approximations.

In this paper we focus on the physical insight that has been collected in the reptation theory on the $\mathcal{L}_{1kt}$ level. We translate a part of it from the language used on the $\mathcal{L}_{1kt}$ level to the language used on the $\mathcal{L}_{ct}$ level and take it then as a basis for writing governing equations on the $\mathcal{L}_{ct}$ level. These equations become thus directly supported by the reptation physics (but formulated in another language) as the kinetic equations are in the original reptation theory. The direct physical interpretation as well as the mathematical simplicity of the governing equations are essential in the pursuit of our eventual goal to involve the reptation theory in the rheological model of nanocomposites developed in Eslami et al. (2007). The complexity brought by the presence of the nano charge makes the kinetic theory based rheological models practically unusable.

Two comments about the reptation physics expressed in this paper in terms of the conformation tensors are in order. The comments are particularly relevant if we try to compare interpretations of rheological predictions implied by models on both levels. In the first comment we note that not all the reptation physics developed originally on the level of kinetic theory has been translated in this paper to the level $\mathcal{L}_{ct}$. We discuss this in some detail in Section 5.2.2.3. We recall that beside leaving off some aspects of the reptation physics introduced on the level $\mathcal{L}_{1kt}$, we have also introduced some new ones. In the second comment we note that the exact meaning of the physics changes in the translation. We illustrate it on the following example. The local inextensibility means in kinetic theory that the tangent vectors to the chain are all vectors of constant length. The only way we can express the local inextensibility on the level $\mathcal{L}_{ct}$ is by saying that the trace of all the conformation tensors is a constant. But this, if we see it on the level of kinetic theory, is the statement that the length of the tangent vector is constant in average (i.e. fluctuations are allowed).

We recall the sequence of steps leading to the model. The point of departure is the rigid dumbbell model (or alternatively the FENE-P model) in which the conformation tensor $\boldsymbol{c}$ serves as the structural state variable. Next, we pass from an isolated rigid (or FENE-P dumbbell) to a local rigid (or FENE-P dumbbell) imbedded in the chain. In terms of the state variables, we thus pass from $\boldsymbol{c}$ to $\boldsymbol{c}(s)$, where $-1 \leq s \leq 1$ is the coordinate along the backbone of the chain. Following the GENERIC framework, the rheological model is constructed by specifying kinematics of $\boldsymbol{c}(s)$, free energy, and dissipation. The kinematics of $\boldsymbol{c}(s)$ is the same as the kinematics of $\boldsymbol{c}$. The rigid dumbbell (or FENE-P) free energy of isolated dumbbells is naturally extended to local dumbbells by adding a term depending on the derivative of $\boldsymbol{c}(s)$ with respect to s. From the physical point of view, such term expresses, in the case of locally rigid dumbbells, the energy involved in bending the chain. The dissipation is driven in the GENERIC framework (as well as in the framework of classical nonequilibrium thermodynamics) by dissipative thermodynamic forces. In the case of isolated dumbbells, there is one such force, namely the derivative of the free energy with respect to the conformation tensor. Similarly as in the specification of the free energy, we can naturally introduce in the case of chains an additional thermodynamic force by simply differentiating the classical rigid dumbbell (or FENE-P) force with respect to chain coordinate s. The new dissipative mechanism arising in this way has the physical interpretation of reptation, i.e. diffusion along the backbone of the chain.

Among the questions that remain in this paper unanswered we mention in particular two. The first one is of what are the additional state variable (i.e. in addition to the conformation tensor) that would allow us to formulate on the level $\mathcal{L}_{ct}$ the reptation physics (developed on the level of kinetic theory) more accurately. The second question is how to replace the passive advection of chains with a more realistic active advection (see [Gu and Grmela (2008)]).

Acknowledgements

The authors acknowledge the financial support provided by the Natural Sciences and Engineering Research Council (NSERC) of Canada.

References

1. Beris AN, BJ Edwards (1994) Thermodynamics of flowing systems. 1 st ed., Oxford University Press, New York.

2. Beris AN, BJ Edwards (1990) Poisson bracket formulation of viscoelastic flow equations of differential type: A unified approach. J. Rheol. 34:55-78.

3. Bird RB, Dotson PJ , Johnson NL (1980) Polymer solution rheology based on a finitely extensible bead-spring chain model. J. Non-Newtonian Fluid Mech. 7:213.

4. Bird RB, Armstrong RC, Hassager O, (1987) Dynamics of polymeric fluids. Vol. 1, Wiley, New York.

5. Cahn JW, Hilliard JE (1958) Free energy of a nonuniform system. I. Interfacial free energy. Journal of Chemical Physics 28:258-267.

6. De Gennes PG (1971) Reptation of a polymer chain in the presence of fixed obstacles. Journal of Chemical Physics 55:572-579.

7. Des Cloizeaux J (1988) Double reptation vs simple reptation in polymer melts. Europhys. Lett. 5:437-442.

8. Edwards BJ, Dressler M, Grmela M, Ait-Kadi A(2003) Rheological models with microstructural constraints. Rheol. Acta 42, 64-72.

9. Doi M, Edwards SF (1986) The Theory of Polymer Dynamics. Oxford University Press, New York.

10. Edwards SF, (1976) Configurations and dynamics of the polymer chain. Molecular Fluids edited by R. Balin and G. Weill (London: Gordon and Breach) 151-208.

11. Eslami H, Ramazani A, Khonakdar HA (2004) Predictions of some internal microstructural models for polymer melts and solutions in shear and elongational flows. Macromol. Theory Simul. 13:655-664.

12. Eslami H, Grmela M, Bousmina M (2007) A mesoscopic rheological model of polymer/layered silicate nanocomposites. J. Rheol 51:1189-1222.

13. Fang J, Kroger M, Ottinger HC (2000) A thermodynamically admissible reptation model for fast flows of entangled polymers. II. Model predictions for shear and extensional flows. J. Rheol. 44:1293-1317.

14. Grmela M (1984) Particle and bracket formulations of kinetic equations. Contemp. Math. 28:125-132.

15. Grmela M (1985) Stress tensor in generalized hydrodynamics. Phys. Letters A 111:41-44.

16. Grmela M (1986) Bracket formulation of diffusion-convection equations. Physica D 21:177-212.

17. Grmela M (1990) Thermodynamic and rheological modeling: polymeric liquid crystals. 55-81, in Polymer Rheology and Processing, Collyer AA, Utracki LA (eds) Elsevier.

18. Grmela M (1991) Mesoscopic dynamic and thermodynamic: Application to polymer fluids. Lecture Notes in Physics 381:99-126.

19. Grmela M (2002) Reciprocity relations in thermodynamics: Physica A 309:304-328.

20. Grmela M, Ottinger HC (1997) Dynamics and thermodynamics of complex fluids. I. Development of a general formalism. Phys. Rev. E. 55:6620-6632.

21. Gu JF, Grmela M GENERIC model of active advection. J. NonNewtonian Fluid Mech. (in press) doi: 10.1016/j.jnnfm. 2007.05.001

22. Kindt P and Briels WJ (2007) A single particle model to simulate dynamics of entangled polymer melts. J. Chem. Phys. 127:134901-1-12.

23. Kroger M, Hess S (1993) Viscoelesticity of polymeric melts and concentrated solutions, the effect of flow-induced alignment of chain ends. Physica A 195, 336-353.

24. Likhtman AE, McLeish TCB (2002) Quantitative theory for linear dynamics of linear entangled polymers. Macromolecules 35:6332-6343.

25. Leygue A, Bailly C, Keunings R (2006) A tube-based constitutive equation for polydisperse entangled linear polymers. J. Non-Newtonian Fluid Mech. 136:1-16.

26. Leygue A, Bailly C, Keunings R (2006) A differential tube-based model for predicting the linear viscoelastic moduli of polydisperse entangled linear polymers. J. Non-Newtonian Fluid Mech. 133:28-34.

27. Leygue A, Beris AN, Keunings R (2001) A constitutive equation for entangled linear polymers inspired by reptation theory and consistent with non-equilibrium thermodynamics. J. Non-Newtonian Fluid Mech. 101:95-111.

28. McLeish TCB (2002) Tube theory of entangled polymer dynamics. Advances in Physics. 51:1379-1527.

29. Marrucci G, Greco F, Lanniruberto G (2001) Integral and differential constitutive equations for entangled polymers with simple versions of CCR and force balance on entanglements. Rheol Acta 40:98-103.

30. Marrucci G, Grizzuti N (1988) Fast flow of concentrated polymers: Predictions of the tube model on chain stretching. Gazz. Chim. Ital. 118:179-185.

31. Mead DW, Leal LG (1995) The reptation model with segmental stretch I. Basic equations and general properties. Rheol. Acta 34:339-359.

32. Mead DW, Yavich D, Leal LG (1995) The reptation model with segmental stretch II. Steady flow properties. Rheol. Acta 34:360-383.

33. Ottinger HC, Grmela M (1997) Dynamics and thermodynamics of complex fluids. II. Illustrations of a general formalism. Phys. Rev. E. 56:6633-6655.

34. Ottinger HC (1999) A thermodynamically admissible reptation model for fast flows of entangled polymers. J. Rheol. 43:1461-1493.

35. Ottinger HC, (2005) Beyond Equilibrium Thermodynamics, Wiley

36. Padding JT, Briels WJ (2001), Uncrossability constraints in mesoscopic polymer melt simulations: Non-Rouse behavior of $C_{120}H_{242}$. J. Chem. Phys. 115:2846-2859.

37. Pattamaprom C, RG Larson (2001) Constraint release effects in monodisperse and bidisperse polystyrenes in fast transient shearing flows. Macromolecules 34:5229-5237.

38. Rouse Jr PE (1953) A Theory of the linear viscoelastic properties of dilute solutions of coiling polymers, J.Chem.Phys. 21:1272-1280.

39. Wolfram S (1991) Mathematica-A system for doing mathematics by computer. 2nd ed. Wesley-VCH, New York.

40. Zimm BH (1956) Dynamics of polymer molecules in dilute solution: viscoelesticity, flow birefringence and dielectric loss J.Chem.Phys. 24:269-278.

CHAPTER 6

A MESOSCOPIC TUBE MODEL OF POLYMER/LAYERED SILICATE NANOCOMPOSITES

Hassan Eslami[a], Miroslav Grmela[a1] , Mosto Bousmina[b,c]

[a] Center for Applied Research on Polymers and Composites (CREPEC)
Ecole Polytechnique de Montreal, C.P.6079 suc. Centre-ville,
Montreal, H3C 3A7, Quebec, Canada

[b] Canada Research Chair on Polymer Physics and Nanotechnology
and Center for Applied Research on Polymers and Composites (CREPEC)
Department of Chemical Engineering, Laval University, Ste-Foy,
G1K 7P4, Quebec, Canada

[c] Hassan II Academy of Sciences and Technology, Rabat, Marocco

Rheologica Acta (2009) 48:317-331

[1]corresponding author: e-mail: miroslav.grmela@polymtl.ca

Abstract

Rheology of isothermal suspensions of completely exfoliated silicate lamellae in polymer melts is investigated. In order to express more faithfully the physics involved in low shear rates and low frequencies we model the polymer molecules composing the melt as chains whose motion is confined to a tube formed by surrounding chains and lamellae. In the absence of lamellae, the model reduces to the mesoscopic model of reptating chains developed in Eslami and Grmela (2008). If the chains are seen only as FENE-P dumbbells, the model reduces to the model developed in Eslami et al. (2007). Responses to oscillatory, transient and steady shear flows are calculated and compared with available experimental data. The particular attention is payed to region of low shear rate and low frequency.

6.1 Introduction

The physical system investigated in this paper is the same as in Eslami et al. (2007). It is an incompressible and isothermal suspension of homogeneously distributed and completely exfoliated clay lamellae in polymer melts. In the model formulated in Eslami et al. (2007) (hereafter called Model I), the polymer macromolecules composing the melt are represented by FENE-P dumbbells. The model includes the lamella-lamella and lamella-polymer interactions, it is formulated on a mesoscopic level on which conformation tensors serve as microstructural state variables, and in the modular framework of GENERIC. As for the results, predictions of nonlinear rheology are relatively easily calculated (the calculations consist of solving a system of ordinary differential equations) and show a good agreement with results of experimental observations except for the measurements revealing the long range structures (i.e. low deformation nonlinear rheology and low frequency linear rheology). The objective of this paper is to extend Model I to include the physics involved in the larger structures.

We make two modifications of Model I. First, we replace the FENE-P dumbbells by reptating chains. The motion of one selected chain is constrained by a tube formed by surrounding chains and surrounding lamellae. On the mesoscopic level of description adopted

in this paper, the reptating motion is expressed mathematically as a diffusion alongside of the backbone of the chain and the lamellae participation in the reptation as a coupling of the diffusion to the conformation of the plates. Microscopic details about the influence of the lamellae on the motion of the chains is out of the reach of the mesoscopic description. The second modification that we are introducing in Model II is that the renormalization of the number densities of the polymer molecules and the lamellae are let to depend on the concentration of the lamellae. The renormalization is needed in Model I as well as in the model developed in this paper (hereafter called Model II) in order to resolve in the mathematical formulation, that uses only one-chain and one-lamella characterizations, the disparity of sizes of lamellae and polymer molecules. As in Eslami et al. (2007), Model II is constructed in the framework of GENERIC. In the absence of lamellae, Model I reduces to the FENE-P model and Model II to the mesoscopic tube model developed in Eslami and Grmela (2008).

The paper is organized as follows. In Section 6.2 we formulate the governing equations of the model. In Section 6.3 we present the results and compare them with results of experimental observations (in particular the results collected in the low deformation nonlinear rheology and low frequency linear rheology).

6.2 Model formulation

Classical hydrodynamics begins with a general framework for the time evolution equations whose solutions are guaranteed to agree with the observed conservation of the total mass, the total energy, and the total momentum. The framework (the local balance laws) is then filled with the particular physics of the particular fluid under consideration in the second step called a specification of constitutive relations. The second step becomes very difficult for complex fluids (for example for the suspensions discussed in this paper). In order to simplify it we may suggest to begin by modifying the first step. This type of extension of the strategy of classical hydrodynamics, suitable in particular to complex fluids, is called

GENERIC Grmela and Ottinger (1997); Ottinger and Grmela (1997).

Instead of requiring just mass, energy and momentum conservations, we require more. Solutions to the governing equations are required to be compatible with mechanics and with thermodynamics. The former requirement means that in the absence of dissipation the dynamics is Hamiltonian, the latter means that solutions of the governing equations approach (in the absence of external forces) equilibrium states at which the equilibrium thermodynamics is applicable. The framework for equations possessing the properties mentioned above is called GENERIC. Its main advantage is the wide range of applicability. The GENERIC framework is formulated for any set of state variables while the framework of classical hydrodynamics only for the classical hydrodynamic fields. The complex fluids are complex because they have an internal structure that evolves in time on the scale comparable to the scale on which the classical hydrodynamic fields evolve. The internal structure has to be thus represented in the state variables and in the time evolution. Consequently, the framework of classical hydrodynamics (a set of local balance laws for the classical hydrodynamic fields) does not apply to complex fluids.

The GENERIC framework is recalled in Appendix. The GENERIC constitutive relations representing the nano suspension are discussed in the next section.

6.2.1 GENERIC constitutive relations

Hereafter, we limit ourselves to isothermal fluids. In order to transform (6.18) into equations governing the time evolution of the nano suspension discussed in this paper, we have to express the particular physics of the suspension in the specification of x, L, Ξ, Φ, called GENERIC constitutive relations. We shall make the specifications, one after the other, below.

6.2.1.1 State variables

Beside being isothermal and incompressible, we consider the suspension under consideration in this paper to be spatially homogeneous. The state variables are thus independent of the

position vector $\boldsymbol{r}$.

The polymer molecules composing the polymer melts are regarded as chains. States of the melt in tube theories De Gennes (1971); Doi and Edwards (1986); Likhtman and McLeish (2002); McLeish (2002) are characterized by one chain configuration space distribution function $\psi(\boldsymbol{R}, s)$, where $\boldsymbol{R}$ is the vector tangent to the chain and $-1 \leq s \leq 1$ is the coordinate on the backbone of the chain. We follow Eslami and Grmela (2008) and choose the conformation tensor $\boldsymbol{c}(s)$ to characterize states of chains. The conformation tensor is a symmetric positive definite three-by-three tensor. It has the physical interpretation of the deformation tensor. It can also be interpreted as a second moment of $\psi(\boldsymbol{R}, s)$. By choosing $\boldsymbol{c}$ instead of ψ, we gain the simplicity in solving the governing equations but we loose the richness of details of the physics that we can express. Results reported in Eslami and Grmela (2008) indicate that the details we loose are of lesser importance in the investigation of the rheological behavior of our interest.

Now, we have to decide what are the variables that we shall use to describe states of the lamellae. In this paper we make the simplest choice. Let $\boldsymbol{n}$ be a unit vector perpendicular to the lamella. The distribution of the lamellae for homogeneous distribution is described by the distribution function $\psi(\boldsymbol{n})$. Its second moment is a tensor denoted by the symbol $\boldsymbol{a}$ (i.e. $a_{\alpha\beta} = \int d\boldsymbol{n} n_\alpha n_\beta \psi(\boldsymbol{n})$). The constraint $|\boldsymbol{n}| = 1$ is expressed on the conformation tensor level as $tr\boldsymbol{a} = 1$. This means that the surface area of one lamella remains unchanged during the time evolution.

Altogether, the state variables considered in this paper are:

$$(\boldsymbol{u}(\boldsymbol{r}),\ \boldsymbol{c}(s),\ \boldsymbol{a})\,;\quad tr(\boldsymbol{a}) = 1 \tag{6.1}$$

where $\boldsymbol{u}(\boldsymbol{r})$ is the field of momentum. In the context of rheology, the momentum field is imposed from outside. In accordance with our assumption of spatial homogeneity, we shall consider below only $\boldsymbol{u}$ that depends linearly on $\boldsymbol{r}$.

6.2.1.2 Kinematics

We use the same kinematics for $\boldsymbol{c}(s)$ as in Eslami and Grmela (2008) and for $\boldsymbol{a}$ as in Eslami et al. (2007). We therefore write directly the nondissipative time evolution equations, i.e. the first term on the right hand side of (6.18):

$$\frac{\partial u_\alpha}{\partial t} = -\partial_\beta\left(\frac{u_\alpha u_\beta}{\rho}\right) - \partial_\alpha p - \partial_\beta \sigma_{\alpha\beta} \tag{6.2}$$

$$\frac{\partial c_{\alpha\beta}}{dt} = -\frac{1}{2}\left(\boldsymbol{\Omega}\cdot\boldsymbol{c} - \boldsymbol{c}\cdot\boldsymbol{\Omega}\right)_{\alpha\beta} + \frac{1}{2}\left(\dot{\boldsymbol{\gamma}}\cdot\boldsymbol{c} + \boldsymbol{c}\cdot\dot{\boldsymbol{\gamma}}\right)_{\alpha\beta} \tag{6.3}$$

$$\frac{d\boldsymbol{a}}{dt} = -\frac{1}{2}\left(\boldsymbol{\Omega}\cdot\boldsymbol{a} - \boldsymbol{a}\cdot\boldsymbol{\Omega}\right) + \xi\left(-\frac{1}{2}\left(\dot{\boldsymbol{\gamma}}\cdot\boldsymbol{a} + \boldsymbol{a}\cdot\dot{\boldsymbol{\gamma}}\right) + tr(\boldsymbol{a}\,.\,\dot{\boldsymbol{\gamma}})\boldsymbol{a}\right) \tag{6.4}$$

and the corresponding to them expression for the extra stress tensor $\boldsymbol{\sigma}$

$$\sigma_{\alpha\beta} = -2\int_{-1}^{1} ds\; c_{\alpha\varepsilon}\Phi_{c_{\varepsilon\beta}} + 2\,\xi\; a_{\alpha\varepsilon}\Phi_{a_{\varepsilon\beta}} - 2\,\xi\; a_{\alpha\beta}\; tr(\boldsymbol{a}\,.\,\Phi\boldsymbol{a}) \tag{6.5}$$

By $\dot{\gamma}_{\alpha\beta} = \frac{\partial\Phi_{u_\alpha}}{\partial r_\beta} + \frac{\partial\Phi_{u_\beta}}{\partial r_\alpha}$ and $\boldsymbol{\Omega}_{\alpha\beta} = \frac{\partial\Phi_{u_\alpha}}{\partial r_\beta} - \frac{\partial\Phi_{u_\beta}}{\partial r_\alpha}$ we denote the strain rate and the vorticity tensor respectively; $\alpha, \beta = 1, 2, 3$. We use in (6.5) and in the rest of the paper the summation convention (i.e. summation over repeated indices). Note that (6.4) implies $dtr\boldsymbol{a}/dt = 0$.

The advection of $\boldsymbol{c}(s)$ and of $\boldsymbol{a}$ is different because of the following three differences in the tensors $\boldsymbol{c}(s)$ and $\boldsymbol{a}$: (i) the tensors $\boldsymbol{c}(s)$ are unconstrained and the tensor $\boldsymbol{a}$ is constrained by $tr\boldsymbol{a} = 1$, (ii) $\boldsymbol{c}(s)$ are the second moments of the vector that itself is advected by the flow, while $\boldsymbol{a}$ is the second moment of the vector that is perpendicular to the plate that is advected by the flow, and (iii) the advection of $\boldsymbol{c}$ is affine and the advection of $\boldsymbol{a}$, involving the parameter ξ, is nonaffine. The nonaffine modification of the advection makes the nondissipative time evolution non Hamiltonian. It should be seen as an approximation of an active advection, introduced in Gu and Grmela (2008) that is Hamiltonian. The formula (6.5) arises as a consequence of the Hamiltonian structure. In the case of the nonaffine (i.e. non Hamiltonian) advection, the formula (6.5) can be derived from thermodynamic considerations Grmela (1985). In this paper we consider ξ to be a phenomenological parameter. We note that it is the only phenomenological parameter entering the nondissipative time evolution. All

the other parameters expressing the individual nature of the suspension will enter in the dissipative part.

6.2.1.3 Dissipation

From the general formulation (see Appendix) we know that the dissipation potential Ξ is a function of $\Phi_{\boldsymbol{c}(s)}$ and $\Phi_{\boldsymbol{a}}$ satisfying certain properties. The physics that we want to express in it is that the chain whose states are described by $\boldsymbol{c}(s)$ is confined to a tube formed by surrounding chains and also surrounding plates. Inside the tube the chains moves predominantly along its backbone. This motion, called also a reptation motion, can be seen as a diffusion along the backbone. The force generating diffusion in $\mathbf{R}^3$ is a gradient with respect to the position coordinate $\boldsymbol{r} \in \mathbf{R}^3$. The force generating diffusion along the backbone is thus a gradient with respect to s. In addition to the thermodynamic force $\Phi_{\boldsymbol{c}}$ we thus introduce a new force $(\Phi_{\boldsymbol{c}})_s$ (denoting the derivative of $\Phi_{\boldsymbol{c}}$ with respect to s).

The thermodynamic force generating dissipation in the motion of the plates has to be chosen in such a way that the constraint $tr\boldsymbol{a} = 1$ remains unchanged during the time evolution Edwards et al. (2003). We can easily verify that the force

$$A_{ij} = \Phi_{a_{ij}} - \frac{1}{3} tr\Phi_a \, \delta_{ij} \tag{6.6}$$

has this property. Indeed, $d\boldsymbol{a}/dt = -\partial\Xi/\partial\Phi_a$ implies $dtr\boldsymbol{a}/dt = -tr\left(\partial\Xi/\partial\Phi_a\right) = 0$ provided the dissipation potential Ξ is a function of $\mathring{A}$ (i.e. it depends on $\Phi_{\boldsymbol{a}}$ only through its dependence on $\mathring{A}$).

If we limit ourselves to states that are not too far from equilibrium (i.e. the states for which Φ_c and Φ_a are not too large), we can choose the dissipation potential Ξ to be the

following quadratic function of the thermodynamic forces

$$\Xi = \left(\Phi_{c_{ij}}\ ,\ \left(\Phi_{c_{ij}}\right)_s\ ,\ A_{ij}\right) \mathbf{\Lambda} \begin{pmatrix} \Phi_{c_{kl}} \\ \\ \left(\Phi_{c_{kl}}\right)_s \\ \\ A_{kl} \end{pmatrix}, \tag{6.7}$$

where

$$\mathbf{\Lambda} = \begin{pmatrix} \frac{\Lambda^{11}}{1-\alpha} & 0 & \frac{\Lambda^{13}}{\alpha(1-\alpha)} \\ \\ 0 & \frac{\Lambda^{22}}{1-\alpha} & \frac{\Lambda^{23}}{\alpha(1-\alpha)} \\ \\ \frac{\Lambda^{13}}{\alpha(1-\alpha)} & \frac{\Lambda^{23}}{\alpha(1-\alpha)} & \frac{\Lambda^{33}}{\alpha} \end{pmatrix} \tag{6.8}$$

Λ^{11}, Λ^{22}, Λ^{33},Λ^{13} and Λ^{23}, called hereafter mobility tensors, are phenomenological parameters representing the suspension in the model. By α we denote the volume fraction of the suspended lamellae. In order that (6.7) satisfies the properties required from the dissipation potential (see appendix), the matrix $\mathbf{\Lambda}$ has to be positive definite. This then serves as a constraint for the phenomenological parameters Λ^{11}, Λ^{22}, Λ^{33},Λ^{13} and Λ^{23}.

In the absence of the lamellae (i.e, in the absence of the thermodynamic force $\mathring{A}$) the dissipation potential (6.7) reduces to Ξ introduced in Eslami and Grmela (2008). The thermodynamic force $(\Phi_{\boldsymbol{c}})_s$ generates the reptation motion of the polymer chains. Now, we introduce the lamellae into the polymer melt. In the mathematical formulation, we express it by coupling the reptation force $(\Phi_{\boldsymbol{c}})_s$ to $\mathring{A}$ (i.e. $\Lambda_{23} \neq 0$). From the physical point of view, the coupling represents a modification of the diffusion along the backbone of the chain (i.e. the reptation motin) by the presence of the lamellae. The microscopic details of the lamellae-chain interactions are outside the scope of the mesoscopic formulation adopted in this paper. The newly introduced parameter Λ_{23}, quantifying the influence of the lamellae on the reptation, is considered as a phenomenological material parameter whose value is obtained by fitting experimental data.

As for the choice of the mobility tensors $\mathbf{\Lambda}$, we follow Beris and Edwards (1990, 1994) and use polynomial functions of $\boldsymbol{c}$ and $\boldsymbol{a}$. More specifically, we choose:

$$\mathbf{\Lambda}^{11} = \Lambda_0^{11}\left[f_1\widehat{\boldsymbol{c}\boldsymbol{\delta}} + f_2\widehat{\boldsymbol{c}\boldsymbol{c}}\right] \tag{6.9}$$

and

$$\mathbf{\Lambda}^{22} = \Lambda_0^{22}\left(1 + \widetilde{\Lambda_0^{22}}\left(tr\boldsymbol{c} - tr\boldsymbol{c}_{eq}\right)^2\right)\left[f_1\widehat{\boldsymbol{c}\boldsymbol{\delta}} + f_2\widehat{\boldsymbol{c}\boldsymbol{c}}\right] \tag{6.10}$$

$$\mathbf{\Lambda}^{33} = \Lambda_0^{33}\left(f_3\widehat{\boldsymbol{a}\boldsymbol{\delta}} + f_4\widehat{\boldsymbol{a}\boldsymbol{a}} + f_5\widehat{\boldsymbol{a}\boldsymbol{a}\boldsymbol{a}}\right) \tag{6.11}$$

$$\begin{aligned} \mathbf{\Lambda}^{13} &= \Lambda_0^{13}\widehat{\boldsymbol{c}\boldsymbol{a}} \\ \mathbf{\Lambda}^{23} &= \Lambda_0^{23}\widehat{\boldsymbol{c}\boldsymbol{a}} \end{aligned} \tag{6.12}$$

The coefficients $f_i (i = 1 - 5)$ appearing in (6.9),(6.10) and (6.11) equal either 0 or 1. We are introducing them in order to be able to explore in the next sections consequences of choosing linear and/or quadratic dependence on $\boldsymbol{c}$ and higher order dependency of $\boldsymbol{a}$. If $(f_3 = 1, f_4 = 0, f_5 = 0)$ (resp. $(f_4 = 1, f_3 = 0, f_5 = 0)$ or $(f_5 = 1, f_3 = 0, f_4 = 0)$), we call $\mathbf{\Lambda}^{33}$ a first order (resp. the second or third order) mobility tensor.The symbol $\boldsymbol{c}_{eq}$ arising in (6.9) and (6.10) denotes the conformation tensor $\boldsymbol{c}$ at equilibrium. $\mathbf{\Lambda}$ are all fourth order tensors,$\widehat{\ }$ means symmetrization in the four indices, and Λ_0^{11}, Λ_0^{22}, $\widetilde{\Lambda_0^{22}}$, Λ_0^{33}, Λ_0^{13} and Λ_0^{23} are phenomenological coefficients.

The physical interpretation of the coefficients Λ_0 is the following: $(\Lambda_0)^{-1} \sim \lambda_0$ where λ_0 are relaxation times. In the two component fluid under consideration (polymers and lamellae), we need a mixing rule for the relaxation times. We choose the simplest one. We pass from λ_0^{11} to $(1-\alpha)\lambda_0^{11}$, from λ_0^{33} to $\alpha\lambda_0^{33}$, and from λ_0^{13} and λ_0^{23} to $\alpha(1-\alpha)\lambda_0^{13}$ and $\alpha(1-\alpha)\lambda_0^{23}$. The volume fraction α of the lamellae is related to the weight fraction w by $\alpha = \rho_c w/(\rho_a - (\rho_a - \rho_c)w)$, where ρ_c (resp. ρ_a) is a mass density of the polymer (resp. lamellae). The other place where the volume fraction α enters the governing equations (6.3 and 6.4) is in the free energy discussed below.

6.2.1.4 Free energy

Finally, we turn to the specification of the free energy Φ. We write it as a sum of four terms:

$$\Phi = \Phi^{kin} + \Phi^{c} + \Phi^{a} + \Phi^{ca} \tag{6.13}$$

where $\Phi^{kin} = \frac{\boldsymbol{u}^2}{2\rho}$ is the kinetic energy part , ρ is the mass density assumed to be a constant, and Φ^c, Φ^a is the free energy of the polymer matrix, and the lamellae respectively. The term Φ^{ca} is the contribution to the free energy due to the polymer-plate interaction.

As for the free energy of polymer matrix Φ^c, we follow what we have done in Eslami and Grmela (2008) by considering locally FENE-P dumbbell model:

$$\Phi^c = \frac{1}{V}\int d\boldsymbol{r}\int_{-1}^{1} ds\left[-n_c H Q_0^2 \ln\left(1 - tr\ \mathbf{c}\right) + K tr(\boldsymbol{c}_s \cdot \boldsymbol{c}_s) - \frac{1}{2} n_c k_B T \ln(\det \mathbf{c})\right] \tag{6.14}$$

By $\boldsymbol{c}_s$ we denote $\frac{d\boldsymbol{c}}{ds}$.

The first term is the FENE-P intramolecular energy, H is the modulus of the local spring, and R_0 its maximal length.

The second term represents a nonlocal (in s) contribution to the intramolecular energy. In the case when the local FENE-P dumbbell is replaced by a rigid dumbbell, it is the energy associated with the bending of the chain. The coefficient K is the modulus of this type of intramolecular interactions.

The third term represents the entropy S multiplied by the temperature T. By n_c we denote the number density of the polymer chains ($n_c = \frac{(1-\alpha)\rho_c N_A}{M_c}$; α is the volume fraction of the lamellae, N_A is the Avogadro number and M_c molecular weight of the polymer).

As for free energy of lamellae Φ^a, its energy part will be neglected. The entropy part is chosen to be a linear combination of the classical Boltzmann entropy and the Khokhlov-Semenov entropy [Khokhlov and Semenov (1985); Grmela (1990)] accounting for the flexibility of the plates:

$$\begin{aligned}\Phi^a &= G\ tr\boldsymbol{a} - \frac{1}{2} n_a \left(1 - K_{flex}\right) k_B T \ln(\det \mathbf{a}) + n_a K_{flex} k_B T tr\mathbf{a}^{-1} \\ &\quad + \kappa n_a^2 k_B T \left((tr\boldsymbol{a})^2 - tr(\boldsymbol{a}\ .\ \boldsymbol{a})\right)\end{aligned} \tag{6.15}$$

where n_a is the number density of plates ($n_a = \frac{\alpha}{A_0 h}$; A_0 is the surface area of the lamella and h is its thickness); K_{flex} denotes a parameter characterizing the flexibility of plates ($0 < K_{flex} < 1$), and κ is a modulus of the plate-plate interaction. The first term in the free energy express the constraint $tr\boldsymbol{a} = 1$ and the parameter G is the Lagrange coefficient.

Finally, the polymer lamellae interaction free energy Φ^{ca}, is chosen as follows:

$$\Phi^{ca} = \kappa' \, n_c n_a k_B T tr(\boldsymbol{c} \, . \, \boldsymbol{a}) \tag{6.16}$$

where κ' is phenomenological parameters measuring the polymer-plate topological interactions. The expressions in (6.16) is the Onsager entropy adapted to the plate-chain topological interactions expressed in terms of the conformation tensors rather than distribution functions (see more in Eslami et al. (2007)).

The choice of the parameters entering the free energy is restricted by requiring the thermodynamic stability, i.e. by requiring that the matrix

$$\begin{pmatrix} \Phi^{c}_{cc} & \Phi^{ca}_{ca} \\ \\ \Phi^{ca}_{ca} & \Phi^{a}_{aa} \end{pmatrix}$$

is positive definite. we use the notation: $\Phi^{c}_{cc} = \frac{\partial^2 \Phi^c}{\partial c^2}$, $\Phi^{a}_{aa} = \frac{\partial^2 \Phi^a}{\partial a^2}$ and $\Phi^{ca}_{ca} = \frac{\partial^2 \Phi^{ca}}{\partial c \partial a}$.

When we are combining the free energies Φ^a, Φ^c and Φ^{ca}, we have to face the problem of the disparity of shapes and sizes of the polymer macromolecules and the lamellae. Due to the large surface area of the rigid lamellae, one lamella interacts simultaneously with not one but a whole group of macromolecules. In other words, the particular shape and the rigidity of the lamellae makes its interaction with surrounding macromolecules (that are flexible and have a very different shape) very nonlocal. To account for this effect, we rescale n_a. We multiply it by a factor χ. After the rescaling we can regard the lamellae and the macromolecules as equal partners in the interactions. In Eslami et al. (2007), the scaling parameter χ was assumed to be a constant. In this paper we let it depend appropriately on the volume fraction α. The other parameters entering the free energy will, in general, also depend on α. We expect

however this dependence to be of lesser importance and leave it out of our consideration in this paper.

6.2.2 Material parameters

At this point we have completed the formulation of the governing equations of the model. In the next sections we turn to their solutions. Before engaging ourselves in the process of finding solutions, we make a general comment about the parameters introduced in them. Every theory, formulated on any level of description, needs parameters (called material parameters) expressing the individual features of the systems under consideration. For instance, in classical mechanics, it is the mass and all the parameters entering the characterization of the forces, in hydrodynamics of simple fluids, the material parameters are the viscosity and the heat conductivity coefficients and all the parameters entering the local fundamental thermodynamic relation. The mapping: *physical systems* $\rightarrow$ *material parameters* can be obtained by following two routes: (route 1) by staying inside the level, or (route 2) by investigating relations to other levels. Below, we shall make a few brief comments about both routes.

(route 1)

Let the level on which we place ourselves be denoted by the symbol $\mathcal{L}_0$. Among all experimental observations made on the level $\mathcal{L}_0$ (we shall denote them by the symbol $\mathcal{O}_0$) we select some ($\mathcal{O}_0^{metr} \subset \mathcal{O}_0$) that will be regarded as measurements of the material parameters. The values of the parameters are obtained by fitting the results of the observations $\mathcal{O}_0^{metr}$ with predictions of the theory. The success or the failure of the theory is then seen in the comparison of the results of the remaining $\mathcal{O}_0 \setminus \mathcal{O}_0^{metr}$ observations with predictions of the theory. This route is traditionally followed on all well established levels as for example in classical thermodynamics, classical mechanics, and classical hydrodynamics.

(route 2)

Let the level $\mathcal{L}_1$ be more microscopic (i.e. involving more details) than the level $\mathcal{L}_0$. For instance, let $\mathcal{L}_0$ be the level of classical hydrodynamics and $\mathcal{L}_1$ the level of Boltzmann kinetic

theory. Both levels $\mathcal{L}_0$ and $\mathcal{L}_1$ are autonomous (i.e. neither of them needs the other to be formulated and applied) but since the level $\mathcal{L}_1$ is more microscopic we can anticipate that an analysis of solutions of the governing equations on the level $\mathcal{L}_1$ can lead to a derivation of the theory on the level $\mathcal{L}_0$. The process of the derivation can be seen as a pattern recognition process in the set of solutions (trajectories) obtained on the level $\mathcal{L}_1$. For instance, in the case of $\mathcal{L}_1$ being the Boltzmann kinetic theory and $\mathcal{L}_0$ the hydrodynamics, such passage $\mathcal{L}_1 \to \mathcal{L}_0$ is provided by the famous Chapman-Enskog method. Let the material parameters associated with the level $\mathcal{L}_1$ resp. $\mathcal{L}_0$ be denoted $\mathcal{P}_1$ resp. $\mathcal{P}_0$. The passage $\mathcal{L}_1 \to \mathcal{L}_0$ induces the passage $\mathcal{P}_1 \to \mathcal{P}_0$. The material parameters $\mathcal{P}_0$ can be thus obtained by independent measurements made on the level $\mathcal{L}_1$. For example, by using the Chapman-Enskog method, we obtain the viscosity and the heat conductivity coefficients expressed in terms of the material parameters used in the Boltzmann kinetic theory.

In the context of the model introduced in this paper, we note first that the material parameters have all a clear physical meaning. Each of them appear in either the free energy or the dissipation potential, each of them is associated with a specific physics expressed on the mesoscopic level on which the model is formulated. We do not attempt in this paper to see the suspensions under consideration from a more microscopic point of view (e.g. from the point of view of kinetic theory) and consequently our only option to specify the material parameters is the route 1. The main problem is that we do not have in our disposition a large enough pool of experimental data to both measure and predict. The post processing of the model, i.e. a systematic analysis of the influence of the material parameters on the results that are compared with results of experimental observations, that we do in the next section, is found to be very useful in the determination of the mapping *physical systems* $\to$ *material parameters*.

6.3 Results and discussion

As for the imposed flows, we consider shear flows and oscillatory flows. We calculate both the linear and the non-linear viscoelastic behavior.

A simple shear flow is given by the momentum field $u_1 = \dot{\gamma}_{(t)} x_2$, $u_2 = u_3 = 0$. The velocity gradient $\dot{\gamma}_{(t)}$ is, in general, a function of time. The absolute value of $\dot{\gamma}_{(t)}$ is called a shear rate. In this paper, we follow the standard notation for the viscosity coefficient η, shear stress σ and the first normal stress differences N_1. The governing equations of the model represent, from the mathematical point of view, a system of partial differential equations (PDEs). The initial conditions are the equilibrium solutions (i.e. $\Phi_c = 0$ and $\Phi_a = 0$). As for the boundary conditions of PDEs we follow Eslami and Grmela (2008). We solve the time evolution equations numerically by using the MATHEMATICA software package [Wolfram (1991)].

In the linear viscoelastic regime with small sinusoidal strain $\gamma(t) = \gamma_0 \, sin \, \omega t$, the shear stress tensor is presented by $\sigma(t) = \gamma_0 \, (G' \, sin \, \omega t + G'' \, cos \, \omega t)$ where G' and G'' are the storage and loss moduli, respectively. Again, in order to model the linear viscoelastic behavior of nanocomposites, we shall follow the procedure used in Eslami and Grmela (2008) and express the conformation tensors $\boldsymbol{c}$ and $\boldsymbol{a}$ as a linear function of $\gamma_0 \, \omega$. Finally, we solve the reduced equations numerically to find the linear viscoelastic functions.

6.3.1 Model predictions

We turn now to the post-processing of the model, i.e. to finding the relation between model parameters and rheological measurements in different flows.

It is useful to regard rheological models as an input-output systems. The input is the microscopic or mesoscopic physics used in its formulation, the output are predictions of the observed rheological behavior. Both input and output have many components. In the input they are the particular physical features involved (e.g. the local extensibility, the constraints, tube formation, etc.) and in the output they are the features of the observed behavior (e.g.

the length of the plateau in the curve η versus $\dot{\gamma}$ for pure polymer, the slope of this curve as $\dot{\gamma} \rightarrow \infty$, the slope of this curve at low shear rate which is an indication of yield stress, etc.). The passage between the input and the output is made by solving the (in general very nonlinear) governing equations of the model. An understanding gained by the model is often measured by the success in establishing direct passages between individual components of the input and individual components of the output. For example, as we shall see below, the nonlinear dependence of the dissipative kinetic coefficients is seen to influence mainly the length of the plateau in the case of pure polymer, the nonlocal intramolecular interactions influence mainly the linear rheological behavior, dependency of rescaling parameter to clay volume fraction influence the material function at low shear rate and low frequency, etc.). A word of caution is in order. The input-output passage involves solutions of complex nonlinear equations. In general, the input-output relation is very complex and simple passages between single components of the input and the output do not exist. Having this in mind, we proceed to investigate the input-output passage of the model presented in this paper.

In the following calculations of model predictions, the model parameters are chosen as follows: $\Lambda_0^{11} = 10^{-5}, \Lambda_0^{22} = 10^{-7}, \widetilde{\Lambda_0^{22}} = 1.75 \times 10^5, \Lambda_0^{33} = 10^{-8}, \Lambda_0^{23} = 10^{-8}, \Lambda_0^{13} = 10^{-8}, b = \frac{2HQ_0^2}{k_BT} = 2.5, K = 3 \times 10^5, \kappa = 10^{-24}, \kappa' = 10^{-24}, K_{flex} = 0.1, \chi = 6000\ \alpha^{0.75}$ and $\xi = 0.99$. Prediction of transient material functions is made at $\dot{\gamma}_0 = 0.1s^{-1}$ and 5 wt % clay.

6.3.1.1 Effects of the shear rate on transient material functions

Figures 6.1(a) and 6.1(b) depict the effects of shear rate on the transient material functions, η^+ and N_1^+ respectively. The results show that for small shear rates, the viscosity reaches its steady state value monotonically.

As the shear rate increases, the curve of viscosity versus time shows an overshoot. The size of the overshoot increases and the time at which the overshoot appears decreases when the shear rate increases. Similar results are obtained for the first normal stress differences (see Figure 6.1(b)). The overall qualitative features of the curves are essentially the same as the ones seen in the experimental data collected for polymer melts and solutions [Bird et al.

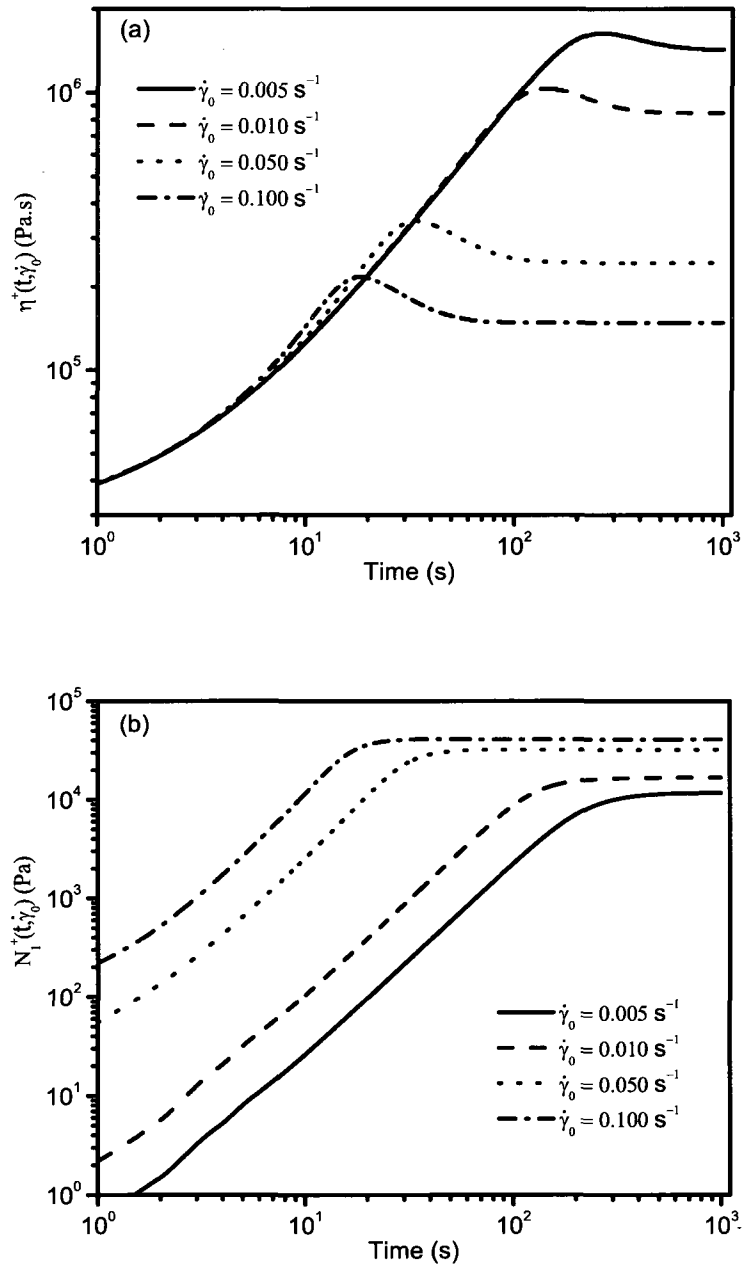

Figure 6.1: Effect of shear rate on stress growth material functions (a) shear viscosity (b)first normal stress differences

(1987a); Eslami et al. (2004)], miscible polymer blend [Eslami et al. (2003)] and polymer nanocomposites [Wu et al. (2005); Ayyer and Leonov (2004)].

6.3.1.2 Effects of the mobility coefficients on the material functions

Figures 6.2(a) and 6.2(b) depict the influence of the plate mobility coefficient Λ_0^{33} on the transient material functions, η^+ and N_1^+ respectively. As seen on Figure 6.2(a), both the stationary value and the size of the overshoot increase with decreasing Λ_0^{33}. Figure 6.2(b) indicates that similarly as the shear viscosity, the stationary values of the first normal stress difference increase with decreasing Λ_0^{33}. However, N_1^+ is less sensitive to increasing the size of the overshoot than η^+ (the size of the overshoots becomes visible more clearly if the curves are drawn in the normalized form).

Changing the plate mobility coefficient means, from the physical point of view, changing the friction among the plates. With increasing the plate mobility coefficient, the friction among the platelets decreases which in turn means decreasing the obstacles in the suspension and thus decreasing the viscosity.

As for the overshoot in the viscosity curve we can interpret it as follows: With decreasing plate mobility coefficient the friction among platelets increases which then means that the suspension is more anisotropic and consequently the overshoots are more pronounced. It should be also noted that we let the plate mobility to depend on the plate orientation tensor $\boldsymbol{a}$ (see Eq.(6.11)). From the physical point of view, the higher is the order on the nonlinearity of the function $\Lambda(\boldsymbol{a})$ the more anisotropic is the suspension.

Figures 6.3(a) and 6.3(b) present the influence of the polymer plate mobility coefficients Λ_0^{13} and Λ_0^{23} on the stress growth viscosity. The former is related to the classical dissipation mechanism and the latter to the reptation mechanism.

Again, one can relate the interaction mobility coefficient to the friction among the macromolecules and plates: Λ_0^{13} is related to the friction among polymer chains and platelets while Λ_0^{23} can be interpreted as the level of friction between the chain segments and the platelets.

Figure 6.3(a) shows that with increasing Λ_0^{13} the stationary values of the shear viscos-

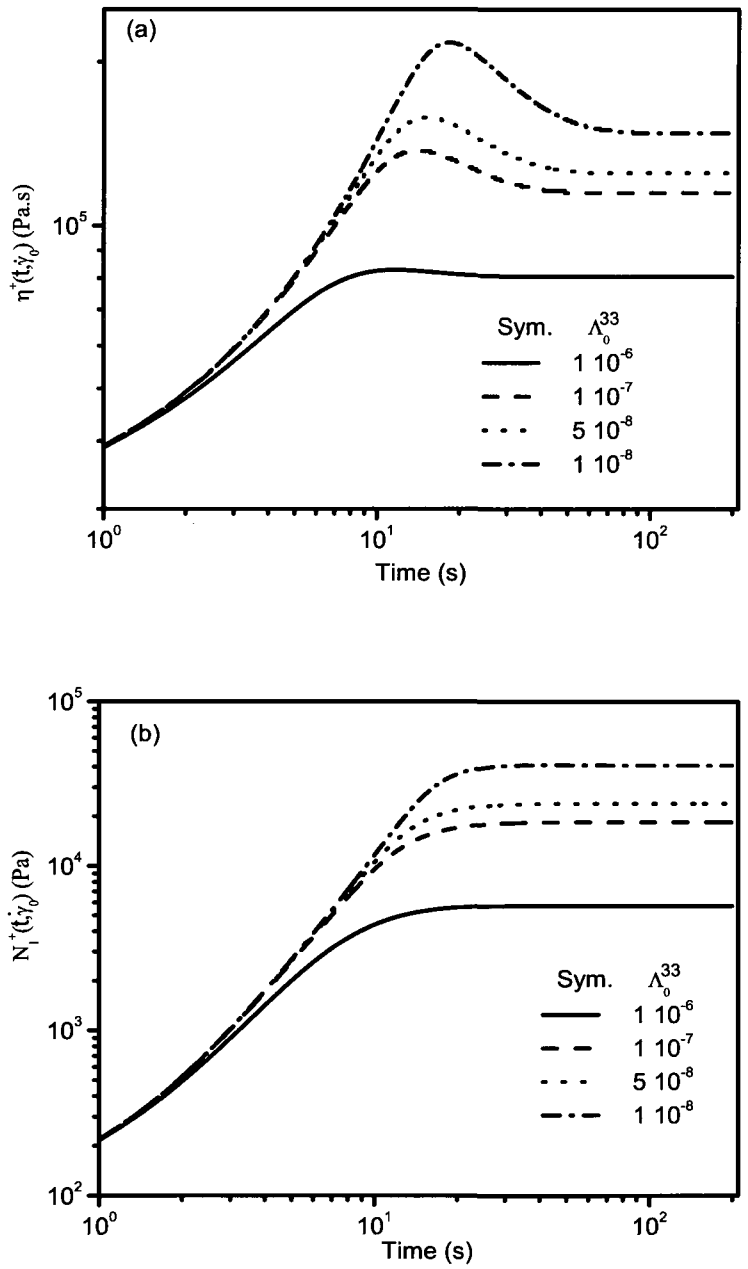

Figure 6.2: Effect of plate mobility coefficient Λ_0^{33} on stress growth material functions (a) shear viscosity (b)first normal stress differences

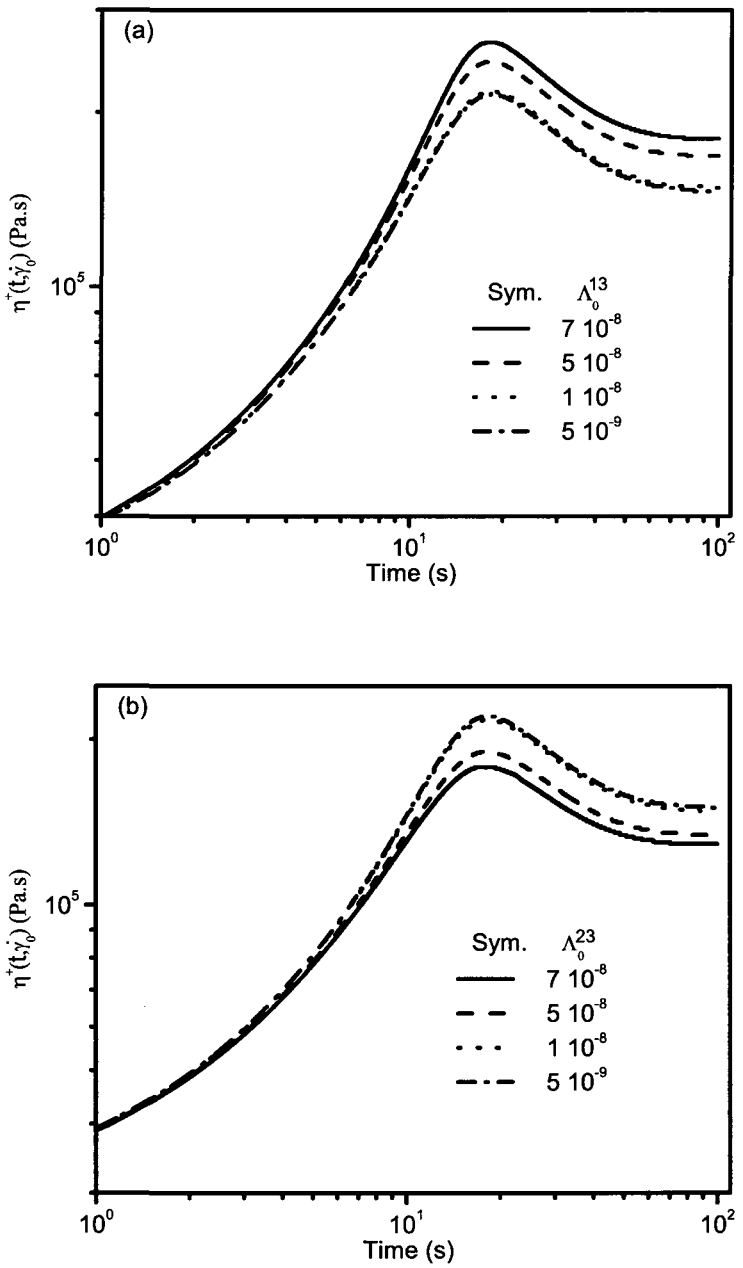

Figure 6.3: Effect of polymer plate interaction mobility coefficient on stress growth viscosity (a) effect of Λ_0^{13} (b) effect of Λ_0^{23}

ity increases. One can also see slight changes in the size of the overshoot with increasing Λ_0^{13}. As mentioned above, increasing Λ_0^{13} means increasing the interaction between chains and platelets. Depending on the morphology of the chain this interaction manifests itself differently. At low shear rates the coil-like morphology of the chains offers more obstacles for the motion of the platelets and consequently we see the viscosity to increase (i.e. the friction among polymer chains and platelets increases). However, at high shear rates where the chains are more extended and oriented, increasing the interaction mobility coefficient of polymer and plate means decreasing the friction among polymer chain and platelets which then decreases the viscosity of the suspension (results for high shear rates are not shown here for the sake of brevity).

Figure 6.3(b) shows that with increasing Λ_0^{23} the stationary value of the shear viscosity decreases while the size of the overshoot does not change. The same interpretation as above can explain also this behavior. As mentioned earlier, Λ_0^{23} is related to the interaction between chain segments and platelets and since we assume that the segments are very small (for more detail see Eslami and Grmela (2008)) the flow situation (low or high shear rates) does not change the overall behavior of this curve.

6.3.1.3 Effects of the nano-particle loading on the material functions

As mentioned earlier, the volume fraction of nano-particle α is introduced on three places: in the dissipation potential, in the free energy, and in the rescaling parameter. The reason why we let the rescaling parameter to be a function of the volume fraction of the silicate plates is that the number of polymer macromolecules that are in contact with a plate changes when the number of plates changes. At this point we assume a simple dependency of the rescaling parameter to α.

The transient shear stress and the first normal stress differences of polymer nanocomposites at different contents of nano-particles are presented on Figures 6.4(a)-and 6.4(b). As expected, the rheology of polymer nanocomposites is significantly influenced by the nano-particle loading. As it increases, i.e. as α increases, the effects become more significant.

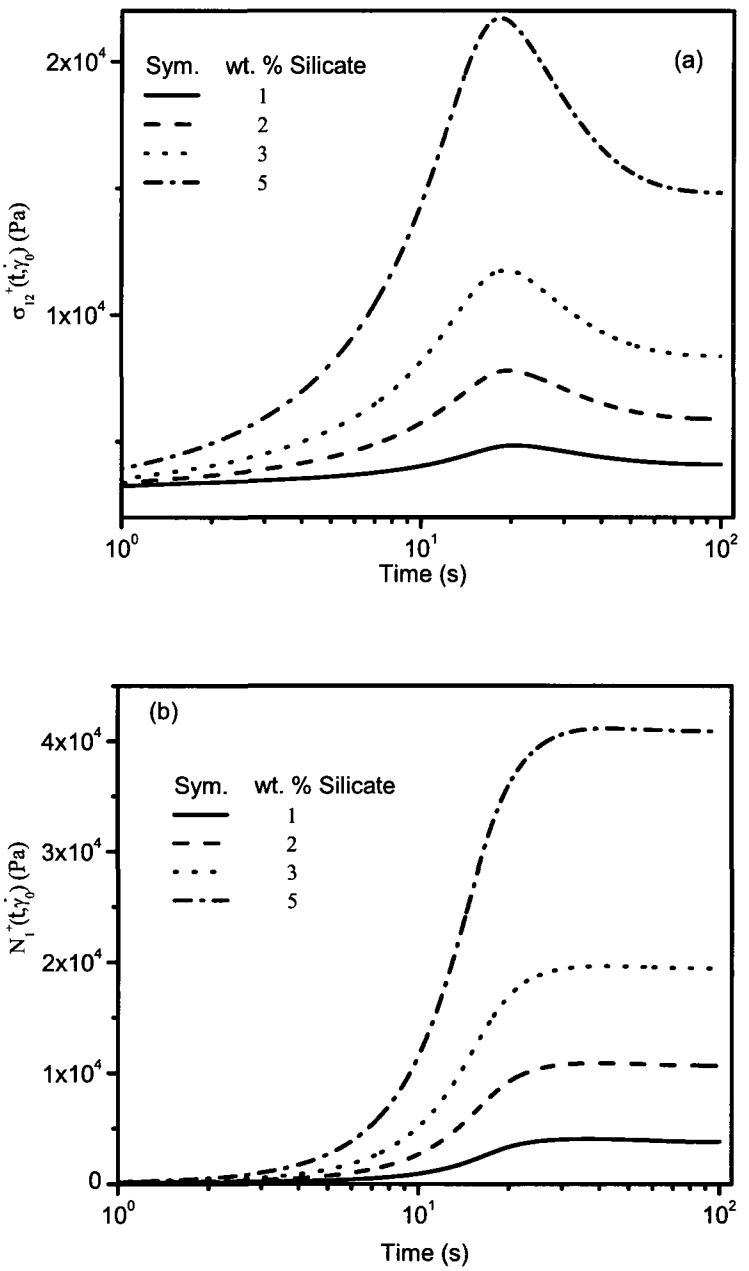

Figure 6.4: Effect of the nano-particle weight fraction on stress growth material functions (a) shear stress (b) first normal stress differences

These results show that both the stationary values and the size of the overshoots increase with increasing the nano-particle loading. The dependence of the overshoots on α is more pronounced in σ^+ than in N_1^+. The stationary values of N_1^+ (i.e. $N_1^+|_{t\to\infty}$) depend on α more sensitively than the stationary values of the shear stress. From the physical point of view, this is because by increasing the clay loading the elasticity increases which then shows itself in the overshoot in the shear stress and in the absolute values of the first normal stress differences.

Figure 6.5(a) shows the steady state viscosity of polymer nanocomposites for a wide range of shear rates and different nano-particle contents. It is found that increasing the clay loading results in a significant increase in the viscosity at low shear rates and in lesser extent at high shear rates. In other words, when the nano-particle loading increases the behavior for all ranges of shear rates becomes non-Newtonian (shear thinning). The model prediction shows that at high shear rates the viscosity is almost independent of the silicate loading and is comparable to that of the polymer matrix. This is because at high shear rates the plates are all oriented in the direction of the flow and the viscosity of the suspension is dominated by the polymer matrix. The effect of the clay loading at low shear rates is depicted in the small figure imbedded in Figure 6.5(a). As it is clearly seen on this figure, the slope of the curve of shear stress versus shear rate decreases with increasing the clay loading and at the high clay loading it almost becomes a plateau which indicates a large value of the yield stress. We will discuss this issue in the Figure 6.8 where we compare the model with experimental data.

The empirical Cox-Merz relation which requires $\eta^*(\omega) = \eta(\dot{\gamma})$ where $\omega = \dot{\gamma}$ is proved to be applicable for homopolymers. Figure 6.5(b) shows that the rule fails for polymer nanocomposites. Even though our model does not predict well the Cox-Merz relation for the polymer matrix at high shear rates, it does predict it for low and medium shear rates. In the case of nanocomposites the Cox-Merz rule fails in the whole range of shear rates. Such a failure has been previously observed for filled polymer systems. The reason for the failure is that by applying steady shear flow the silicate layers become preferentially oriented in the direction of the flow even at low shear rates. The failure of the Cox-Merz rule can also be

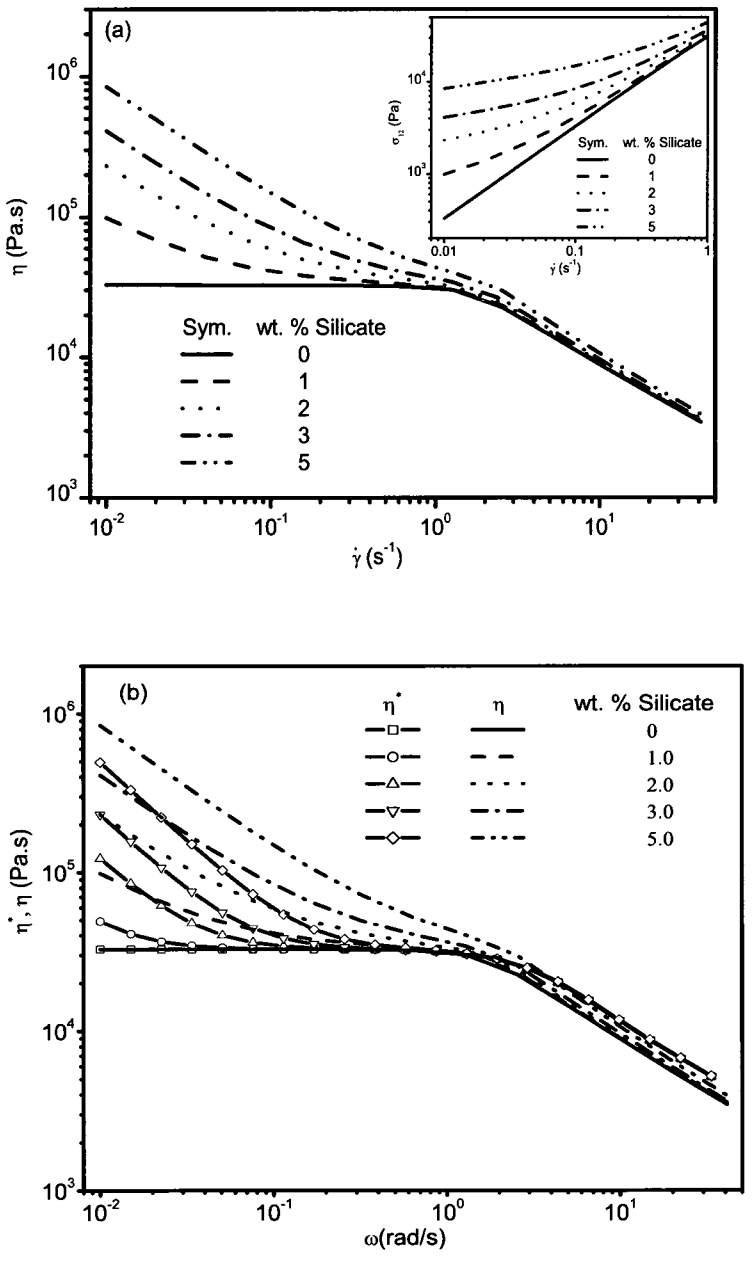

Figure 6.5: Effect of the nano-particle weight fraction on the (a) steady state viscosity (b) Cox-Merz relation

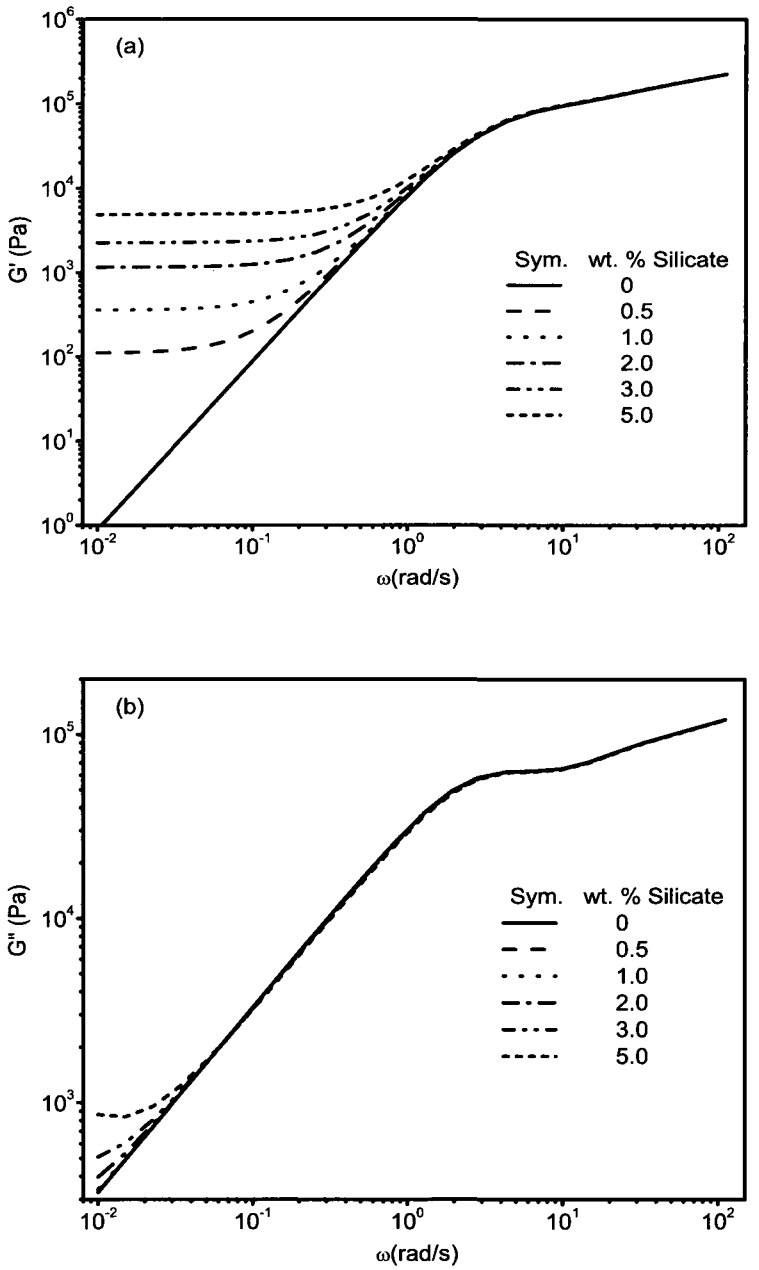

Figure 6.6: Effect of the nano-particle weight fraction on the (a) storage modulus G' (b) loss modulus G''

related to the formation of a network structure of silicate layers. An extension of the Cox-Merz rule concentrated suspensions and materials with a yield stress has been introduced by Doraiswamy et al. (1991). We hope to discuss this issue in near future.

Figures 6.6(a) and 6.6(b) represent the linear viscoelastic behavior as a function of the angular frequency for polymer nanocomposites at different nano-particle loading. As we have already seen in Figure 6.5(a), the flow behavior of nanocomposites differs significantly from the one corresponding to the pure matrix fluid in the nonlinear viscoelastic zone. Results of Figure 6.6(a) show that the storage modulus G' is dramatically influenced by the presence of silicate platelets while Figure 6.6(b) shows a lesser sensitivity of loss modulus G'' on the clay loading. As seen from Figure 6.6(a), the slopes of $\log G'$ versus $\log \omega$ are much smaller than 2 which is normally expected to be the case for noncrosslinked polymer melts. Such large deviation, which normally occurs in the presence of small amount of layered silicate loading, may be due to the formation of a clay network structure. In general, the model predictions are qualitatively consistent with experimental data for polymer layered silicate nanocomposites [Wu et al. (2005); Ayyer and Leonov (2004); Krishnamoorti et al. (2001); Ren and Krishnamoorti (2003)].

6.3.2 Comparison with experimental data

Model predictions are compared with a complete set of experimental data for polymer/layerd silicate nanocomposites in steady and oscillatory shear flows.

The experimental data has been taken from [Krishnamoorti et al. (2001); Ren and Krishnamoorti (2003)] where the rheological tests were performed over a wide rage of shear rate and angular frequency. In the comparison between model predictions and experimental data the model parameters are considered to be: $\Lambda_0^{11} = 2\times10^{-7}, \Lambda_0^{22} = 3\times10^{-6}, \widetilde{\Lambda_0^{22}} = 1.5\times10^{4}, \Lambda_0^{33} = 8\times10^{-10}, \Lambda_0^{13} = 2\times10^{-10}, \Lambda_0^{23} = 5\times10^{-10}, b = 2.5, \kappa = 10^{-25}, \kappa' = 10^{-25}, K_{flex} = 0.15, \chi = 800\,\alpha^{0.75}, \xi = 0.98, K = 3\times10^{5}$.

Figures 6.7(a)and 6.7(b) show the effect of clay loading on the steady state viscosity and first normal stress differences respectively. As can be seen in Fig. 6.7(a), this set of

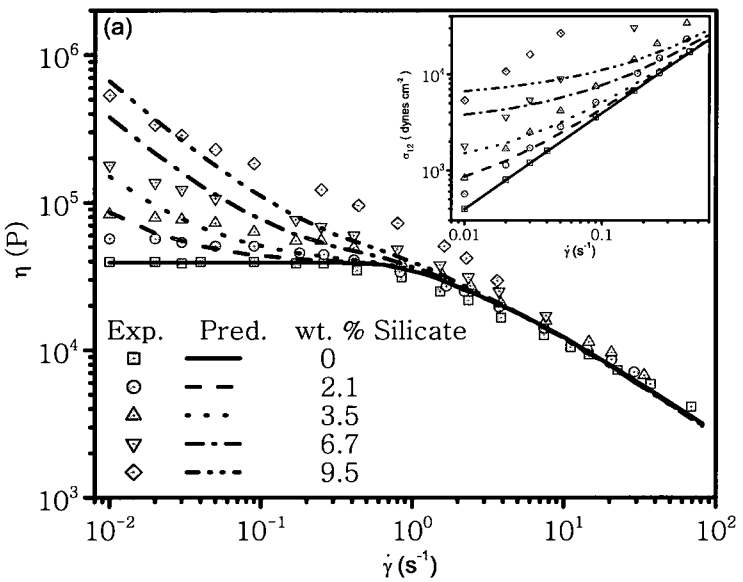
(a)
η (P)
γ̇ (s⁻¹)
Exp. Pred. wt. % Silicate
0
2.1
3.5
6.7
9.5
σ12 (dynes cm⁻²)
γ̇ (s⁻¹)

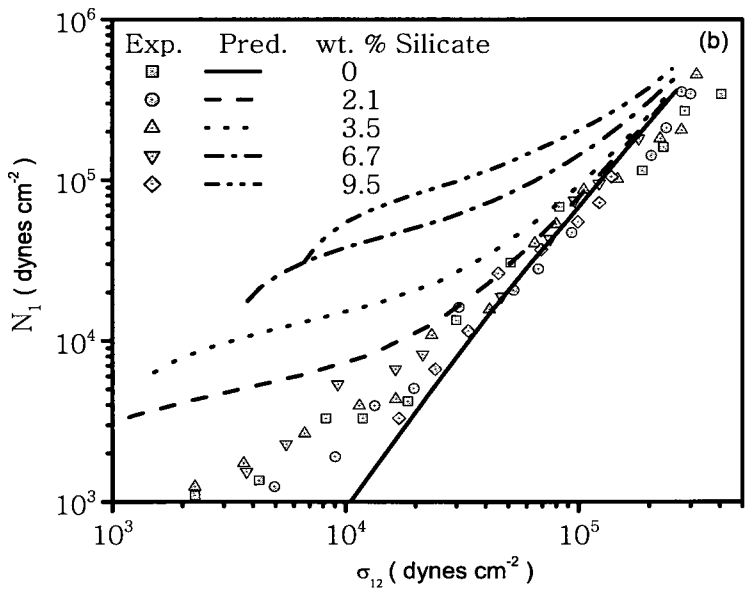
(b)
Exp. Pred. wt. % Silicate
0
2.1
3.5
6.7
9.5
N1 (dynes cm⁻²)
σ12 (dynes cm⁻²)

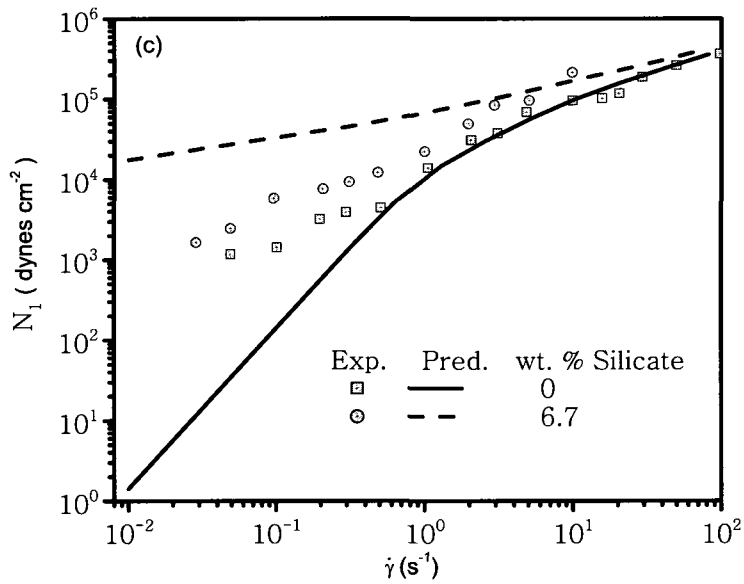

Figure 6.7: Model predictions and comparison with experimental data in steady shear flow (a) steady viscosity (b) steady first normal stress versus shear stress (c) steady first normal stress versus shear rate

experimental data is very well predicted by the model over the whole range of extended shear rates. In order to faithfully compare Model I and Model II, we use the same experimental data which has been used in (Eslami et al. 2007). We found that the prediction of Model II is much closer to experimental data than Model I, specially at high silicate loading.

The melt elasticity of polymeric systems can be measured by the first normal stress differences N_1. The effect of silicate loading on the elasticity of polymer nanocomposites has been previously investigated by measuring the dependence of N_1 on the clay loading [Gupta et al. (2005); Krishnamoorti et al. (2001); Ren and Krishnamoorti (2003)]. According to Gupta et al. (2005) in the case of exfoliated nanocomposites, the melt elasticity of nanocomposites decreases with increasing the clay loading. The authors claimed that this reduction of the elasticity may be related to the high interaction between clay layers and polymer chains in the case of exfoliated nanocomposites.

Krishnamoorti et al. (2001) and Ren and Krishnamoorti (2003) are also measured the first normal stress differences N_1 as a function of the shear stress at different clay loading. They reported that N_1 is independent of the silicate loading (see Figure 6.7(b)). The authors suggest that this observation can be a consequence of the flow induced orientation of silicate layers.

We also compared our model predictions with experimental data reported in [Krishnamoorti et al. (2001); Ren and Krishnamoorti (2003)]. As seen in Figure 6.7(b) our predictions do not agree with their observations. In other words, with increasing the clay loading the the first normal stress differences N_1 increases. We suggest that the increase of the value of N_1 is a consequence of the solid like behavior of nanocomposites (becoming stronger with increasing the clay loading). Our results show that at high shear stress (high shear rates) N_1 is nearly independent of the clay loading. This observation at high shear stress is in agreement with experimental observation in [Krishnamoorti et al. (2001); Ren and Krishnamoorti (2003)]. It should also be noted that an unusual decrease in N_1 is observed at very low shear rates.

In Figure 6.7(c) we plot N_1 versus shear rate where the model predictions are compared

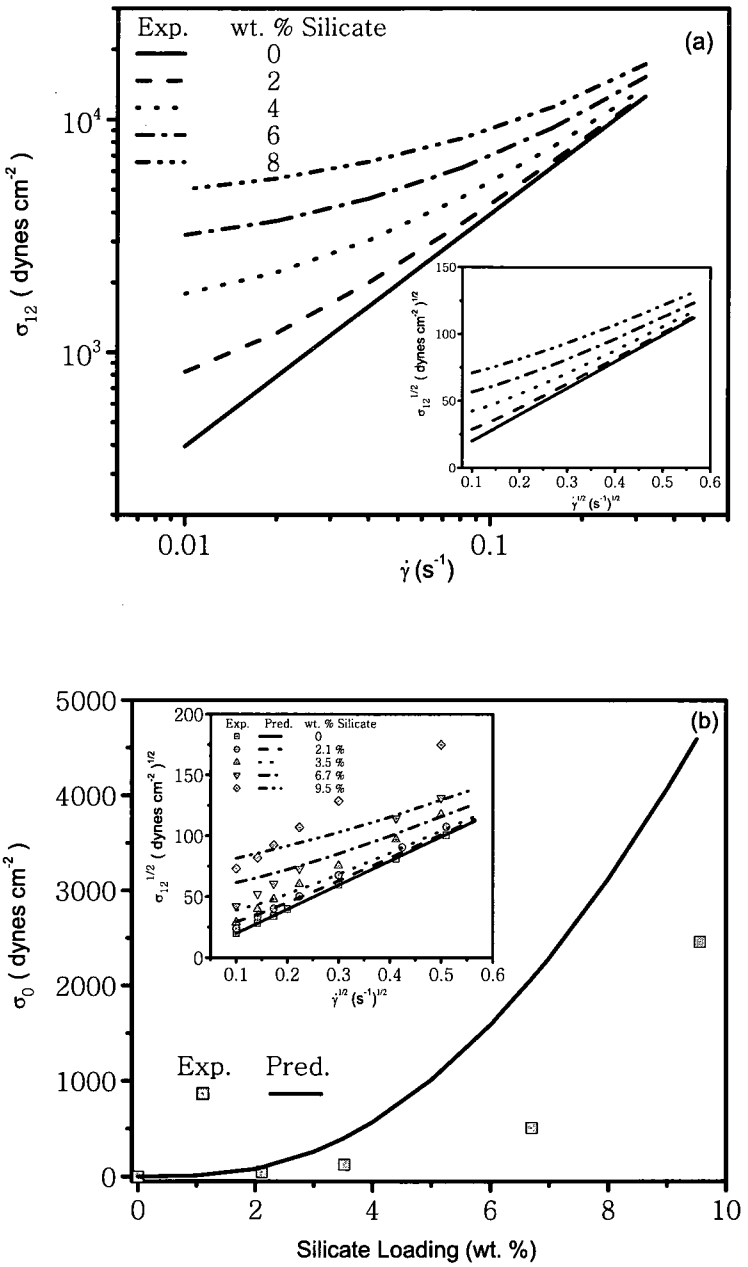

Figure 6.8: Model predictions and comparison with experimental data (a) Yield stress at different silicate loading, model predictions (b) Yield stress, comparison between model and experimental data.

with experimental data. Again, we see a less satisfactory agreement between the model predictions and the experimental data especially at low shear rates.

One of the highlighted characteristic of the rheology of filled polymer system, especially at high concentration, is the emergence of the yield stress. This means that at stresses that are lower than yield stress the suspension behaves like a solid (it deforms only elastically) while at stresses that are higher than the yield stress it behaves like a liquid. From the physical point of view, the emergence of the yield stress is related to high filler-filler interactions which becomes important at concentrated suspensions. According to Casson, the yield stress can be determined by the following equation [Malkin (1990)]:

$$\sigma_{12}^{1/2} = \sigma_0^{1/2} + \beta\, \dot{\gamma}^{1/2} \tag{6.17}$$

Where σ_0 is yield stress and β an arbitrary constant.

Figure 6.8(a) shows the prediction of the model for the shear stress versus shear rate at low shear rates where we calculate the yield stress. The yield stress is calculated by fitting Eq.(6.17) for different clay loading (see the small graph imbedded in Figure 6.8(a)).

Yield stresses predicted by the model are also compared with experimental data (see Figure 6.8(b)). The results indicate that the model predictions overestimate the yield stress especially at high silicate loadings. These results are qualitatively in agreement with highly shear thinning behavior of nanocomposites with high silicate loading at low shear rates (upward viscosity at low shear rates).

Model predictions are also compared with linear viscoelastic properties of polymer/layerd silicate nanocomposites obtained by Krishnamoorti et al. (2001) and Ren and Krishnamoorti (2003). The extension of the experimental angular frequency ω window was obtained using the time temperature superposition. The storage modulus G' and complex viscosity η^* are presented at the reference temperature $T_0 = 85°C$. Figures 6.9(a) and 6.9(b) show the model predictions with this set of experimental data. As it is clear from these figures, model is able to capture qualitatively the overall feature of polymer/layerd silicate nanocomposites, namely plateau in G' at low frequency and upward complex viscosity at low frequency. However, the

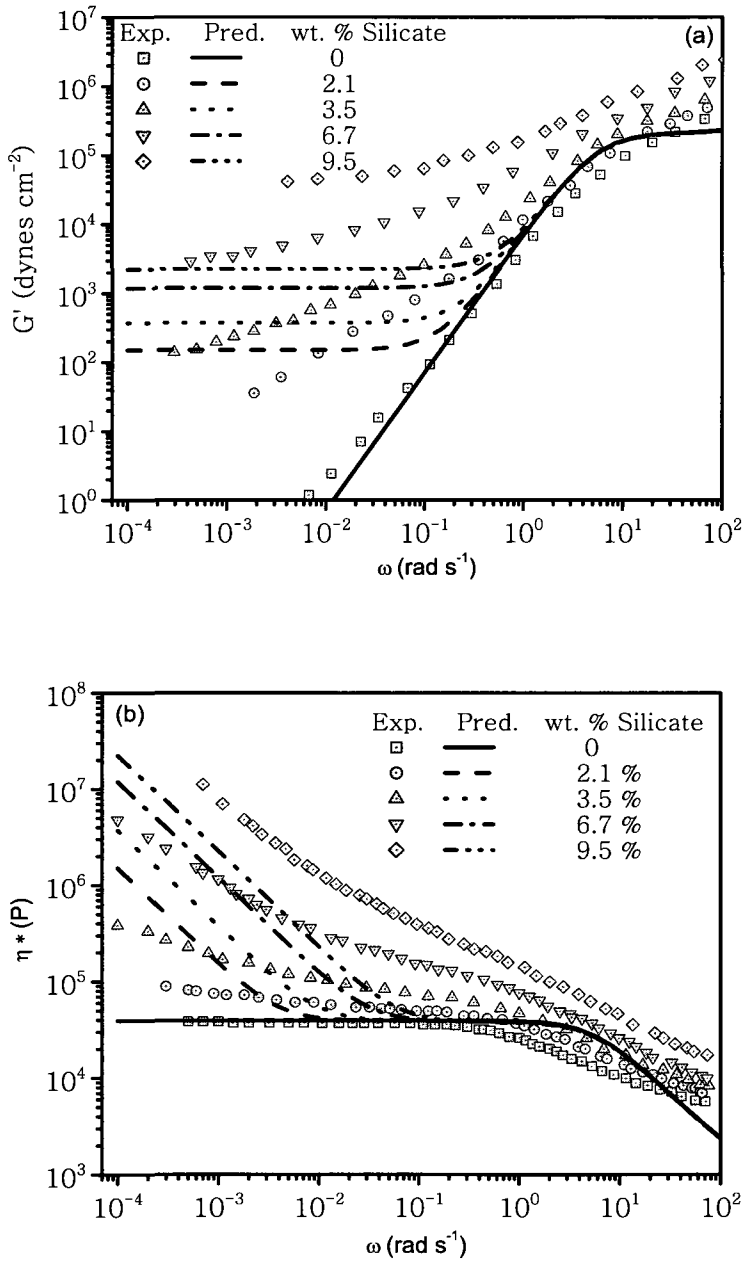

Figure 6.9: Model predictions and comparison with experimental data in oscillatory shear flow (a) storage modulus G' (b) complex viscosity η^*.

quantitative agreement is less satisfactory.

In general, the reasons for the less satisfactory agreement may be partially due to the fact that the silicate lamellae in experimentally prepared suspensions are rarely completely exfoliated and consequently some new physical processes, that are not included in our model, become important.

6.4 Conclusion

A mesoscopic rheological model of a spatially homogeneous and isothermal suspension of completely exfoliated clay lamellae in polymer melts is formulated. Due to polymer-polymer and polymer-plate interaction, macromolecules of the polymer melt are effectively confined into tube formed by other macromolecules and the plates. The mesoscopic formulation does not allow us however to enter into microscopic details of the mechanism involved in the lamellae participation in the reptating motion. The model is constructed by combining the mesoscopic rheological model of polymer/layered silicate nanocomposites [Eslami et al. (2007)] with the mesoscopic rheological model of melts composed of reptating macromolecules [Eslami and Grmela (2008)]. Having chosen the state variables, the model is formulated by, first, writing down a framework for the governing equations (guaranteeing the compatibility with mechanics and thermodynamics) and second, filling the framework by specifying the kinematics of the state variables, the free energy, and the dissipation potential. The mesoscopic level of description chosen in this paper appears to be a good compromise between microscopic details and overall simplicity of the governing equations. On the one hand, we are able to express in the model important features of the physics involved (like for example reptation of polymer chain, polymer-plate and plate-plate interactions) and on the other hand, the governing equations are easily solved numerically by standard software packages. The calculated rheological data for steady, transient and oscillatory shear flows are reported. The particular attention is payed to the region of low shear rate and low frequency. The results show that the model is able to capture the overall rheological behavior of polymer layered

silicate nanocomposites.

An important issue which still remains to be considered in more detail is the case when the lamellae are not completely exfoliated. The challenge is to identify the physical processes that become important in this situation and to express them in the model. The framework of the model will remain unchanged since we shall again require the agreement of model predictions with the observed compatibility with thermodynamics.

6.5 Appendix: GENERIC framework

Let x denote the state variables. If we limit ourselves to isothermal and incompressible fluids then the compatible with thermodynamics and mechanics time evolution of x is governed by [Grmela (1984, 1986, 1991); Beris and Edwards (1994); Grmela and Ottinger (1997); Ottinger and Grmela (1997); Grmela (2002); Ottinger (2005)]

$$\dot{x} = L\Phi_x - \frac{\partial \Xi}{\partial \Phi_x} \tag{6.18}$$

called in [Grmela and Ottinger (1997); Ottinger and Grmela (1997)] GENERIC. By $\dot{x}$ we denote the time derivative of x. The first term on the right hand side of (6.18) expresses the compatibility with mechanics, the second the compatibility with thermodynamics. The symbols appearing in (6.18) have the following meaning.

6.5.1 Free energy

$\Phi(x)$, a real valued function of x, has the physical meaning of the total free energy. By Φ_x we denote the derivative of Φ with respect to x.

6.5.2 Kinematics

The operator L, hereafter called a Poisson bivector, transforms a covector (a gradient of a potential) into a vector. From the physical point of view, L expresses kinematics of the state variables x. In the particular case of classical mechanics of particles (the state variables in

this case are $x = (p, q)$, where q are position vectors and p the momenta of the particles), $L = \begin{pmatrix} 0 & 1 \\ -1 & 0 \end{pmatrix}$. This is the Poisson bivector transforming in classical mechanics the gradient of energy $E(q, p)$ into a vector field. In the general setting, L is required to satisfy the following properties: $\{A, B\} =< A_x, LB_x >$ is a Poisson bracket, i.e. $\{A, B\} = -\{B, A\}$, and satisfies the Jacobi identity $\{A, \{B, C\}\} + \{B, \{C, A\}\} + \{C, \{A, B\}\} = 0$; A, B, C are sufficiently regular real valued functions of x, $<, >$ denotes the inner product.

6.5.3 Dissipation

$\Xi(\Phi_x)$, called a dissipation potential, is a sufficiently regular real valued function of Φ_x satisfying the following properties: (i) $\Xi(0) = 0$, (ii) Ξ reaches its minimum at 0, (iii) Ξ is concave in a neighborhood of 0.

6.5.4 Properties of solutions of GENERIC

The properties required from L, Ξ appearing in (6.18) imply that solutions to (6.18) satisfy the following inequality:

$$\frac{d\Phi}{dt} \leq 0 \tag{6.19}$$

The free energy Φ can thus only remain unchanged or decrease during the time evolution. To see that (6.19) indeed holds, we note that $\frac{d\Phi}{dt} =< \Phi_x, L\Phi_x > - < \Phi_x, \frac{\partial \Xi}{\partial \Phi_x} >\leq 0$. The last inequality follows from $< \Phi_x, L\Phi_x >= 0$ and from the properties required from the dissipation potential Ξ. The inequality (6.19) together with the thermodynamic stability requirement (i.e. Φ is a convex function of x) allows us to consider Φ as a Lyapunov function. This then means that solutions to (6.18) tend, as $t \to \infty$, to states that minimize the free energy (i.e. the states, called equilibrium states, that are solutions of $\Phi_x = 0$).

Acknowledgements

The authors acknowledge the financial support provided by the Natural Sciences and Engineering Research Council (NSERC) of Canada.

References

1. Ayyer RK, Leonov AI (2004) Comparative rheological studies of polyamide-6 and its low loaded nanocomposite based on layered silicates. Rheol Acta 43:283-292

2. Beris AN, Edwards BJ (1994) Thermodynamics of flowing systems. 1 st edn. Oxford University Press, New York

3. Beris AN, Edwards BJ (1990) Poisson bracket formulation of viscoelastic flow equations of differential type: A unified approach. J. Rheol 34:55-78

4. Bousmina M (2006) Study of intercalation and exfoliation processes in polymer nanocomposites. Macromolecules 39:4259-4263

5. De Gennes PG (1971) Reptation of a polymer chain in the presence of fixed obstacles. Journal of Chemical Physics 55:572-579

6. Edwards, BJ, Dressler M, Grmela M, Ait-Kadi A (2003) Rheological models with microstructural constraints. Rheol Acta 42:64-72

7. Doi M, Edwards SF (1986) The Theory of Polymer Dynamics. Oxford University Press, New York

8. Doraiswamy D, Mujumdar AN, Tsao I, Beris AN, Danforth SC, and Metzner AB (1991)The CoxMerz rule extended: A rheological model for concentrated suspensions and other materials with a yield stress. J. Rheol 35:647-685.

9. Eslami H, Ramazani A, Khonakdar HA (2004) Predictions of some internal microstructural models for polymer melts and solutions in shear and elongational flows. Macromol. Theory Simul 13:655-664

10. Eslami H, Ramazani A, Khonakdar HA (2003) Volume preserving conformational rheological models for multi-component miscible polymer blends using the GENERIC formalism. Macromol. Theory Simul 12:524-530

11. Eslami H, Grmela M, Bousmina M (2007) A mesoscopic rheological model of polymer/layered silicate nanocomposites. J. Rheol 51:1189-1222

12. Eslami H, Grmela M (2008) Mesoscopic formulation of reptation. Rheol Acta 47:399415.

13. Grmela M (1984) Particle and bracket formulations of kinetic equations. Contemp Math 28:125-132

14. Grmela M (1985) Stress tensor in generalized hydrodynamics. Phys Lett A 111:41-44

15. Grmela M (1986) Bracket formulation of diffusion-convection equations. Physica D 21:177-212

16. Grmela M (1990) Thermodynamic and rheological modeling: polymeric liquid crystals. In Collyer AA, Utracki LA (eds) Polymer rheology and processing, Elsevier, Amsterdam, pp 55-81

17. Grmela M (1991) Mesoscopic dynamic and thermodynamic: Application to polymer fluids. Lecture Notes in Physics 381:99-126

18. Grmela M (2002) Reciprocity relations in thermodynamics. Physica A 309:304-328

19. Grmela M, Ottinger HC (1997) Dynamics and thermodynamics of complex fluids. I. Development of a general formalism. Phys Rev E 55:6620-6632

20. Gu JF, Grmela M (2008) GENERIC model of active advection. J. Non-Newtonian Fluid Mech. 152:12-26.

21. Gupta RK, Pasanovic-Zujo V, Bhattacharya SN (2005) Shear and extensional rheology of EVA/layered silicate-nanocomposites. J. Non-Newtonian Fluid Mech 128:116-125

22. Khokhlov AR Semenov AN (1985) On the theory of liquid-crystalline ordering of polymer chains with limited flexibility. Journal of Stat Phys 38:161-182

23. Krishnamoorti R, Ren J, Silva AS (2001) Shear response of layered silicate nanocomposites. J. Chem. Phys 114:4968-4972

24. Likhtman AE, McLeish TCB (2002) Quantitative theory for linear dynamics of linear entangled polymers. Macromolecules 35:6332-6343.

25. Malkin AY (1990) Rheology of filled polymer. Advances in polymer science. 96:69-97

26. McLeish TCB (2002) Tube theory of entangled polymer dynamics. Advances in Physics. 51:1379-1527

27. Ottinger HC (2005) Beyond Equilibrium Thermodynamics. Wiley

28. Ottinger HC, Grmela M (1997) Dynamics and thermodynamics of complex fluids. II. Illustrations of a general formalism. Phys. Rev.E 56:6633-6655

29. Ren J, Krishnamoorti R (2003) Nonlinear viscoelastic properties of layered silicate based intercalated nanocomposites. Macromolecules 36:4443-4451

30. Wolfram S (1991) Mathematica-A system for doing mathematics by computer. 2nd ed., Wesley-VCH, New York

31. Wu D, Zhou Ch, Hong Z, Mao D, Bian Z (2005) Study on rheological behaviour of poly(butylene terephthalate)/montmorillonite nanocomposites. European Polymer Journal 41:2199-2207

CHAPTER 7

LINEAR AND NONLINEAR RHEOLOGY OF POLYMER/LAYERED SILICATE NANOCOMPOSITES

Hassan Eslami[a], Miroslav Grmela[a1] , Mosto Bousmina[b,c]

[a] Center for Applied Research on Polymers and Composites (CREPEC)

Ecole Polytechnique de Montreal, C.P.6079 suc. Centre-ville,

Montreal, H3C 3A7, Quebec, Canada

[b] Canada Research Chair on Polymer Physics and Nanotechnology

and Center for Applied Research on Polymers and Composites (CREPEC)

Department of Chemical Engineering, Laval University, Ste-Foy,

G1K 7P4, Quebec, Canada

[c] Hassan II Academy of Sciences and Technology, Rabat, Marocco

Submitted to Journal of Rheology

[1]corresponding author: e-mail: miroslav.grmela@polymtl.ca

Abstract

Linear and nonlinear (in both steady and transient shear flows) rheological properties of polymer/layered silicate nanocomposites prepared by melt mixing of poly[butylene succinate-co-adipate] and organically modified montmorillonite are investigated. Morphology of the nanocomposites is observed by X-ray diffraction and by transmission electron microscopy. Linear viscoelastic measurements in oscillatory shear with small strain amplitude show a low frequency plateau for storage modulus (an indication of a pseudo-solid like structure). A strong shear-thinning behavior for all ranges of shear rates is observed for high clay loading. An unusual behavior is observed for steady state normal stress differences. At low shear rate their values are greater than those observed for pure polymer. An inverse relation is observed at relatively high shear rates. The two models [Eslami et al. J.Rheol.(2007) and Rheol. Acta (2009)] that we have developed previously allow us to relate the observed rheological behavior to the physics taking place in the nanocomposites on a mesoscopic level. The models take into account the polymer chain-polymer chain, polymer chain-lamella and lamella-lamella interactions. With their help, we are also able to separate contributions from the polymer and the nano charge.

7.1 Introduction

We report a new set of experimental data for polymer/layered silicate nanocomposites together with their evaluation made with the help of two mesoscopic models that we have developed previously. The experimental data contribute to the large pool of the data existing in literature for polymer/layered silicate nanocomposites by an original choice of the polymer (of particular interest due to its biodegradability) and by their completeness (that we need for the comparison with model predictions). We report results of both linear and nonlinear (in both steady and transient shear flows) rheological measurements.

The physical picture that has been suggested and that we anticipate to confirm and complement is the following: due to the small size of the suspended nanoparticles, their number

density is very high even in relatively small volume fraction suspensions. Consequently, the particle-particle and the particle-polymer interactions play in the suspensions an important role. In particular, in the absence of driving forces, the nanoparticles tend to form clusters that are then responsible for certain characteristic to nanocomposites rheological behavior as for example the lack of plateau in the viscosity at steady shear flows at low shear rates. Under the influence of larger external forces, the clusters disintegrate and smaller formations (up to single lamellae) begin to play the dominant role. After cessation of the externally applied forces, the larger clusters are again formed.

What is the rheological model in which we could express the above physical picture and, at the same time, calculate relatively easily its rheological consequences? The first model of this type, developed in Eslami et al. (2007) and called hereafter Model I, uses one conformation tensor $\boldsymbol{a}$ to denote states of the silica plates and one conformation tensor $\boldsymbol{c}$ to denote states of the polymer macromolecules. The model takes into account the plate-plate and the plate-polymer interactions as well as the flexibility of the lamellae. The second model, developed in Eslami et al. (2009b) and called hereafter Model II, extends Model I by replacing the polymer macromolecules modeled as FENE-P dumbbells in Model I by chains. In the mathematical formulation this extension is made (following Eslami and Grmela (2008)) by replacing $\boldsymbol{c}$ with $\boldsymbol{c}(s)$, where $s \in \mathbb{R}$ is a one dimensional parameter denoting the coordinate along the backbone of the chain. From the physical point of view, this extension allows us to include nonlocal intramolecular interactions and the collective behavior of the macromolecules manifested in the formation of tube-like constraints in which both the chains and the lamellae participate. In the next extension, called Model III, we should bring in also the collective nature of the lamellae. Following the extension $\boldsymbol{c} \rightarrow \boldsymbol{c}(s); s \in \mathbb{R}$, we can suggest the extension $\boldsymbol{a} \rightarrow \boldsymbol{a}(\zeta); \zeta \in \mathbb{R}^3$, where ζ is a three dimensional coordinate in the network-like clusters formed from the lamellae. In addition, Model III has to include dynamics (absent in the case of chains) of their creation and annihilation (induced by the imposed flow).

In this paper we remain with only Model I and Model II because of the feasibility of making all the numerical calculations needed to derive model predictions. Since our objective is to

deal with a large pool of experimental data, we need to find many solutions of the governing equations. The effort needed to find them increases considerably already in the extension from Model I to Model II. The effort will undoubtedly further increase in the extension from Model II to Model III. We hope to present Model III as well as a limited number of its predictions in a future paper. In this paper we shall express the collective behavior of the lamellae by taking advantage of the mesoscopic nature of Model I and Model II. We reinterpret $\boldsymbol{a}$ as well as the interactions and the material parameters involved in Model I and Model II as quantities referring to larger entities than single lamellae.

The paper is organized as follows: First, the experimental procedure is explained in Section 7.2. Next, in Section 7.3, the two recently developed mesoscopic rheological models [Eslami et al. (2007, 2009b)] are briefly recalled and extended to incompletely exfoliated nanocomposites. Finally, in Section 7.4, the experimental results are presented and compared with predictions of the two extended models.

7.2 Experimental

7.2.1 Materials

Polymer matrix in this study is poly (butylene succinate-co-adipate) (PBSA), a commercial product from Showa High Polymer Ltd, Japan, with the designation BIONOLLE 3001. According to the supplier, PBSA has a molecular weight 190 kg/mol and mass density of 1230 kg/m^3. The organically modified montmorillonite (OMMT) used in this study is Cloisite 30B (C30B) supplied by Southern Clay products. According to the supplier, Cloisite 30B is treated with surfactant having the chemical structure: methyl, tallow, bis(2-hydroxyeethyl), quaternary ammonium chloride. The organic content in C30B reported by supplier is 30 wt.%. We have verified this percentage of the organic content by using both thermal gravimetry analysis (TGA) and by burning the samples in the furnace at the temperature 800 $°C$. Both PBSA and C30B were dried under vacuum at 50 $°C$ for 72 hours prior to the process.

This particular combination of polymer matrix and organically modified montmorillonite is chosen for three reasons: first, because of the biodegradability nature of PBSA, second, because of the strong interaction between the "CO" group on the PBSA and the diols on the Cloisite 30B which make them compatible, and third, because of a relatively easy processability of PBSA in the melt state at relatively low temperature. The "green" feature of PBSA makes it a promising polymer for various applications such as: grocery, bags for waste composting, mulch films, service ware, molded objects and a lot more. However, its properties (e.g. mechanical properties, barrier properties, ...) for end-use applications need to be improved [Sinha Ray and Bousmina (2005a)]. These improvements can partially be achieved by making its nanocomposites with clay layers while its biodegradation ability in the soil is retained [Steeves et al. (2007)].

7.2.2 Nanocomposite preparation

The nanocomposites were prepared by melt mixing of PBSA and C30B using thermo Haake mixer operated at 150 °C under nitrogen purge. PBSA and C30B were mixed at the rotor speed of 90 rpm for 10 min. Four compositions with silicate concentrations of 1.5± 0.1, 3.4± 0.1, 5.7± 0.1 wt % and 7.3± 0.1 wt % were prepared by using PBSA and C30B. Hereafter, these four nanocomposites are abbreviated as PBSAC30BN1,PBSAC30BN2, PBSAC30BN3 and PBSAC30BN4 that correspond to PBSA/C30Bs with silicate concentrations of 1.5, 3.4, 5.7wt % and 7.3wt % respectively. The silicate concentrations were determined by using both TGA and furnace as we explained before.

In order to have a reference sample, the pure PBSA was also processed at the same condition. The processed samples were dried under vacuum at 50 °C for 12 h in order to remove any possible residual water. Dried samples were then converted in discs with diameter 25 mm and thickness of around (1.5-2) mm with a laboratory press operated at 3 MPa and 150 °C for 10 min. (5 min. preheating and 5 min. under pressure) under nitrogen purge. The molded samples were cooled between metal plates in cold press and dried again under vacuum at 50 °C for 24 h and then kept in the desiccator under vacuum at room temperature

for further tests.

7.2.3 X-ray diffraction

The mean interlayer spacing of the (001) plane, d_{001}, for organically modified montmorillonite and nanocomposites were determined by X-ray diffraction (XRD) using a Philips X'pert diffractometer (Cu Kα radiation λ = 1.54 $°A$, generator voltage = 50 kV, current = 40 mA). For the reference, a test was also performed for pure PBSA. Disc shape samples of approximately 2 mm thickness were used for pure PBSA and its nanocomposites. Cloisite 30B was studied in the form of powder. The scans were performed in 2θ ranges from 1 ° to 10 ° at a rate of 1/min.

7.2.4 Transmission electron microscopy

The nanoscale structure of the nanocomposite was investigated by high resolution transmission electron microscopy (TEM) (JEOL model JEM-2100F) operated at an accelerating voltage of 200 kV without staining. The ultrathin sectioning (around 40-60 nm) was performed in liquid nitrogen at $T = -100\ °C$ with a diamond knife.

7.2.5 Rheological measurements

All rheological measurements were performed in a strain-controlled rheometer (TA Instruments, ARES), with parallel plate geometry (25 mm diameter). A specimen was first let to rest in the parallel plate fixture for 15 min. and then the gap was adjusted to 1.3 mm by gradually squeezing the sample. Temperature in the rheological experiments was kept at 140 $°C$ unless otherwise specified. Linear viscoelastic domain for PBSA and all nanocomposites were carefully determined by performing dynamic strain sweep test at two different frequencies (1 rad/s and 10 rad/s) for a wide range of strain. A critical strain was specified for each material where storage modulus G' was decreased less than 5 % of its value at small strain and then all the linear viscoelastic measurements were performed at the specified critical strain.

Following Vermant et al. (2007) thermal stability of the polymer matrix and nanocomposites were investigated by performing dynamic time sweep at high frequency (100 rad/s) to avoid interference between changes in the structure of nanocomposites and thermal degradation of the polymer matrix and surfactant. Dynamic time sweep test was performed for a period of 1 hour while storage modulus and complex viscosity η^* were monitored. Variation in G' and η^* was less than 5 % for this period of time. Dynamic frequency sweep experiments were performed in the linear viscoelastic regime in the frequency between 0.01 and 100 rad/s.

Nonlinear rheological measurements were performed in sequential tests. In order to remove the flow history during the sample preparation and loading, a pre-shear ($\dot{\gamma} = 0.1s^{-1}$), was applied to the sample until a steady state was reached and then the sample was let to relax. During the relaxation, both the shear stress and the normal force were monitored to ensure that they remain unchanged before proceeding to the next step. Nonlinear transient rheological tests (start-up and relaxation) were then performed at different shear rates ($\dot{\gamma}$ = 0.01, 0.025, 0.05, 0.1, 0.2, 0.5, 1, 2 s^{-1}). For each test a fresh sample was used. Steady flow curves (steady state viscosity and steady state normal stress differences versus shear rate) were then obtained from the steady state values of the start-up tests.

7.3 Modeling

In this section we recall Model I and Model II [Eslami et al. (2007, 2009b)] and adapt them to incompletely exfoliated polymer/layered silicate nanocomposites. The material parameters that we use to characterize the individual nature of the nanocomposits are introduced in the models. The way they arise in the models also determines their physical interpretation. In Section 7.4 we shall find their values by comparing model predictions with results of observations.

7.3.1 Model I

The physical systems investigated in Model I are incompressible and isothermal suspensions of homogeneously distributed and completely exfoliated clay lamellae in polymer melts. States of the macromolecules composing the polymeric matrix are described by a conformation tensor $\boldsymbol{c}$ (a symmetric and positive definite three-by-three tensor) that is the second moment (in the end-to-end vector of the macromolecule) of the distribution function of the macromolecules. States of the suspended lamellae are characterized by another conformation tensor $\boldsymbol{a}$ (also a symmetric and positive definite three-by-three tensor that is moreover constrained by the relation $tr\boldsymbol{a} = A_0$; where A_0 is the surface area of the clay platelet) that is the second moment (in the unit vector perpendicular to the lamellae) of the distribution function of the lamellae. The constraint $tr\boldsymbol{a} = A_0$ expresses the fact that the area of the lamellae remains constant (i.e. the vector perpendicular to the lamella is a unit vector). The complete set of state variables in the Model I is: $(\boldsymbol{u}(\boldsymbol{r}), \boldsymbol{c}, \boldsymbol{a})$, where $\boldsymbol{u}(\boldsymbol{r})$ is the momentum field of the suspension, $\boldsymbol{r}$ is the position vector.

Having chosen the state variables, the time evolution equations are constructed by invoking the requirement of the compatibility of thermodynamics according to which solutions to the governing equations of the model should agree with observations representing experimental basis of equilibrium thermodynamics (i.e. the observation that the suspension, if left undisturbed, reaches a state at which its behavior is found to be well described by equilibrium thermodynamics). It has been shown [Grmela (1984, 1986, 1991, 2002); Beris and Edwards (1994); Grmela and Ottinger (1997); Ottinger and Grmela (1997); Ottinger (2005)] that this requirement provides a framework (called in [Grmela and Ottinger (1997); Ottinger and Grmela (1997)] GENERIC) for the governing equations. To fill out the framework the kinematics of the state variables (expressed mathematically in a Poisson bracket), the dissipation potential Ξ, and the free energy Φ must be specified. The kinematics is uniquely associated with the state variables. Since the choice of state variables is fixed, the kinematics is fixed (i.e. no adjustable parameters are involved in the kinematics). The one parameter

ξ, that is involved in the kinematics of $\boldsymbol{a}$, arises due to the nonaffine (i.e. non Hamiltonian) advection of the lamellae. The individual nature of the polymer matrix, clay lamellae, and their interactions are expressed in the model in the parameter ξ, in the free energy Φ, and in the dissipation potential Ξ. Here the final time evolution equations and parameters therein will be explicitly written. The detail of the physics behind in the formulation is out of the scope of this work and interested reader is referred to Eslami et al. (2007).

Total free energy of the suspension of clay lamellae in polymer melt is specified as follow:

$$\begin{aligned}\Phi \;=\; & -\frac{1}{2}n_c H Q_0^2 \ln\left[1 - tr\left(\frac{\boldsymbol{c}}{Q_0^2}\right)\right] - \frac{1}{2}n_c k_B T \ln\left[\det\left(\frac{\boldsymbol{c}}{Q_0^2}\right)\right] \\ & -\frac{1}{2}n_a G A_0 tr\left(\frac{\boldsymbol{a}}{A_0}\right) - \frac{1}{2}n_a k_B T\left(1 - K_{flex}\right)\ln\left[\det\left(\frac{\boldsymbol{a}}{A_0}\right)\right] \\ & +\frac{1}{2}n_a k_B T K_{flex} tr\left(A_0 \boldsymbol{a}^{-1}\right) - \frac{1}{2}n_a^2 k_B T \kappa\left[tr\left(\frac{\boldsymbol{a}}{A_0}\cdot\frac{\boldsymbol{a}}{A_0}\right) - \left(tr\frac{\boldsymbol{a}}{A_0}\right)^2\right] \\ & +\frac{1}{2}n_c n_a k_B T \kappa' tr\left(\frac{\boldsymbol{c}}{Q_0^2}\cdot\frac{\boldsymbol{a}}{A_0}\right) \end{aligned} \tag{7.1}$$

The symbols appearing in (7.1) have the following meaning: k_B is the Boltzmann constant, T is the temperature, Q_0 is the largest extension of the dumbbell, H is the elastic modulus of the dumbbell spring, n_c is the number density of the polymer macromolecules and n_a is the number density of clay lamellae ($n_c = \frac{(1-\alpha)\rho_c N_A}{M_c}$; $n_a = \frac{\alpha}{A_0 h}$, N_A is the Avogadro number, M_c is the molecular weight of the polymer, ρ_c is the mass density of the polymer, α is the clay volume fraction, A_0 is the surface area of the lamella and h its thickness), κ and κ' are phenomenological parameters measuring the topological plate-plate and polymer-plate interactions, K_{flex} is a phenomenological parameter expressing the flexibility of clay platelets and tr and det are the trace and determinant.The choice of the parameters entering the free energy (7.1) is restricted by requiring the thermodynamic stability, i.e. by requiring that its second derivative is positive definite.

In the terminology of non-equilibrium thermodynamic, the derivatives of the free energy with respect to state variables are called thermodynamic forces which drive, in the absence of external forces, the system to equilibrium. For the states that are not too far from equilibrium (i.e. the states for which Φ_c and Φ_a are not too large), dissipation potential Ξ can be chosen

to be the following quadratic function of the thermodynamic forces:

$$\Xi = (\Phi_{\boldsymbol{c}} \quad \boldsymbol{A}) \begin{pmatrix} \frac{\boldsymbol{\Lambda}^{cc}}{1-\alpha} & \frac{\boldsymbol{\Lambda}^{ca}}{\alpha(1-\alpha)} \\ \\ \frac{\boldsymbol{\Lambda}^{ca}}{\alpha(1-\alpha)} & \frac{\boldsymbol{\Lambda}^{aa}}{\alpha} \end{pmatrix} \begin{pmatrix} \Phi_{\boldsymbol{c}} \\ \\ \boldsymbol{A} \end{pmatrix} \tag{7.2}$$

where $\boldsymbol{\Lambda}^{cc}$, $\boldsymbol{\Lambda}^{aa}$, and $\boldsymbol{\Lambda}^{ca}$ are phenomenological mobility tensors representing the friction coefficients in polymer macromolecules, clay lamellae and polymer-lamellae coupling respectively. $\boldsymbol{A}$ is a quantity depending on $\Phi_{\boldsymbol{a}}$ in such a way that the constraint $tr\boldsymbol{a} = A_0$ is preserved during the dissipative time evolution. It is easy to verify that by choosing $\boldsymbol{A} = \Phi_{\boldsymbol{a}} - \frac{1}{3}tr\Phi_{\boldsymbol{a}}\boldsymbol{\delta}$ the condition $tr\left(\Xi_{\Phi_{\boldsymbol{a}}}\right) = 0$ is satisfied.

The mobility tensors are proposed to be polynomial functions of $\boldsymbol{c}$ and $\boldsymbol{a}$:

$$\begin{aligned} \boldsymbol{\Lambda}^{cc} &= \Lambda_0^{cc}\left(\widehat{\boldsymbol{c}\boldsymbol{\delta}} + \widehat{\boldsymbol{c}\boldsymbol{c}}\right) \\ \boldsymbol{\Lambda}^{aa} &= \Lambda_0^{aa}\left(f_1\widehat{\boldsymbol{a}\boldsymbol{\delta}} + f_2\widehat{\boldsymbol{a}\boldsymbol{a}} + f_3\widehat{\boldsymbol{a}\boldsymbol{a}\boldsymbol{a}}\right) \\ \boldsymbol{\Lambda}^{ca} &= \Lambda_0^{ca}\widehat{\boldsymbol{c}\boldsymbol{a}} \end{aligned} \tag{7.3}$$

where $\boldsymbol{\Lambda}$ are all fourth order tensors, $\widehat{\ }$ means symmetrization in the four indices, and Λ_0^{cc}, Λ_0^{aa} and Λ_0^{ca} are phenomenological parameters. The coefficients f_1, f_2, f_3 equal either 0 or 1.

Leaving the free energy Φ unspecified, equations governing the time evolution of $\boldsymbol{c}$ and $\boldsymbol{a}$ take the form:

$$\begin{aligned} \frac{d\boldsymbol{c}}{dt} &= -\frac{1}{2}\left(\boldsymbol{\Omega}\cdot\boldsymbol{c} - \boldsymbol{c}\cdot\boldsymbol{\Omega}\right) + \frac{1}{2}\left(\dot{\boldsymbol{\gamma}}\cdot\boldsymbol{c} + \boldsymbol{c}\cdot\dot{\boldsymbol{\gamma}}\right) \\ &\quad -\frac{8\,\Lambda_0^{cc}}{(1-\alpha)}\left(\frac{1}{2b}\left(\boldsymbol{c}\cdot\Phi_c + \Phi_c\cdot\boldsymbol{c}\right) + \frac{1}{b^2}\boldsymbol{c}\cdot\Phi_c\cdot\boldsymbol{c}\right) \\ &\quad -\frac{4\,\Lambda_0^{ca}}{\alpha(1-\alpha)\,b}\left(\frac{1}{6}(\boldsymbol{c}\,.\,\Phi_a\,.\,\boldsymbol{a} + \boldsymbol{a}\,.\,\Phi_a\,.\,\boldsymbol{c})\right. \\ &\quad \left. +\frac{1}{18}(\boldsymbol{a}\,.\,\boldsymbol{c} + \boldsymbol{c}\,.\,\boldsymbol{a})\,tr\Phi_a)\right) \\ \frac{d\boldsymbol{a}}{dt} &= -\frac{1}{2}\left(\boldsymbol{\Omega}\cdot\boldsymbol{a} - \boldsymbol{a}\cdot\boldsymbol{\Omega}\right) + \xi\left(-\frac{1}{2}\left(\dot{\boldsymbol{\gamma}}\cdot\boldsymbol{a} + \boldsymbol{a}\cdot\dot{\boldsymbol{\gamma}}\right) + \frac{1}{3}tr(\boldsymbol{a}\,.\,\dot{\boldsymbol{\gamma}})\boldsymbol{a}\right) \\ &\quad -\frac{8\,\Lambda_0^{aa}}{\alpha}\left[\frac{f_1}{3}\left(\frac{1}{2}(\boldsymbol{a}\cdot\Phi_a + \Phi_a\cdot\boldsymbol{a}) - \frac{1}{3}\boldsymbol{\delta}tr(\boldsymbol{a}\cdot\Phi_a) - \frac{1}{3}\boldsymbol{a}tr\Phi_a + \frac{1}{9}\boldsymbol{\delta}tr\boldsymbol{a}tr\Phi_a\right)\right. \\ &\quad +\frac{f_2}{9}\left(\boldsymbol{a}\cdot\Phi_a\cdot\boldsymbol{a} - \frac{1}{3}\boldsymbol{\delta}tr(\boldsymbol{a}\cdot\Phi_a\cdot\boldsymbol{a}) - \frac{1}{3}\boldsymbol{a}\cdot\boldsymbol{a}tr\Phi_a + \frac{1}{9}\boldsymbol{\delta}tr(\boldsymbol{a}\cdot\boldsymbol{a})tr\Phi_a\right) \end{aligned} \tag{7.4}$$

$$+\frac{f_3}{27}\left(\frac{1}{2}(\boldsymbol{a}\cdot\Phi_a\cdot\boldsymbol{a}\cdot\boldsymbol{a}+\boldsymbol{a}\cdot\boldsymbol{a}\cdot\Phi_a\cdot\boldsymbol{a})-\frac{1}{3}\boldsymbol{\delta}tr(\boldsymbol{a}\cdot\boldsymbol{a}\cdot\Phi_a\cdot\boldsymbol{a})\right.$$
$$\left.-\frac{1}{3}\boldsymbol{a}\cdot\boldsymbol{a}\cdot\boldsymbol{a}tr\Phi_a+\frac{1}{9}\boldsymbol{\delta}tr(\boldsymbol{a}\cdot\boldsymbol{a}\cdot\boldsymbol{a})tr\Phi_a\right)\Bigg]$$
$$-\frac{4\,\Lambda_0^{ca}}{\alpha(1-\alpha)\,b}\left(\frac{1}{6}(\boldsymbol{c}\,.\,\Phi_c.\boldsymbol{a}+\boldsymbol{a}\,.\,\Phi_c\,.\,\boldsymbol{c})-\frac{1}{9}\,\boldsymbol{\delta}\,tr(\boldsymbol{c}\,.\,\Phi_c\,.\,\boldsymbol{a})\right) \tag{7.5}$$

It should be noted that the expression for the extra stress tensor $\boldsymbol{\sigma}$

$$\boldsymbol{\sigma}=-2\,\boldsymbol{c}\,.\,\Phi_c+2\,\xi\,\left(\boldsymbol{a}.\Phi_a-\frac{1}{3}\,\boldsymbol{a}\,tr(\boldsymbol{a}\,.\,\Phi_a)\right) \tag{7.6}$$

arises automatically as a part of the time evolution equations. The following notation is used: $\dot{\gamma}_{\alpha\beta}=\frac{\partial v_\alpha}{\partial r_\beta}+\frac{\partial v_\beta}{\partial r_\alpha}$ and $\boldsymbol{\Omega}_{\alpha\beta}=\frac{\partial v_\alpha}{\partial r_\beta}-\frac{\partial v_\beta}{\partial r_\alpha}$, $\boldsymbol{v}(\boldsymbol{r})$ is the overall velocity field, ξ is the Gordon-Schowalter phenomenological parameter representing the nonaffine advection of the clay platelets.

7.3.2 Model II

The physical systems investigated in the Model II are the same as in Model I. In order to express more faithfully the physics involved in low shear rates and low frequencies, the FENE-P dumbbells representing the macromolecules in Model I are replaced by reptating chains whose motion is constrained by a tube formed by surrounding chains and surrounding lamellae. Model II as well as Model I are constructed by using the modular framework of GENERIC.

States of the molecular chains composing the melt are chosen to be described by the conformation tensor $\boldsymbol{c}(s,t)$ where $-1<s<+1$ is the parameter along the backbone of the chain, $\boldsymbol{c}(s)$ is the second moment of the distribution function $\psi(\boldsymbol{R},s)$ (i.e. $c_{ij}(s)=\int d\boldsymbol{R}R_iR_j\psi(\boldsymbol{r},s)$), where $\boldsymbol{R}$ is the tangent vector to the backbone at s. The end points of the chains are assumed to be at equilibrium at all times independently of the imposed flow. From the physical point of view, this means that the end points of the chain evolve in time much faster than the whole chain and we thus assume that on the scale on which we observe the fluid and the chains the end points are always at equilibrium. The conformation tensor $\boldsymbol{a}$,

describing sates of the lamellae, is the same as in Model I. The complete set of state variables is thus:

$$(\boldsymbol{u}(\boldsymbol{r}),\ \boldsymbol{c}(s),\ \boldsymbol{a})\,;\quad tr(\boldsymbol{a}) = 1 \tag{7.7}$$

The first step in finding equations governing the time evolution of the state variables (7.7) is to identify their kinematics formulated in terms of Poisson brackets. From the kinematics of these state variables the following time evolution equations are obtained:

$$\begin{aligned}\frac{\partial \boldsymbol{c}}{\partial t} &= -\frac{1}{2}(\boldsymbol{\Omega}\cdot\boldsymbol{c}-\boldsymbol{c}\cdot\boldsymbol{\Omega}) + \frac{1}{2}(\dot{\boldsymbol{\gamma}}\cdot\boldsymbol{c}+\boldsymbol{c}\cdot\dot{\boldsymbol{\gamma}}) \\ &\quad -\frac{\partial \Xi}{\partial \Phi_{\boldsymbol{c}}} \end{aligned} \tag{7.8}$$

$$\begin{aligned}\frac{d\boldsymbol{a}}{dt} &= -\frac{1}{2}(\boldsymbol{\Omega}\cdot\boldsymbol{a}-\boldsymbol{a}\cdot\boldsymbol{\Omega}) + \xi\left(-\frac{1}{2}(\dot{\boldsymbol{\gamma}}\cdot\boldsymbol{a}+\boldsymbol{a}\cdot\dot{\boldsymbol{\gamma}}) + tr(\boldsymbol{a}\,.\,\dot{\boldsymbol{\gamma}})\boldsymbol{a}\right) \\ &\quad -\frac{\partial \Xi}{\partial \Phi_{\boldsymbol{a}}} \end{aligned} \tag{7.9}$$

and the expression for the extra stress tensor $\boldsymbol{\sigma}$:

$$\sigma_{\alpha\beta} = -2\int_{-1}^{1} ds\; c_{\alpha\varepsilon}\Phi_{c_{\varepsilon\beta}} + 2\,\xi\; a_{\alpha\varepsilon}\Phi_{a_{\varepsilon\beta}} - 2\,\xi\; a_{\alpha\beta}\; tr(\boldsymbol{a}\,.\,\Phi_{\boldsymbol{a}}) \tag{7.10}$$

The first two terms on the right hand side of Eqs.(7.8),(7.9) represent the advection of the tensors $\boldsymbol{c}$ and $\boldsymbol{a}$ by the flow (i.e. by the momentum field $\boldsymbol{u}(\boldsymbol{r})$) and the third term in Eqs.(7.8),(7.9) represents dissipation.

The role of the last two terms in Eqs.(7.8) and (7.9) is to bring, by following the time evolution, the free energy Φ to its minimum. For states that are not too far from equilibrium (i.e. the states for which Φ_c and Φ_a are not too large), the dissipation potential Ξ can be chosen to be the following quadratic function:

$$\Xi = \left(\Phi_{c_{ij}}\ ,\ \left(\Phi_{c_{ij}}\right)_s\ ,\ A_{ij}\right)\begin{pmatrix} \frac{\Lambda^{11}_{ijkl}}{1-\alpha} & 0 & \frac{\Lambda^{13}_{ijkl}}{\alpha(1-\alpha)} \\ 0 & \frac{\Lambda^{22}_{ijkl}}{1-\alpha} & \frac{\Lambda^{23}_{ijkl}}{\alpha(1-\alpha)} \\ \frac{\Lambda^{13}_{ijkl}}{\alpha(1-\alpha)} & \frac{\Lambda^{23}_{ijkl}}{\alpha(1-\alpha)} & \frac{\Lambda^{33}_{ijkl}}{\alpha} \end{pmatrix}\begin{pmatrix} \Phi_{c_{kl}} \\ \left(\Phi_{c_{kl}}\right)_s \\ A_{kl} \end{pmatrix} \tag{7.11}$$

where Λ^{11}, Λ^{22}, Λ^{33},Λ^{13} and Λ^{23}, called hereafter mobility tensors, are phenomenological parameters expressing in the model the polymer-polymer, plate-plate, and polymer-plate interactions in dissipative processes and α is the volume fraction of the suspended lamellae. Their choice is restricted in such a way that the three-by-three matrix in the equation (7.11) to be positive definite. In order to satisfy moreover the constrain $tr\boldsymbol{a} = 1$, the same as in Model I, Ξ must depend on Φ_a only through its dependence on $A_{ij} = \Phi_{a_{ij}} - \frac{1}{3}tr\Phi_a\,\delta_{ij}$.

As for the choice of the mobility tensors, following Beris and Edwards (1994) a polynomial functions of $\boldsymbol{c}$ and $\boldsymbol{a}$ are chosen as follow:

$$\boldsymbol{\Lambda}^{11} = \Lambda_0^{11}\left[f_1\widehat{\boldsymbol{c}\boldsymbol{\delta}} + f_2\widehat{\boldsymbol{c}\boldsymbol{c}}\right] \tag{7.12}$$

$$\boldsymbol{\Lambda}^{22} = \Lambda_0^{22}\left(1 + \widetilde{\Lambda_0^{22}}\left(tr\boldsymbol{c} - tr\boldsymbol{c}_{eq}\right)^2\right)\left[f_1\widehat{\boldsymbol{c}\boldsymbol{\delta}} + f_2\widehat{\boldsymbol{c}\boldsymbol{c}}\right] \tag{7.13}$$

$$\boldsymbol{\Lambda}^{33} = \Lambda_0^{33}\left(1 + \widetilde{\Lambda_0^{33}}\left(II - II_{eq}\right)^2\right)\left[f_3\widehat{\boldsymbol{a}\boldsymbol{\delta}} + f_4\widehat{\boldsymbol{a}\boldsymbol{a}} + f_5\widehat{\boldsymbol{a}\boldsymbol{a}\boldsymbol{a}}\right] \tag{7.14}$$

$$\begin{aligned}\boldsymbol{\Lambda}^{13} &= \Lambda_0^{13}\widehat{\boldsymbol{c}\boldsymbol{a}}\\ \boldsymbol{\Lambda}^{23} &= \Lambda_0^{23}\widehat{\boldsymbol{c}\boldsymbol{a}}\end{aligned} \tag{7.15}$$

where $II = (tr\boldsymbol{a})^2 - tr(\boldsymbol{a}.\boldsymbol{a})$. The coefficients $f_i(i = 1-5)$ appearing in (7.12,7.13 and 7.14) equal either 0 or 1. The symbol (eq) arising in (7.13) and (7.14) denotes the equilibrium state. $\boldsymbol{\Lambda}$ are all fourth order tensors,$\widehat{\ }$ means symmetrization in the four indices, and Λ_0^{11}, Λ_0^{22}, $\widetilde{\Lambda_0^{22}}$, Λ_0^{33}, Λ_0^{13} and Λ_0^{23} are phenomenological coefficients. It should be noted that the clay mobility tensor (7.14) is slightly modified to take into account some new phenomena at low shear rates.

The free energy of the system under consideration is chosen to be:

$$\begin{aligned}\Phi = &\int_{-1}^{1} ds\left[-n_c H Q_0^2 \ln\left(1 - tr\ \mathbf{c}\right) + Ktr(\mathbf{c}_s\cdot\mathbf{c}_s) - \frac{1}{2}n_c k_B T\ln(\det\mathbf{c})\right]\\ &-\frac{1}{2}n_a\left(1 - K_{flex}\right)k_B T\ln(\det\mathbf{a}) + n_a K_{flex}k_B T tr\mathbf{a}^{-1}\\ &+\kappa n_a^2 k_B T\left((tr\boldsymbol{a})^2 - tr(\boldsymbol{a}\ .\ \boldsymbol{a})\right) + \kappa'\ n_c n_a k_B T tr(\boldsymbol{c}\ .\ \boldsymbol{a})\end{aligned} \tag{7.16}$$

By $\mathbf{c}_s$ we denote $\frac{\partial\mathbf{c}}{\partial s}$. The first term in (7.16) is the kinetic energy, the second term is the intramolecular energy, third term represents the energy associated with interactions among

the dumbbells that are neighbors on the chain and the fourth term represent the entropy S multiplied by the temperature T. The coefficient K is the modulus associated with this type of interactions. All other parameters entering in (7.16) have the same meaning in (7.1). The choice of the parameters entering the free energy is restricted by requiring the thermodynamic stability.

7.3.3 Exfoliated and intercalated lamellae

Both Model I and Model II assume that the clay lamellae in polymer melts are completely exfoliated. This is not however the case in the nanocomposites, prepared by direct melt mixing, that we investigate experimentally. The models have to be therefore appropriately modified to account for the presence of exfoliated lamellae as well as tactoids with expanded interlayer spacing. Since we do not know the distribution of tactoid's thickness, we shall regard all tactoids as having one representative (average) size. Single clay lamellae in Model I and Model II are replaced by clay tactoids, all of a single average thickness. The physics on which Model I and Model II is based applies to this new nanocomposite provided the polymeric chains inside the clay galleries do not play a significant role in determining the rheology of suspensions. We make such assumption.

The question that remains to be answered is what is the average thickness of clay tactoids in the suspension. There are two ways to determine it. First, we can use an image analysis software to analyze the TEM images and calculate the average thickness from such analysis. Second, following Ren et al. (2000), we can use linear viscoelastic data to determine the percolation threshold and calculate the average thickness from this quantity. In this paper we follow the second route.

The number of silicate layers per tactoid is related in Ren et al. (2000) to the percolation threshold. In the reformulation of the relation presented in Vermant et al. (2007), the average aspect ratio of the tactoids A_f is given by:

$$A_f = \frac{3\,\phi_{per}}{4\,\alpha_{per}} \tag{7.17}$$

where ϕ_{per} is the percolation threshold volume fraction for randomly packed spheres in three dimensions (calculated to be 0.3, see Isichenko (1992) for more details), and α_{per} is the percolation threshold seen in linear viscoelastic experimental data.

Having specified the governing equations and the material parameters entering them, the equations have to be solved to provide rheological predictions. From the mathematical point of view, the equations arising in Model I are ordinary differential equations (ODEs) and in Model II partial differential equations (PDEs) in two dimensions. We solve both numerically by using the MATHEMATICA software package [Wolfram (1991)].

7.4 Results and discussion

In this section we report results of our measurements of morphology (in Section 7.4.1 and rheology (in Sections 7.4.2 and 7.4.3) as well as model predictions and their comparison with the experimental data (in Section 7.4.4).

7.4.1 X-ray and microscopic analysis

In PLS nanocomposites, the state of dispersion of silicate layers in polymer matrix is usually monitored by using wide angle x-ray diffraction (WAXD) analysis and transmission electron microscopic observations. WAXD offers a convenient method to identify the structure of intercalated nanocomposite by monitoring the position, shape, and intensity of the basal reflections of distributed silicate layers in the polymer matrix. Figure 7.1 shows the WAXD patterns of pure PBSA, Cloisite 30B and PBSAC30BNs. As seen in figure 7.1, the diffraction peak of nanocomposites shifts to the lower angle which means an increase of the interlayer spacing of clay layers. By using angular location of the peaks in figure 7.1 and by applying Bragg's law the interlayer spacing of clay lamellae can be determined [the equation $n\ \lambda = 2\ d\ sin\theta$ is called Bragg's law; d is the distance between diffractional lattice planes, λ is the wave length of the incident X-ray beam used in the diffraction experiment, n is an integer and θ is the measured diffraction angle]. The computed values show no significant changes

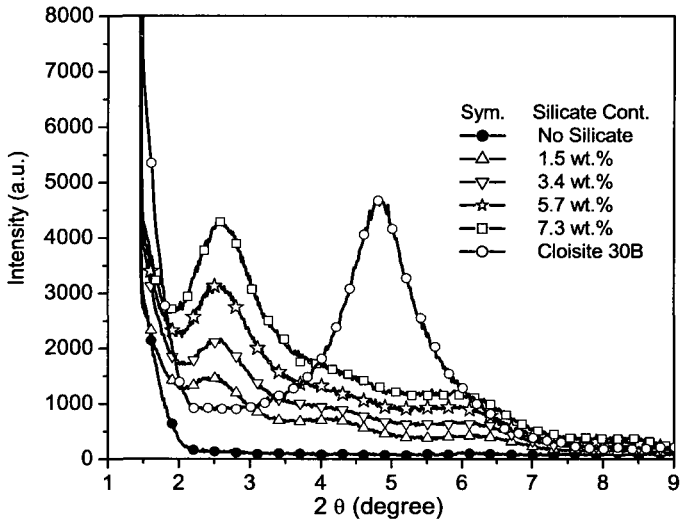

Figure 7.1: X-ray patterns of pure PBSA, Cloisite 30B and PBSAC30BNs

on the layer spacing of clay lamellae when silicate concentration is changed (the results are not shown here for the sake of brevity). The same behavior has been previously observed in Solomon et al. (2001).

In the case of large separated clay layers (i.e. $d > 8$ nm but still ordered silicate layers) or for exfoliated clay lamellae with disordered structure WAXD no longer presents diffraction peaks [Alexandre and Dubois (2000)]. In these cases, a qualitative understanding of the state of dispersion and internal structure of PLS nanocomposites can be obtained by TEM images. Figures 7.2 and 7.3 show the TEM images of PBSAC30BN1 and PBSAC30BN4 respectively where the white areas are polymer matrix, and the dark entities are the cross section of the stacks and possibly individual clay layers. The images are reported in two different magnifications for each nanocomposite. These images clearly show a coexistent of intercalate/exfoliate nanocomposite. In other words, from these images not only tactoids of clay consist of a few silicate layers but also individual silicate layers can be seen. The results of WAXD together with TEM images reveal that some clay tactoids (i.e. ordered structure of

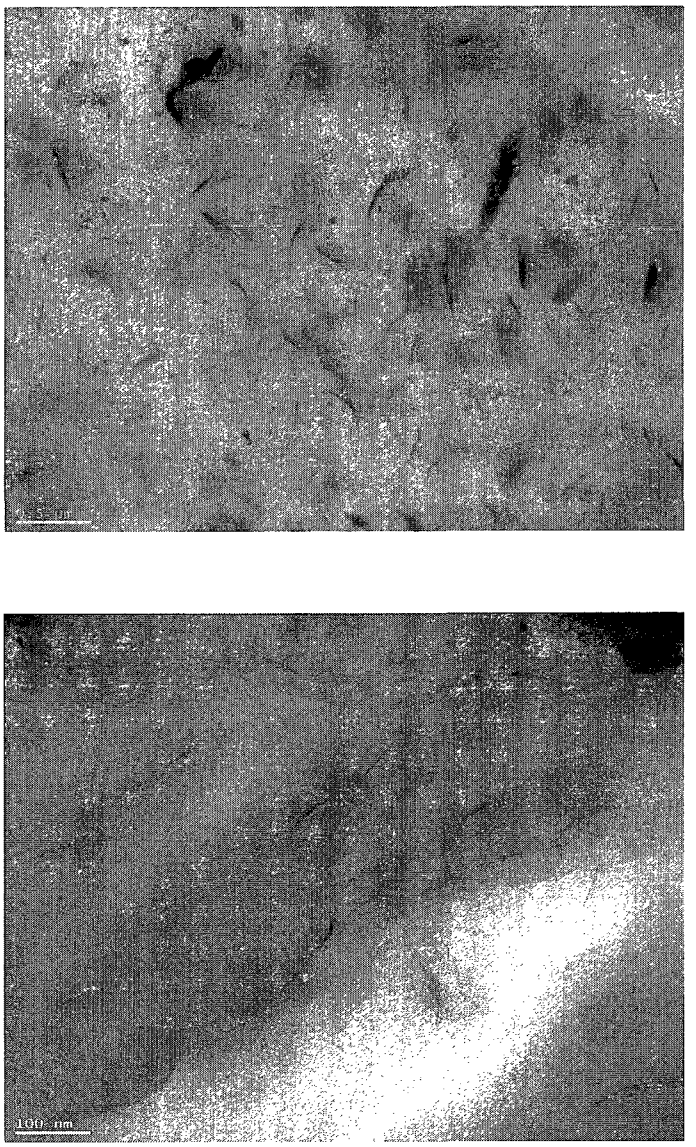

Figure 7.2: TEM images of PBSAC30BN1 with two different magnifications

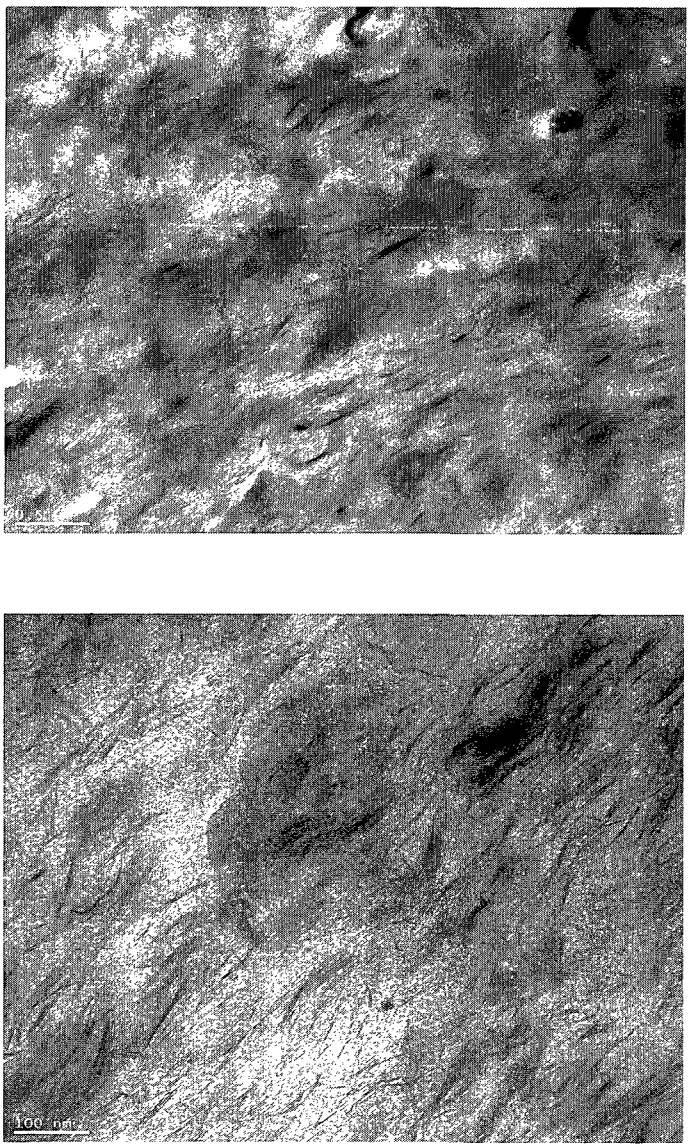

Figure 7.3: TEM images of PBSAC30BN4 with two different magnifications

clay platelets) are still remained in the nanocomposites which manifest themselves by Bragg peaks where the individual silicate layers are invisible.

7.4.2 Linear viscoelastic properties

One of the characteristic features of polymer nanocomposites is that their structure evolves in time. It is therefore crucial to specify precisely the experimental procedure in order to obtain reliable and reproducible data for all samples. As noted in Vermant et al. (2007), there is always a compromise between annealing time after squeezing the sample and degradation of polymer and surfactant.

As mentioned earlier, the sample was let to rest in the rheometer 15 min. before squeezing it. After squeezing, a dynamic time sweep was performed at $\omega = 1$ rad/s while G' was monitored. The aim of this time sweep was to determine how long the sample should let to anneal in the rheometer between squeezing and starting the subsequent test. The result of this time sweep (not shown here for the sake of brevity) showed that the storage modulus increases sharply with time and then the rate of increase becomes slower. The reason why storage modulus increases is that the structure of nanocomposites is ruptured during the loading and squeezing and then it builds-up again during annealing [Vermant et al. (2007)]. By compromising between this time, time for degradation and time requiring for the subsequent test (especially frequency sweep which takes longer time), an additional 15 min. rest was considered for annealing the structure prior to the subsequent test.

It has been observed that the linear viscoelastic region corresponding to the filled polymer system is sensitive to the presence of filler and it usually becomes narrower with increasing filler content. In the case of polymer nanocomposites, because of the nanometric size of the clay platelets and a strong interaction between polymer and clay, the linear viscoelastic region becomes even more sensitive with increasing clay loading. Figure 7.4 plots the normalized storage modulus versus strain for pure PBSA and its nanocomposites at $\omega = 1$ rad/s. This figure shows that the deviation from linear behavior for PBSAC30BN4 occurs at the strain around 0.5% while for pure PBSA it occurs at the strain approximately 50%. Transition from

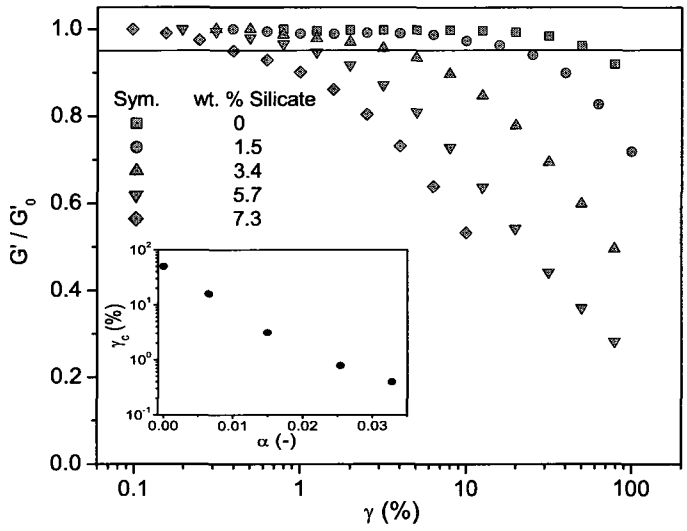

Figure 7.4: Normalized storage modulus versus strain for pure PBSA and its nanocomposites

linear to nonlinear behavior (specified by a line in figure 7.4) was defined as a point where the storage modulus decreases more than 5 % of its values at small strain (i.e. $G'/G'_0 \simeq 0.95$ where G'_0 is storage modulus at small strain). In the small figure imbedded in figure 7.4, the critical strain γ_c is plotted as a function of the volume fraction(α) of silicate layers. As it is clear from this figure, the linear viscoelastic range is very sensitive to the clay volume fraction.

Frequency sweep test was performed in the linear viscoelastic region for each sample using the procedure described earlier (15 min. rest before squeezing the sample and 15 min. annealing after squeezing the sample between parallel plate). The tests were repeated at least twice, always with a fresh sample. The error bars are shown on the figures. The storage modulus and complex viscosity of pure PBSA and PBSAC30BNs are compared in figure 7.5(a) and figure 7.5(b) respectively. In the traditional filled polymer system it has been observed that addition of the fillers leads to an increase in the overall viscoelastic properties (i.e. an increase in the storage modulus G', loss modulus G'' and complex viscosity η^*) in

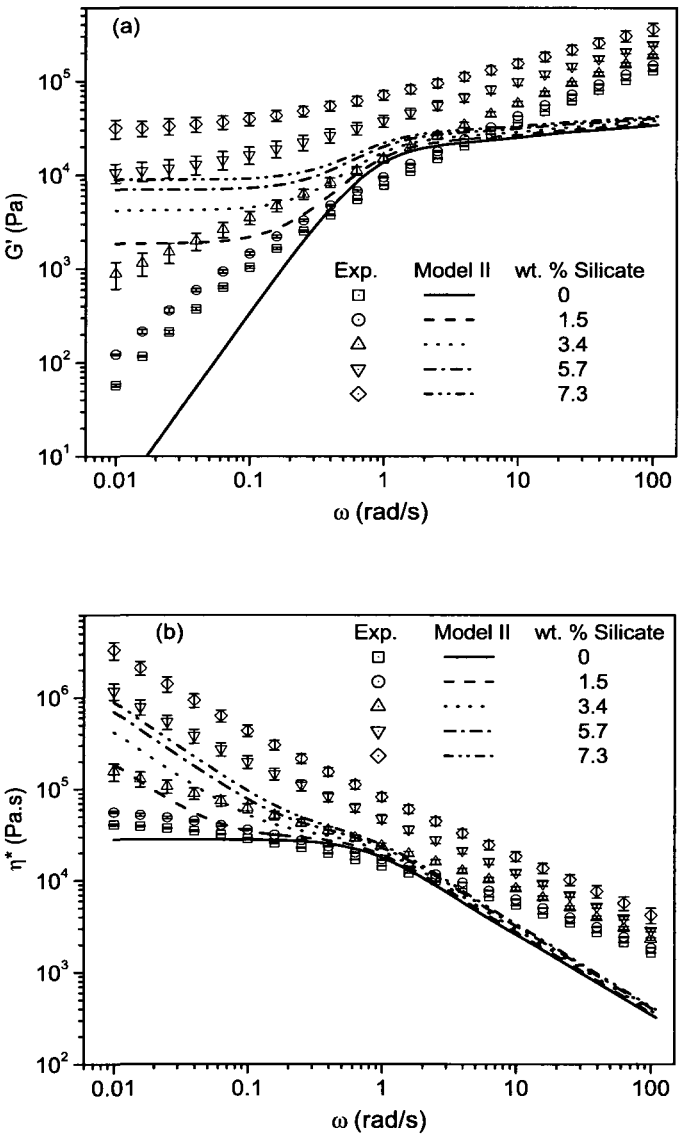

Figure 7.5: Linear viscoelastic data (a) storage modulus (b) complex viscosity

the whole range of frequencies.

Figures 7.5(a) and 7.5(b) show the dependence of the linear viscoelastic properties on the silicate layer concentrations. The results show that at high frequencies G' and η^* increase monotonically with increasing clay loading which is also observed for traditional filled polymer system. At low frequencies, a significant effect of clay loading is observed. It is in particular the apparent plateau in G' and the upward complex viscosity at relatively low clay loading. This feature makes the nanocomposites different from the traditional filled polymer system. Figure 7.5(a) shows that the frequency dependence of the storage modulus becomes weaker with increasing clay loading and nearly independent of the frequency at high clay loading (e.g. for 5.7 wt.% and 7.3 wt.% clay loading). It should also be noted that at the high clay loading no terminal regime is observed for nanocomposites within the experimental window. This observation means that the characteristic relaxation time is longer than 100 second. Such behavior have been previously observed for both intercalated and exfoliated nanocomposites [Krishnamoorti et al. (1996); Krishnamoorti and Giannelis (1997); Ren et al. (2000); Lim and Park (2001); Solomon et al. (2001); Galgali et al. (2001); Li et al. (2003); Jeon et al. (2004); Aubry et al. (2005); Gupta et al. (2005); Sinha Ray and Bousmina (2005b); Sinha Ray et al. (2005); Xu et al. (2005); Wu et al. (2005); Kim et al. (2007); Vermant et al. (2007)].

The question then arises: what is the physical interpretation of the behavior observed for PLS nanocomposites? We will return to this issue in Section 7.4.4 where we discuss predictions of the models and their comparison with experimental data.

In order to determine the percolation threshold, we plot the values of G' at low frequency ($\omega = 0.01\ rad/s$) versus clay volume fraction α (following Letwimolnun et al. (2007), the clay volume fraction is calculated by taking the density of the montmorillonite equals to 2860 kg/m^3). As observed in figure 7.6, G' increases dramatically after a certain value of α which is called percolation volume fraction α_{per}. The percolation threshold has been determined by first performing the linear regression in two regions: low clay volume fraction and high clay volume fraction. The intersection of the two lines determines the percolation threshold.

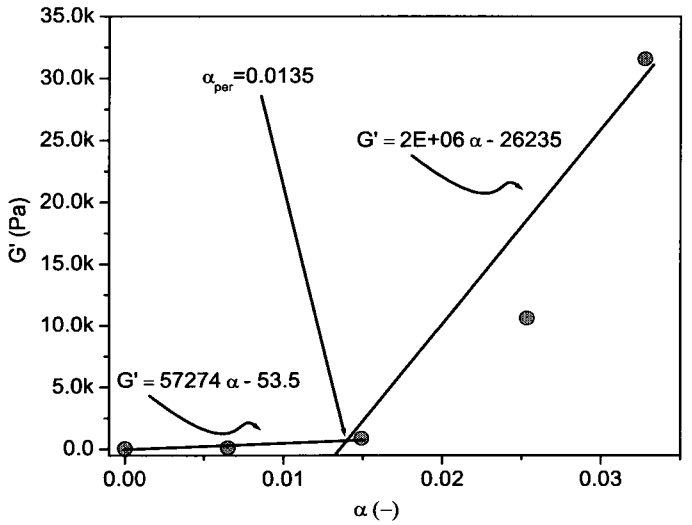

Figure 7.6: Storage modulus at low frequency ($\omega = 0.01 rad/s$) versus clay volume fraction. Lines are the linear regression through the corresponding data points.

7.4.3 Nonlinear viscoelastic properties

In this section we turn to steady and transient shear flow material functions of polymer matrix and its nanocomposites. Three measurable stress quantities, shear stress σ_{12}, first normal stress difference $N_1 = \sigma_{11} - \sigma_{22}$ and second normal stress difference $N_2 = \sigma_{22} - \sigma_{33}$ are usually reported as quantities characterizing the nonlinear viscoelastic properties. Following Bird et al. (1987a), the plus sign is used for start-up material functions, and the minus sign for relaxation material functions and no sign for steady state material functions.

As mentioned before in Section 7.2, rheological measurements were performed in the parallel plate geometry where the shear rate is not constant throughout the sample. Consequently, the experimental rheological data have to be corrected. For steady shear flows, the viscosity and normal stress difference ($N_1 - N_2$) can be expressed as functions of shear rate at rim $\dot{\gamma}_R$ as follow: [Bird et al. (1987a); Carreau et al. (1997); Marrison (2001)]:

$$\eta(\dot{\gamma}_R) = \frac{T}{2\pi R^3 \dot{\gamma}_R}\left[3 + \frac{d\ln\left(\frac{T}{2\pi R^3}\right)}{d\ln\dot{\gamma}_R}\right] \tag{7.18}$$

$$N_1(\dot{\gamma}_R) - N_2(\dot{\gamma}_R) = \frac{2F}{\pi R^2}\left(1 + \frac{1}{2}\frac{d\ln F}{d\ln \dot{\gamma}_R}\right) \tag{7.19}$$

where T and F are torque and normal force respectively. Equation 7.19 has been derived by using the fact that the total thrust on the upper (or the lower) plate in the parallel plate geometry is related to $(N_1 - N_2)$. For unfilled polymeric materials, the second normal stress difference N_2 is usually assumed to be negligible (the so-called Weissenberg hypothesis, $N_2 = 0$). However, for filled polymeric systems, especially for the polymer nanocomposites where the particle-particle interactions become important, N_2 is not necessarily zero but remains unknown. Therefore, in the rest of this paper we will not neglect the contribution of the second normal stress difference to the total thrust and report hereafter the normal stress difference $(N_1 - N_2)$.

The derivatives appearing in Eqs.7.18 and 7.19 are obtained by plotting $\ln(T/2\pi R^3)$ and $\ln F$ versus $\ln \dot{\gamma}_R$ and taking the slope of the regression line through the data points at different shear rate ranges.

7.4.3.1 Effects of the shear rate on transient material functions

Transient (start up and relaxation after cessation of a flow) material functions at different shear rates for polymer matrix (PBSA) and its nanocomposites with 3.4 wt.% clay (PBSAC30BN2) are shown in figures 7.7-7.12. In order to make the amplitude of the overshoot in shear stress and normal stress difference clearer, the normalized form of each graph is also reported. The majority of the transient data are presented on a log-linear scale to highlight the behavior at short times.

Figures 7.7(a) and 7.7(b) show the effect of shear rate on the shear stress σ_{12}^{+} and the normal stress difference $(N_1 - N_2)^{+}$ respectively for pure PBSA. The results show that at low shear rates both the shear stress and the normal stress difference reach their steady state values monotonically while at higher shear rates a small overshoot is observed for σ_{12}^{+} and no overshoot for $(N_1 - N_2)^{+}$ (the magnitude of the overshoots become clearer if the curves are presented in the normalized form, for the sake of brevity we do not show the normalized

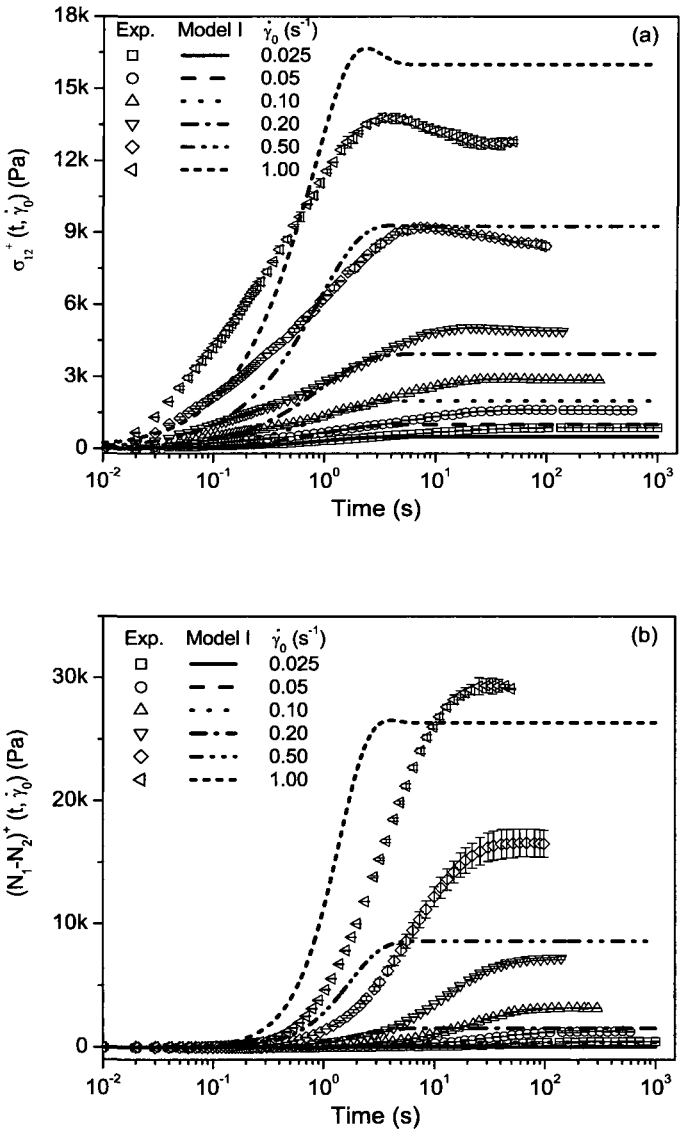

Figure 7.7: Effect of shear rate on the start-up material functions of pure PBSA (a) shear stress (b) normal stress difference

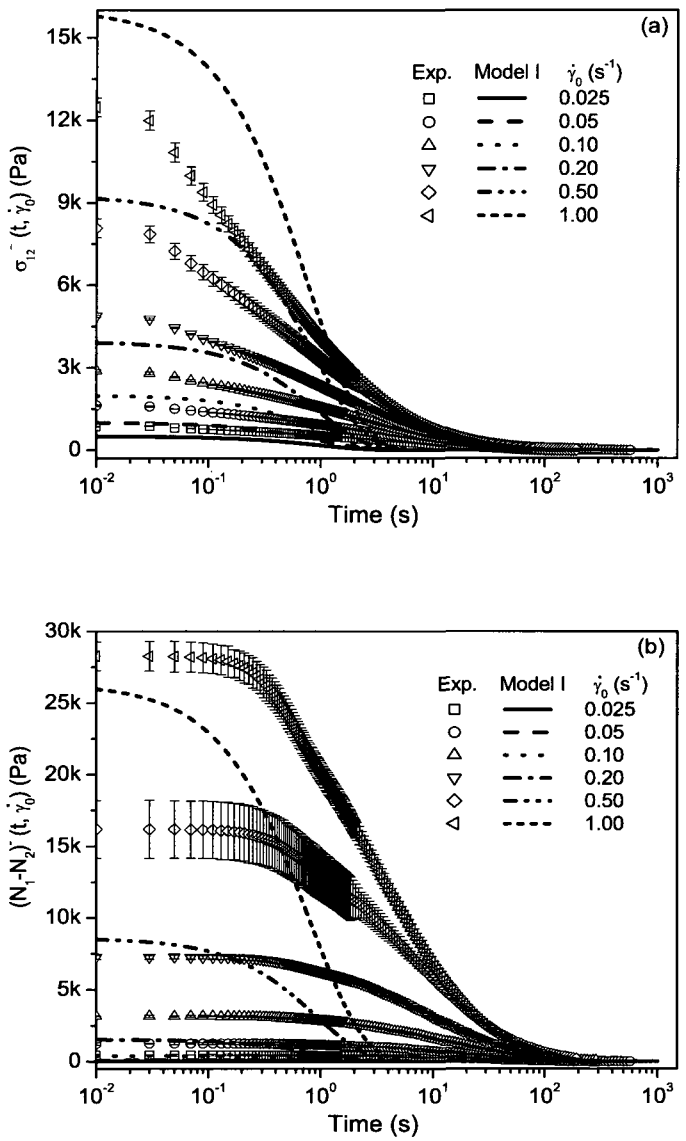

Figure 7.8: Effect of shear rate on the relaxation material functions of pure PBSA (a) shear stress (b) normal stress difference

curves). The stationary values of the shear stress and the normal stress difference (i.e. σ_{12} and $(N_1 - N_2)$) increase with increasing shear rate.

In the stress relaxation experiment, the motion of a fluid that is undergoing steady shear flow with a given shear rate is suddenly stopped and the decay of the stresses (including the shear stress and the normal stress differences) are then measured.

The relaxation behavior of pure PBSA at different shear rates are depicted in figures 7.8(a) and 7.8(b) for σ_{12}^- and $(N_1 - N_2)^-$ respectively. Results show that at a given shear rate, shear stress relaxes faster than the normal stress difference. With increasing shear rate, both σ_{12}^- and $(N_1 - N_2)^-$ relax faster. These observations agree well with the observations made for polymeric melts and solutions reported in Bird et al. (1987a) and Eslami et al. (2004).

The effect of shear rate on the transient shear stress for PBSAC30BN2 is depicted on figure 7.9(a). The results show that for small shear rates, σ_{12}^+ reaches its steady state value monotonically. As the shear rate increases, the stationary value of the shear stress increases and the curve of σ_{12}^+ versus time shows an overshoot. The magnitude of the overshoot increases and the time at which the overshoot appears decreases when the shear rate increases. Qualitatively, similar results are obtained for the normal stress difference $(N_1 - N_2)^+$ (see Figure 7.9(b)). As seen from the the figures 7.10(a) and 7.10(b), at any given shear rate there are two distinct differences between σ_{12}^+ and $(N_1 - N_2)^+$ in the stress growth experiment. First, the normal stress difference goes to its steady state values slower than the shear stress. Second, the magnitude of the overshoot in the shear stress is larger than that in the normal stress difference. The reason why there are such differences maybe due to the fact that in the simple shear flow the normal force which generates the normal stress difference is a secondary effect. By this we mean that in the simple shear flow the shear stress is applied to the sample through the torque and the normal force is generated because of the applied torque.

Stress relaxation data are shown in figures 7.11(a) and 7.11(b) for the shear stress relaxation σ_{12}^- and the normal stress difference relaxation $(N_1 - N_2)^-$ respectively. The results show that both stresses (the shear stress and the normal stress difference) relax monotonically

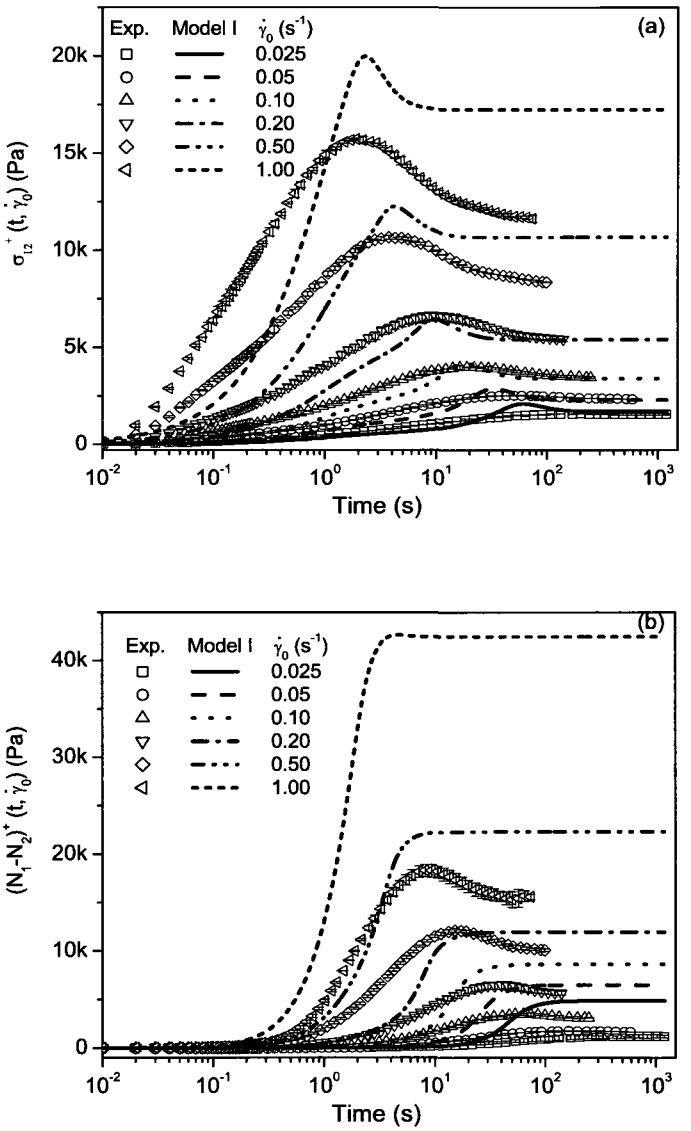

Figure 7.9: Effect of shear rate on the start-up material functions of PBSAC30BN2 (a) shear stress (b) normal stress difference

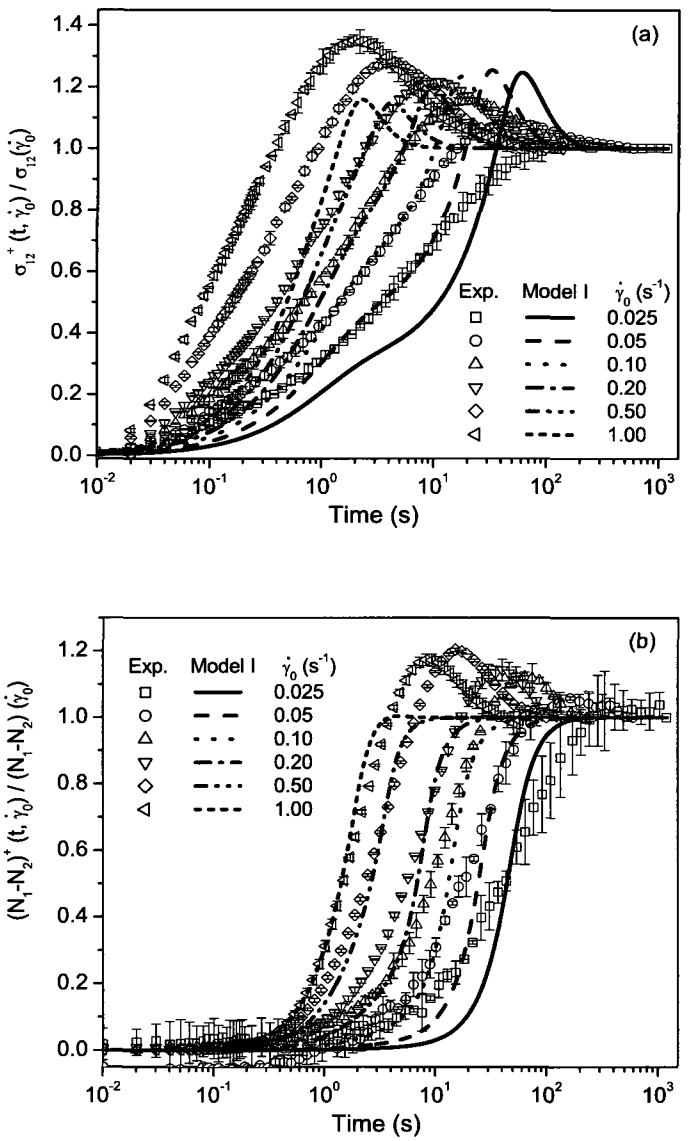

Figure 7.10: Effect of shear rate on the normalized start-up material functions of PB-SAC30BN2 (a) shear stress (b) normal stress difference

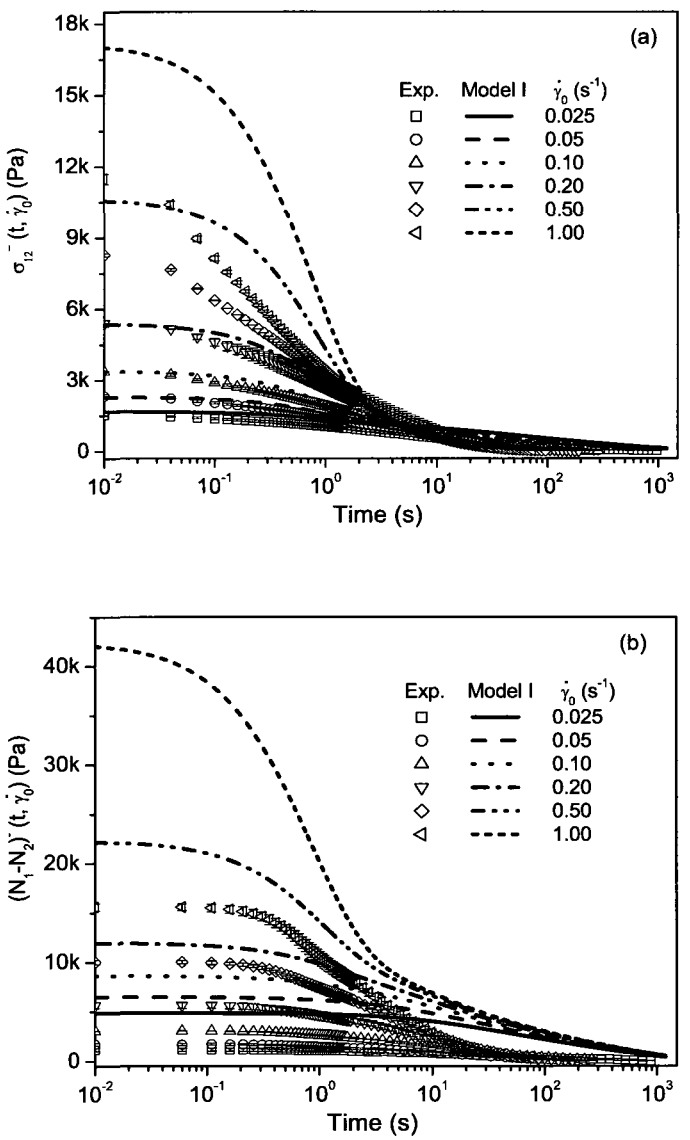

Figure 7.11: Effect of shear rate on the relaxation material functions of PBSAC30BN2 (a) shear stress (b) normal stress difference

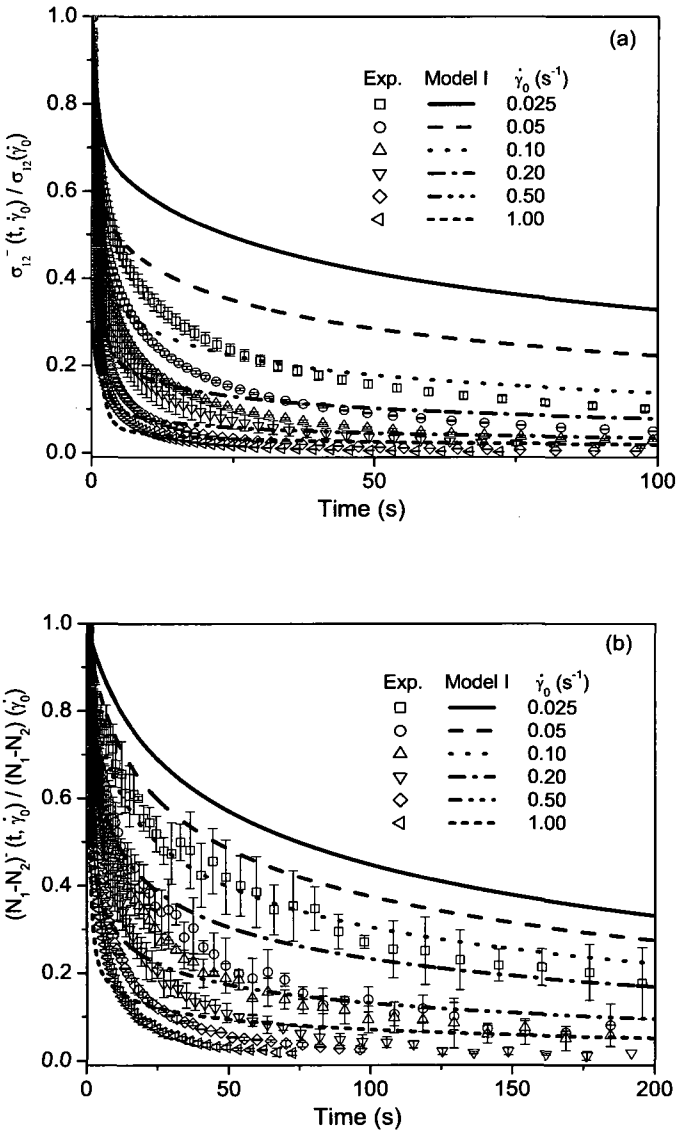

Figure 7.12: Effect of shear rate on the normalized relaxation material functions of PB-SAC30BN2 (a) shear stress (b) normal stress difference

in low shear rates and more rapidly as the shear rate increases. This observation becomes clearer if the relaxation data are normalized at different shear rates. This is exactly what is done in figures 7.12(a) and 7.12(b) for shorter intervals of time. These data are also presented in the linear-linear scale to highlight the relaxation behaviors with changing shear rate. We also see that the shear stress relaxes more rapidly than the normal stress difference which is in agreement with the slower response of the normal stress difference in the stress growth experiment.

One question remains to be answered: why do we observe an overshoot in the shear stress and the normal stress difference in start-up experiments? We shall answer it with the help of our models in Section 7.4.4.

7.4.3.2 Effects of the clay loading on the material functions

In this section we show how the steady state and transient material functions (i.e. η^+, σ_{12}^-, η, $(N_1 - N_2)^+$, $(N_1 - N_2)^-$ and $(N_1 - N_2)$) for PLS nanocomposites depend on the clay loading. The normal stress difference of polymer nanocomposites (especially the transient normal stress difference) has received much less attention than the shear viscosity. In this paper we pay therefore a special attention to the normal stress difference in PLS nanocomposites.

Figure 7.13(a) shows the steady state viscosity of polymer nanocomposites for a wide range of shear rates and different silicate contents. As previously observed for traditional filled polymer system, the addition of clay layers leads to an increase in the overall viscosity of the nanocomposites. Moreover, it is found that an increase in the clay loading results in a significant increase in the viscosity at low shear rates. This, to the best of our knowledge, have not been observed, at least for such low filler content, in the traditional filled polymer systems. In other words, for pure polymers and the nanocomposites with low clay loading (e.g. 1.5 wt.%) the behavior is near Newtonian at low shear rates and it becomes shear thinning at higher shear rates. However, for higher clay loading (e.g. 3.4 wt.% and 5.7 wt.%) the behavior becomes non-Newtonian for all ranges of shear rates. At low shear rate the slope of the curve of viscosity versus shear rate becomes larger with increasing clay loading which

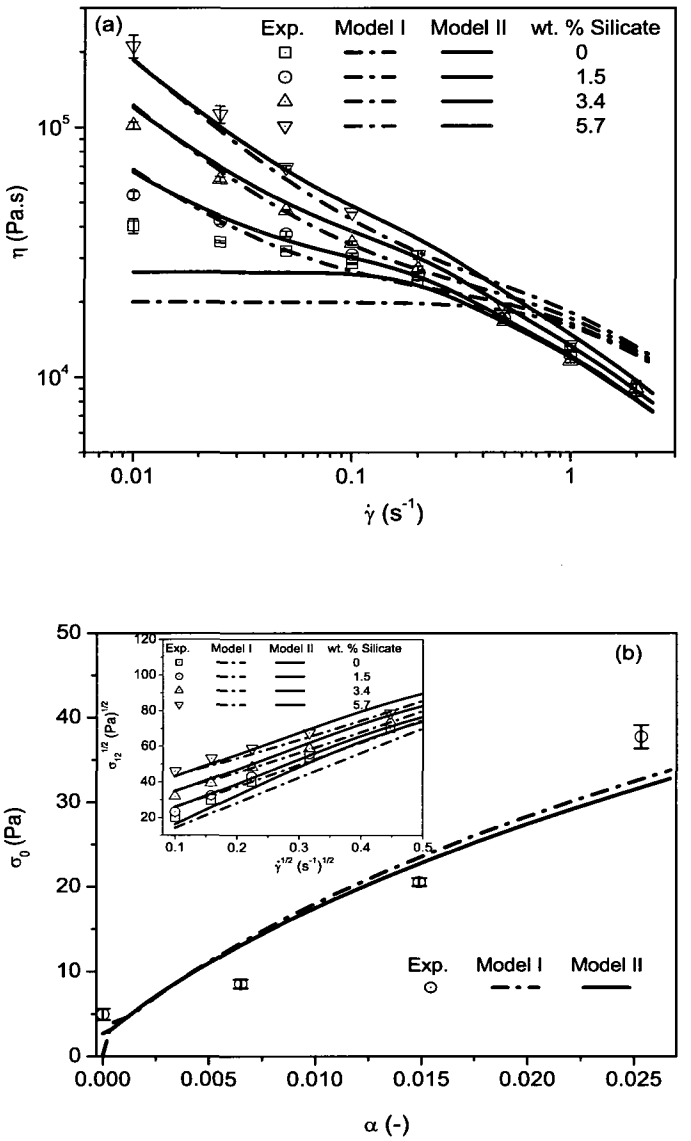

Figure 7.13: Effect of clay loading on the (a) steady state viscosity (b) yield stress

leads to yielding behavior. At higher shear rate the behavior of polymer matrix is dominant and the viscosity of nanocomposites becomes almost the same as that of polymer matrix. This is because at high shear rates the silicate layers are all oriented in the flow direction. Similar behavior has been previously observed for other nanocomposites [Krishnamoorti et al. (2001); Gupta et al. (2005); Sinha Ray and Bousmina (2005b); Sinha Ray et al. (2005); Ren and Krishnamoorti (2003); Vermant et al. (2007); Letwimolnun et al. (2007)].

The emergence of the yield stress is one of the most important features that emerge in the rheology of concentrated filled system. At stresses that are lower than the yield stress these systems behave like a solid and at stresses that are higher than the yield stress they behave like a liquid. Yielding behavior, from the physical point of view, can be related to the filler-filler interactions in the concentrated suspensions where the number density of fillers becomes large. According to Casson, the yield stress can be easily determined from the steady state shear stress σ_{12} by the following equation [Malkin (1990)]:

$$\sigma_{12}^{1/2} = \sigma_0^{1/2} + \beta\, \dot{\gamma}^{1/2} \tag{7.20}$$

where σ_0 is the yield stress and β an arbitrary constant.

Figure 7.13(b) shows the yield stress of PBSAC30BNs evaluated from Eq.(7.20). It can be seen that the pure polymers and the nanocomposites with low clay loading (1.5 wt.%) show a small value of the yield stress. However, with increasing clay loading, nanocomposites show a large value of the yield stress which becomes more pronounced with increasing the clay loading. In the small figure imbedded in figure 7.13(b) the way in which yield stress is calculated is shown.

The time-dependent shear stress and viscosity of polymer matrix and its nanocomposites with different clay loading at a given shear rate ($\dot{\gamma} = 0.1s^{-1}$) are presented on figure 7.14. Results of figure 7.14(a) where the effect of clay loading on the start-up viscosity is reported show that the viscosity of pure polymer goes to its steady state value monotonically without showing any overshoot while an overshoot is observed for PBSAC30BNs. The amplitude of the overshoot increases with increasing clay loading. The time required to attain the steady

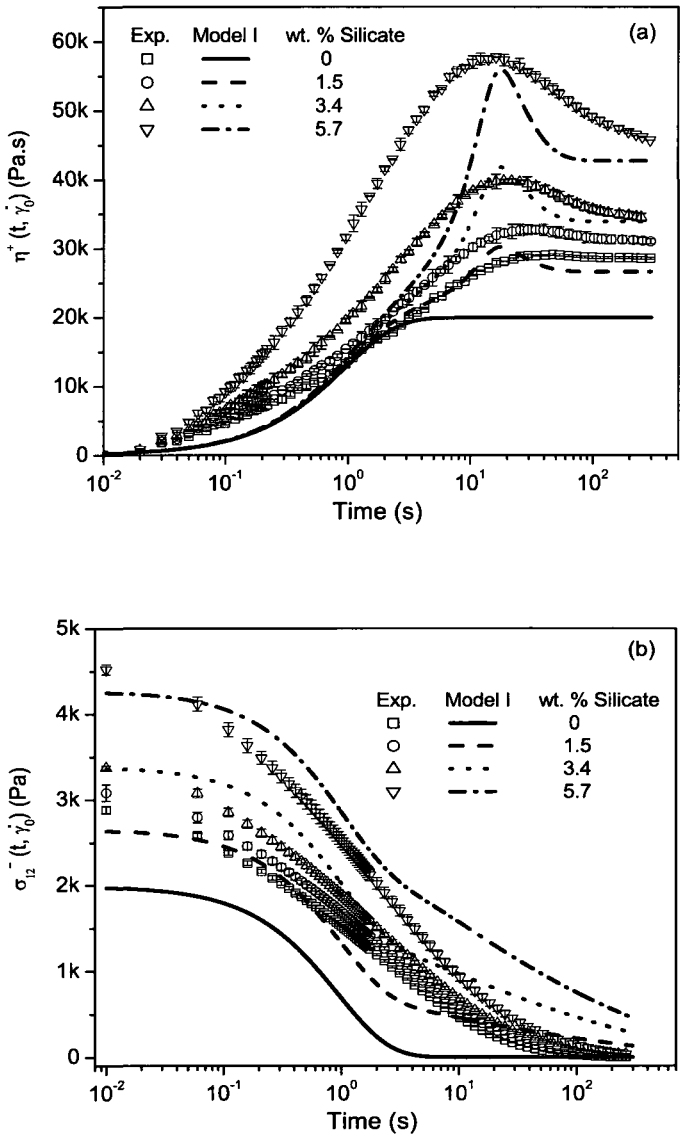

Figure 7.14: Effect of clay loading on the (a) start-up viscosity (b) stress relaxation

state increases as the clay concentration increases. As expected, the stationary value of the viscosity ($\eta^+|_{t\to\infty}$) also increases with increasing clay loading. In figure 7.14(b) the stress relaxation data are shown for pure polymer and its nanocomposites. The result show that pure polymer relaxes faster than nanocomposites and the rate of relaxation becomes slower with increasing clay loading.

Now, we turn to the steady state and transient (start-up and relaxation) normal stress difference that are less represented in otherwise abundant experimental rheological data that can be found in the literature about polymer nanocomposites. Traditionally, the normal stresses have been considered as representative of the elasticity of polymeric materials and some phenomena like die swell have been related to the emergence of normal forces.

The rheology of filled polymer system has been reviewed in Malkin (1990) where the author explored different aspects of the rheology of filled system including the normal stresses. According to Malkin (1990) even though the rigidity of the polymeric material increases in the presence of a solid particle, it is not obvious how the presence of the filler reflects itself on the elasticity of the filled system. Many studies have shown that adding filler to a polymer diminishes the the elasticity of the system which is usually demonstrated by reduction of die swell.

In the case of polymer nanocomposites, only a few papers report measurements of the normal stress difference in shear flows [Krishnamoorti et al. (2001); Ren and Krishnamoorti (2003); Gupta et al. (2005)]. Different state of dispersion (e.g. intercalate, exfoliate) in PLS nanocomposite makes it even more difficult to make a general conclusion about the elasticity of the system. The question then arises of what can be a parameter representing elasticity in the polymer nanocomposites? In the traditionally filled polymer system it is, according to [Malkin (1990)], a dimensionless ratio N_1/σ_{12} (the recoverable strain or Weissenberg number). This dimensionless ratio is a measure of how the first normal stress difference grows in comparison with shear stress when the sample is subjected to shear flow.

Gupta et al. (2005) used the same dimensionless ratio N_1/σ_{12} to evaluate the elasticity of their (completely exfoliated) nanocomposites. Gupta et al. (2005) plot N_1 versus σ_{12} and

conclude that the melt elasticity of nanocomposites decreases with increasing the clay loading. They suggest an explanation based on the assumption of strong interactions between clay layers and polymer chains. Krishnamoorti et al. (2001) and Ren and Krishnamoorti (2003) investigated the melt elasticity of intercalated nanocomposites by plotting N_1 versus σ_{12}. According to Krishnamoorti et al. (2001), recoverable strain N_1/σ_{12} is independent of the silicate loading. The authors suggest that this observation can be related to the orientation of silicate layers in the flow field. Although Gupta et al. (2005) investigate the effect of clay loading on the elasticity of their nanocomposites, they do not report the effect of different clay contents on the first normal stress difference N_1 at different shear rates. Results presented in Krishnamoorti et al. (2001), namely N_1 versus $\dot{\gamma}$ for polymer matrix and one concentration of their nanocomposite, show that N_1 slightly increases in the presence of clay particles. Therefore, effects related to different silicate layer concentrations on the melt elasticity and rigidity of PLS nanocomposites remain still to be investigated.

As we have already mentioned, due to the use of the parallel plate geometry, we measure the normal stress difference $(N_1 - N_2)$ instead N_1. Therefore, in our investigation we suggest $(N_1 - N_2)/\sigma_{12}$ to be a dimensionless ratio representative of the elasticity and $(N_1 - N_2)$ a measure of the rigidity of the nanocomposites.

Figures 7.15(a) and 7.15(b) present the steady state normal stress difference versus shear rate and the steady state normal stress difference versus shear stress respectively. Figure 7.15(a) shows that $(N_1 - N_2)$ increases with increasing the clay loading at low shear rates and shows an inverse behavior at relatively high shear rates. In other words, at higher shear rates the normal stress difference of pure polymer is larger than that of the nanocomposites. Higher value of $(N_1 - N_2)$ for nanocomposites at low shear rate is expected. This is because at low shear rates nearly randomly oriented clay platelets in polymer melts increase the rigidity of the nanocomposites. However, because of the nearly perfect alignment of clay platelets in the flow direction at higher shear rates, $(N_1 - N_2)$ of nanocomposites is smaller than that of pure polymers. On the other hand, the results depicted on figure 7.15(b) reveal that the steady state shear stress grows as fast as the steady state normal stress difference. In other

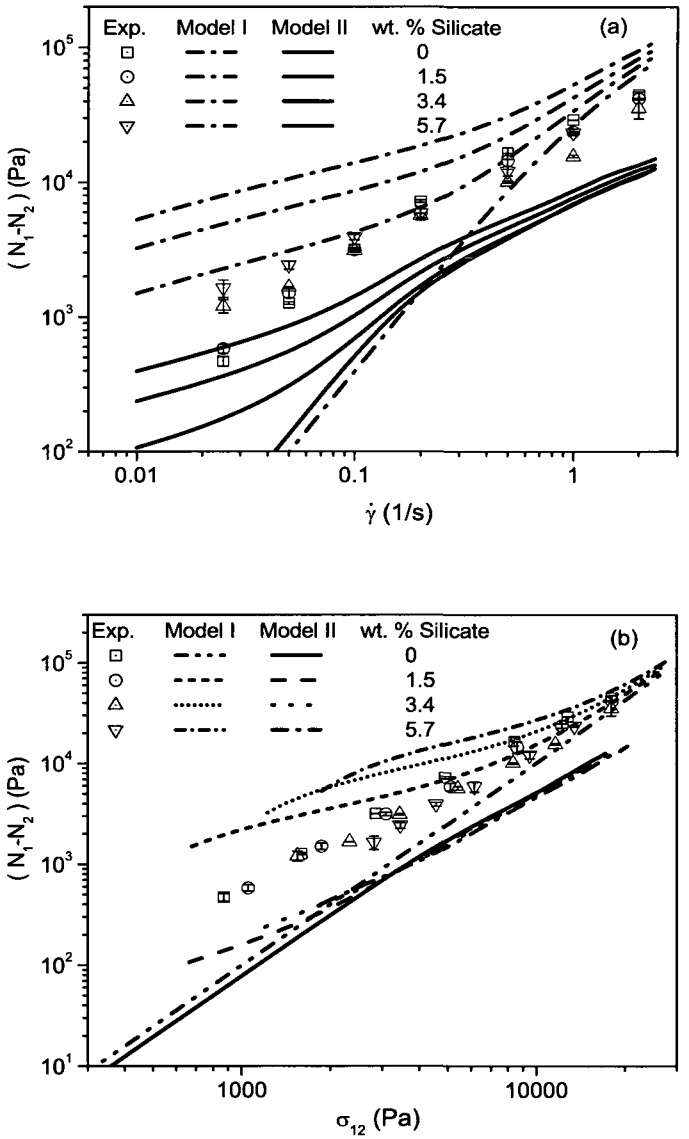

Figure 7.15: Effect of clay loading on the steady state material functions (a) normal stress difference versus shear rate (b) normal stress difference versus shear stress

words, in the competition between the normal stress difference and the shear stress there is a tie which means that the elasticity of the nanocomposites is independent of clay loading. This observation agrees with the one made by Krishnamoorti et al. (2001) and Ren and Krishnamoorti (2003).

The question then arises why do we observe such unusual behavior for the normal stress difference? Regarding this question, we should mention that in polymer nanocomposites the normal stress difference arises from two parts, namely from the contribution of the polymer matrix and the contribution of the clay platelets. At low shear rates the clay platelets and tactoids are not oriented and still bound into a network structure which itself helps to generate additional normal force as compared to pure polymer. At high shear rate however these network structure is destroyed and all the platelets are oriented in the flow direction which reduces also the ability of polymer chains to return to their coil shape and consequently a smaller normal force will is generated. Generally speaking, we would like to point out that at high shear rates the normal force of nanocomposites is mainly due to the pure polymer and the oriented platelets make it smaller. At low shear rate, because of the presence of clay network, a part of the normal force is related to the ability of clay network to retain their network structure and the other part is related to the ability of polymer chains to regain their coil shape.

Start-up and relaxation normal stress difference for pure PBSA and various representative nanocomposites are presented in figures 7.16(a) and 7.16(b) respectively. Figure 7.16(a) shows that, at a given shear rate, $(N_1 - N_2)^+$ of pure PBSA reaches its steady state value monotonically. With increasing clay loading $(N_1 - N_2)^+$ passes through a maximum and then levels off to its steady state value. The amplitude of the overshoot increases with increasing the clay loading (see the small figure imbedded in figure 7.16(a)). Relaxation data reported in figure 7.16(b) indicate that clay platelets hinder the relaxation process of polymer nanocomposites. In other words, $(N_1 - N_2)^-$ of nanocomposites relaxes slower than that of pure polymer and it becomes slower with increasing clay loading.

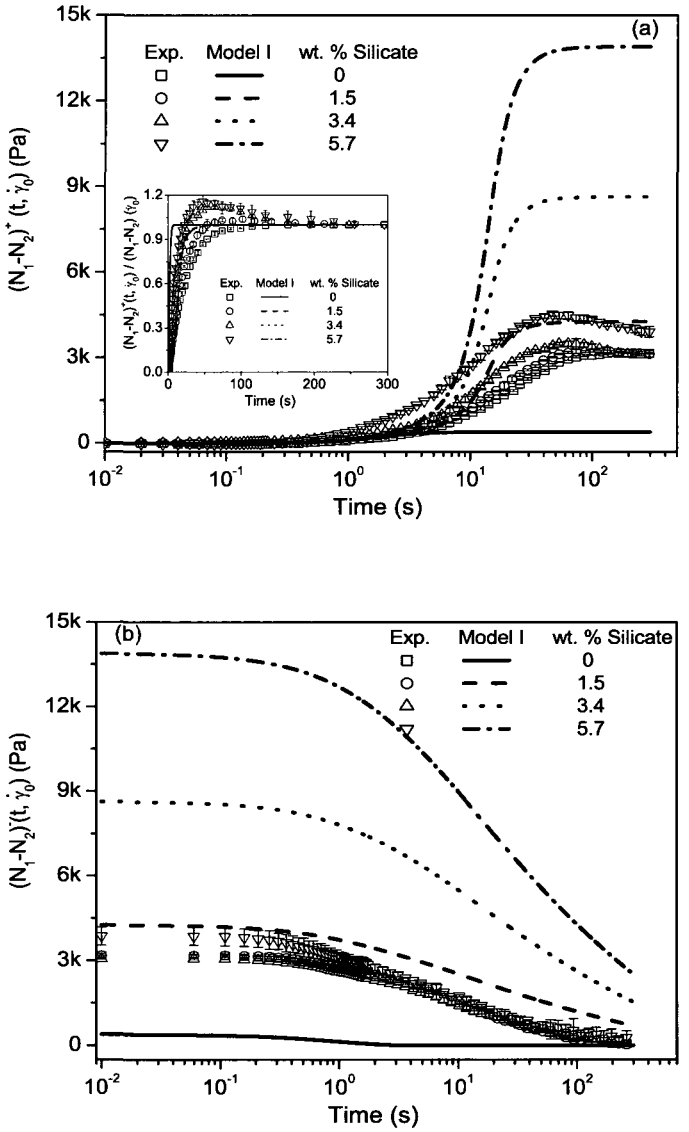

Figure 7.16: Effect of clay loading on the normal stress difference (a) start-up (b) relaxation

7.4.4 Model predictions and comparison with experimental data

Model predictions are compared with experimental data. All nonlinear experimental data are compared with predictions of Model I with the the following single set of material parameters: $b = 7.5, \kappa = 5 \times 10^{-24}, \kappa' = 3 \times 10^{-24}, K_{flex} = 0.2, \chi = 2.5 \times 10^4, \xi = 0.99, \Lambda_0^{cc} = 6.12 \times 10^{-5}, \Lambda_0^{aa} = 7 \times 10^{-8}$ and $\Lambda_0^{ca} = 5 \times 10^{-8}$. Linear viscoelastic experimental data, namely storage modulus and complex viscosity, are compared with predictions of Model II that is more appropriate for linear viscoelastic properties than Model I. Predictions of Model II are however also compared with the steady state nonlinear rheological data. The material parameters entering Model II have been chosen as follows: $\Lambda_0^{11} = 4.5 \times 10^{-6}, \Lambda_0^{22} = 2.5 \times 10^{-6}, \widetilde{\Lambda_0^{22}} = 2 \times 10^4, \Lambda_0^{33} = 2 \times 10^{-9}, \Lambda_0^{13} = 3 \times 10^{-10}, \Lambda_0^{23} = 5 \times 10^{-10}, \widetilde{\Lambda_0^{33}} = 5 \times 10^7, b = 2.5, \kappa = 2 \times 10^{-25}, \kappa' = 3 \times 10^{-25}, K_{flex} = 0.2, \chi = 10^5, \xi = 0.99, K = 2 \times 10^4$. As in the case of Model I, all predictions that we are comparing with experimental data are calculated with this singe set of material parameters. The third order mobility tensor for plates is used in both Model I and Model II. Following Ren et al. (2000), silicate layers are modeled by uniform disks with diameter 500 nm and with an average thickness introduced in Section 7.3.3. The method that we used to identify the material parameters is the same as the one applied in Eslami et al. (2007, 2009b).

The comparison of model predictions of linear rheology (storage modulus and complex viscosity) with observations is shown in figure 7.5. The observed low frequency plateau in the storage modulus and the upward complex viscosity is clearly predicted by the model. However, we have to conclude that the model fails to capture quantitatively the linear viscoelastic experimental data. We believe that this is mainly because the linear viscoelasticity is influenced by physics that is not fully included in the models. The physics in question is the formation of a network-like structure in platelets in low shear rates. The collective behavior of platelets is expected to be visible in particular at low frequencies and less so in higher frequencies revealing small scale structures. The lack of a quantitative agreement with our experimental observations of linear rheology is for us a strong motivation to extend

Model I and Model II to Model III mentioned in Introduction.

Now we turn to the nonlinear rheology. Comparison of model predictions with our experimental observations of the transient data for pure PBSA and its nanocomposites with 3.4 wt.% silicate layers at different shear rates are shown in figures 7.7-7.12. The results show that in general there is a rather good agreement for the start-up and the relaxation shear stress. However, in experimental data the magnitude of the stress overshoot increases with increasing the shear rate while model predicts almost the same stress overshoot amplitude for all shear rates (see figure 7.10(a)).

Roughly speaking, agreement of experimental data with predictions of the normal stress difference are less satisfactory. Results depicted in figures 7.9(b) and 7.10(b) show that contrary to experimental data, the model predicts no overshoot with increasing shear rate. The model also overestimates the steady state values of the $(N_1 - N_2)^+$. Predictions of the model in relaxation experiments are qualitatively in line with experimental data. However, the results of figures 7.12(a) and 7.12(b) reveal that for both the shear stress and the normal stress difference the model predicts slower relaxation than that seen in experimental data.

Now, we address the question asked in Section 7.4.3.1 regarding emergence of an overshoot in the shear stress and the normal stress difference in start-up flows of nanocomposites. Even though the overshoot in σ_{12}^+ and $(N_1 - N_2)^+$ can also be observed at high shear rates for the pure polymer (such overshoot at $\dot{\gamma} = 1\ s^{-1}$ is clearly seen in figure 7.7(a) in both model predictions and experimental data), we look at the nanocomposites in which the overshoot in the polymer matrix is less important and the observed overshoot is mainly attributed to the presence of platelets. We suggest the following explanation: In the beginning of the start-up flow, the orientation of clay layers and tactoids are nearly random. This is because each start-up test begins with a pre-shear followed by a period of rest. When the flow is switched on, the randomly dispersed clay platelets and tactoids begin to orient in the flow direction. Transition from one state of orientation (in ideal case random orientation when $t = 0$, this is what is considered in calculating our model predictions) to another state of orientation in the flow direction (less at low and intermediate shear rates and more at very high shear rates

when $t \longrightarrow \infty$) leads to the emergence of an overshoot in the shear stress and the normal stress difference.

The effect of clay loading on the steady state and transient material functions are compared with model predictions in figures 7.13-7.16. Even though both Model I and Model II can predict the overall features of the flow curve (the curve of viscosity versus shear rate), the predictions of Model II is much closer to experimental data than that of Model I (see figure 7.13(a)). In the commentary to figure 7.13(a) we mentioned that the viscosity of the nanocomposites increases dramatically at low shear rates and it becomes almost independent of the clay loading at higher shear rates. We would like to discuss now this issue in more detail with the help of the models. In principle, the stress in polymer nanocomposites is generated by both the polymer matrix and the suspended particles. From the experimental point of view, it is difficult to separate these two contributions but we can use the model to help us. Figure 7.17(a) shows the steady state shear stress components arising from the polymer matrix $\sigma_{12,\,c}$ and from the suspended particles $\sigma_{12,\,a}$ together with the total shear stress σ_{12}. The results of figure 7.17(a) show that at low shear rates the contribution of clay particles in the shear stress is more pronounced than that of the polymer matrix (the shear stress arising from the clay particles are almost five times larger than that of the polymer matrix at $\dot{\gamma} = 0.01\ s^{-1}$). However, at higher shear rates the contributions of the clay particles to the shear stress becomes smaller than that of the polymer matrix ($\sigma_{12,\,a}$ is almost ten times smaller than $\sigma_{12,\,c}$ at $\dot{\gamma} = 2\ s^{-1}$). This is because at high shear rates the clay particles are oriented in the flow direction which leads to a smaller contribution to the shear stress. The ellipsoidal representation of the polymer conformation tensor($\boldsymbol{c}$) and the plate conformation tensor ($\boldsymbol{a}$) are also shown in figure 7.17(a). We see that at high shear rates the platelets are more oriented than the polymer.

Figure 7.13(b) reveals that the predictions of two models for yielding behavior are almost the same and are in rather good agreement with experimental data. In figure 7.14(a) where the model predictions are compared with start-up viscosity, a good agreement between model predictions and experimental data is observed. Model predictions reveal that the time

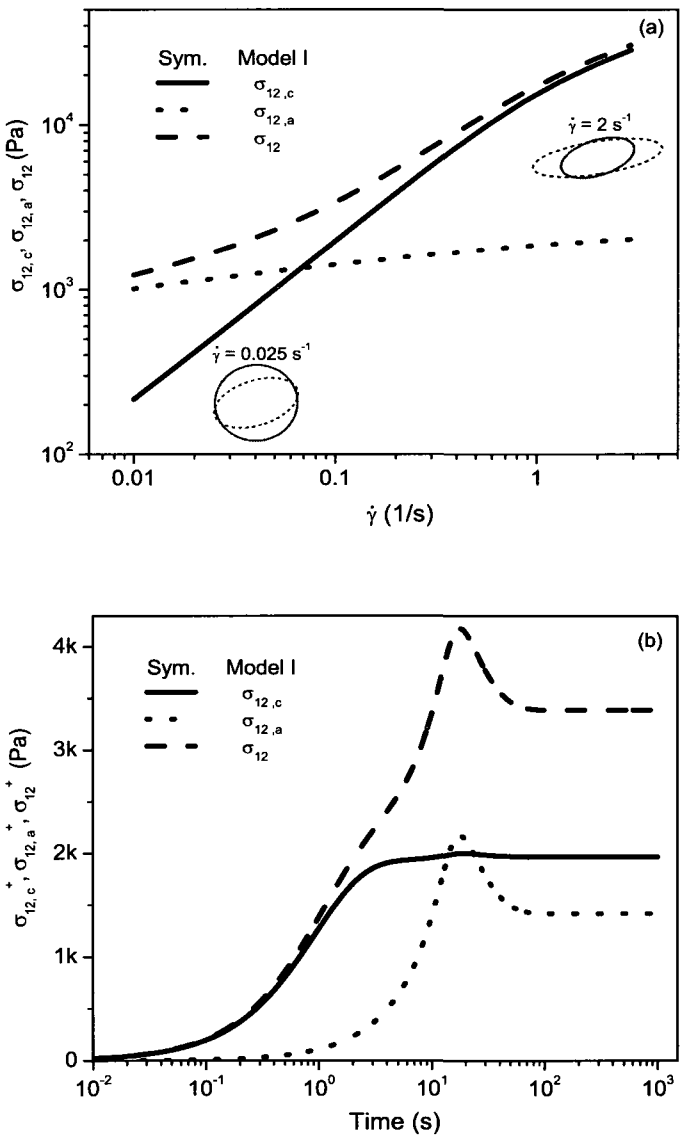

Figure 7.17: Shear stress components arising from polymer contribution $\sigma_{12,\,c}$, particles contribution $\sigma_{12,\,a}$ and total shear stress σ_{12} (a) steady state shear stress (b) transient shear stress.

required for the sample to reach its maximum (i.e. overshoot) remains almost the same as the silicate layer concentration is changed. In figure 7.17(b) the contribution of polymer and particles on the start-up shear stress are presented separately in order to better understand the role of the clay particles on the transient flow, in particular then on the overshoots. The results reveal that at a given shear rate (i.e. $\dot{\gamma} = 0.1\ s^{-1}$) the polymer does not (or almost does not) contribute to the shear stress overshoot. In other words, the overshoot in the total shear stress (σ_{12}^{+}) is generated only by the clay particles. As for the stress relaxation, model predicts slower stress relaxation for nanocomposites which then becomes even slower with increasing the clay loading. This is in agreement with experimental data (see figure 7.14(b)).

Figure 7.15(a) present $(N_1 - N_2)$ versus shear rate at different clay loading. The results show that both models fail to capture the experimental data. However, the predictions of both models agree qualitatively with experimental data at low shear rates(in particular the observation that the normal stress difference increases with increasing clay loading). It should be noted that neither Model I nor Model II is able to predict the phenomena observed at intermediate and high shear rates in the normal stress difference versus shear rate (see figure 7.15(a)). In figure 7.15(b) where the elasticity of PBSA and its nanocomposites is reported, the prediction of Model II is qualitatively in agreement with experimental data (nearly independent of clay loading) while Model I predicts an increase in the elasticity of nanocomposites with increasing clay loading. Start-up and relaxation experimental data of normal stress difference are also compared with model predictions and the results show that model cannot predict the overshoot in $(N_1 - N_2)^{+}$ as discussed earlier (see figure 7.16(a)). The model predictions are also found to agree qualitatively with relaxation data of normal stress difference $(N_1 - N_2)^{-}$ but overestimates their values (see figure 7.16(b)).

7.5 Conclusions

Layered-silicate-based poly[butylene succinate-co-adipate] nanocomposites were prepared by direct melt mixing. WAXD patterns reveal the existence of clay tactoids dispersed in PBSA

matrix. Together with transmission electron microscopic observations they also show a coexistence of intercalate/exfoliate silicate layers. Linear viscoelastic properties show a low frequency plateau in the storage modulus, an observation attributed to the randomly dispersed clay platelets and tactoids in polymer melts and their ability to form network structures seen at large time scales. The effect of the imposed shear rate and the clay loading on the transient (start-up and relaxation) and the steady state behavior have also been investigated. The results of transient tests show that the amplitude of the observed overshoot for the shear stress and the normal stress difference increases with increasing the shear rate and/or the clay loading. For the clay loading that is higher than the percolation threshold, the steady state viscosity shows a significant increase in low shear rates. At relatively high shear rates, the viscosity approaches that of the polymer matrix. Steady state normal stress difference appears to be larger than that of the pure polymer at low shear rates. The inverse dependence is observed at relatively high shear rates (in the range of the shear rates reported in the paper). The behavior at low shear rates is attributed to the rigidity that becomes stronger in the presence of clay particles and tactoids. The phenomena observed at high shear rates are attributed to the orientation of clay platelets and tactoids that are subjected to shear flows. Two mesoscopic rheological models developed earlier, are extended to nanocomposites in which intercalated and exfoliated silicate layers coexist. The extended models are able to captured the overall observed behavior of the PLS nanocomposites discussed in this paper. Other aspects, in particular then the network structure of clay platelets and tactoids, require a further extension of the models.

Acknowledgements

The authors acknowledge the financial support provided by the Natural Sciences and Engineering Research Council (NSERC) of Canada. The authors also grateful to Showa High Polymer Ltd, Japan, company for kindly provided the polymer used in this study.

References

1. Alexandre, M. and Dubois, P. (2000). Polymer-layered silicate nanocomposites: preparation, properties and uses of a new class of materials. Materials Science and Engineering, 28:1-63.

2. Aubry, T., Razafinimaro, T., and Mederic, P. (2005). Rheological investigation of the melt state elastic and yield properties of a polyamide-12 layered silicate nanocomposite. J. Rheol., 49:425-440.

3. Beris, A. N. and Edwards, B. J. (1994). Thermodynamics of flowing systems. Oxford University Press, New York.

4. Bird, R. B., Armstrong, R. C., and Hassager, O. (1987). Dynamics of polymeric fluids, volume 1. Wiley, New York.

5. Carreau, P. J., De Kee, D., and Chhabra, R. P. (1997). Rheology of polymeric systems: Principles and applications. Hanser, Munich.

6. Eslami, H. and Grmela, M. (2008). Mesoscopic formulation of reptation. Rheol. Acta, 47:399-415.

7. Eslami, H., Grmela, M., and Bousmina, M. (2007). A mesoscopic rheological model of polymer/layered silicate nanocomposites. J. Rheol., 51:1189-1222.

8. Eslami, H., Grmela, M., and Bousmina, M. (2009). A mesoscopic tube model of polymer/layered silicate nanocomposites. Rheol. Acta. in press.

9. Eslami, H., Ramazani, A., and Khonakdar, H. A. (2004). Predictions of some internal microstructural models for polymer melts and solutions in shear and elongational flows. Macromol. Theory Simul., 13:655-664.

10. Galgali, G., Ramesh, C., and Lele, A. (2001). Rheological study on the kinetics of hybrid formation in polypropylene nanocomposites. Macromolecules, 34:852-858.

11. Grmela, M. (1984). Particle and bracket formulations of kinetic equations. Contemp. Math., 28:125-132.

12. Grmela, M. (1986). Bracket formulation of diffusion-convection equations. Physica D, 21:177-212.

13. Grmela, M. (1991). Mesoscopic dynamic and thermodynamic: Application to polymer fluids. Lecture Notes in Physics, 381:99-126.

14. Grmela, M. (2002). Reciprocity relations in thermodynamics. Physica A, 309:304-328.

15. Grmela, M. and Ottinger, H. C. (1997). Dynamics and thermodynamics of complex fluids. I. Development of a general formalism. Phys. Rev.E, 55:6620-6632.

16. Gupta, R. K., Pasanovic-Zujo, V., and Bhattacharya, S. N. (2005). Shear and extensional rheology of EVA/layered silicate-nanocomposites. J. Non- Newtonian Fluid Mech., 128:116-125.

17. Isichenko, M. B. (1992). Percolation, statistical topography and transport in random media. Rev. Mod. Phys., 64:961-1043.

18. Jeon, H. S., Rameshwaram, J. K., and Kim, G. (2004). Structure property relationships in exfoliated polyisoprene/clay nanocomposites. Journal of Polymer Science: Part B: Polymer Physics, 42:1000-1009.

19. Kim, D. H., Fasulo, P. D., Rodgers, W. R., and Paul, D. R. (2007). Structure and properties of polypropylene-based nanocomposites: Effect of PP-g-MA to organoclay ratio. Polymer, 48:5308-5323.

20. Krishnamoorti, R. and Giannelis, E. P. (1997). Rheology of end-tethered polymer layered silicate nanocomposites. Macromolecules, 30:4097-4102.

21. Krishnamoorti, R., Ren, J., and Silva, A. S. (2001). Shear response of layered silicate nanocomposites. J. Chem. Phys., 114:4968-4972.

22. Krishnamoorti, R., Vaia, R. A., and Giannelis, E. P. (1996). Structure and dynamics of polymer layered silicate nanocomposites. Chem. Mater., 8:1728-1734.

23. Letwimolnun, W., Vergnes, B., Ausias, G., and Carreau, P. J. (2007). Stress overshoots of organoclay nanocomposites in transient shear flow. J. Non- Newtonian Fluid Mech., 141:167-179.

24. Li, J., Zhou, C., Wang, G., and Zhao, D. (2003). Study on rheological behavior of polypropylene/clay nanocomposites. J. Appl. Polym. Sci., 89:3609-3617.

25. Lim, Y. T. and Park, O. O. (2001). Phase morphology and rheological behavior of polymer/layered silicate nanocomposites. Rheol. Acta, 40:220-229.

26. Malkin, A. Y. (1990). Rheology of filled polymer. Advances in polymer science, 96:69-97.

27. Marrison, F. A. (2001). Understanding rheology. Oxford university press, New York.

28. Ottinger, H. C. (2005). Beyond equilibrium thermodynamics. Wiley-Interscience.

29. Ottinger, H. C. and Grmela, M. (1997). Dynamics and thermodynamics of complex fluids. II. Illustrations of a general formalism. Phys. Rev.E, 56:6633-6655.

30. Ren, J. and Krishnamoorti, R. (2003). Nonlinear viscoelastic properties of layered silicate based intercalated nanocomposites. Macromolecules, 36:4443-4451.

31. Ren, J., Silva, A. S., and Krishnamoorti, R. (2000). Linear viscoelasticity of disordered polystyrene-polyisoprene block copolymer based layered silicate nanocomposites. Macromolecules, 33:3739-3746.

32. Sinha Ray, S. and Bousmina, M. (2005a). Biodegradable polymers and their layered silicate nanocomposites: In greening the 21st century materials world. Prog. Mater Sci., 50:962-1079.

33. Sinha Ray, S. and Bousmina, M. (2005b). Poly(butylene sucinate-co-adipate) montmorillonite nanocomposites: effect of organic modifier miscibility on structure, properties, and viscoelasticity. Polymer, 46:12430-12439.

34. Sinha Ray, S., Bousmina, M., and Okamoto, K. (2005). Structure and properties of nanocomposites based on poly(butylene succinate-co-adipate) and organically modified montmorillonite. Macromol. Mater. Eng., 290:759-768.

35. Solomon, M. J., Almusallam, A. S., Seefeldt, K. F., Somwangthanaroj, A., and Varadan, P. (2001). Rheology of polypropylene/clay hybrid materials. Macromolecules, 34:1864-1872.

36. Steeves, D. M., Farrell, R., and Ratto, J. A. (2007). Investigation of polybutylene succinate-co-adipate(PBSA)/montmorillonite layered silicate (MLS) melt processed nanocomposites. Journal of Biobased Materials and Bioenergy, 1:94-108.

37. Vermant, J., Ceccia, S., Dolgovskij, M. K., Maffettone, P. L., and Macosko, C. W. (2007). Quantifying dispersion of layered nanocomposites via melt rheology. J. Rheol., 51:429-450.

38. Wolfram, S. (1991). Mathematica-A system for doing mathematics by computer. Wesley-VCH, New York.

39. Wu, D., Zhou, C., Hong, Z., Mao, D., and Bian, Z. (2005). Study on rheological behaviour of poly(butylene terephthalate)/montmorillonite nanocomposites. European Polymer Journal, 41:2199-2207.

40. Xu, L., Reeder, S., Thopasridharan, M., Ren, J., Shipp, D. A., and Krishnamoorti, R. (2005). Structure and melt rheology of polystyrene-based layered silicate nanocomposites. Nanotechnology, 16:S514-S521.

CHAPTER 8

STRUCTURE BUILD-UP AT REST IN POLYMER NANOCOMPOSITES: FLOW REVERSAL EXPERIMENTS

Hassan Eslami[a], Miroslav Grmela[a1] , Mosto Bousmina[b,c]

[a] Center for Applied Research on Polymers and Composites (CREPEC)
Ecole Polytechnique de Montreal, C.P.6079 suc. Centre-ville,
Montreal, H3C 3A7, Quebec, Canada

[b] Canada Research Chair on Polymer Physics and Nanotechnology
and Center for Applied Research on Polymers and Composites (CREPEC)
Department of Chemical Engineering, Laval University, Ste-Foy,
G1K 7P4, Quebec, Canada

[c] Hassan II Academy of Sciences and Technology, Rabat, Marocco

Submitted to Journal of Polymer Science, Part B: Polymer Physics

[1]corresponding author: e-mail: miroslav.grmela@polymtl.ca

Abstract

Evolution of the microstructure as well as the shear stress and the normal stress difference of polymer/layered silicate nanocomposites prepared by melt mixing of poly[butylene succinate-co-adipate] and organically modified montmorillonite are investigated in transient forward and reverse start-up shear flows at different clay loading and different shear rates. Special attention is paid to the structure build-up at rest and to the amplitude of the overshoots observed during the reverse start-up test in the shear stress and the normal stress difference. The model that we have developed previously [Eslami et al. (2007)] is employed to suggest an explanation for the observed phenomena.

8.1 Introduction

The complex fluid under investigation in this paper is a suspension of nanoparticles in a viscoelastic polymer. The polymer is poly[butylene succinate-co-adipate] (PBSA) and the nanoparticles are organically modified montmorillonite. We observe how the suspensions respond to sudden changes of the imposed shear flow and compare the observed behavior with predictions of the model developed in [Eslami et al. (2007)]. The sudden changes are of three types: start-up, cessation, and reversion of the imposed shear flow. In the first one, the nanosuspension is initially at rest (at thermodynamic equilibrium) and the shear flow with a given shear rate is suddenly switched on. In the second type of flow, the nanosuspension is let to reach a stationary state and then the imposed flow is suddenly switched off. In the third type of flow, we proceed as in the second but after a period of time the initial imposed shear flow is again switched on but this time in the opposite direction. In all three types of flows we measure systematically both the shear stress and the normal stress difference. All measured results are compared in this paper with predictions of the model developed in [Eslami et al. (2007)]. These time-dependent experiments are known as stress growth (start-up) and stress decay (relaxation) experiments [Bird et al. (1987a); Marrison (2001)]. Generally speaking, these type of experiments provide a valuable insight into the microstructure of complex

fluids. In case of polymer layered silicate (PLS) nanocomposites, an information about the orientation and/or disorientation of silicate layers under flow, and to some extend also about the creation and annihilation of a network structure, can be deduced from an analysis of the location and the amplitude of the overshoots seen in the shear stress and the normal stress differences in start-up experiments. In order to investigate the structure build-up at rest, flow reversal experiments with different time periods between cessation of the forward and introduction of the reverse start-up flows (hereafter called rest time) are needed. Recovery of the structure in the rest period is manifested by reappearance of stress overshoots in the reverse start-up flows.

Flow reversal experiments have been used to investigate polypropylene/clay nanocomposites in Solomon et al. (2001). During the reverse start-up flow, the amplitude of the stress overshoot is found to depend sensitively on the rest time. This indicates that the internal structure of nanocomposites continues to evolve even during the rest time. The authors suggest that the process responsible for the overshoots is the rupture and/or orientation of a mesoscopic particulate domain of multiple ordered platelets (particulate aggregate). The origin of the structure recovery at rest is attributed to the attractive interaction among the multiplatelet domains and not to the Brownian motion.

More recently, flow reversal experiments have been used to investigate a series of nanocomposites with different degrees of dispersion in Letwimolnun et al. (2007). The authors use different mixing devices and different processing conditions to obtain different microstructures. The structure build-up at rest is found to depend sensitively on the degree of exfoliation. The authors suggest that the stress overshoot could be attributed to the breakdown and/or orientation of the structured clay network induced by the imposed shear flow. During the rest time, the disorientation of clay platelets, which becomes nearly isotropic after a long rest time, is assumed to be responsible for the structure build-up at rest.

Some of the results of experimental observations reported in Letwimolnun et al. (2007) are compared in Letwimolnun et al. (2007) with two models. The first one, originally developed for concentrated colloidal suspensions [Yziquel et al. (1999)], consists of two time evolution

equations, one for the extra stress tensor (a modified upper-convected Jeffreys model) and another one, for new scalar microstructural state variable ξ. The material parameters entering the first equations are let to depend on ξ. The second model is the Folgar-Tucker model [Folgar and Tucker (1984)], originally introduced for fiber suspensions, with a modified diffusion coefficient ($C_I\dot{\gamma}$ appearing in the Folgar-Tucker model is replaced by $C_I\dot{\gamma}+D_r$, where D_r is a new material parameter). The first model predicts the amplitudes of stress overshoots as well as their stationary values but it fails to predict the strains at which the stress overshoots appear. The second model can qualitatively predict stress overshoots in the forward start-up flows and an increase in their amplitudes with increasing the rest time before switching on the reverse start-up flow. However, the stress overshoots appear at the strains which decrease with increasing the rest time while in experiments they remain essentially unchanged.

In this paper we contribute to the investigation of PLS nanocomposites in flow reversal experiments by observing systematically both the shear stress and the normal stress difference and by using one model [Eslami et al. (2007)] (involving both the suspended nanoparticles and interacting with them polymer macromolecules) to evaluate all the results of our experimental observations.

The paper is organized as follows: First, the experimental procedure is explained in Section 8.2. Next, in Section 8.3, the mesoscopic rheological model developed in Eslami et al. (2007) is briefly recalled and its extension to incompletely exfoliated nanocomposites discussed. Finally, in Section 8.4, the experimental results are presented and compared with predictions of the extended model.

8.2 Experimental

In this section we describe the experimental procedure.

8.2.1 Materials

Poly (butylene succinate-co-adipate) (PBSA), a biodegradable polyester, is used as polymer matrix. This polymer is a commercial product from Showa High Polymer Ltd, Japan, with the designation BIONOLLE 3001. According to the supplier, PBSA has a molecular weight 190 kg/mol and mass density of 1230 kg/m^3. The organically modified montmorillonite used in this study is Cloisite 30B (C30B) supplied by Southern Clay products. C30B is treated with a surfactant having the chemical structure: methyl, tallow, bis(2-hydroxyeethyl), quaternary ammonium chloride. The reason why we have chosen C30B is the presence of diols on C30B which has a strong interaction with "CO" group on the PBSA backbone [Sinha Ray and Bousmina (2005a,b)]. Both PBSA and C30B were dried under vacuum at 50 $°C$ for 72 hours prior to the process.

8.2.2 Preparation of nanocomposites

Nanocomposites were prepared using thermo Haake mixer operated at 150 $°C$ and a rotor speed of 90 rpm for 10 min. under nitrogen purge (first, PBSA was melted and after 2 min. C30B was added). Nanocomposites with two different concentrations of silicate, 3.4± 0.1 and 5.7± 0.1 wt. %, hereafter called PN3.4S and PN5.7S respectively, were prepared. Thermogravimetric analysis (TGA) was employed to determine the inorganic content in C30B and the nanocomposites. The results of TGA were then also verified by burning a large amount of the sample in the furnace at 800 $°C$ for 24 hours and then measuring the inorganic content. The prepared nanocomposites were dried in the vacuum oven operated at 50 $°C$ for 12 hours to remove any possible residual water. Discs with 25 mm diameter and (1.5-2) mm thickness were prepared with a laboratory press operated at 3 MPa and 150 $°C$ for 10 min. (5 min. preheating and 5 min. under pressure) under nitrogen purge. The samples were subsequently cooled in a cold press and dried again in the oven under vacuum at 50 $°C$ for 24 hours. Finally, the samples were kept in the desiccator under vacuum at room temperature for further tests.

8.2.3 Characterization of nanocomposites

8.2.3.1 WAXD and TEM

The interlayer distance of clay platelets in the C30B and nanocomposites were studied by means of wide angle X-ray diffraction (WAXD) using a Philips X'pert diffractometer (Cu Kα radiation $\lambda = 1.54$ °A, generator voltage = 50 kV, current = 40 mA). The scans were performed in 2θ ranges from 1 ° to 10 ° at a rate of 1/min. The morphology of the samples was examined by a high resolution transmission electron microscopy (TEM) (JEOL model JEM-2100F) operated at an accelerating voltage of 200 kV without staining. For TEM measurements, ultrathin sections were prepared by cryogenic ultra-microtome operated at $T = -100$ °C with a diamond knife.

8.2.3.2 Rheology

Rheological experiments were conducted with a strain-controlled rheometer (TA Instruments, ARES). Parallel plate fixture with 25 mm diameter was used for all experiments and the temperature was set at 140 °C. Before applying any shear, the sample was let to relax in the rheometer for 15 min and then the gap was adjusted to 1.3 mm by squeezing the sample between parallel plates. In order to remove the flow history during the sample preparation and loading, a pre-shear was applied to the sample till steady state was reached and then the sample was let to relax. The normal force signal was monitored to make sure that the normal force became negligible before starting the test. Stress growth (start-up) experiment was then performed in sequential tests. First, a given shear rate (0.1 s^{-1} or 0.2 s^{-1}), was applied to the sample and the resultant stresses were monitored till steady state was reached. Hereafter, the result of this test is called a forward stat-up flow. The flow was stopped suddenly and after a predetermined rest time (between 10 to 1800 sec), the same shear flow in the reverse direction was applied. Hereafter, we refer to it as a reverse stat-up flow. This type of experiments is well known as flow reversal experiments.

Our rheological measurements were performed in the parallel plate geometry where the

shear rate is not constant throughout the sample. Consequently, all experimental rheological data were corrected and reported at rim shear rate. For parallel plate geometry, the shear viscosity η and normal stress difference $(N_1 - N_2)$ can be calculated by using the measured torque T and measured axial force F as functions of shear rate at rim $\dot{\gamma}_R$ as follow: [Bird et al. (1987a); Carreau et al. (1997); Marrison (2001)]:

$$\eta(\dot{\gamma}_R) = \frac{T}{2\pi R^3 \dot{\gamma}_R}\left[3 + \frac{d\ln\left(\frac{T}{2\pi R^3}\right)}{d\ln\dot{\gamma}_R}\right] \tag{8.1}$$

$$N_1(\dot{\gamma}_R) - N_2(\dot{\gamma}_R) = \frac{2F}{\pi R^2}\left[1 + \frac{1}{2}\frac{d\ln F}{d\ln\dot{\gamma}_R}\right] \tag{8.2}$$

In this study, the contribution of the second normal stress difference N_2 to the total thrust is not neglected and throughout this study the difference between the first and the second normal stress difference $(N_1 - N_2)$ is reported. It should be noted that for unfilled polymeric materials, the so-called Weissenberg hypothesis is usually assumed to be valid (i.e. $N_2 = 0$). The quantities $d\ln\left(T/2\pi R^3\right)/d\ln\dot{\gamma}_R$ and $d\ln F/d\ln\dot{\gamma}_R$ appearing in Eqs.8.1 and 8.2 are obtained by plotting $\ln\left(T/2\pi R^3\right)$ and $\ln F$ versus $\ln\dot{\gamma}_R$ and taking the slope of the regression line through the data points at different shear rate regions. In order to calculate these quantities, we used the steady state experimental data of our nanocomposites measured for a wide ranges of shear rate reported in Eslami et al. (2009a).

8.3 Modeling

In order to be able to make a connection between the microscopic physics taking place in the nanocomposites and our experiments we compare results of our experimental observations with predictions of a model that takes into account explicitly the plate-plate and plate-polymer interactions. We use the model that we have developed previously in [Eslami et al. (2007)]. The model is formulated in the GENERIC framework (see Grmela and Ottinger (1997); Ottinger and Grmela (1997) and references cited therein) guaranteeing by itself the agreement of predictions with experimental observations on which equilibrium thermody-

namics is based.

In this section the model is briefly recalled and extended to incompletely exfoliated nanocomposites. The predictions of extended model are then compared with experimental data in the next section. Interested readers can found details of the model formulation in Eslami et al. (2007).

Two state variables $\boldsymbol{c}$ and $\boldsymbol{a}$ (both symmetric and positive definite three-by-three conformation tensors) are used to describe states of the nanocomposites; $\boldsymbol{c}$ is a conformation tensor of the polymer macromolecules and $\boldsymbol{a}$ of clay lamellae. The conformation tensor $\boldsymbol{a}$ is constrained by the relation $tr\boldsymbol{a} = A_0$ where A_0 is the surface area of the silicate layers.

The equations governing the time evolution of $\boldsymbol{c}$ and $\boldsymbol{a}$ have the following form:

$$\begin{aligned} \frac{d\boldsymbol{c}}{dt} &= -\frac{1}{2}\left(\boldsymbol{\Omega}\cdot\boldsymbol{c}-\boldsymbol{c}\cdot\boldsymbol{\Omega}\right)+\frac{1}{2}\left(\dot{\boldsymbol{\gamma}}\cdot\boldsymbol{c}+\boldsymbol{c}\cdot\dot{\boldsymbol{\gamma}}\right) \\ &\quad -\frac{\partial\,\Xi}{\partial\,\Phi_{\boldsymbol{c}}} \end{aligned} \tag{8.3}$$

$$\begin{aligned} \frac{d\boldsymbol{a}}{dt} &= -\frac{1}{2}\left(\boldsymbol{\Omega}\cdot\boldsymbol{a}-\boldsymbol{a}\cdot\boldsymbol{\Omega}\right)+\xi\left(-\frac{1}{2}\left(\dot{\boldsymbol{\gamma}}\cdot\boldsymbol{a}+\boldsymbol{a}\cdot\dot{\boldsymbol{\gamma}}\right)+\frac{1}{A_0}tr(\boldsymbol{a}\,.\,\dot{\boldsymbol{\gamma}})\,\boldsymbol{a}\right) \\ &\quad -\frac{\partial\,\Xi}{\partial\,\Phi_{\boldsymbol{a}}} \end{aligned} \tag{8.4}$$

where $\dot{\gamma}_{\alpha\beta} = \frac{\partial v_\alpha}{\partial r_\beta} + \frac{\partial v_\beta}{\partial r_\alpha}$ and $\boldsymbol{\Omega}_{\alpha\beta} = \frac{\partial v_\alpha}{\partial r_\beta} - \frac{\partial v_\beta}{\partial r_\alpha}$, $\boldsymbol{v}$ is the overall velocity field, ξ is the Gordon-Schowalter phenomenological parameter representing the nonaffine advection of the clay platelets, Ξ and Φ are the dissipation potential and the free energy of the system under consideration respectively. The extra stress tensor $\boldsymbol{\sigma}$ that is compatible with (8.3) and (8.4), arising as an integral part of the GENERIC framework, is given by

$$\boldsymbol{\sigma} = -2\,\boldsymbol{c}\,.\,\Phi_c + 2\,\xi\,\left(\boldsymbol{a}.\Phi_a - \frac{1}{A_0}\,\boldsymbol{a}\,tr(\boldsymbol{a}\,.\,\Phi_a)\right) \tag{8.5}$$

The free energy Φ appearing in Eqs. (8.3), (8.4) and (8.5) is chosen to be:

$$\begin{aligned} \Phi &= -\frac{1}{2}n_c H Q_0^2 \ln\left[1-tr\left(\frac{\boldsymbol{c}}{Q_0^2}\right)\right]-\frac{1}{2}n_c k_B T\ln\left[\det\left(\frac{\boldsymbol{c}}{Q_0^2}\right)\right] \\ &\quad -\frac{1}{2}n_a G A_0 tr\left(\frac{\boldsymbol{a}}{A_0}\right)-\frac{1}{2}n_a k_B T\left(1-K_{flex}\right)\ln\left[\det\left(\frac{\boldsymbol{a}}{A_0}\right)\right] \end{aligned}$$

$$+\frac{1}{2}n_a k_B T K_{flex} tr\left(A_0 \boldsymbol{a}^{-1}\right) - \frac{1}{2}n_a^2 k_B T \kappa \left[tr\left(\frac{\boldsymbol{a}}{A_0}\cdot\frac{\boldsymbol{a}}{A_0}\right) - \left(tr\frac{\boldsymbol{a}}{A_0}\right)^2\right]$$
$$+\frac{1}{2}n_c n_a k_B T \kappa' tr\left(\frac{\boldsymbol{c}}{Q_0^2}\cdot\frac{\boldsymbol{a}}{A_0}\right) \tag{8.6}$$

where k_B is the Boltzmann constant, T is the temperature, Q_0 is the largest extension of the dumbbell, H is the elastic modulus of the dumbbell spring, n_c is the number density of the polymer macromolecules and n_a is the number density of clay lamellae, κ and κ' are material parameters quantifying the topological plate-plate and polymer-plate interactions respectively. Clay platelets are also assumed to be flexible, K_{flex} is another material parameter measuring the flexibility. Moreover, n_c and n_a are defined as $n_c = \frac{(1-\alpha)\rho_c N_A}{M_c}$; $n_a = \frac{\alpha}{A_0 h}$, where N_A is the Avogadro number, M_c is the molecular weight of the polymer, ρ_c is the mass density of the polymer, α is the clay volume fraction and h is its thickness.

For states that are not too far from equilibrium, the dissipation potential Ξ appearing in (8.3) and (8.4) is chosen to be the following quadratic function:

$$\Xi = \begin{pmatrix} \Phi_{\boldsymbol{c}} & , & \Phi_{\boldsymbol{a}} - \frac{1}{3}tr\Phi_{\boldsymbol{a}}\boldsymbol{\delta} \end{pmatrix} \begin{pmatrix} \frac{\boldsymbol{\Lambda}^{cc}}{1-\alpha} & \frac{\boldsymbol{\Lambda}^{ca}}{\alpha(1-\alpha)} \\ \frac{\boldsymbol{\Lambda}^{ca}}{\alpha(1-\alpha)} & \frac{\boldsymbol{\Lambda}^{aa}}{\alpha} \end{pmatrix} \begin{pmatrix} \Phi_{\boldsymbol{c}} \\ \Phi_{\boldsymbol{a}} - \frac{1}{3}tr\Phi_{\boldsymbol{a}}\boldsymbol{\delta} \end{pmatrix} \tag{8.7}$$

where $\boldsymbol{\Lambda}^{cc}$, $\boldsymbol{\Lambda}^{aa}$, and $\boldsymbol{\Lambda}^{ca}$ are respectively polymer, plate and polymer-plate interaction mobility tensors which are chosen to be polynomial functions of $\boldsymbol{c}$ and $\boldsymbol{a}$.

The above model assumes that the clay lamellae are completely exfoliated. This is not however the case in the nanocomposites that we investigate in this paper experimentally. In order to be able to use the model we shall adapt it to partially exfoliated nanocomposites, in which intercalate and exfoliate structures coexist. The fact that the microscopic physics taking place in the nanocomposites is expressed in (8.3) and (8.4) on a mesoscopic level allows us to make a simple adaptation. Single clay lamellae are replaced by clay tactoids with an average thickness. The physical interpretation of the modified model remains unchanged if and only if the amount of the polymeric chains inside the clay galleries do not play a significant role on the rheology of the suspension. This is indeed a reasonable assumption

since the rheology is mainly governed by the bulk of the system and the amount of polymer inside the clay galleries can be ignored.

The question that remains to be answered is what is the average thickness of clay tactoids in the suspension. There are two simple ways to determine it. First, we can use an image analysis software to analyze the TEM images of nanocomposites and from them to calculate the average thickness of the tactoids. Second, following Ren et al. (2000), we can use linear viscoelastic data to determine the percolation threshold and from it to calculate the average thickness of the tactoids. In this paper we follow the second route.

Following the expression introduced in Vermant et al. (2007) (a reformulation of the expression introduced previously in Ren et al. (2000)), the average aspect ratio A_f of the tactoids is written as follows:

$$A_f = \frac{3\,\phi_{per}}{4\,\alpha_{per}} \tag{8.8}$$

where ϕ_{per} is the percolation threshold volume fraction for randomly packed spheres in three dimensions (calculated to be 0.3; i.e. $\phi_{per} = 0.3$, see Isichenko (1992) for more detail), α_{per} is the percolation threshold calculated from linear viscoelastic experimental data. In order to calculate α_{per}, we used the linear viscoelastic data of our nanocomposites measured for a wide ranges of frequency reported in Eslami et al. (2009a). Experimental data are compared with predictions of the model with the the following single set of material parameters: $b = 7.5, \kappa = 5\times10^{-24}, \kappa' = 3\times10^{-24}, K_{flex} = 0.2, \chi = 2.5\times10^{4}, \xi = 0.99, \Lambda_0^{cc} = 6.12\times10^{-5}, \Lambda_0^{aa} = 7\times10^{-8}$ and $\Lambda_0^{ca} = 5\times10^{-8}$. The third order mobility tensor for plates is used. It should also be noted that these material parameters are the same as the one used in Eslami et al. (2009a). Following Ren et al. (2000), silicate layers are modeled by uniform disks with diameter 500 nm and with an average thickness.

Finally, the system of the differential equations is numerically solved by using the MATHEMATICA software package [Wolfram (1991)].

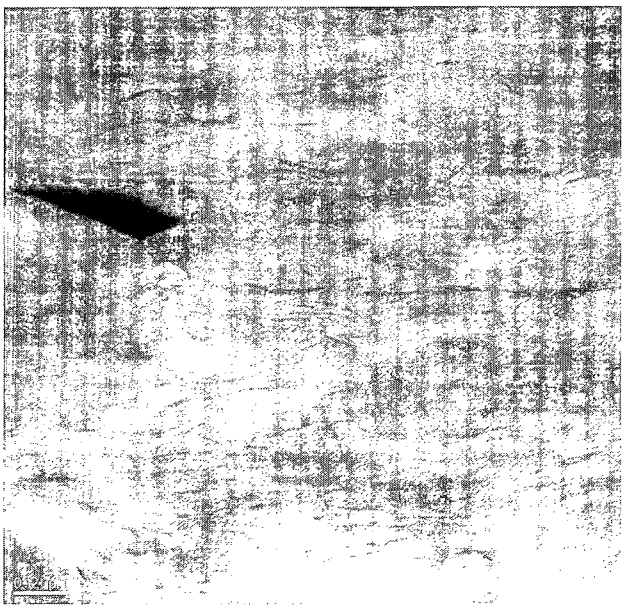

Figure 8.1: TEM micrograph of PN5.7S

8.4 Results and discussion

Results of our measurements of the morphology are presented in Section 8.4.1. Results of our rheological measurements together with their comparison with model predictions are reported in Sections 8.4.2.

8.4.1 Morphology

Typical pictures of the nanocomposites that we investigate in this paper are presented in figure 8.1 and figure 8.2 where the TEM micrograph and WAXD patterns of nanocomposites are shown respectively. The TEM image shows the existence of some individual clay layers and stacks of clay platelets uniformly dispersed in polymer matrix. WAXD patterns of pure PBSA, C30B and nanocomposites reveal that the diffraction peaks of nanocomposites shift to the lower angle when they are compared with C30B's peak (an indication of increasing

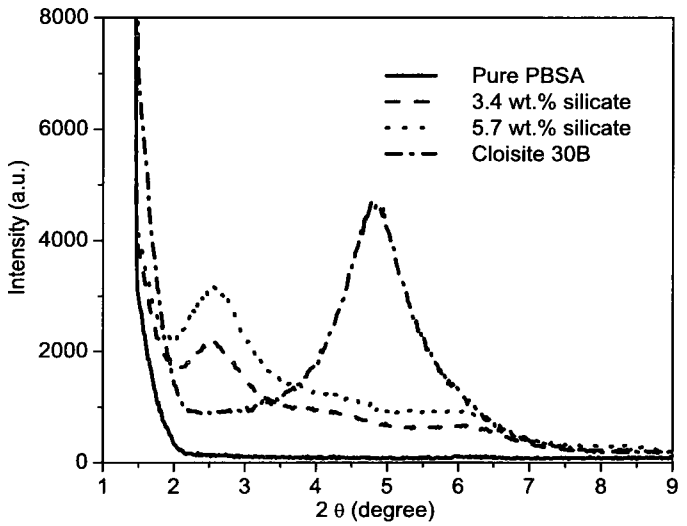

Figure 8.2: WAXD patterns of pure PBSA, C30B and nanocomposites

of the interlayer spacing of clay layers). It should also be noted that the intensity of the diffraction peaks in the nanocomposites is smaller than that of C30B which reveals the existence of some exfoliated silicate layers dispersed in polymer matrix. The results of both TEM and WAXD indicate a coexistence of intercalate/exfoliate structure in nanocomposites. Similar observation has been recently reported in Rajabian et al. (2008) for polypropylene clay nanocomposites and the same conclusion regarding the intensity of the peaks and morphology of nanocomposites has been drown.

8.4.2 Rheology

Response of PN3.4S to start-up flows in the forward direction is shown in figures 8.3(a) and 8.4(a) for the transient shear stress σ_{12}^{+} and the transient normal stress difference $(N_1 - N_2)^{+}$ respectively. For the reference, the transient rheological data of pure PBSA (polymer matrix) measured at the same condition are also shown in these figures. Six other series of data in these figures correspond to the forward experiment for different samples used for subsequent

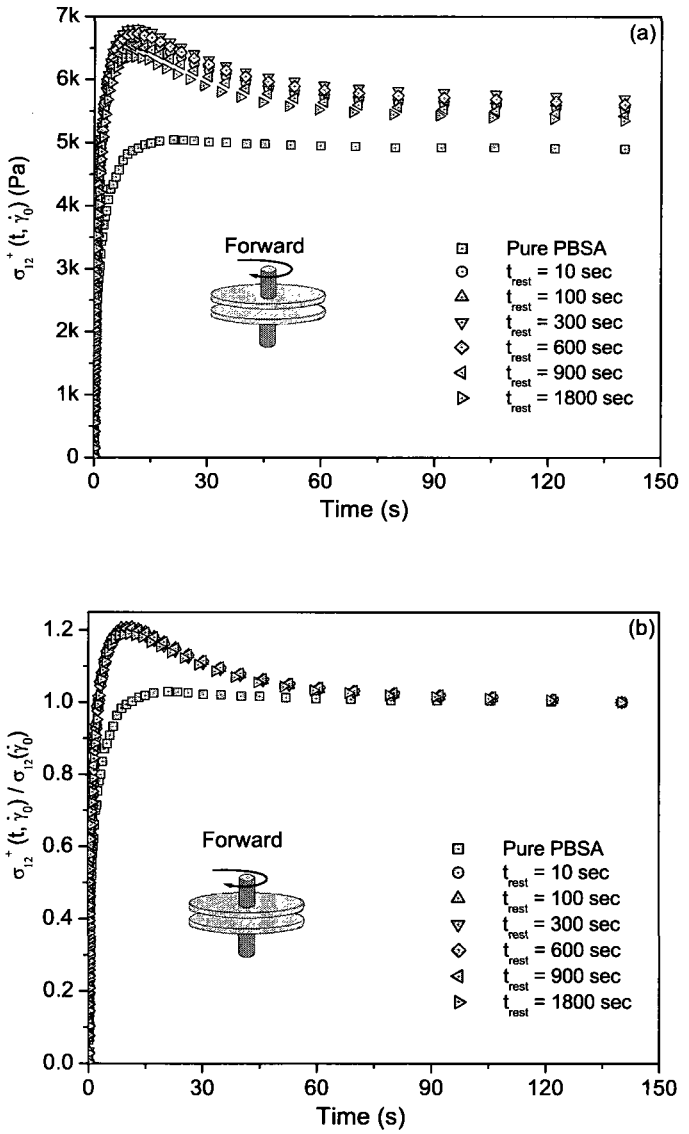

Figure 8.3: Forward start-up experiments for samples used at different reverse start-up flow experiments (a) shear stress and (b) normalized shear stress

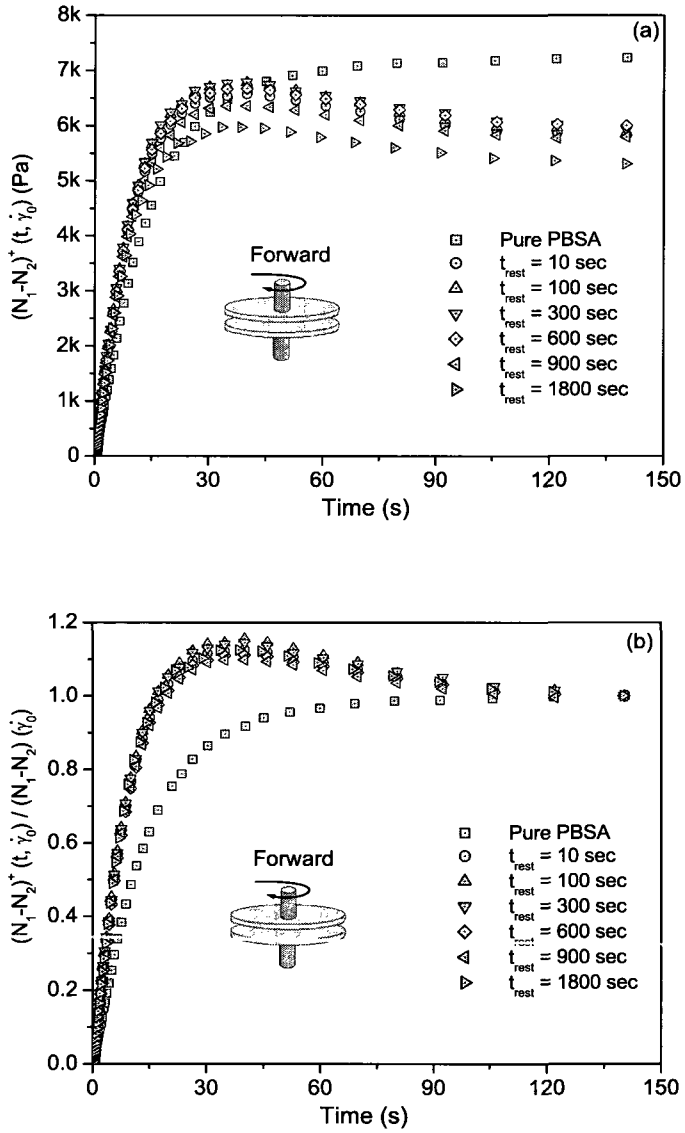

Figure 8.4: Forward start-up experiments for samples used at different reverse start-up flow experiments(a) normal stress difference and (b) normalized normal stress difference

reverse stat-up flow. The amplitude of overshoots in the shear stress and the normal stress difference becomes clearer in the normalized representation of these graphs reported in figures 8.3(b) and 8.4(b). Results shown in figures 8.3(a) and 8.4(a) show that experimental data for different forward stat-up flow are well reproducible in the range of experimental error (up to 10% for the shear stress and up to 15% for the normal stress difference). For the polymer matrix, both σ_{12}^{+} and $(N_1 - N_2)^{+}$ reach their steady state values monotonically. The stationary value of shear stress of nanocomposite is larger than that of the polymer matrix. The steady state value of normal stress difference for polymer matrix is larger than that of nanocomposite at this intermediate shear rate ($\dot{\gamma} = 0.2\ s^{-1}$). This phenomenon (reported also in Eslami et al. (2009a)) attributed to the orientation of clay platelets and tactoids which reduces the ability of polymer chains to return to their coil shape and consequently the normal stress is smaller.

In this paper we focus on the amplitude of the overshoots (in both shear stress and normal stress difference) in forward start-up flows and in relaxation of the structure during the rest time following their cessation. The reappearance of overshoots in reverse start-up flows is interpreted as a sign of the structure recovery during the rest time. As seen in figures 8.3(a) and 8.4(a), σ_{12}^{+} and $(N_1 - N_2)^{+}$ pass through a maximum and then level off to their steady state values. Normalized data presented in 8.3(b) and 8.4(b) show a pronounced overshoot for σ_{12}^{+} and $(N_1 - N_2)^{+}$ while no significant overshoot is observed for the polymer matrix at the intermediate shear rate ($\dot{\gamma}_0 = 0.2\ s^{-1}$). According to these results, the magnitude of the overshoot in the shear stress is larger than that of the normal stress difference and the overshoot in the shear stress occurs sooner than that in the normal stress difference. The presence of overshoots in the shear stress has been previously observed in polymer nanocomposites in [Solomon et al. (2001); Letwimolnun et al. (2007)]. Less attention has been paid to the presence of overshoots in the normal stress difference.

Results of reverse start-up experiments are presented in figures 8.5(a) and 8.5(b) for σ_{12}^{+} and $(N_1 - N_2)^{+}$ respectively. The schematic representation of flow reversal experiments is also depicted. The data in these figures are related to the step 3 of the schematic representation.

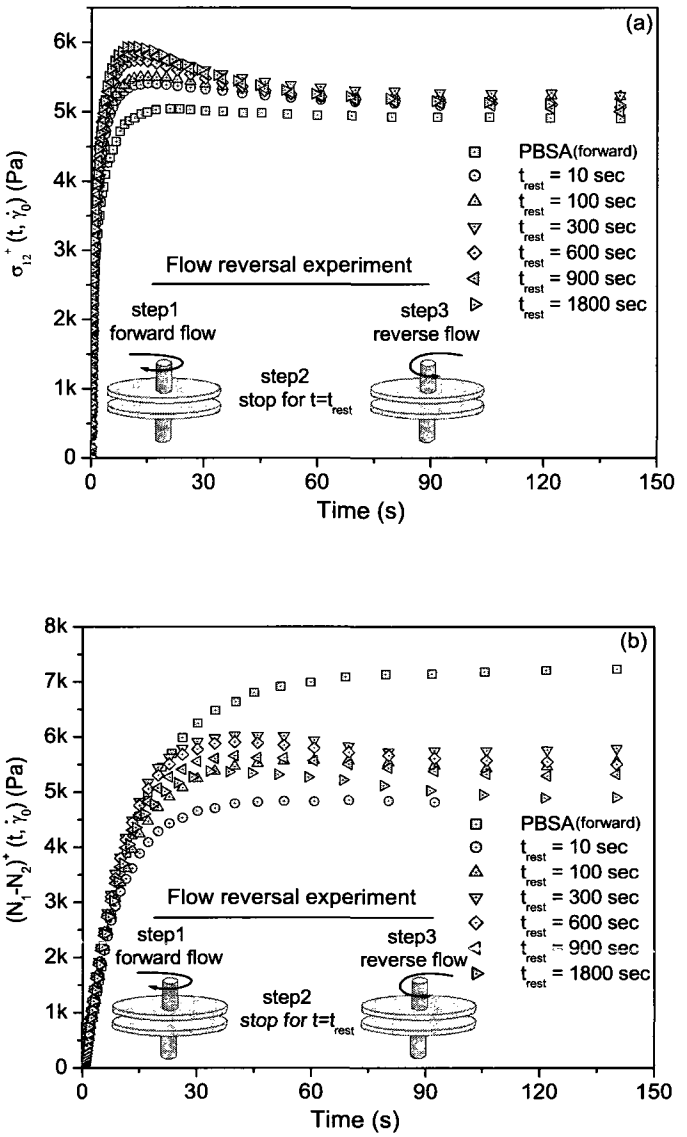

Figure 8.5: Reverse start-up experiments after cessation of the forward start-up flow for various rest times (step 3) (a) shear stress and (b) normal stress difference

Stationary values of the shear stress and the normal stress difference seem to slightly decrease when they are compared with the forward start-up flow. This may be because of a small amount of the sample is ejected when the flow is reversed.

The normalized data of the reverse start-up test of PN3.4S at $\dot{\gamma}_0 = 0.2\ s^{-1}$ are presented in figures 8.6(a) and 8.6(b) for σ_{12}^{+} and $(N_1 - N_2)^{+}$ respectively. For the reference, the average data of the forward start-up test presented in figures 8.3(b) and 8.4(b) are also plotted in these figures. In order to make the observed phenomena clearer, the data are also plotted in shorter ranges (in both x and y axes) and embedded in the corresponding figures. The results show that for the reverse start-up flow after short rest times ($t_{rest} = 10$ sec and $t_{rest} = 100$ sec) a small, but becoming larger with increasing rest time, overshoot is observed for the shear stress. At relatively long rest times (in this case $t_{rest} = 1800$ sec) the magnitude of the overshoot becomes comparable with that of the forward start-up flow. The results of the flow reversal experiment are also reported for PN5.7S at $\dot{\gamma}_0 = 0.2\ s^{-1}$ in figure 8.7. Qualitatively, the results for PN5.7S are the same as those for PN3.4S. However the amplitude of the overshoots in the shear stress for PN5.7S are greater than that of PN3.4S for all rest times. Also model predictions are shown on figures 8.6 and 8.7. On figures 8.6(a) and 8.7(a), we see that the model is able to capture qualitatively the observed behavior in the shear stress during flow reversal experiments. The model also reasonably predicts the amplitude of stress overshoots in the reverse start-up flow with different rest times. However, the shear stress reaches its steady state values faster in model predictions than in experimental observations. Moreover, the time at which the overshoot appears decreases with increasing rest time while in the experimental data it appears essentially at the same time. The amplitude of the overshoot in the normal stress difference during reverse start-up flow are also monitored and compared with that of forward start-up flow. Results are presented in figure 8.6(b) for PN3.4S and in figure 8.7(b) for PN5.7S. As seen from these figures, the magnitude of the overshoot gradually increases with the rest time and approaches that of the forward start-up flow. The model fails to predict overshoots in $(N_1 - N_2)^{+}$ for both forward and reverse start-up flows.

Predicted values of the components of lamellae conformation tensor (a_{ij}) in the forward

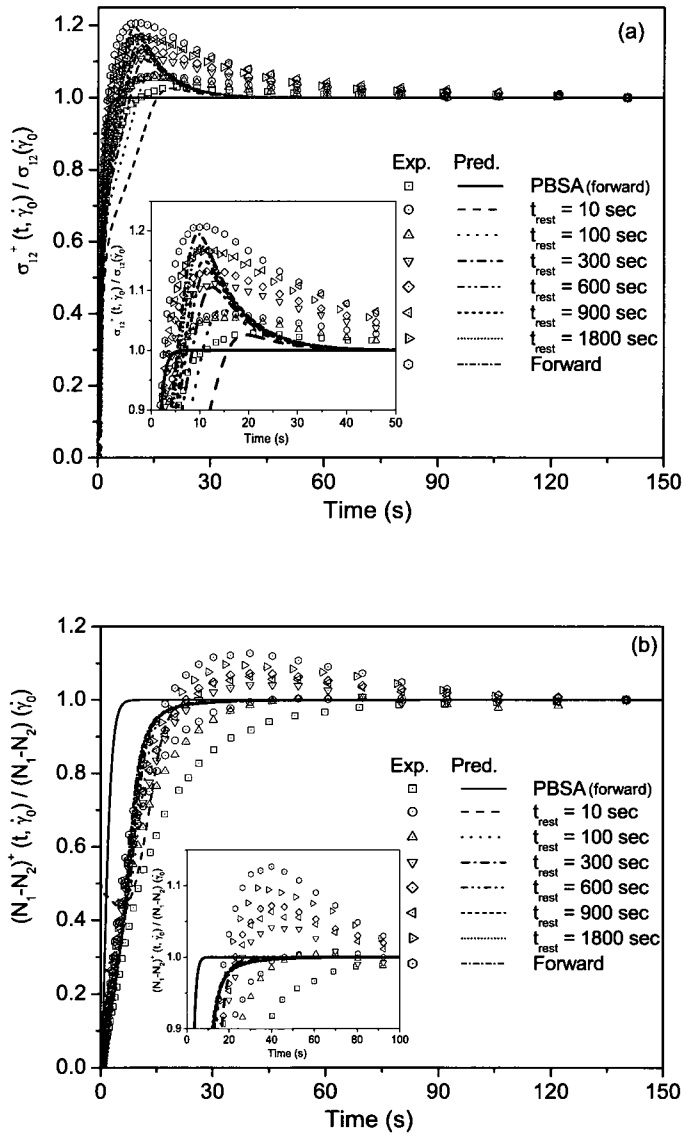

Figure 8.6: Flow reversal experiment for PN3.4S at $\dot{\gamma}_0 = 0.2\ s^{-1}$ (a) normalized shear stress and (b) normalized normal stress difference

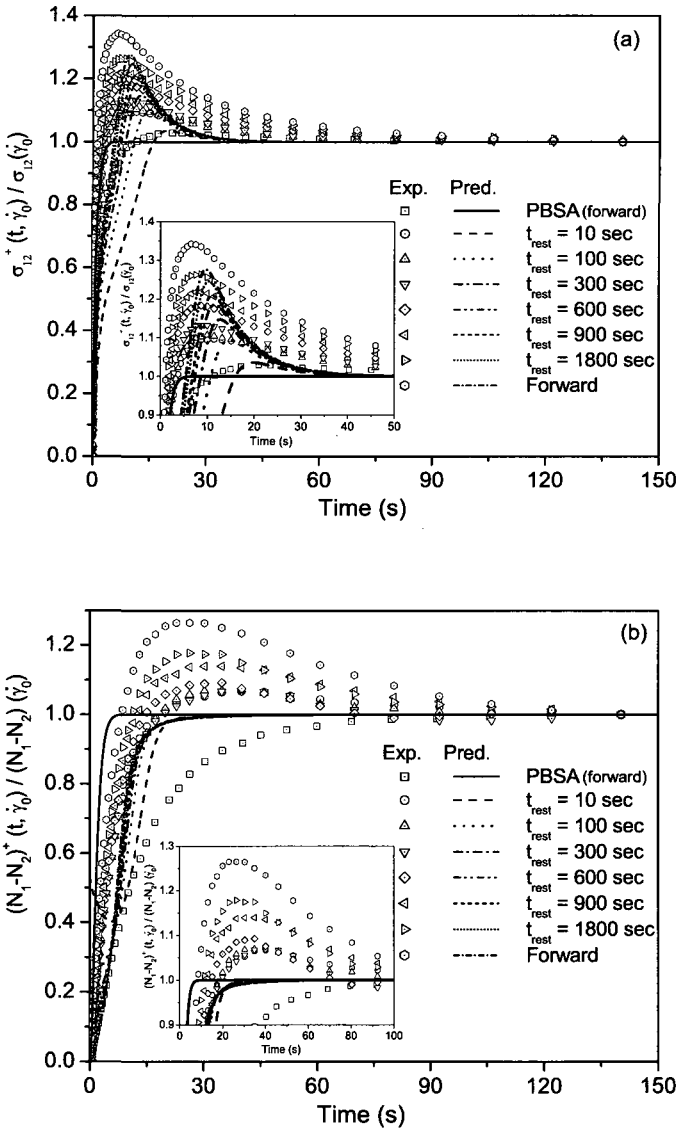

Figure 8.7: Flow reversal experiment for PN5.7S at $\dot{\gamma}_0 = 0.2\ s^{-1}$ (a) normalized shear stress and (b) normalized normal stress difference

start-up flow and after its cessation are reported in figures 8.8(a) and 8.8(b) respectively. The calculated values of the lamellae conformation tensor during start-up flows shown in figure 8.8(a) indicate that the average state of the orientation of the silicate layers and clay tactoids changes with time. At the beginning of the forward start-up flow ($t = 0$), the orientation is chosen to be isotropic (i.e. the lamellae are randomly oriented). When the flow is started, silicate layers and clay tactoids change their orientation and eventually, after a relatively long time, become oriented in the flow direction. The values of a_{11} and a_{33} decrease while the values of a_{22} increase. It should be noted that these values change in such a way that $tr\boldsymbol{a}$ remains constant (i.e. the surface area of the lamellae does not change during flow). This constraint is guaranteed by the way we have constructed the governing equations of the model. The off-diagonal value of $\boldsymbol{a}$ (a_{12}) starts at 0, passes through a minimum, and then levels-off to its steady state value. This behavior of the tensor $\boldsymbol{a}$ is responsible for the stress overshoot observed in the forward start-up flow. Components of the tensor $\boldsymbol{a}$ during the rest time (after cessation of the forward start-up flow) are shown in figure 8.8(b). We see that a_{11}, a_{33} and a_{12} increase and a_{22} decreases with increasing the rest time. Moreover, the diagonal entries of $\boldsymbol{a}$ converge to 1 and its off-diagonal entries tend to 0 after a long rest time (in this case after about 5000 sec). Model predictions show that after a long rest time the state of the orientation of the silicate layers and clay tactoids becomes nearly random (approximately the same as at $t = 0$ in figure 8.8(a)). This behavior is believed to be responsible for the appearance of overshoots in the shear stress and the normal stress difference during reverse start-up flows. The overshoots in the forward and reverse start-up flows are comparable in their size.

The ellipsoidal representation of the polymer conformation tensor $\boldsymbol{c}$ and the lamellae conformation tensor $\boldsymbol{a}$ at different steps in forward start-up tests are presented in figures 8.9(a) and 8.9(b) respectively. Calculation are made for nanocomposite with 3.4 wt.% silicate at a given shear rate ($\dot{\gamma} = 0.2\ s^{-1}$). As seen from these figures, at very short time ($t = 10^{-5}$ sec.), the shape of both conformation tensors ($\boldsymbol{c}$ and $\boldsymbol{a}$) is a sphere. This is because the tensors $\boldsymbol{c}$ and $\boldsymbol{a}$ are chosen to be isotropic at the beginning of start-up tests. With increasing

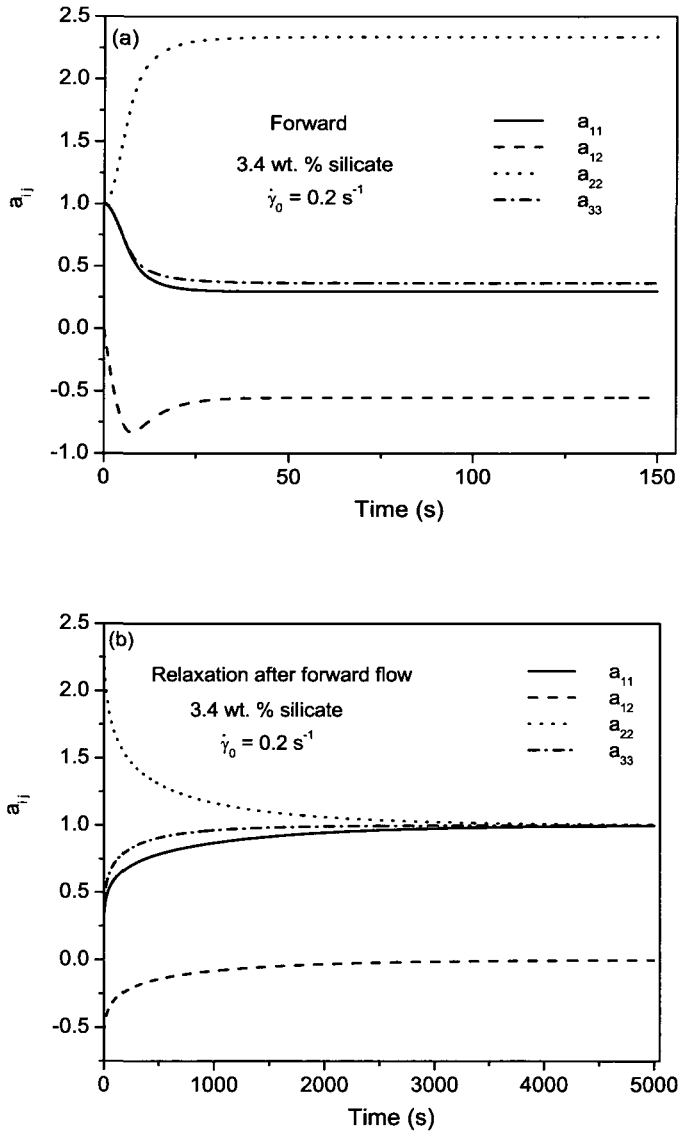

Figure 8.8: Components of the lamellae conformation tensor a_{ij} as functions of time (a) in the forward start-up flow (b) in the relaxation following the forward start-up flow

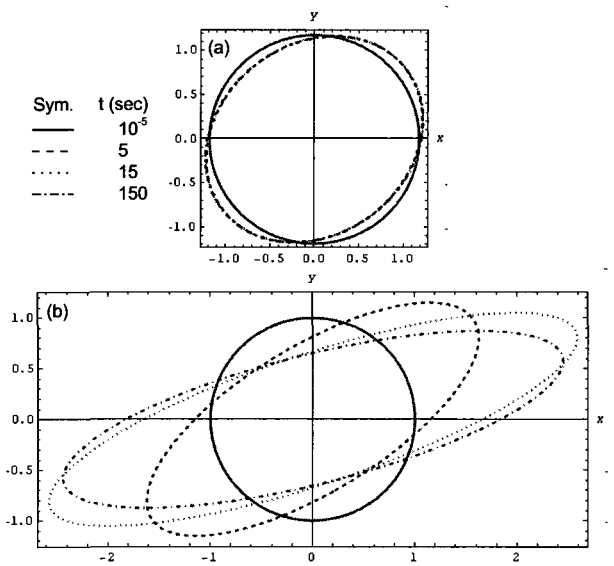

Figure 8.9: Ellipsoidal representation of the conformation tensors during the forward start-up flow (a) polymer conformation tensor (b) lamellae conformation tensor

time, the ellipse representing the polymer macromolecules becomes slightly elongated in the flow direction. When the time is increased even more, no further changes in the ellipsoidal shape are observed (an indication that $\boldsymbol{c}$ reached its steady state, see figure 8.9(a)). This observation confirms that the polymer macromolecules do not play a significant role in the stress overshoot observed for nanocomposite at this intermediate shear rate.

The ellipses representing the tensor $\boldsymbol{a}$ show an interesting behavior during the start-up tests. With increasing time, the shape changes from an initially circle to an elongated ellipse. When the time increases further, the ellipse becomes more elongated in the flow direction, passes through a maximum, and then becomes less elongated in its steady state. It is worth mentioning that the maximum elongated ellipse appears at the time at which the undershoot observed on the off-diagonal component of tensor $\boldsymbol{a}$ (a_{12}) (see figure 8.8(a)) appears. This observation confirms that the suspended particles and not the polymer macromolecules are responsible for the appearance of stress overshoots in polymer nanocomposites in start-up

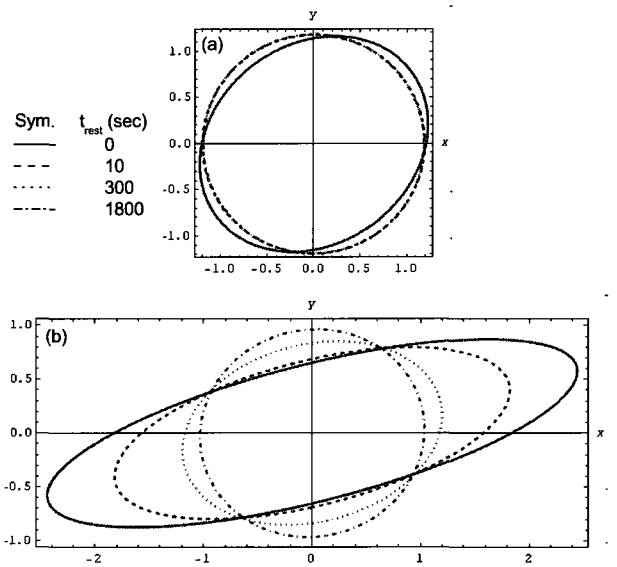

Figure 8.10: Ellipsoidal representation of the conformation tensors after the forward start-up flow at different rest times (a) polymer conformation tensor (b) lamellae conformation tensor

tests. We recall that the long axis of the ellipse represents the average orientation of the clay platelets and tactoids and the short axis (the thickness of the ellipse) shows the dispersion in their orientation.

To monitor the relaxation behavior of tensors $\boldsymbol{c}$ and $\boldsymbol{a}$ after cessation of the forward start-up flow, their ellipsoidal representations at different rest times are presented in figures 8.10(a) and 8.10(b) for tensors $\boldsymbol{c}$ and $\boldsymbol{a}$ respectively. Figure 8.10(a) shows that the polymer macromolecules relax very fast after cessation of the forward start-up flow. As seen in figure 8.10(a), the slightly elongated ellipse at $t_{rest} = 0$ changes to a circle at $t_{rest} = 10$ second. With increasing the time, no further changes in the ellipsoidal shape of tensor $\boldsymbol{c}$ are observed. The ellipsoidal representation of the tensor $\boldsymbol{a}$ presented in figure 8.10(b) shows that the highly elongated ellipse at $t_{rest} = 0$ becomes less elongated with increasing the rest time. At relatively long rest time, the ellipse changes to a circle (i.e. an isotropic orientation of clay platelets and tactoids). Results depicted in figure 8.10 reveal that polymer macromolecules

relax faster than nanoparticles and that the relaxation behavior of polymer nanocomposites is mainly governed by nanoparticles.

Results of flow reversal experiments for different shear rates are also compared with model predictions. For the sake of brevity only the maximum values of normalized σ_{12}^{+} and $(N_1 - N_2)^{+}$ are reported. Figures 8.11 and 8.12 show the magnitude of the overshoot in shear stress and normal stress difference and their comparison with model predictions for nanocomposites at $\dot{\gamma} = 0.1s^{-1}$. The results indicate that the overshoots grow monotonically with the rest time. It is also found that the model predicts well the amplitude of the overshoots in the shear stress in both forward and reverse start-up flows. However, the model again fails to predict the overshoot of normal stress difference in forward start-up flows and its reappearance in the reverse start-up flows. Comparison of these results with the ones reported in figures 8.6 and 8.7 reveals that the recovery of the structure during the rest time takes longer at high shear rates than at low shear rates. To explain this phenomenon, two components (a_{12} and a_{22}) of lamellae conformation tensor along with the ellipsoidal representation of the tensor $\boldsymbol{a}$ at two different shear rates are presented in figure 8.13. The results show that with increasing the shear rate, the silicate layers and clay tactoids become more oriented in the flow direction. This is manifested by a larger value of a_{22}, more elongated ellipses, and smaller inclined angles. More pronounced orientation of silicate layers and clay tactoids at higher shear rate may take longer time to return to their randomly oriented state during the rest time. This can then explain the delay in the reappearance of the stress overshoot in the subsequent reverse start-up flow.

We also note that in contrast to the observation made by Solomon et al. (2001) where a master curve was generated for stress overshoot amplitude at different clay loading, we are unable to generate with their procedure a master curve in neither experimental data nor model predictions. The absent of a master curve is most likely related to the complex mechanism involved in the orientation/disorientation process of silicate layers and clay tactoids during forward and reverse stat-up flows. For example, with changing clay loading, the interaction among clay platelets changes which then leads to different stress overshoots at

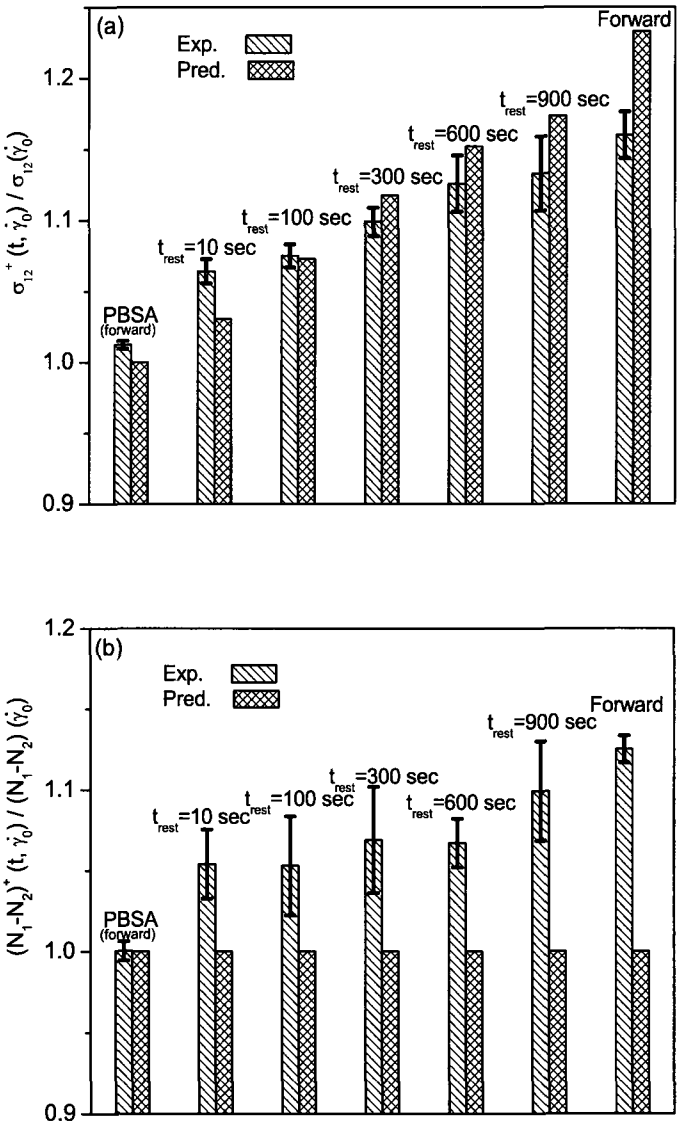

Figure 8.11: Amplitude of the overshoot for PN3.4S at $\dot{\gamma}_0 = 0.1\ s^{-1}$ at different rest times: model predictions and comparison with experimental data (a) shear stress (b) normal stress difference

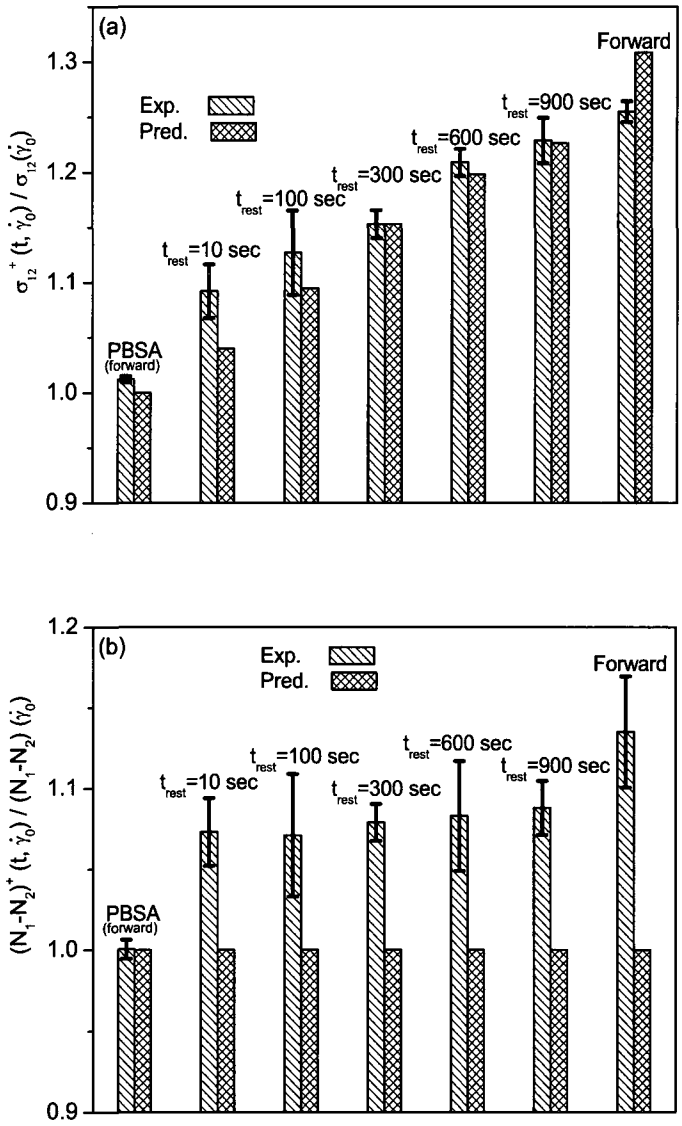

Figure 8.12: Amplitude of the overshoot for PN5.7S at $\dot{\gamma}_0 = 0.1\ s^{-1}$ at different rest times: model predictions and comparison with experimental data (a) shear stress (b) normal stress difference

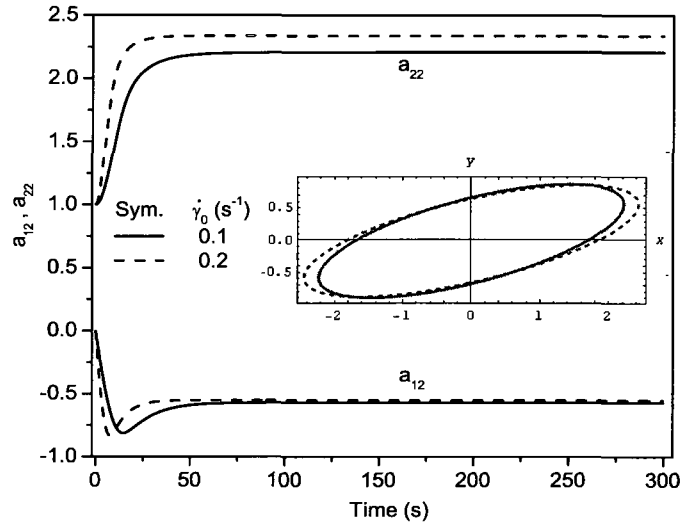

Figure 8.13: Components of the lamellae conformation tensor (a_{12} and a_{22}) as functions of time at different shear rates in the forward start-up flow.

forward start-up flows. Consequently, the recovery of the stress overshoot in reverse start-up flows may not be converted to a master curve simply by dividing the amplitude of the stress overshoot by the clay concentration (see Solomon et al. (2001)). Normalized values of the amplitude of the stress overshoot at different rest times for PN3.4S and PN5.7S are compared in figure 8.14(a). The results show that the values of the stress overshoots increase with increasing clay loading for all rest times. Model predictions are also compared with these data and a rather good agreement is observed. To generate a master curve, we take an approach that is different from the one taken in Solomon et al. (2001). The net size of the stress overshoot in reverse start-up flows $((\sigma_{12}^{+}/\sigma_{12})_{reverse} - 1)$ is divided by the net size of the stress overshoot in the corresponding forward start-up flows $((\sigma_{12}^{+}/\sigma_{12})_{forward} - 1)$ at different rest times. The results show a master curve for both model predictions and experimental data (see figure 8.14(b)).

One possible explanation for the structure build-up at rest in PLS nanocomposites pro-

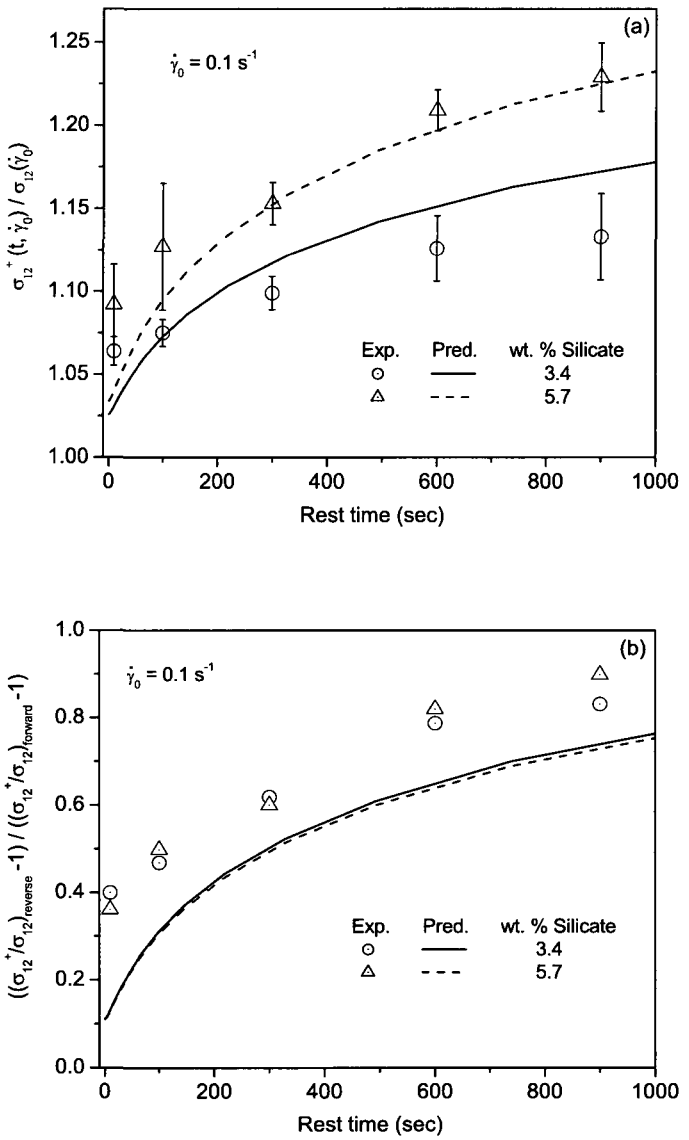

Figure 8.14: Effect of clay loading on the amplitude of stress overshoots at $\dot{\gamma}_0 = 0.1\ s^{-1}$ at different rest times: model predictions and comparison with experimental data (a) normalized stress overshoot amplitude (b) master curve

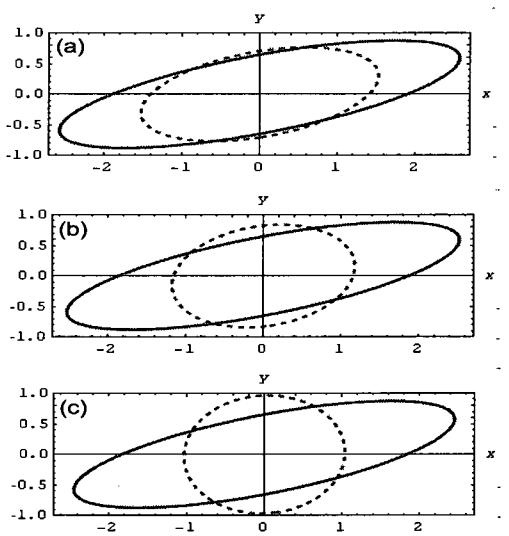

Figure 8.15: Effect of the plate-plate interaction parameter on the structure build-up during the rest time (a) $\kappa = 1 \times 10^{-22}$ (b) $\kappa = 7 \times 10^{-23}$ (c) $\kappa = 3 \times 10^{-24}$. (—) and (...) indicate the ellipsoidal representation of lamellae conformation tensor at the end of the forward start-up flow and 30 min. after cessation of the forward start-up flow respectively.

ceeds as follow: Silicate platelets and clay tactoids are oriented in the flow direction during forward start-up tests. When the flow is stopped, the oriented particles are disoriented and suspension with a more developed microstructure is formed. This structure becomes stronger with increasing rest time. The question then arises of what are the driving forces for disorientation of particles during the rest time. We answer it with the help of the mesoscopic model introduced in Section 8.3. Two thermodynamic forces ($\Phi_{\boldsymbol{c}}$ and $\Phi_{\boldsymbol{a}}$), driving the suspension to equilibrium, are introduced in the model. Since the polymer macromolecules relax faster than the suspended particles, $\Phi_{\boldsymbol{a}}$ plays more important role than $\Phi_{\boldsymbol{c}}$ in the relaxation process of nanocomposites (see figures 8.10(a) and 8.10(b) and their description in the text). $\Phi_{\boldsymbol{a}}$ involves three parameters: (i) polymer-particle topological interaction, (ii) particle-particle topological interaction and (iii) Brownian motion.

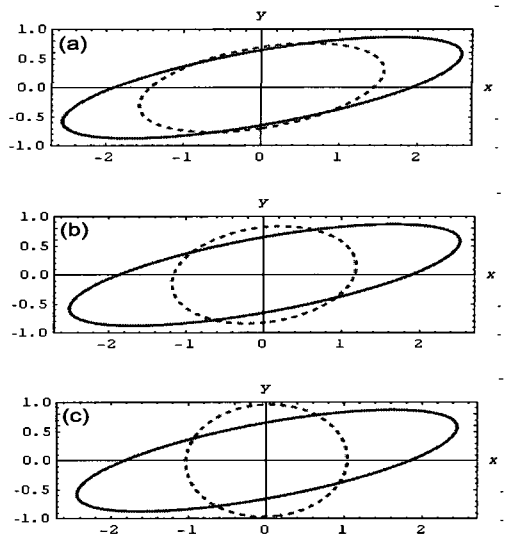

Figure 8.16: Effect of the polymer-plate interaction parameter on the structure build-up during the rest time (a) $\kappa' = 1 \times 10^{-22}$ (b) $\kappa' = 6 \times 10^{-23}$ (c) $\kappa' = 5 \times 10^{-24}$. (—) and (...) depict the ellipsoidal representation of lamellae conformation tensor at the end of the forward start-up flow and 30 min. after cessation of the forward stat-up flow respectively.

The effect of plate-plate topological interaction on the structure build-up at rest in polymer nanocomposites is shown in figures 8.15(a), 8.15(b) and 8.15(c) for three different interaction parameters. In each figure, the ellipse drawn by the solid line represents the tensor $\boldsymbol{a}$ at the end of the forward start-up flow and the ellipse drawn by dash line represents the tensor $\boldsymbol{a}$ 30 min. after the cessation of the forward start-up flow. The interaction parameters are chosen in such a way that approximately the same orientation is achieved at the end of the forward start-up test (it can be seen by solid line ellipses having approximately the same axes in figures 8.15(a), 8.15(b) and 8.15(c)). As seen from these figures, the ellipse drawn by dash line becomes less elongated (an indication of more isotropic orientation) with decreasing plate-plate topological interaction parameter. It should also be noted that the topological interaction is a repulsive interaction. In our model, a smaller value of the topo-

logical interaction parameter indirectly implies a larger value of the attractive plate-plate interaction. The effect of the polymer-plate topological interaction on the structure build-up at rest in polymer nanocomposites is also presented in figure 8.16. The results show that the polymer-plate topological interaction influences more the behavior in the rest time (i.e. in the period between switching off the forward flow and switching on the reverse flow) than in the time when the flow is switched on. Indeed, figures 8.15 and 8.16 reveal that an increase in the attractive interactions between polymer-particle and particle-particle leads to a more developed structure in polymer nanocomposites during the rest time while no significant changes occur immediately after switching-off the forward flow. The more developed structure gives then rise to larger overshoots in shear stress and normal stress difference during reverse start-up flows.

8.5 Conclusion

Nanocomposites of PBSA with two different concentrations of C30B were prepared by direct melt mixing. The interlayer spacing of silicate layer in PBSA matrix was characterized by WAXD. Its patterns reveal the existence of clay tactoids dispersed in the polymer matrix. WAXD patterns together with TEM observations show a coexistence of intercalated/exfoliated nanocomposites. Stress growth experiments (in the forward direction) show an overshoot in both the shear stress and the normal stress difference while no significant overshoot is observed in the pure polymer matrix. The magnitude of these overshoots increases with increasing shear rate. In the normalized representation of these data, the amplitude of overshoots in the shear stress are larger than that in the normal stress difference. Results of flow reversal experiments reveal that at short rest times no significant overshoot is observed for both the shear stress an the normal stress difference. When the rest time is increased, the nanocomposites form a more global structure that presents itself by a reappearance of overshoots in subsequent reverse start-up tests. At relatively long rest times, the magnitude of overshoots in the reverse flow becomes comparable with the one observed in the forward

flow. A rather good agrement is observed between model predictions and experimental data in both forward and reverse start-up tests.

Acknowledgements

The authors acknowledge the financial support provided by the Natural Sciences and Engineering Research Council (NSERC) of Canada. The authors also grateful to Showa High Polymer Ltd, Japan, company for kindly provided the polymer used in this study.

References

1. Bird, R. B., Armstrong, R. C., and Hassager, O. (1987). Dynamics of polymeric fluids, volume 1. Wiley, New York.

2. Carreau, P. J., De Kee, D., and Chhabra, R. P. (1997). Rheology of polymeric systems: Principles and applications. Hanser, Munich.

3. Eslami, H., Grmela, M., and Bousmina, M. (2007). A mesoscopic rheological model of polymer/layered silicate nanocomposites. J. Rheol., 51:1189-1222.

4. Eslami, H., Grmela, M., and Bousmina, M. (2009). Linear and nonlinear rheology of polymer/layered silicate nanocomposites. J. Rheol. submitted.

5. Folgar, F. P. and Tucker, C. L. (1984). Orientation behaviour of fibers in concentrated suspensions. J. Reinf. Plast. Compos., 3:98-119.

6. Grmela, M. and Ottinger, H. C. (1997). Dynamics and thermodynamics of complex fluids. I. Development of a general formalism. Phys. Rev.E, 55:6620-6632.

7. Isichenko, M. B. (1992). Percolation, statistical topography and transport in random media. Rev. Mod. Phys., 64:961-1043.

8. Letwimolnun, W., Vergnes, B., Ausias, G., and Carreau, P. J. (2007). Stress overshoots of organoclay nanocomposites in transient shear flow. J. Non-Newtonian Fluid Mech., 141:167-179.

9. Marrison, F. A. (2001). Understanding rheology. Oxford university press, New York.

10. Ottinger, H. C. and Grmela, M. (1997). Dynamics and thermodynamics of complex fluids. II. Illustrations of a general formalism. Phys. Rev.E, 56:6633- 6655.

11. Rajabian, M., Naderi, G., Beheshty, M., Lafleur, P., Dubois, C., and Carreau, P. J. (2008). Experimental study and modeling of flow behavior and orientation kinetics of layered silicate/polypropylene nanocomposites in start-up of shear flows. International Polymer Processing, 23:110-118.

12. Ren, J., Silva, A. S., and Krishnamoorti, R. (2000). Linear viscoelasticity of disordered polystyrene-polyisoprene block copolymer based layered silicate nanocomposites. Macromolecules, 33:3739-3746.

13. Sinha Ray, S. and Bousmina, M. (2005a). Biodegradable polymers and their layered silicate nanocomposites: In greening the 21st century materials world. Prog. Mater Sci., 50:962-1079.

14. Sinha Ray, S. and Bousmina, M. (2005b). Poly(butylene sucinate-co-adipate) montmorillonite nanocomposites: effect of organic modifier miscibility on structure, properties, and viscoelasticity. Polymer, 46:12430-12439.

15. Solomon, M. J., Almusallam, A. S., Seefeldt, K. F., Somwangthanaroj, A., and Varadan, P. (2001). Rheology of polypropylene/clay hybrid materials. Macromolecules, 34:1864-1872.

16. Vermant, J., Ceccia, S., Dolgovskij, M. K., Maffettone, P. L., and Macosko, C. W. (2007). Quantifying dispersion of layered nanocomposites via melt rheology. J. Rheol., 51:429-450.

17. Wolfram, S. (1991). Mathematica-A system for doing mathematics by computer. Wesley-VCH, New York.

18. Yziquel, F., Carreau, P. J., Moan, M., and Tanguy, P. (1999). Rheological modelling of concentrated colloidal suspension. J. Non-Newtonian Fluid Mech., 86:133-155.

CHAPTER 9

SUMMARY AND RECOMMENDATIONS

9.1 General discussion and conclusions

The physical systems under investigation in this thesis are suspensions of nano-size lamellae in viscoelastic polymer melts (PLS nanocomposites). The main contributions consist of: (i) Development of a model (or models) allowing to predict rheological behavior, both linear and nonlinear, observed in stationary, oscillatory and transient shear flows, as well as basic features of the morphology. (ii) Experimental observations of responses of one specific nanocomposite, namely the nanocomposite based on poly[butylene succinate-co-adipate] (PBSA) and an organically modified montmorillonite (Cloisite 30B), to imposed shear flows - steady, oscillatory, transient (start-up and relaxation), and reversal. (iii) Comparison of model predictions with results of the measurements and with the experimental data reported in the literature.

The models have been constructed in the thermodynamic framework (GENERIC). Two microstructural state variables (i.e. two conformation tensors) have been chosen to characterize states of nanoparticles and polymer macromolecules. In the first model, developed in Eslami et al. (2007) (reported in Chapter 4 and called Model I), two conformation tensors

denoted by the symbols $\boldsymbol{a}$ and $\boldsymbol{c}$ are chosen to characterize the states of the silicate platelets and the polymer macromolecules respectively where macromolecules are simplified as FENE-P dumbbells. In the second model, developed in Eslami et al. (2009b) (reported in Chapter 6 and called Model II), Model I is extended by replacing the FENE-P dumbbells with chains confined to a tube formed by surrounding chains. In the mathematical formulation this extension is made by replacing $\boldsymbol{c}$ with $\boldsymbol{c}(s)$, where $s \in \mathbb{R}$ is a one dimensional parameter denoting the coordinate along the backbone of the chain. Chain view of macromolecules allows us to include nonlocal intramolecular interactions and the collective behavior of the macromolecules manifested in the formation of tube-like constraints in which both the chains and the lamellae participate. The models are formulated by, first, writing down a thermodynamic framework (GENERIC framework) for the governing equations and second, filling the framework by specifying the kinematics of the state variables, the free energy, and the dissipation potential. The expressions for the extra stress tensor arise automatically as a part of the governing equations. Important physics taking place in PLS nanocomposites for example the polymer chain-polymer chain, polymer chain-lamella and lamella-lamella interactions as well as the flexibility of the lamellae are taken into account in the formulation of the models.

To formulate our models, we have chosen a mesoscopic level with conformation tensors as morphological state variables rather than more frequently used kinetic theory level on which the morphological state variables are chosen to be distribution functions. Our description of the morphology lacks therefore details depicted by kinetic theories. We have turned to the mesoscopic level for the following two reasons: first, our investigation of suspensions of nanoparticles in polymeric fluids needs to be relatively simple (from the point of view of the effort needed to solve the governing equations of the model) in order to be practically useful, second, we expect to improve understanding of the physics involved by taking a multilevel view. Following GENERIC framework, the mesoscopic level of description is considered as an autonomous level and some basic elements of the reptation physics and the physics involved in lamellae-polymer interactions (introduced originally on kinetic theory level) are formulated on it. In the formulation of the model, the polymer melts under consideration

are assumed to be incompressible homogeneous and isothermal fluids. The macromolecules composing the polymer melts are modeled as worm-like chains that only locally are regarded as dumbbells. Two types of dumbbells, namely the finitely extensible FENE-P dumbbells and inextensible rigid dumbbells, are systematically considered in the formulation. The passage from a dumbbell to a local dumbbell (i.e. a dumbbell depending on the coordinate s) allows us to introduce two new features namely a new dissipative mechanism (the reptation, i.e. the diffusion along the chain), and a new type of energy (i.e. the energy associated with non-local intra-chain interactions).

Predictions of Model I as well as Model II agree with experimental observations constituting the basis of equilibrium thermodynamics. This is guaranteed already by the way the governing equations of the models are constructed. Other predictions of the models, obtained by solving numerically their governing equations (a set of ordinary differential equations in Model I and a set of partial differential equations in Model II), are responses of the PLS nanocomposites to transient (start-up and relaxation), steady and oscillatory shear flows.

Predictions of models in response to stress growth and stress decay experiments show that for small shear rates, the viscosity reaches its steady state value monotonically. With increasing shear rate, the curve of viscosity versus time shows an overshoot. Its magnitude increases and the time at which it appears decreases when shear rate increases. Predictions of the models in response to stress relaxation experiment show that the viscosity relaxes monotonically to zero in low shear rate and then it relaxes more rapidly as the shear rate increases. Effect of clay loading on the transient material functions show that both the stationary values and the amplitude of the overshoots increase with increasing clay loading. The dependence of overshoots on clay loading appears to be stronger in viscosity than in first normal stress coefficients. Predictions also show that all material functions relax more slowly with increasing clay loading. This in turn means that increasing nano-particle content causes a delay in relaxation phenomena. The overall predictions of two models are essentially the same in response to transient (start-up and relaxation) shear flows.

Predictions of models in responses to steady shear flows show that an increasing clay

loading results in an increase in viscosity at low shear rates and a very small change at high shear rates. In other words, at high shear rates the viscosity is almost independent of the silicate loading and is comparable to that of the polymer matrix. This is because at high shear rates the plates are all oriented in the direction of the flow and the viscosity of the suspension is dominated by the polymer matrix. The slope of the curve of shear stress versus shear rate at low shear rate region decreases with increasing the clay loading and at the high clay loading it almost becomes a plateau which indicates a large value of the yield stress.

Model predictions (Model II) in response to small angle oscillatory shear flow show that the flow behavior of nanocomposites differs significantly from the one corresponding to the pure matrix fluid in the linear viscoelastic zone. More specifically, the results show that the storage modulus G' is dramatically influenced by the presence of silicate platelets where a low frequency plateau is observed for low level of clay loading. However, a lesser sensitivity of loss modulus G'' on the clay loading is seen. The slopes of $\log G'$ versus $\log \omega$ are much smaller than 2 which is normally expected to be the case for noncrosslinked polymer melts. Such large deviation, which normally occurs in the presence of small amount of clay loading, can be attributed to the formation of a more global structure in polymer nanocomposites. It should be noted that Model I is not able to fully capture the phenomena observed at liner viscoelastic zone. This is because the macromolecules are oversimplified in Model I where only one relaxation time is assumed for polymer chain (i.e. macromolecules are modeled as FENE-P dumbbell).

The empirical Cox-Merz relation, which requires $\eta^*(\omega) = \eta(\dot{\gamma})$ where $\omega = \dot{\gamma}$, is proved to be applicable for homopolymers. Prediction of Model II show that the Cox-Merz rule fails in the whole range of shear rates for PLS nanocomposites. The reason for the failure is that by applying the steady shear flow the silicate layers become preferentially oriented in the direction of the flow even at low shear rates. The failure of the Cox-Merz rule can also be related to the formation of a more global structure and collective behavior of silicate layers and polymer chains in the suspension.

In the experimental part of this work, a complete set of standard linear and nonlinear

rheological measurements along with the flow reversal measurements of nanocomposites prepared by melt mixing of PBSA and Cloisite 30B together with their evaluation made with the help of two mesoscopic rheological models (Model I and Model II) are reported. Moreover, the morphology of the nanocomposites is observed by X-ray diffraction and by transmission electron microscopy. The results of WAXD together with TEM images reveal that some clay tactoids (i.e. ordered structure of clay platelets) still remain in the nanocomposites. This is manifested by Bragg peaks where the individual silicate layers are invisible (an indication of a coexistence of intercalate/exfoliate structure).

Linear viscoelastic measurements in oscillatory shear with small strain amplitude show that at high frequencies G' and η^* increase monotonically with increasing clay loading. At low frequencies, a significant effect of clay loading is observed. It is manifested in particular in the appearance of a plateau in G' (an indication of a pseudo-solid like structure) and the upward complex viscosity at relatively low clay loading. The frequency dependence of the storage modulus becomes weaker with increasing clay loading and nearly independent of the frequency at high clay loading. The linear viscoelastic limit is also found to be very sensitive to the clay loading. The observed low frequency plateau in the storage modulus and the upward complex viscosity is clearly predicted by the second model. However, the model fails to capture quantitatively the observed linear viscoelastic experimental data. This is mainly because the linear viscoelasticity is influenced by physics that is not fully included in the models. The physics in question is the formation of a network-like structure of clay platelets in the suspension. The collective behavior of platelets is expected to be visible in particular at low frequencies and less so in higher frequencies revealing small scale structures.

Transient experimental data show that at low shear rate both the shear stress and the normal stress difference approach their steady state values monotonically while an overshoot is observed at intermediate shear rates. Moreover, the normal stress difference approaches its steady state values more slowly than the shear stress and the magnitude of the overshoot in the shear stress is larger than that in the normal stress difference. In general, for the transient shear stress, there is a rather good agreement between predictions of the model

and experimental data. However, in the experimental data the magnitude of the stress overshoot increases with increasing the shear rate while the model predicts almost the same stress overshoot amplitude for all shear rates. Roughly speaking, agreement of experimental data with predictions of the normal stress difference are less satisfactory. In contrast to the experimental data, the model predicts no overshoot with increasing the shear rate. The model also overestimates the steady state values of the normal stress difference.

The steady state experimental data of shear viscosity show that for pure polymers and the nanocomposites with low clay loading the behavior is near Newtonian at low shear rates and it becomes shear thinning at higher shear rates. However, for higher clay loading the behavior becomes non-Newtonian for all ranges of shear rates. Moreover, at low shear rate the slope of the curve of viscosity versus shear rate becomes larger with increasing clay loading which leads to yielding behavior. Even though both Model I and Model II predict the observed behavior for PLS nanocomposites, the prediction of Model II is much closer to experimental data than that of Model I.

The experimental data of the steady state normal stress difference show that its value increases with increasing the clay loading at low shear rates while an inverse behavior is observed at relatively high shear rates. In other words, at higher shear rates the normal stress difference of pure polymer is larger than that of the nanocomposites. Higher values of normal stress difference for nanocomposites at low shear rate are expected. This is because at low shear rates nearly randomly oriented clay platelets in polymer melts increase the rigidity of the nanocomposites. However, because of the nearly perfect alignment of clay platelets in the flow direction at higher shear rates, normal stress difference of nanocomposites is smaller than that of pure polymers. In polymer nanocomposites the normal stress difference arises from two sources: contribution of the polymer matrix, and contribution of the clay platelets. At low shear rates, the clay platelets and tactoids are not oriented and still bound to a network structure which itself helps to generate additional normal force as compared to pure polymer. At high shear rates however this network structure is destroyed and all the platelets are oriented in the flow direction which reduces also the ability of polymer chains to

return to their coil shape and consequently a smaller normal force is generated. Predictions of both models agree qualitatively with experimental data at low shear rates (in particular the observation that the normal stress difference increases with increasing clay loading). However, neither Model I nor Model II predict the behavior observed at intermediate and high shear rates.

Forward stress growth experiments show an overshoot in both the shear stress and the normal stress difference for nanocomposites where no significant overshoot is observed for pure polymer. The magnitude of these overshoots increases with increasing the shear rate. Reverse stress growth experiments reveal that at short rest times no significant overshoot is observed for both the shear stress an the normal stress difference. When the rest time is increased, the nanocomposites form a more global structure that presents itself by a reappearance of overshoots in subsequent reverse start-up tests. At relatively long rest times, the magnitude of overshoots in the reverse flow becomes comparable with the one observed in the forward flow. A rather good agrement is observed between model predictions and experimental data in both forward and reverse start-up flows.

In general, the mesoscopic level of description chosen in the formulation of the models (Model I and Model II) appears to be a good compromise between microscopic details and overall simplicity of the governing equations. On the one hand, the important features of the physics involved (like for example polymer-plate and plate-plate interactions (in Model I) and the polymer chain-polymer chain, polymer chain-lamella and lamella-lamella interactions (in Model II) as well as the flexibility of the lamellae (in both models)) are expressed in the models and on the other hand, the governing equations are relatively easily solved numerically by standard software packages.

9.2 Recommendations

The following recommendations for future works are suggested:

1. The mesoscopic rheological models developed in this work can be extended by adopting

the active advection introduced recently in Gu and Grmela (2008).

2. The collective nature of the lamellae (i.e. the network-like clusters formed from the lamellae) becomes important particularly at low shear rates and low frequencies. This physics can be included in the models by inspiring of mesoscopic formulation of reptation introduced in Eslami and Grmela (2008).

3. Modeling of nonhomogeneous suspension: To model the nonhomogeneous suspension of silicate layers in polymer melts, the field of the volume fraction of the silicate layers should be included into the set of state variables. This generalization allows us to investigate an interesting phenomenon of diffusion of clay lamellae into the polymer matrix.

4. Modeling the barrier properties of polymer/layered silicate nanocomposites: A non-Fickian diffusion taking place under isothermal condition can be formulated using the GENERIC framework.

The challenge is to identify the physical processes that become important in these situations and to express them in the model. The framework of the model remains unchanged since the agreement of model predictions with the observed compatibility with thermodynamics is required.

Bibliography

Ajayan, P. M., Schadler, L. S., and Braun, P. V. (2003). *Nanocomposite science and technology.* Wiley Inter Science.

Alexandre, M. and Dubois, P. (2000). Polymer-layered silicate nanocomposites: preparation, properties and uses of a new class of materials. *Materials Science and Engineering*, 28:1–63.

Aubry, T., Razafinimaro, T., and Mederic, P. (2005). Rheological investigation of the melt state elastic and yield properties of a polyamide-12 layered silicate nanocomposite. *J. Rheol.*, 49:425–440.

Ayyer, R. K. and Leonov, A. I. (2004). Comparative rheological studies of polyamide-6 and its low loaded nanocomposite based on layered silicates. *Rheol. Acta*, 43:283–292.

Beris, A. N. and Edwards, B. J. (1990). Poisson bracket formulation of viscoelastic flow equations of differential type: A unified approach. *J. Rheol.*, 34:55–78.

Beris, A. N. and Edwards, B. J. (1994). *Thermodynamics of flowing systems.* Oxford University Press, New York.

Bird, R. B., Armstrong, R. C., and Hassager, O. (1987a). *Dynamics of polymeric fluids*, volume 1. Wiley, New York.

Bird, R. B., Dotson, P. J., and Johnson, N. L. (1980). Polymer solution rheolgy based on a finitely extensible bead-spring chain model. *J. Non-Newtonian Fluid Mech.*, 7:213.

Bird, R. B., Hassager, O., Armstrong, R. C., and Curtiss, C. F. (1987b). *Dynamics of polymeric fluids*, volume 2. Wiley, New York.

Bousmina, M. (2006). Study of intercalation and exfoliation processes in polymer nanocomposites. *Macromolecules*, 39:4259–4263.

Brenner, H. (1974). Rheology of a dilute suspension of axisymmetric brownian particles. *Int. J. Multiphase Flow*, 1:195–341.

Cahn, J. W. and Hilliard, J. E. (1958). Free energy of a nonuniform system. i. interfacial free energy. *Journal of Chemical Physics*, 28:258–267.

Carreau, P. J., De Kee, D., and Chhabra, R. P. (1997). *Rheology of polymeric systems: Principles and applications.* Hanser, Munich.

De Gennes, P. G. (1971). Reptation of a polymer chain in the presence of fixed obstacles. *Journal of Chemical Physics*, 55:572–579.

Des Cloizeaux, J. (1988). Double reptation vs simple reptation in polymer melts. *Europhys. Lett.*, 5:437–442.

Doi, M. and Edwards, S. F. (1986). *The theory of polymer dynamics.* Oxford University Press, New York.

Doraiswamy, D., Mujumdar, A. N., Tsao, I., Beris, A. N., Danforth, S. C., and Metzner, A. B. (1991). The coxmerz rule extended: A rheological model for concentrated suspensions and other materials with a yield stress. *J. Rheol.*, 35:647–685.

Edwards, B. J., Dressler, M., Grmela, M., and Ait-Kadi, A. (2003). Rheological models with microstructural constraints. *Rheol. Acta*, 42:64–72.

Edwards, S. F. (1976). *Configurations and dynamics of the polymer chain*, chapter Molecular Fluids, pages 151–208. Gordon and Breach, London.

Eshelby, J. D. (1957). The determination of the elastic field of an ellipsoidal inclusion, and related problems. *Proc. R. Soc. London A*, 241:376–396.

Eshelby, J. D. (1959). The elastic field outside of an ellipsoidal inclusion. *Proc. R. Soc. London A*, 252:561–569.

Eslami, H. and Grmela, M. (2008). Mesoscopic formulation of reptation. *Rheol. Acta*, 47:399–415.

Eslami, H., Grmela, M., and Bousmina, M. (2007). A mesoscopic rheological model of polymer/layered silicate nanocomposites. *J. Rheol.*, 51:1189–1222.

Eslami, H., Grmela, M., and Bousmina, M. (2009a). Linear and nonlinear rheology of polymer/layered silicate nanocomposites. *J. Rheol.* submitted.

Eslami, H., Grmela, M., and Bousmina, M. (2009b). A mesoscopic tube model of polymer/layered silicate nanocomposites. *Rheol. Acta*, 48:317–331.

Eslami, H., Ramazani, A., and Khonakdar, H. A. (2003). Volume preserving conformational rheological models for multi-component miscible polymer blends using the GENERIC formalism. *Macromol. Theory Simul.*, 12:524–530.

Eslami, H., Ramazani, A., and Khonakdar, H. A. (2004). Predictions of some internal microstructural models for polymer melts and solutions in shear and elongational flows. *Macromol. Theory Simul.*, 13:655–664.

Folgar, F. P. and Tucker, C. L. (1984). Orientation behaviour of fibers in concentrated suspensions. *J. Reinf. Plast. Compos.*, 3:98–119.

Forest, M. G. and Wang, Q. (2003). Monodomain response of finite-aspect-ratio macromolecules in shear and related linear flows. *Rheol. Acta*, 42:20–46.

Forest, M. G. and Wang, Q. (2005). Hydrodynamic theories of mixtures of polymers and rodlike liquid crystalline polymers. *Phys. Rev. E*, 72:041805–1–17.

Franchini, E., Galy, J., and Gerard, J.-F. (2009). Sepiolite-based epoxy nanocomposites: Relation between processing, rheology, and morphology. *Journal of Colloid and Interface Science*, 329:38–47.

Galgali, G., Ramesh, C., and Lele, A. (2001). Rheological study on the kinetics of hybrid formation in polypropylene nanocomposites. *Macromolecules*, 34:852–858.

Gordon, R. and Schowalter, W. (1972). Anisotropic fluid theory: A different approach to the dumbbell theory of dilute polymer solutions. *Trans. Soc. Rheol.*, 16:79–97.

Grmela, M. (1984). Particle and bracket formulations of kinetic equations. *Contemp. Math.*, 28:125–132.

Grmela, M. (1985). Stress tensor in generalized hydrodynamics. *Phys.Letters A*, 111:41–44.

Grmela, M. (1986). Bracket formulation of diffusion-convection equations. *Physica D*, 21:177–212.

Grmela, M. (1990). *Thermodynamic and rheological modeling: Polymeric liquid crystals*, chapter Polymer Rheology and Processing, pages 55–81. Elsevier.

Grmela, M. (1991). Mesoscopic dynamic and thermodynamic: Application to polymer fluids. *Lecture Notes in Physics*, 381:99–126.

Grmela, M. (2002). Reciprocity relations in thermodynamics. *Physica A*, 309:304–328.

Grmela, M. and Carreau, P. J. (1987). Conformation tensor rheological models. *J. Non-Newtonian Fluid Mech.*, 23:271–294.

Grmela, M. and Ottinger, H. C. (1997). Dynamics and thermodynamics of complex fluids. I. Development of a general formalism. *Phys. Rev.E*, 55:6620–6632.

Gu, J. F. and Grmela, M. (2008). GENERIC model of active advection. *J. Non-Newtonian Fluid Mech.*, 152:12–26.

Guo, R., Azaiez, J., and Bellehumeur, C. (2005). Rheology of fiber filled polymer melts: Role of fiber-fiber interactions and polymer-fiber coupling. *Polym. Eng. Sci.*, 45:385–399.

Gupta, R. K., Pasanovic-Zujo, V., and Bhattacharya, S. N. (2005). Shear and extensional rheology of EVA/layered silicate-nanocomposites. *J. Non-Newtonian Fluid Mech.*, 128:116–125.

Hooper, J. B. and Schweizer, K. S. (2006). Theory of phase separation in polymer nanocomposites. *Macromolecules.*, 39:5133–5142.

Hyun, Y. H., Lim, S. T., Choi, H. J., and Jhon, M. S. (2001). Rheology of poly(ethylene oxide)/organoclay nanocomposites. *Macromolecules*, 45:8084–8093.

Isichenko, M. B. (1992). Percolation, statistical topography and transport in random media. *Rev. Mod. Phys.*, 64:961–1043.

Jeffery, G. B. (1922). The motion of ellipsoidal particles immersed in a viscous fluid. *Proc. R. Soc. Lond. A*, 102:181–179.

Jeon, H. S., Rameshwaram, J. K., and Kim, G. (2004). Structure property relationships in exfoliated polyisoprene/clay nanocomposites. *Journal of Polymer Science: Part B: Polymer Physics*, 42:1000–1009.

Kagarise, C., Koelling, K. W., Wang, Y., and Bechtel, S. E. (2008). A unified model for polystyrene-nanorod and polystyrene-nanoplatelet melt composites. *Rheol. Acta*, 47:1061–1076.

Kairn, T., Daivis, P. J., Ivanov, I., and Bhattacharya, S. N. (2005). Molecular-dynamics simulation of model polymer nanocomposite rheology and comparison with experiment. *Journal of Chemical Physics*, 123:194905–1–7.

Khokhlov, A. R. and Semenov, A. N. (1985). On the theory of liquid-crystalline ordering of polymer chains with limited flexibility. *Journal of Stat Phys*, 38:161–182.

Kim, D. H., Fasulo, P. D., Rodgers, W. R., and Paul, D. R. (2007). Structure and properties of polypropylene-based nanocomposites: Effect of PP-g-MA to organoclay ratio. *Polymer*, 48:5308–5323.

Kim, K., Utracki, L. A., and Kamal, M. (2004). Numerical simulation of polymer nanocomposites using self-consistent mean-field model. *J. Chem. Phys.*, 121:10766–10777.

Kim, S. and Karilla, S. J. (1991). Microhydrodynamics. *Butterworth-Heinemann.*

Kindt, P. and Briels, W. J. (2007). A single particle model to simulate dynamics of entangled polymer melts. *J. Chem. Phys.*, 127:134901–1–12.

Krishnamoorti, R. and Giannelis, E. P. (1997). Rheology of end-tethered polymer layered silicate nanocomposites. *Macromolecules*, 30:4097–4102.

Krishnamoorti, R., Ren, J., and Silva, A. S. (2001). Shear response of layered silicate nanocomposites. *J. Chem. Phys.*, 114:4968–4972.

Krishnamoorti, R., Vaia, R. A., and Giannelis, E. P. (1996). Structure and dynamics of polymer layered silicate nanocomposites. *Chem. Mater.*, 8:1728–1734.

Kroger, M. and Hess, S. (1993). Viscoelesticity of polymeric melts and concentrated solutions, the effect of flow-induced alignment of chain ends. *Physica A*, 195:336–353.

Laske, S., Kracalik, M., Gschweit, M., Feuchter, M., Maier, G., Pinter, G., Thomann, R., Friesenbichler, W., and Langecker, G. R. (2009). Estimation of reinforcement in compatibilized polypropylene nanocomposites by extensional rheology. *Journal of Applied Polymer Science*, 111:2253–2259.

Lee, K. M. and Han, C. D. (2003). Rheology of organoclay nanocomposites: effects of polymer matrix/organoclay compatibility and the gallery distance of organoclay. *Macromolecules*, 36:7165–7178.

Letwimolnun, W., Vergnes, B., Ausias, G., and Carreau, P. J. (2007). Stress overshoots of organoclay nanocomposites in transient shear flow. *J. Non-Newtonian Fluid Mech.*, 141:167–179.

Leygue, A., Bailly, C., and Keunings, R. (2006a). A differential tube-based model for predicting the linear viscoelastic moduli of polydisperse entangled linear polymers. *J. Non-Newtonian Fluid Mech.*, 133:28–34.

Leygue, A., Bailly, C., and Keunings, R. (2006b). A tube-based constitutive equation for polydisperse entangled linear polymers. *J. Non-Newtonian Fluid Mech.*, 136:1–16.

Leygue, A., Beris, A. N., and Keunings, R. (2001). A constitutive equation for entangled linear polymers inspired by reptation theory and consistent with non-equilibrium thermodynamics. *J. Non-Newtonian Fluid Mech.*, 101:95–111.

Li, J., Zhou, C., Wang, G., and Zhao, D. (2003). Study on rheological behavior of polypropylene/clay nanocomposites. *J. Appl. Polym. Sci.*, 89:3609–3617.

Likhtman, A. E. and McLeish, T. C. B. (2002). Quantitative theory for linear dynamics of linear entangled polymers. *Macromolecules*, 35:6332–6343.

Lim, S. T., Hyun, Y. H., Choi, H. J., and Jhon, M. S. (2002). Synthetic biodegradable aliphatic polyester/montmorillonite nanocomposites. *Chem. Mater.*, 14:1839–1844.

Lim, Y. T. and Park, O. O. (2001). Phase morphology and rheological behavior of polymer/layered silicate nanocomposites. *Rheol. Acta*, 40:220–229.

Liu, L. M., Qi, Z. N., and Zhu, X. G. (1999). Studies on the nylon 6/clay nanocomposites by melt intercalation process. *J. Appl. Polym. Sci.*, 71:1133.

Ma, W. K. A., Chinesta, F., Ammar, A., and Mackley, M. R. (2008). Rheological modeling of carbon nanotube aggregate suspensions. *J. Rheol.*, 52:1311–1330.

Maier, W. and Saupe, A. (1960). *Naturforschung*, 15:287.

Malkin, A. Y. (1990). Rheology of filled polymer. *Advances in polymer science*, 96:69–97.

Malkin, A. Y. (2009). The state of the art in the rheology of polymer: Achievements and challenges. *Polymer Science, Ser. A.*, 51:80–102.

Marrison, F. A. (2001). *Understanding rheology.* Oxford university press, New York.

Marrucci, G., Greco, F., and Lanniruberto, G. (2001). Integral and differential constitutive equations for entangled polymers with simple versions of CCR and force balance on entanglements. *Rheol. Acta*, 40:98–103.

Marrucci, G. and Grizzuti, N. (1988). Fast flow of concentrated polymers: Predictions of the tube model on chain stretching. *Gazz. Chim. Ital.*, 118:179–185.

McLeish, T. C. B. (2002). Tube theory of entangled polymer dynamics. *Advances in Physics*, 51:1379–1527.

Mead, D. W. and Leal, L. G. (1995). The reptation model with segmental stretch I. Basic equations and general properties. *Rheol. Acta*, 34:339–359.

Mead, D. W., Yavich, D., and Leal, L. G. (1995). The reptation model with segmental stretch II. Steady flow properties. *Rheol. Acta*, 34:360–383.

Mobuchon, C., Carreau, P. J., and Heuzey, M. C. (2007). Effect of flow history on the structure of a non-polar polymer/clay nanocomposite model system. *Rheol Acta*, 46:1045–1056.

Naderi, G., Lafleur, P. G., and Dubois, C. (2008). The influence of matrix viscosity and composition on the morphology, rheology, and mechanical properties of thermoplastic elastomer nanocomposites based on EPDM/PP. *Polymer Composites*, 29:1301–1309.

Okamoto, M., Morita, S., and Kotaka, T. (2001). Dispersed structure and ionic conductivity of smectic clay/polymer nanocomposites. *Polymer*, 42:2685–8.

Okamoto, M., Morita, S., Taguchi, H., Kim, Y. H., Kotaka, T., and Tateyama, H. (2000). Synthesis and structure of smectic clay/poly(methyl methacrylate) and clay polystyrene nanocomposites via in situ intercalative polymerization. *Polymer*, 41:3887–90.

Onsager, L. (1949). The effects of shape on the interaction of colloidal particles. *Ann. N.Y. Acad. Sci.*, 51:627–659.

Ottinger, H. C. (1999). A thermodynamically admissible reptation model for fast flows of entangled polymers. *J. Rheol.*, 43:1461–1493.

Ottinger, H. C. (2005). *Beyond equilibrium thermodynamics.* Wiley-Interscience.

Ottinger, H. C. and Grmela, M. (1997). Dynamics and thermodynamics of complex fluids. II. Illustrations of a general formalism. *Phys. Rev.E*, 56:6633–6655.

Padding, J. T. and Briels, W. J. (2001). Uncrossability constraints in mesoscopic polymer melt simulations: Non-rouse behavior of $c_{120}h_{242}$. *J. Chem. Phys.*, 115:2846–2859.

Pattamaprom, C. and Larson, R. G. (2001). Constraint release effects in monodisperse and bidisperse polystyrenes in fast transient shearing flows. *Macromolecules*, 34:5229–5237.

Rajabian, M., Dubois, C., and Grmela, M. (2005). Suspension of semiflexible fibers in polymeric fluids: rheology and thermodynamics. *Rheol. Acta*, 44:521–535.

Rajabian, M., Naderi, G., Beheshty, M., Lafleur, P., Dubois, C., and Carreau, P. J. (2008). Experimental study and modeling of flow behavior and orientation kinetics of layered silicate/polypropylene nanocomposites in start-up of shear flows. *International Polymer Processing*, 23:110–118.

Ramazani, A., Ait-Kadi, A., and Grmela, M. (2001). Rheology of fiber suspensions in viscoelastic media: Experiments and model predictions. *J. Rheol.*, 45:945–962.

Ren, J. and Krishnamoorti, R. (2003). Nonlinear viscoelastic properties of layered silicate based intercalated nanocomposites. *Macromolecules*, 36:4443–4451.

Ren, J., Silva, A. S., and Krishnamoorti, R. (2000). Linear viscoelasticity of disordered polystyrene-polyisoprene block copolymer based layered silicate nanocomposites. *Macromolecules*, 33:3739–3746.

Rouse, J. P. E. (1953). A theory of the linear viscoelastic properties of dilute solutions of coiling polymers. *J. Chem. Phys.*, 21:1272–1280.

Sarti, G. S. and Marrucci, G. (1973). Thermomechanics of dilute polymer solutions: multiple bead-spring model. *Chem. Eng. Sci.*, 28:1053–1059.

Sarvestani, A. S. and Picu, C. R. (2005). A frictional molecular model for the viscoelasticity of entangled polymer nanocomposites. *Rheol. Acta*, 45:132–141.

Singh, A. P. and Rey, A. D. (1998). Microstrucure constitutive equations for discotic nematic liquid crystalline materials. *Rheol. Acta*, 37:374–386.

Sinha Ray, S. (2006). Rheology of polymer/layered silicate nanocomposites. *J. Ind. Eng. Chem.*, 12:811–842.

Sinha Ray, S. and Bousmina, M. (2005a). Biodegradable polymers and their layered silicate nanocomposites: In greening the 21st century materials world. *Prog. Mater Sci.*, 50:962–1079.

Sinha Ray, S. and Bousmina, M. (2005b). Poly(butylene sucinate-co-adipate) montmorillonite nanocomposites: effect of organic modifier miscibility on structure, properties, and viscoelasticity. *Polymer*, 46:12430–12439.

Sinha Ray, S., Bousmina, M., and Okamoto, K. (2005). Structure and properties of nanocomposites based on poly(butylene succinate-co-adipate) and organically modified montmorillonite. *Macromol. Mater. Eng.*, 290:759–768.

Sinha Ray, S. and Okamoto, M. (2003a). New polylactide/layered silicate nanocomposites, melt rheology and foam processing. *Macromol. Mater. Eng.*, 288:936–944.

Sinha Ray, S. and Okamoto, M. (2003b). Polymer/layered silicate nanocomposites: a review from preparation to processing. *Prog. Polym. Sci.*, 28:1539–1641.

Solomon, M. J., Almusallam, A. S., Seefeldt, K. F., Somwangthanaroj, A., and Varadan, P. (2001). Rheology of polypropylene/clay hybrid materials. *Macromolecules*, 34:1864–1872.

Song, Y. S. and Youn, J. R. (2004). Modeling of rheological behavior of nanocomposites by brownian dynamics simulation. *Korea-Australia Rheology Journal*, 16:201–212.

Steeves, D. M., Farrell, R., and Ratto, J. A. (2007). Investigation of polybutylene succinate-co-adipate(PBSA)/montmorillonite layered silicate (MLS) melt-processed nanocomposites. *Journal of Biobased Materials and Bioenergy*, 1:94–108.

Tung, J., Gupta, R. K., Simon, G. P., Edward, G. H., and Bhattacharya, S. N. (2005). Rheological and mechanical comparative study of in situ polymerized and melt-blended nylon 6 nanocomposites. *Polymer*, 46:10405–10418.

Vermant, J., Ceccia, S., Dolgovskij, M. K., Maffettone, P. L., and Macosko, C. W. (2007). Quantifying dispersion of layered nanocomposites via melt rheology. *J. Rheol.*, 51:429–450.

Wang, Y., Xu, J., Bechtel, S. E., and Koelling, K. W. (2006). Melt shear rheology of carbon nanofiber/polystyrene composites. *Rheol. Acta*, 45:919–941.

Wolfram, S. (1991). *Mathematica-A system for doing mathematics by computer.* Wesley-VCH, New York.

Wu, D., Zhou, C., Hong, Z., Mao, D., and Bian, Z. (2005). Study on rheological behaviour of poly(butylene terephthalate)/montmorillonite nanocomposites. *European Polymer Journal*, 41:2199–2207.

Xu, L., Reeder, S., Thopasridharan, M., Ren, J., Shipp, D. A., and Krishnamoorti, R. (2005). Structure and melt rheology of polystyrene-based layered silicate nanocomposites. *Nanotechnology*, 16:S514–S521.

Yziquel, F., Carreau, P. J., Moan, M., and Tanguy, P. (1999). Rheological modelling of concentrated colloidal suspension. *J. Non-Newtonian Fluid Mech.*, 86:133–155.

Zhao, J., Morgan, A. B., and Harris, J. D. (2005). Rheological characterization of polystyrene clay nanocomposites to compare the degree of exfoliation and dispersion. *Polymer*, 46:8641–8660.

Zimm, B. H. (1956). Dynamics of polymer molecules in dilute solution: viscoelesticity, flow birefringence and dielectric loss. *J. Chem. Phys.*, 24:269–278.